THE UNIVERSITY
of EDINBURGH

Strain softening and strain localisation in irreversible deformation of snow

Thomas W Barraclough

Ph.D.

The University of Edinburgh

2014

Abstract

The aim of this work was to visualise heterogeneous deformation in snow under controlled laboratory conditions. Heterogeneous deformation was observed for both homogenous and heterogeneous loading conditions. Understanding deformation of snow is important in many scientific fields including vehicle traction, avalanche forecasting, and winter sports.

This thesis investigates the deformation behaviour of snow on the centimetre scale under moderate strain rates (0.005 to 0.1 s^{-1}) when subject to one-dimensional compression or to indentation. In order to allow controlled and repeatable snow deformation experiments, a new type of artificial snow was developed. This snow type was examined by low temperature scanning electron microscopy and by traditional avalanche observer's methodology. Penetrometer experiments were conducted on the artificial snow and on natural seasonal snow in Scotland. The two snow types were found to be similar: results obtained on artificial snow are thus applicable to natural snow. A reproducible technique of manufacture and a thorough characterisation of the artificial snow are presented.

One-dimensional compression experiments were conducted on the artificial snow. The experiments were in confined compression in a specially constructed apparatus, designed to provide for back-lit photography. Images were taken at 0.25 second intervals and analysed using digital image correlation, thus providing 2D strain fields. With careful control of photographic parameters, it is demonstrated that process of applying tracer substances to the snow is not necessary, thus allowing an unprecedented resolution.

Spontaneously-forming strain localisations were observed for the first time, indicating strain softening behaviour. Damage was observed to propagate through the specimen as a moving front, resembling a wave. The force required to propagate the front remained nearly constant until the whole specimen was compacted, at which point a new front formed and the process repeated.

The experimental method was extended to 2D indention experiments with a range of sizes and shapes of indenter. Complex deformation fields were observed, extending up to 6 times the width of the indenter on each side. Observed deformation included tensile tearing as well as compression and shear. The maximum local strain achieved in the indentation experiments was similar to that achieved by the first compaction front in one-dimensional compression.

The work here presented has implications for snow deformation generally: strain localisation introduces a characteristic length, which may prevent scaling of models or results. The indentation results are particularly relevant to snow penetrometry, where indentation experiments are used to try and extract microstructural information from buried snow layers for the purpose of avalanche prediction. The common assumption that the penetrometer interacts only with snow very close to its tip may need to be reconsidered.

Lay summary

It is difficult to predict and understand the mechanical properties and behaviour of snow. This is because it is made of small particles which are joined to their neighbours; these joins are easily broken but quickly re-form. Snow also comes in many different types and has a wide range of strengths, densities and microstructural forms.

In order to simplify the situation, and to be able to conduct experiments which can be directly compared to each other, the snow needs to be the same every time. A type of manmade snow was developed to allow this, and was used in the experiments.

Snow was compressed and indented (using both sharp and rounded indenters). The required force was measured and photographs were taken at regular intervals. The photographs were analysed with a technique called Digital Image Correlation, which makes it possible to see where the snow is deformed and by how much (the strain field).

It was found that the snow did not deform evenly, but the deformation (strain) tended to be concentrated in certain areas. In the case of compression, deformation occurs in bands stretching across the specimen which move up or down until the whole specimen is deformed. For indentation, the strain field is complex and extends considerable distances from the indenters.

Understanding the mechanical properties of snow is important in many fields (such as vehicle traction, avalanche formation, or snow sports). One field of particular interest is avalanche prediction. It has been suggested that pushing instrumented rods (known as penetrometers) into snow and measuring the force required may provide a new way of predicting avalanches, and the work described in this thesis will help the development of that technique.

Declaration

I declare that this thesis has been composed by me and:

a) is my own work except where otherwise stated, and
b) has not been published elsewhere except where otherwise stated, and
c) has not been submitted for any other degree or award.

_____

Thomas W Barraclough

July 2014

Contribution statement

Chapters I and II are entirely my own work, prepared with the benefit of advice from Jane Blackford.

Chapter III builds on previous work at the University and this is acknowledged in the text. It is in preparation for publication in a different form in Journal of Physics D: applied physics with the working title *A new technique for making artificial snow and its characterisation using low temperature SEM.* The authors will be Jane R Blackford, Tom W Barraclough, G Skouvaklis and James Floyer. GS and JB developed the original snow making process. I improved and developed the process. JF and I performed the characterisation including preparation for LT-SEM. The LT-SEM was operated by Chris Jeffrey. JB and I prepared the manuscript of the paper.

The work described in Chapter IV has been published in a different form as a proceeding paper at the 2010 International snow science workshop. The title was *Snow in Scotland: SnowMicroPen analysis of natural and artificial snow samples*. The authors were Tom W Barraclough, Jane R Blackford and Michael Zaiser. JB and I conducted the fieldwork with assistance from James Floyer. I conducted the laboratory experiments. I wrote the manuscript of the paper with assistance from JB and MZ.

Chapters V and VI are my own work, conducted with the benefit of advice from Jane Blackford, Michael Zaiser (especially design of the experiment, chapter V) and Tim Stratford (especially DIC, chapter VI). These chapters have not been published elsewhere, but are introduced in the Nature Materials paper mentioned below.

Work presented in chapter VII is under review for publication in a different form in Nature Materials with the title *Propagating compaction bands in confined compression of snow: experiment and modelling.* The authors will be T W Barraclough, J R Blackford, S Liebenstein, S Sandfeld, T J Stratford, G Weinlander and M Zaiser. I designed the experiments with assistance from TS and JB (chapters V and VI). I conducted the experiments. SL, SS, GW and MZ contributed to models which are not reported in this thesis. MZ prepared the manuscript of the paper. SL wrote a program to visualise the data which has been used to create some of the figures in chapter VII.

Chapters VIII and IX are my own work, conducted with the benefit of advice from Jane Blackford and Michael Zaiser.

Acknowledgements

First and foremost, I wish to recognise the contribution of Jane Blackford, my principal supervisor, for her advice, guidance, patience and support throughout my PhD and also for proofreading the thesis. I also wish to thank Michael Zaiser and Vasileios Koutsos, my secondary supervisors, who have also given invaluable advice and assistance.

I would like to thank James Floyer, who accompanied me in some of the experimental work in the laboratory and in the field, and who and gave me an introduction to the avalanche observer's craft. I also wish to thank Chris Jeffree for his help in acquiring the SEM images which illustrate this thesis and Tim Stratford for his advice on using GeoPIV.

Special thanks to the university technical team, who manufactured the experimental equipment from my designs and who help to keep the laboratories running smoothly.

I am grateful to EPSRC who provided funding for my project, and to Michelin, whose investment in winter tyre research at the University of Edinburgh has created a facility without which this research would not have been possible.

Finally, I wish to thank my friends, family and officemates, too numerous to name here, for their efforts in keeping me sane, and for their encouragements and support, especially towards the end of the process. A special mention in this regard to my partner Holly Spice for supporting me throughout.

Glossary

General terms

CPT	Cone penetration test, used in the context of the established geotechnical investigation technique rather than typical modern snow penetrometers.
DIC	Digital image correlation. Tracking the movement of object in a series of digital images by means of computerised image analysis.
GeoPIV	The DIC programme used in this work.
Metamorphism	Changes occurring to snow particles or snowpack due to temperature humidity, time etc.
Penetrometer	Device intended for insertion into snowpack and capable of measuring the properties of said snow.
SEM	Scanning electron microscope.
SnowMicroPen	High resolution force-measuring penetrometer instrument developed by Jerome Johnson and Martin Schneebeli.
Snowpack	Layered natural snow on the ground.
SMP	SnowMicroPen.
Texture	The combination of shape and contrast required for DIC to succeed.

Snow types and symbols according to particle shape

⟋	Decomposed precipitation	Broken angular precipitation particles.
⛆	Groupel	Frosty round particles up to 3 or 4 mm across, similar to hail but softer.
▬	Icecrust	Thin very hard layer in the snowpack usually caused by surface melting but subsequently buried. Harder than a meltcrust.
◎◎	Meltcrust	Thin very hard layer in the snowpack usually caused by surface melting but subsequently buried. Not as hard as an icecrust.
○	Melt Form	Part melted and rounded particles.
↔	Needles	Needle like or long thin cylinders.
⚘	Polycrystals	Groups of rounded particles sintered together.
∨	Rime	A delicate frosty crystal growing from a surface, also called surface hoar.
●	Rounds	Rounded or near spherical particles produced by metamorphism.
=	Rain crust	Thin very hard layer in the snowpack caused by surface rainfall, may be subsequently buried.
*	Stellars	Classic snowflake 6-fold star, also includes dendritic forms.

Snow types, general descriptive terms

Firn	Old hard snow surviving from previous seasons.
Powder snow	Fresh soft snow.
Wet snow	Snow with significant liquid water content, usually with rounded particles or polycrystals.
Windslab	Hard snow layer formed by wind-blown and broken snow particles.

Words with specific meanings in this thesis

Incremental	Referring to changes occurring, or time elapsed, between images in the DIC experiments.
Irreversible	in regard to deformation, refers to deformation that will not be revered when stress is removed. Plastic deformation, brittle fracturing or any process involving non-negligible bond breaking is thus said to be irreversible.

Table of contents

Chapter I: Introduction

Aim

The aim of this chapter is to introduce the field of snow mechanics and provide the reader with an outline of the thesis.

1. General Introduction

Snow is many things: a playground; an avalanche threat; a water source; an impediment to transport; an indicator of the passing seasons. It is famous for its intricate and symmetric structures on the micro scale and its majestic beauty on the macro scale. As with any other substance found in such copious amounts in populated areas, it is necessary for mankind to work with, on, or around snow. In this respect it must be examined and understood in the manner of an engineering material. Some of the problems (and opportunities) caused by snow are outlined below – the engineering invested in solving (or exploiting) them is covered in chapter II.

One of the most serious interactions between man and snow is in case of an avalanche. Injuries and fatalities occur across the globe every year. In addition, avalanches destroy property and resources must be invested in preventative action, such as slope stabilisation and protective structures.

Most everyday vehicles struggle for traction on snowy surfaces. Transport is critical to economic activity as well as leisure pursuits in the modern world, so efforts are made to address this. Snow may be ploughed aside or chemically removed (e.g. by adding salt to encourage melting) and tyre manufactures provide specialist winter tyres designed for ice and snow. For specialist use, tacks or balloon tyres are an option, but even these can be overwhelmed.

Occasionally there is a need to build structures on snow. Examples include Antarctic research bases and military installations in the polar north. Ice roads provide vital access to remote mining caps in northern Canada and other remote communities in cold regions.

Recent concerns over climate change have also focused attention on snow, as it is the raw material from which glaciers and ice sheets form. The transition from snow, through firn into ice must be understood in order to predict the future of the world's ice masses, and thus the sea level rise in the coming decades.

One final application for snow science is snow sports. Aside from the safety risk posed by avalanches, understanding snow provides opportunities for sportsmen to improve performance, and for ski resorts to improve customer experience (and therefore revenue).

The work presented in this thesis cannot claim to address everything mentioned above, but provides a building block for more applied research that will follow. It addresses a weakness in the current understanding of snow: what is the origin of the observed mechanical properties, and how does it relate to the deformation patterns?

2. Outline of the thesis

The thesis describes experiments to visualise the deformation flow in snow and the development of the tools needed to do so. It is divided into 9 chapters, the first of which is this brief introduction. A glossary of terms is provided at the front.

Chapter II reviews past work by other authors, and explains the need for further understanding of snow deformation. The chapter should provide an adequate introduction to the field to place the later chapters in context, and will also direct to reader to some of the more important papers and reviews, should they wish to learn more.

Chapter III describes the development of an artificial snow type which was used in the subsequent experiments, along with the rationale for using artificial snow in place of natural snow. The resulting snow type is thoroughly characterised including imaging by low temperature SEM. The provision of the cold laboratory is also described, including an assessment of its temperature and humidity characteristics.

Chapter IV describes experiments conducted in the field in Scotland using a SnowMicroPen instrument, and compares the results to those obtained on laboratory made artificial snow. The experiments provide a validation of the artificial snow as a model material for natural snow, as well as an introduction to penetrometer instruments.

Chapter V describes the experiments I aimed to conduct, and develops a specification for an experimental apparatus. The specification is developed into a working machine, including a description of the design process.

Chapter VI describes the analytical methods which were developed and applied in order to interpret the results from the experiments. The concept of digital image correlation is introduced, and a method of using it to derive the deformation flow and strain visualisations is described.

Chapter VII presents the results of one-dimensional compression experiments. Observed strain localisation phenomena are described, and a possible explanation is put forward.

Chapter VIII presents the results of the indentation experiments. The deformation flow field is described for three different indenters, with comparisons between them. Relationships between deformation events and the force required to drive the indenter forward are highlighted.

Chapter IX presents the general conclusions, including a summary of techniques developed or improved upon and the implications of the experimental results. Some suggestions for further work are also made.

Chapter II: Literature review

Aim

The aim of this chapter is to introduce the field of snow mechanics and review past work relevant to the remainder of the thesis.

1. Introduction

Snow is a term describing small particles of water ice, but must also encompass liquid and the ever-present water vapour which plays a major role in the development and metamorphism of snow. The word could apply to particles falling through the atmosphere but this work concentrates on snow on the ground or in the laboratory which forms a coherent mass. In this form snow may be considered to fall within the definitions of a cohesive granular material or an open-cell foam.

The field of snow mechanics has been pursued for many years with very diverse motivation including avalanche prediction, avalanche survival, winter sports, vehicle traction, construction of runways and research bases, hydrology and the life cycle of glaciers. Shapiro et al (1997) and Petrovic (2003) provide reviews of snow science and its applications.

As the work presented later is predominately experimental, I concentrate on past experimental work. Theory and models are included only briefly to put the experiments in perspective.

2. Formation and evolution of natural snow

Snow begins as an excess of water vapour in the air. Ice crystals will nucleate and begin to fall to earth, growing as they do so. Many different crystal forms are possible, depending on temperature and the amount of water vapour present. Understanding the development of the crystals is a wide field of work in its own right, and has been reviewed by Libbrecht (2005). Some example crystal morphologies are found in Figure 1.

Once the snow crystals reach the ground they immediately bond to their neighbours to form a cohesive mass. The density of the resulting snow (which, as discussed later, is critical to mechanical properties) is determined by a process known as ballistic deposition. Yang et al (2000) and Kadu and Herrmann (2011) explore this process, whilst it was applied specifically to snow by Löwe et al (2007). The density of the resulting snow is found to depend heavily on: particle size (and therefore mass); particle velocity; and the strength of instantaneously-formed bonds.

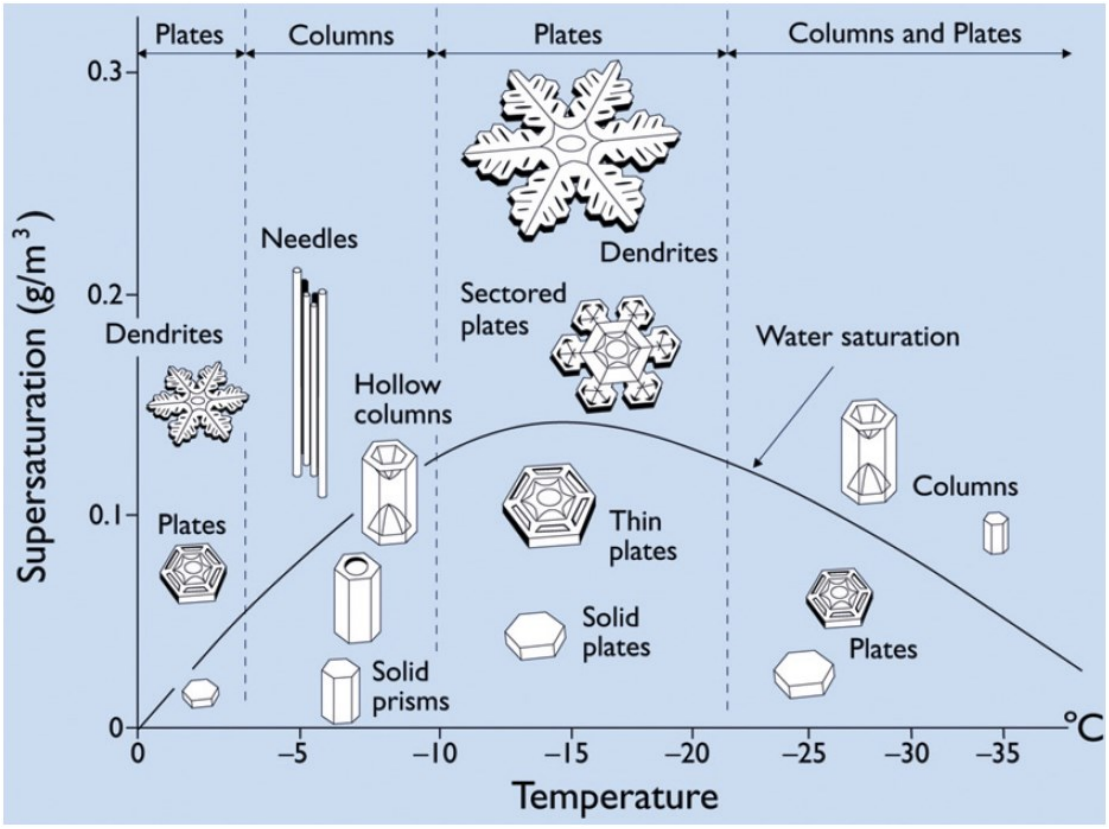

Figure 1: Diagram of ice crystal morphology according to temperature and vapour content. Reproduced from Libbrecht (2005).

Snow particles bond to their neighbours via sintering. This process begins very rapidly: Szabo and Schneebeli (2007) measured bond strength after sintering for contact times as little as 20 ms. The strength of sintering according to temperature and time is summarised in Figure 2. After initial bonding, which serves to hold particles in place, sintering will continue at a rate determined by temperature and stress. Sintering of ice particles has been reviewed by Blackford (2007), the processes at work are summarised in Figure 3.

Snow on the ground will experience changes in mechanical properties due to metamorphism. Historically, metamorphism had been divided into two types, equilibrium and kinetic. Equilibrium metamorphism occurs under isothermal conditions, especially at higher temperatures. It is dominated by sintering and rounding of particles, with reduction in surface area and strengthening of inter-particle bonds.

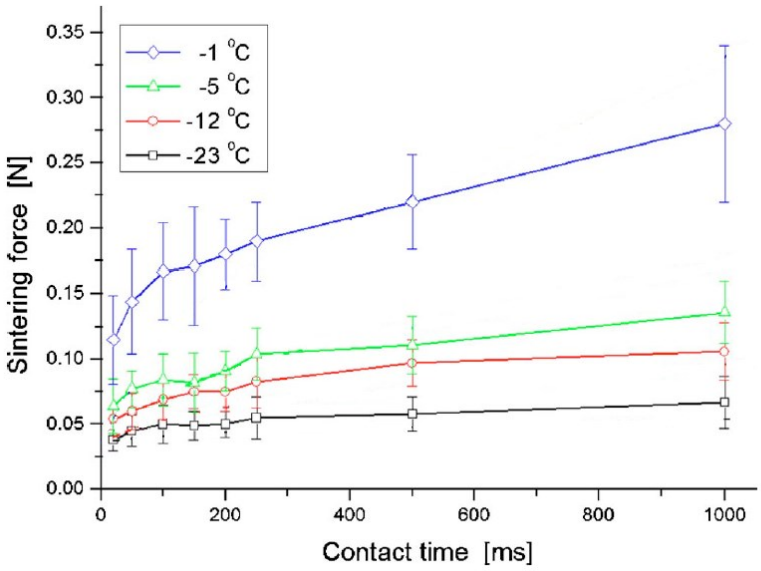

Figure 2: Force required to separate two sintered 3 mm radius ice particles as a function of time in contact. Reproduced from Szabo and Schneebeli (2007)

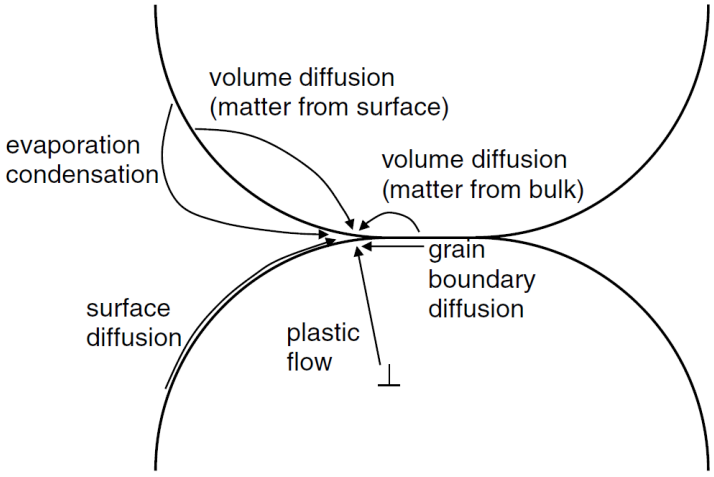

Figure 3:The mechanisms of transport during sintering. Reproduced from Blackford (2007).

Kinetic metamorphism tends to weaken the snow and is driven by (macroscopic) temperature gradients. It tends to produce angular and weakly bonded particles. Colbeck (1982) provides an overview of the processes at work and the grain forms that result.

Snow pack is built up in layers corresponding to different snowfall events, and with different metamorphic histories. This leads to large differences in mechanical properties within a vertical profile. Large variability is also found in profiles from different locations. Differences occur due to wind direction, aspect of slope, insolation and other environmental conditions, but apparently similar and closely located sample sites can also show significant variability. Schweizer et al (2008) review spatial variability.

In order to assist the measurement, recording and researching of natural snow, an internationally accepted standard classification has been developed (Fierz et al 2009). It provides 9 snow types with 37 subcategories, and also sets out standard methods for assessing particle size, liquid water content, hardness, and a range of other parameters.

3. Aims and motivations of past work

In order to place past work in perspective, it is necessary to understand why it was undertaken. I will briefly describe the main fields which draw on snow mechanics, and which provide motivation for further studies of it.

3.1. Avalanches

Perhaps the oldest and most established field of snow research is avalanche prediction, prevention and survival. Schweizer et al (2003) reviews the formation of avalanches, including the development of the snow pack and moment of release. It has often been assumed that avalanches start as shear failure, but recent work by Heierli et al (2008) proposes an interesting alternative: a weak layer in the snow pack may fail in compression, with the fracture able to propagate over long distances using energy released by the descending slab. With the weak layer destroyed, friction between the substrate and overlying slab then determines the probability of an avalanche. There is a clear need to understand both shear and compressive behaviour of snow in order to develop the competing theories further.

In the day to day work of avalanche risk forecasting, tests are performed on snow in the field. There is a need to understand the mechanics behind these techniques, which are discussed in section 4. If the behaviour of the snow under test was better understood, it may be possible to improve the tests to reduce the subjective role of the observer and improve the quality and quantity of data available to forecasters.

Alongside prediction of avalanches, there are efforts to prevent them. This could be by holding the snow in place or by removing it in frequent small avalanches to prevent larger deposits accumulating. Shapiro et al (1997) describes the development of snow holding structures and the theories used to predict loads on them. He points out that design guidelines for Japan are quite different to those developed in Switzerland, due to wide variation in snow properties.

Deliberate triggering of avalanches to dispose of excess snow is frequently undertaken by means of explosive charges. The response of snow to such treatment is the topic of ongoing research, but the very rapid transient nature of this loading has little in common with the deformation behaviour explored in this work

3.2. Snow sports

Safety in snow sports depends heavily on predicting and avoiding avalanches, which are discussed in the previous section. In addition to the safety concerns, snow plays an obvious role in sports performance. The art of preparing pistes for skiers has been described by Fauve et al (2002). Tilling and compacting the snow feature heavily, with the aim of increasing hardness and thereby improving piste life. Equipment manufactures also show an interest in friction, (usually reducing it for high sped performance in skis, snowboards and the like) but friction is considered outwith the scope of this work.

3.3. Vehicle Traction

There are three prerequisites for successful vehicle motion on snow:

- The friction between the vehicle tracks or tyres and the snow must be sufficient to propel the vehicle forward against any drag or slope.

- The load bearing strength of the snow must be sufficient to support the vehicle via its tracks or tyres. If the vehicle sinks to the point that its load is carried by parts other than those intended, the normal force required for friction is lost. Shapiro (1997) described the formation of a pressure bulb under the vehicle, and states that both shear strength and compressive strength contribute to supporting it.
- The shear strength of the snow under the tracks or wheels must be sufficient to transmit tractive force to the underlying ground.

Friction between snow and other media is considered beyond the scope of this work, but compressive strength and shear behaviour will be examined more closely in section 5.

3.4. Structures, roads and runways built on snow

Shapiro et al (1997) describes the development of snow roads and runways. The process displays remarkable similarities to the development of pistes, with snow being compacted or tilled to increase density and strength.

Structures built on snow depend principally on the compressive response to long term fixed loading, or creep, rather than the faster deformations explored in this work.

Figure 4: Lockheed LC-130 Hercules equipped with skis and rockets performing a take-off from a snow runway in Greenland. Photo credit: Søren Wedel Nielsen, copyright licence: Creative Commons BY-SA 3.0.

3.5. Hydrology and the life cycle of glaciers

Snow on the ground forms an important reservoir of water for populations across the world, and sudden melting can cause flooding. To understand and predict these phenomena, the amount of water present in the reservoir has to be known. This so called *snow water equivalent* is a function of density and depth of snow cover, and so the mechanical properties of snow are not especially relevant.

The processes by which snow is compacted and sintered to become glacial ice is perhaps more similar to the kind of behaviour studied in this work, but the extraordinarily long timescales involved do limit the applicability of experiments carried out at much higher strain rates.

4. Properties overview

Snow is an open pored ice structure. Density (and therefore porosity) vary quite widely, and it is no great surprise to find that many of its mechanical properties depend on density and therefore show considerable variation also. Mellor (1975) and Shapiro (1995) provide good overviews of mechanical properties. The density of ice is 940 kg m^{-3}, so solid fraction and porosity can readily be estimated with the following rules of thumb:

$$Solid\ fraction \approx \frac{density\ in\ kg\ m^{-3}}{1000} \qquad Porosity \approx 1 - \frac{density\ in\ kg\ m^{-3}}{1000}$$

Equation 1 & 2

It is my preference to describe snow by its density in kg m^{-3} rather than by porosity or solid fraction, and this is also the normal choice in literature.

Density for fresh fallen snow tends to be in the range of 50 to 300 kg m^{-3}, but this increases with overburden, wind-driven repacking, liquid/vapour transport and time. A typical, established seasonal Scottish snowpack might range from 100 to 500 kg m^{-3}. The upper limit for what could be called snow is somewhat arbitrary: partial melting and refreezing can lead

to material much resembling snow with densities of 500 to 700 kg m^{-3}, whilst pore close-off due to overburden in glaciers tends to occur at densities in excess of 800 kg m^{-3}.

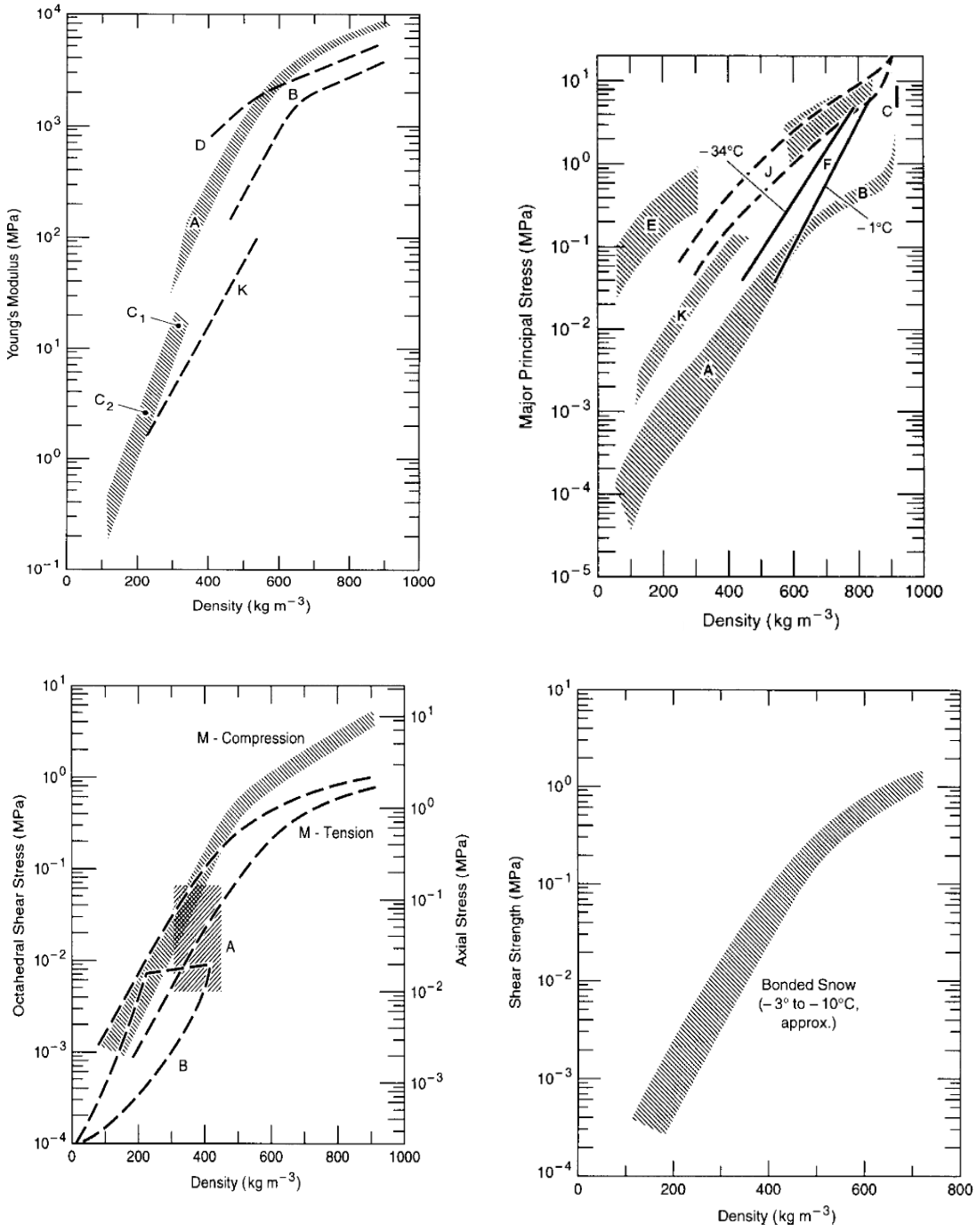

Figure 5: Stiffness and strength (peak stress) figures reproduced from Shapiro (1995), showing strength and stiffness to be correlated with density.

Snow shows a range of deformation behaviour – discussed later – which leads to a few different definitions of strength. The graphs presented in Figure 5 are based on maximum stresses attained during experiments, this being an easy definition to apply in all cases. Strength varies across several orders of magnitude from 0.1 kPa to 10 MPa. It is correlated with density, but even for a fixed density the range is still considerable, as microstructural parameters like bond strength and coordination number play a role. Stiffness shows a similarly wide variation to strength, but is better correlated to density. The typical range for stiffness is 0.1 MPa to 10 GPa.

Less data exists for Poisson's ratio, despite some interesting results which may warrant further investigation. At higher densities (>500 kg m^{-3}) it ranges form 0.2-0.3, and converges towards the value for ice (0.33) as density increases. At lower densities Poisson's ratio appears smaller, though with some range. Bader (1962) presents data showing Poisson's ratio of 0.1 at 200 kg m^{-3} rising to 0.2 at 500 kg m^{-3}, whilst Roch (1948)[1] has results as low as 0.04 for densities in the 200 kg m^{-3} to 350 kg m^{-3} range. Salm (1971) found his results were best explained by assuming a Poisson's ratio of zero at densities around 300 kg m^{-3}. These figures are rather low in comparison to other materials, but it is not impossible to imagine how load bearing microstructures in snow could fail with relatively little lateral displacement, said displacement being provided for by pore space. In this case little or no lateral load would be transmitted through the microstructure and thus Poisson's ratio would be low. This would particularity be the case if only a modest proportion of the microstructure was loadbearing at any given time, a circumstance which could result from the ballistic deposition described in section 2.

5. Field techniques and their results

Field tests are carried out routinely in order to understand the condition of the snowpack at a given place and time. Manual snow pit techniques remain the principal form of observation, but there has been considerable work on penetrometers which could be used to attain less subjective measurements, and are much quicker as they do not require the practitioner to dig a pit.

[1] Original in French. Data summarised in English in Sanger (1964)

5.1. Traditional avalanche observer's methods

There is a long established standard method of observation employed in avalanche forecasting. The current methodology is set out in Fierz et al (2009). The observer will generally dig a pit to the base of the snow or to a layer they are confident is stable. They will then record the grain form, temperature, hardness and sometimes density for each layer in the snowpack. Hardness is expressed as the largest of the following which a can be inserted into the snow with only moderate force: fist, flat hand, finger, pencil or knife. This technique has the advantage that very little equipment has to be carried on the hill and that which is required is very reliable.

The technique for measuring hardness is potentially quite subjective. A range of devices have been proposed to address this including a thin blade devices (Fukue 1977, Borstad and McClung 2011) and round pistons or disks (Klein 1946, Takeuchi et al 1998).

These devices differ from penetrometers as discussed later in that they are designed to assess the hardness of one layer in isolation, not the whole snowpack. Such devices have not gained widespread popularity, possibly because the increase in accuracy of measurement is not considered to justify the expense, weight and reduced reliability.

In addition to the snow pit observations, stability tests may be performed. These tests aim to replicate the initiation of an avalanche by isolating a column of snow and then loading it to failure. The column may be pulled forward, in the manner of a shear test, or loaded vertically, relying on the angle of slope to produce downslope movement. The classic test in this form is the Rutsch block, believed to originate from Swiss army practices in the 1960s. A column 2 m cross slope, 1 m upslope and tall enough to include all potential failure planes is isolated and the loaded by the weight of a skier. A 7 point scale ranging from the column failing in isolation to surviving repeated jumping indicates stability. The technique and its limitations have been examined by Jamieson and Johnson (1993), and it remains one of the premier methods of assessing avalanche risk in existing snow pack.

The large size of a Rutsch block means that the test takes considerable time and effort to conduct. In a shovel shear test a 30 cm square column is pulled forward by a shovel placed behind. A column test is similar, it uses the same size column but it is "tapped" downwards on its top. In both cases the fracture surface may be examined, with smoother surfaces indicating lower stability. Schweizer and Jamieson (2010) reviewed and compared this type

of test, along with the propagation saw test, which consists isolating a section of slab and sawing out a known weak layer until failure occurs.

Traditional field observations have proved useful tools for predicting avalanche risk, but many techniques remain subjective. The high level of preparation required for some tests limits the number of samples which can be taken and thus leaves the results vulnerable to the spatial variability of the snow pack.

5.2. Field penetrometers

The idea of extracting useful information from layered snowpack simply by pushing an instrument into it without having to dig a snow pit is appealing: more sample locations could be measured more quickly, improving the probability of detecting localised features and reducing the risk that data was unrepresentative of the wider snowpack. The first instrument to be used for this purpose was the Swiss Rammsonde. It consisted of a rod with a conical tip (60° tip, 40 mm diameter), which was driven into the snow by the impact of a falling weight. The device is quick and easy to use, but the relatively large cone prevents detection of thin layers. This limits its usefulness for avalanche forecasting work but Wong et al (1992) found that Rammsonde data can be used to help predict tracked vehicle performance and load bearing ability. A comprehensive assessment of construction of snow roads and runways by Abele (1990) compared Rammsonde data to mechanical properties of snow. Unconfined compressive strength and shear strength were both found to be correlated with ram hardness but the data shows considerable scatter.

More recently, other penetrometers have been developed. They seek to improve resolution by using smaller tips. Examples include the resistograph (Bradley 1968) which measured force required to pull two cones back up though the snowpack after initial insertion; the electric cone penetrometer (Schaap and Fohn 1987) and SABRE (Mackenzie and Payten 2002) which both measured the force required to drive a small tip downwards; and the SnowMicroPen (SMP hereafter), presented by Johnson and Schneebeli (1999). This device has a 5 or 6 mm diameter 60° conical tip and is motor driven at 20 mm s^{-1}. The force required to drive the tip is measured at 4 μm intervals, and some versions also measure snow temperature.

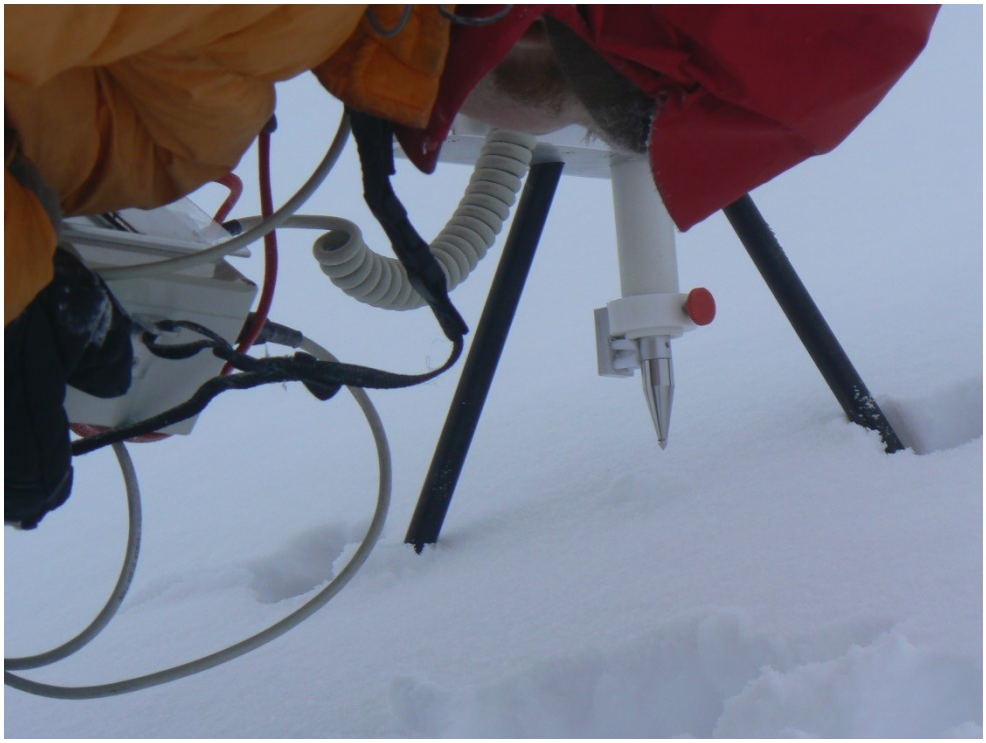

Figure 6: The SnowMicroPen in use (top). The tip about to enter the snow (bottom)

Whilst all the above devices measure force, penetrometers were also developed to measure other properties, including albedo, electrical conductivity and capacitance. A more detailed review of penetrometers is available in Floyer (2008).

The development of these smaller-tipped devices corresponds to a new use of penetrometers: they are not viewed as a means of recovering bulk properties but rather to characterise the 'texture' of the snow – texture[2] being linked to microstructure.

Schneebeli et al (1999) presented a model for extracting such textural parameters from the very detailed force record provided by the SMP. This model was based on previous work in ceramic foams (Gibson and Ashby 1988, Ashby et al 1986) and describes snow in terms of a randomly distributed network of elastic brittle elements, which are removed from the model on rupture. It is assumed that the instrument only interacts with elements in contact with the tip, not with a wider interaction volume.

The flexing and subsequent rupture of element in the model is assumed to cause a triangular shaped peak in the force record, as illustrated in Figure 7. By examining the sequence of peaks, a number of parameters may be extracted as detailed in Table 1. This model has been improved upon by Marshall and Johnson (2009), who tested the reliability of the parameter extraction under various conditions and suggested adaptations to improve accuracy at higher densities and to take account of limited time-domain resolution of the instrument. Löwe and Herwijnen (2012) compare the force record to Poisson shot noise as an alternative method of deriving parameters.

This model has a degree of appeal in avalanche forecasting because the recovered parameters resemble those used in current best practice forecasting with manual observation pits. They could therefore be viewed as more useful than bulk properties like strengths or stiffnesses.

[2] This is not the same definition of texture used later in the thesis for discussion of digital image correlation techniques.

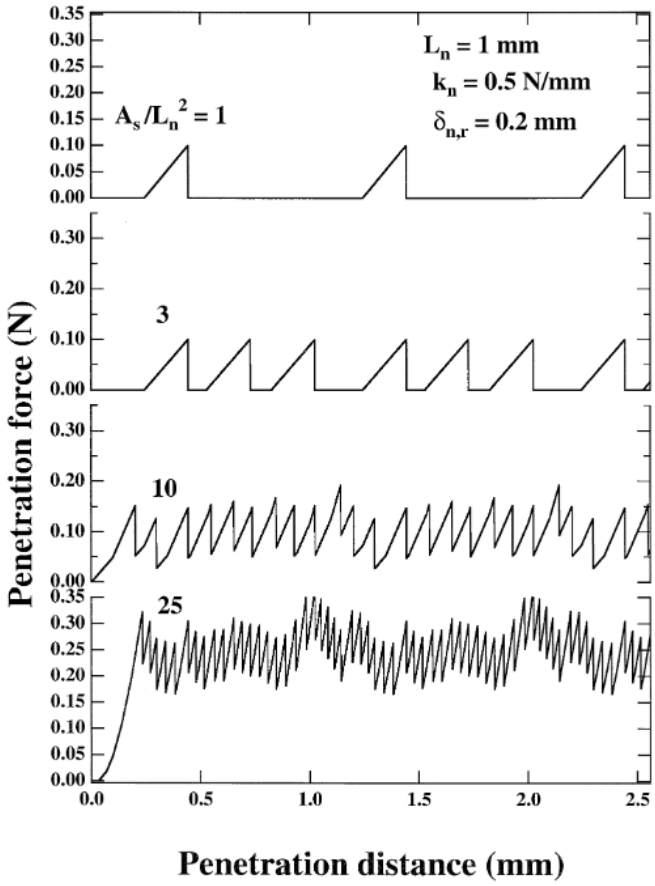

Figure 7: Triangular shaped peaks combine to create a form closely resembling the force data from the SMP. This example from Monte Carlo simulations of the proposed model, with progressively larger frontal area of the penetrometer.

Later authors including Pielmeier and Schweizer (2007) Bellaire et al (2009) Pielmeier and Marshall (2009) and Bellaire and Schweizer (2011) have taken a phenomenological approach to connect these abstracted parameter to avalanche stability. They compare SMP results to more traditional stability tests, such as rutschblocks, seeking some correlation between traditional tests and SMP based criteria (the selection of criteria for statistical testing being informed by the above models, but not exclusively so).

Pielmeier and Schweizer (2007) tested a wide range of different parameters extracted from SMP data for their ability to predict the stability of individual layers. The most promising of these parameters, in order of significance, were: the structural length; mean hardness; difference in structural length between the failure layer and adjacent layer; and micro-elastic modulus. A classification tree based on the first two these parameters was claimed to be 75% accurate.

Modelled feature	**Element property**	**Relationship**
Number of peaks per mm (n)	Structural length (L_n)	$L_n = \left(\frac{z\,A}{n}\right)^{\frac{1}{3}}$ Where z is the distance travelled by the penetrometer and A is its frontal area.
Peak to trough height	Element rupture strength (f_r)	equal
Mean force (F), rupture strength (f_r), and structural length (L_n).	Element deflection at rupture (δ)	$\delta = \frac{2{L_n}^3 F}{F_r A}$
Rupture force and element deflection at rupture	Element coefficient of elasticity (k)	$k = \frac{f_r}{\delta(1 + \mu \cot\theta)\sin\theta}$ Where μ is the coefficient of friction between the instrument and the snow and θ is the half-angle of the indenter cone.

Table 1: Relationships between features in the force data and element properties, according to Johnson and Schneebeli (1999).

Pielmeier and Marshall (2009) undertook a more complex, multivariate, statistical analysis including an investigation into the effect of repeat SMP measurements on the success of the classifier. They propose a microscale strength parameter for classification, defining it as rupture force over the square of element length, and report an improvement in classification accuracy to c. 88% depending on the number of SMP datasets available.

The previous studies had required the SMP data to be manually divided into layers for analysis, with weak layers manually identified before being tested for stability with the relevant classifier. Bellaire and Schweizer (2011) aim to avoid the need for manual

intervention, cautioning that it would be subjective, as well as time consuming. They approach this problem with four principal assumptions: that element lengths are larger in weak snow; that rupture forces are smaller; that large discontinuities are risk factors; and that deeply buried layers are harder to trigger. From these assumptions they developed a system which identified weak layers and then proposed which was the weakest. Failure occurred in an identified weak layer 90% of the time, but the algorithm could only specify which in 60% of tests. They note that minimum penetration resistance is relatively unhelpful in identifying the failure layer with minimum penetration resistance and failure corresponding in only 10% of cases.

Attempts have been made to better understand the flow of material around the tip of the penetrometer, and are described in section 5.3.

Penetration testing is widely used in other materials this is covered in section 9.

6. Laboratory experiments and their results

Several authors have undertaken laboratory experiments to better understand the mechanical properties of snow. It is possible to conduct better controlled experiments using more complex apparatus in the laboratory than is practical in the field, and the aim is generally to further scientific understanding of snow, rather than to ascertain the snow pack conditions at a given place and time.

6.1. Compression testing

It is generally accepted that snow exhibits ductile behaviour at low strain rates and brittle behaviour at higher rates. Ductile in this case applies to rising stress with increasing compressive strain, brittle in the case of sudden drops in stress, implying local failure of some type. The succession of sudden drops in stress gives a plateau effect, after which stress starts to rise (confined tests) or macroscopic failure occurs (unconfined tests). The critical strain rate at which this brittle-ductile transition occurs appears to vary according to the snow type, density, and age. Fukue (1977) performed confined (zero radial strain at boundary) and unconfined (zero radial stress at boundary) compression tests on 15 cm columns of sintered

artificial snow from a crushing process. The transition from ductile to brittle was observed to occur at strain rates of 2.6 $x10^{-4}$ to 2 $x10^{-2}$ s^{-1}, with larger values found in younger, less sintered snow with a lower compressive strength, as illustrated in Figure 8.

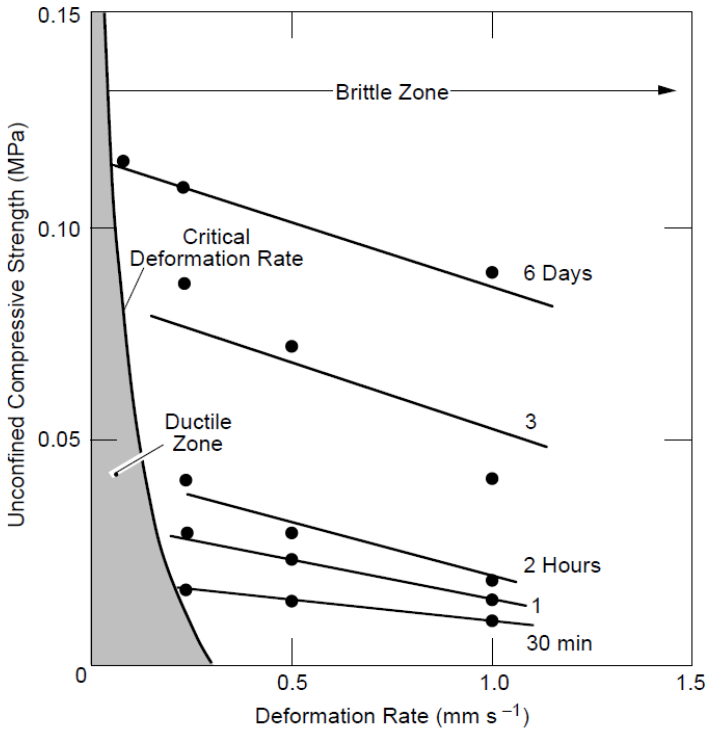

Figure 8: Compressive strength of snow according to deformation rate and sintering time. Brittle and ductile zones also indicated. Reproduced form Shapiro (1997), original data Fukue (1977).

It is in the brittle region that the more interesting behaviour is observed, as illustrated in Figure 9. The plateaux in his force measurements (analogous to stress) hint at strain softening behaviour not leading to macro failure. This is interesting because confined compression in other materials does not normally exhibit strain softening. Stain softening in unconfined tests is more common, but generally leads to failure, rather than recovery or plateaux behaviour. His confined and unconfined results are remarkably similar, given the different boundary conditions. This may in part be due to the low Poisson's ratio of snow, which minimises radial expansion (in case on an unconfined specimen) or radial stress (in case of the confined tests) thus reducing the differences between the tests. One interesting observation occurs in some unconfined tests close the brittle ductile transition. Here, multiple shallowly angled slip planes became visible at the specimen boundaries, indicating

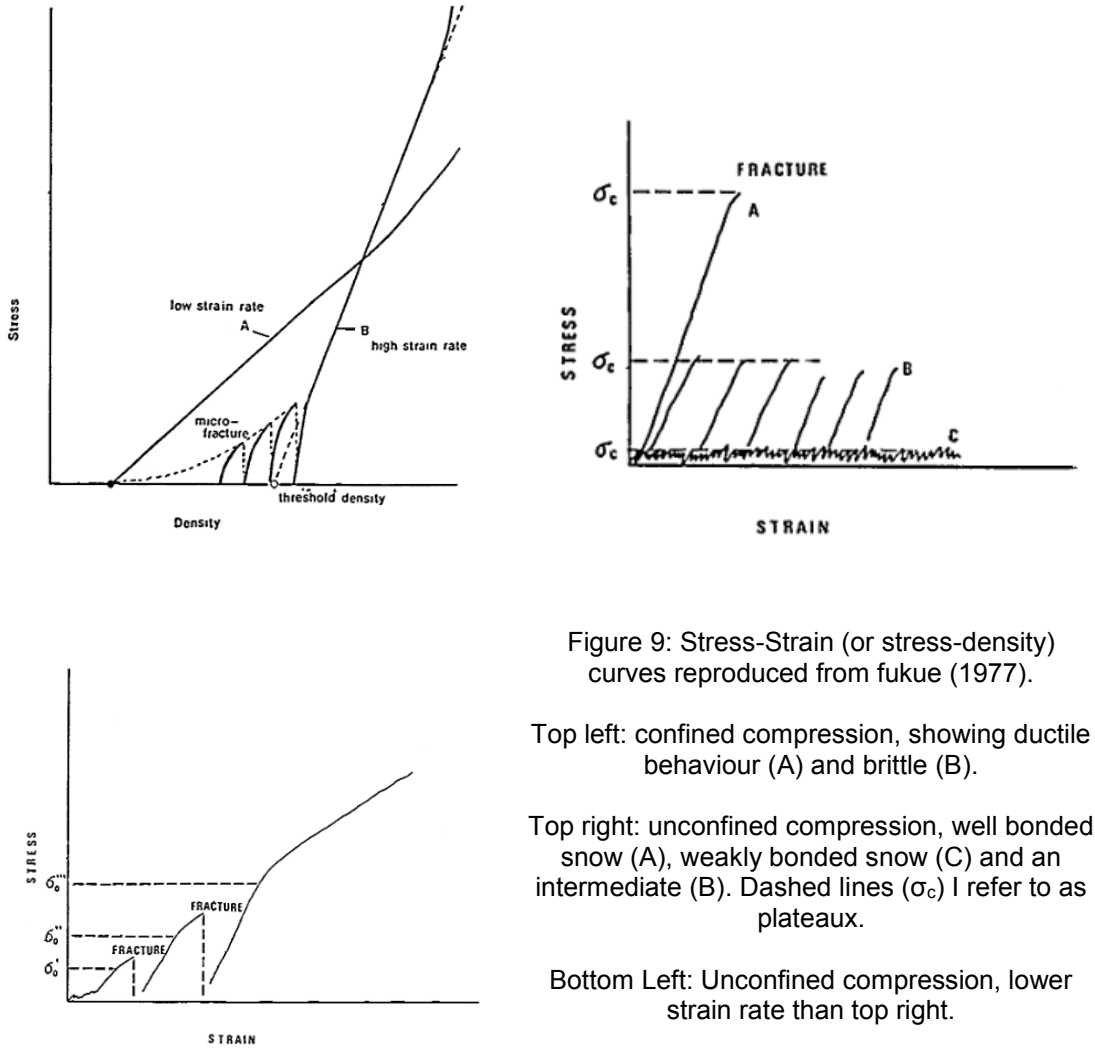

Figure 9: Stress-Strain (or stress-density) curves reproduced from fukue (1977).

Top left: confined compression, showing ductile behaviour (A) and brittle (B).

Top right: unconfined compression, well bonded snow (A), weakly bonded snow (C) and an intermediate (B). Dashed lines (σ_c) I refer to as plateaux.

Bottom Left: Unconfined compression, lower strain rate than top right.

(figures are described as “typical”, actual strain rates or velocities are not given)

softening (in the formation of said plane) and subsequent recovery (preventing failure of the whole specimen). This is indicated in Figure 10.

Yong and Metaxas (1985) explored the effect of age hardening. They reported that the force required to compact snow in confined compression (zero lateral strain) is initially low, but rises abruptly when a critical strain or density is reached. This critical strain did not vary with aging, but the stress increased with age. The initial low strain period should be seen as analogous to the plateaux behaviour described above.

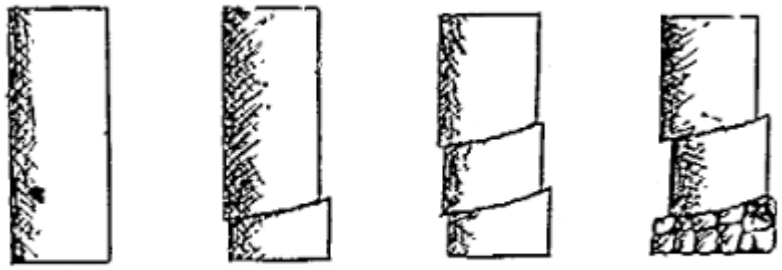

Figure 10: Multiple slip planes appear in unconfined compression (followed by disintegration of snow in contact with the lower platen). Reproduced from Fukue (1977)

Microstructural changes brought about by compression have been examined by Fukue (1977) and in more detail by Agrawal and Mittal (1995). In both cases, the testing was confined compression[3]. Grains do not simply become closer together, but also rotate to place their longest axis normal to the direction of loading. Co-ordination number rises, pore length reduces, and bond diameters increase (though bond diameter changes may in part be attributable to post-strain sintering).

When compression testing data was reviewed by Mellor (1975) a strong correlation between density and compressive strength was observed. Abele and Gow (1976) conducted further experiments on pre-compacted snow and found a similar trend. Other authors (Fukue 1977) assert that density alone is not sufficient to predict strength by providing a counter example: snow is known to sinter at constant density leading to increased strength.

6.2.Shear testing

Avalanches have often been assumed to begin with shear failures. Whilst recent work calls this into question (see section 3.1), there has been a considerable effort to understand shear strength in snow. As with compression testing, there is a transition between low speed ductile deformation and higher speed brittle failure. (Fukue 1977) conducted direct shear[4]

[3] Fukue defines confined as zero lateral strain. Agrawal and Mittal do not specify the nature of confinement but it is thought likely to be zero lateral strain.
[4] In a direct shear test a column of snow is placed in an assembly of two aligned rings. The rings are then displaced to force shear deformation along in the plane between the rings. A load normal to the direction of movement may be applied.

tests with normal loads up to 40 kPa, defining ductile behaviour as defined as having an increasing strength as shear proceeds, whilst brittle behaviour is that which shows a drop in force, corresponding to fracture. He attempts to fit his data to a Mohr-Coulomb relationship and finds that the friction angle depends heavily on shear velocity. de Montmollin (1982) provides a good summary of work up to that date alongside his own results. He used a torque shear apparatus known as a Bevameter with normal loading from 0 to 4.3 kPa. He observed a shear zone less than the full sample height, but did not define its thickness, and gives his results in terms of velocity not strain. The transition from ductile to brittle was found in the range of 1-5 mm s^{-1}. Fukuzawa and Narita (1993) conducted their experiments using a simple box apparatus (in the manner of a direct shear test with no normal load) on snow with a known weak layer. They define a brittle to ductile transition in terms of strain rate, at 8×10^{-5} s^{-1}. Schweizer (1998) conducted experiments in simple shear[5] with a normal stress of 470 Pa, and gives a transition according to strain rate, at 10^{-3} s^{-1}. The wide variation (more than an order of magnitude) is presumed attributable to differences in the snow used for the experiments, though also possibly due to differences in technique and specimen size.

More recently Reiweger et al (2010) developed an apparatus for testing simple shear in snow and examining the deformation distribution using digital image correlation (DIC). Specimens were spray painted to provide texture for the DIC system to track. This work noted the localisation of shear failure in a band, and the apparatus has since been used to examine shear failure in thin weak layers in the snowpack (Reiweger and Schweizer 2010)

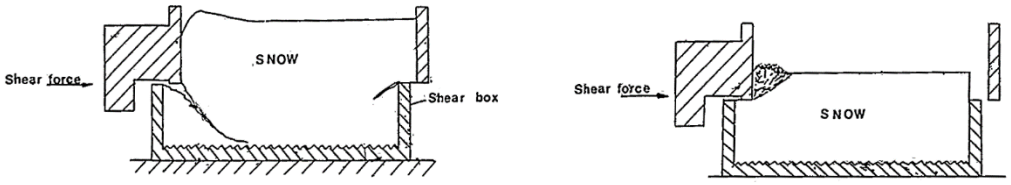

Figure 11: Direct shear test failure modes reproduced form Fukue (1977) described by him as tensile (right) or irregular (left). Irregular failure attributed to specimens which are too shallow, with tensile failure occurring when normal loads are low.

[5] In a simple shear test, a volume of snow is attached to a plate at the top and bottom which are then displaced. Shear stress is expected to be evenly distributed through the specimen, as opposed to the direct shear mentioned above, where it is concentrated around a plane. A load normal to the direction of movement may be applied.

Fukue (1977) also remarked that direct shear tests on snow do not necessarily result in failure on a well-defined plane, as illustrated in Figure 11. He proposes to avoid these modes by increasing normal load and specimen height, though other authors resort to adding extra transverse webs to their shear boxes to reduce the stress in proximity to the boundary.

That some authors quote strain and others velocity is understandable. It is in general desirable to be able to consider deformation behaviour in terms of stress and strain, as it provides for scaling of results. This is only appropriate however when stress and strain are evenly distributed through the volume over which they are calculated. Once strain starts to localise, regions of the specimen become inactive, but still contribute to the dimensions used to calculate strain. It is therefore more appropriate to express results in terms of velocity once deformation has localised. An alternate view is that neither velocity nor strain is sufficient: the experimental results are only properly described if spatial structuring of the deformation is described. This is the option I will pursue later in the thesis.

6.3. Indentation testing

The practice of using penetrometer instruments to discern layering in snow, disused in section 5.2, has driven demand for laboratory experiments to look at how such devices interact with the snow.

Indentation testing of snow has been performed with a range of different sized indenters. They can be divided into two general forms: large flat plates, and smaller tipped rods or blades. Yong and Fukue (1977) examined plate loading, and found that it could be adequately described by shear zones at the edges of the plate, with compression beneath it. Smaller tipped indenters show different results, with material pushed aside the indenter proceeds.

Fukue (1977) used a thin blunt blade. He defines slow deformation (up to 0.2 mm s^{-1}) as ductile, with force linearly related to speed. In this regime a plug of material develops ahead of the indenter and to both sides, but the experiment was not continued for long enough for a steady state to develop. At higher speeds he described the behaviour as brittle, with speed having little effect on force. Deformation in the brittle region was almost confined to a column below the indenter, and penetration force was found to be linearly correlated with unconfined compressive strength. Floyer and Jamieson (2010) also conducted rate

experiments using a hand driven penetrometer with rounded 12mm tip, and found little difference in force for speeds of 0.1 to 1.2 m s^{-1}.

Floyer and Jamieson (2006) used digital image correlation to track the movement of snow ahead of a range of tips. They found that a thin 40 mm by 2 mm blade disturbed the least material and a rounded or conical 12 mm tip the most, with little difference between the rounded and conical tips. Johnson (2003) noted that a build-up of material can occur in front of the tip, which does not further deform but is instead pushed ahead of the device. He terms the edge of this zone the *penetrometer effective surface*. This phenomenon is stronger with round tipped indenters than with conical ones.

Penetration testing has been explored in more detail for testing in other materials, this is covered in section 9.

7. Models of snow mechanics

The rapid changes in microstructure and properties of snow, along with the wide range of possible forms are cited as an obstacle to the development of models for snow (Nicot 2004). Despite this models have be developed with some success, at least for a few snow types and strain rates.

Modelling of snow can be broadly divided into two categories: models which describe snow as a continuum, and those which attempt to derive bulk properties by examining processes at the granular scale. I will look at these microstructural models first, with continuum models after.

7.1. Modelling microstructural processes

Real microstructures, derived from X-ray Microtomography, have been modelled using finite element method (Schneebeli and sokratov 2004, Chandel and et al 2014, Hagenmuller et al 2014). By this technique microstructural morphology is fully accounted for and the constitutive model for snow is replaced with that for ice. The behaviour of ice is relatively well understood, but computational limitations require the authors to simplify the constitutive models by assuming only either brittle (in the case of Hagenmuller) or plastic

(Chandel and Mahajan) behaviour rather than rate-dependent behaviour. The original mirotomography does not resolve the direction of the crystal axes in the ice particles, so the anisotropy of ice must also be ignored.

Even with these simplifications the computational load is significant. Chandel et al (2014) reported that 2 x10^5 elements were required to model each cubic millimetre of snow. This computational cost prohibits modelling of large volumes. At large strains it would be necessary to track changes in geometry and repeat the meshing process to account for the formation of new interparticle bonds. Bond growth would need to be characterised experimentally or else a model developed to include sintering phenomena (vapour transport and liquid-like layers playing a significant role at higher temperatures). This is not viable with current computational resources but could become so in future.

In summary, this technique shows promise in light of increasing computational resources, but is currently limited to small specimens where deformation is relatively small or where failure occurs in tension (where formation of new bonds would be minimal).

To substantially reduce computational loads, one can consider the ice particles as discrete elements (Johnson 2005). Little work has been done in this direction, possibly because of the difficulty of describing the ice particles in a way that offers appropriate densities, coordination numbers, and contact characteristics without having to model the complex shape of snow crystals. To pursue this option, knowledge of time-dependent contact dynamics and bond formation is also required. Limited experimental data is available for tensile failure of freshly formed bonds (Szabo and Schneebeli 2007) but equivalent data for bending or shear of interparticle bonds is not currently available.

7.2. Modelling snow as a continuum

Given the difficulty of modelling accurately the microstructural processes, significant effort has been spent on the development of more phenomenological continuum models. In some cases these models are informed by – or even derived from – microstructural considerations. In others they are purely an attempt to replicate observed phenomena.

Snow exhibits three different phenomenological deformation cases: At high strains it is brittle, with evidence of strain softening. At lower strains it is ductile, and at very low strains

it exhibits creep. It is the nature of phenomenological models that they tend to address only part of that spectrum.

The simplest case is for creep, as no yield criterion is required. A Maxwell model placed in series with a Voight model (as shown in Figure 12) has was parametrised by several authors in the 50s and 60s[6], and is accepted to work well, though parameters do vary with different mountain ranges and climates around the world. In some circumstances it is reasonable to neglect parts of the model (for example η_2 would dominate the strain response in a low-stress long-time environment) (Shapiro 1997). Models of this type are applied to low strain rate scenarios such as the downslope creep of snowpack against structures over the course of a winter season.

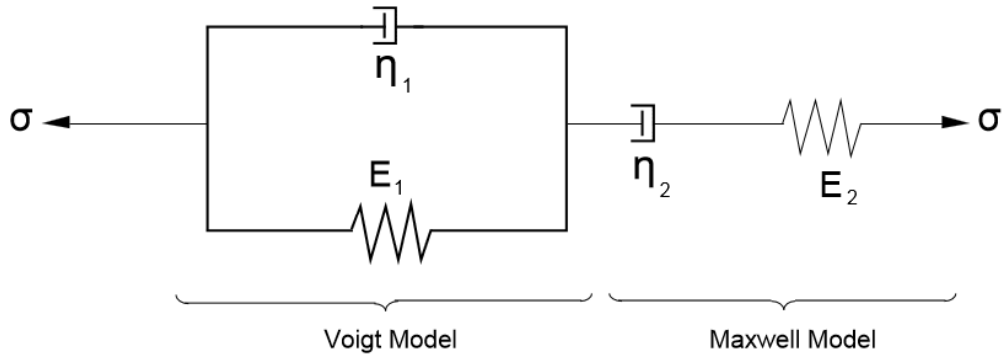

Figure 12: Maxwell and Voight models attached in series. The model requires two elastic parameters (here as E) and two dissipative parameters (here as η), though it is reasonable to neglect parameters in certain circumstances (Shapiro 1997).

More rapid deformation, where defined yielding is present, requires different models, most of which are solved for real applications in a finite element environment. By treating snow as a continuum the need to resolve the mechanical processes on the microstructural scale is avoided.

Meschke et al (1996) proposed a rate-independent model using a modified Cam-Clay yield function. Deformation was elastic up to the yield point and plastic thereafter. This model was improved upon by Cresseri et al (2005, 2010) who introduced a viscoplastic behaviour and attempted to account for intergranular bond changes by including a bond strength variable. This bond strength rises according to age and falls according to local strain, both volumetric

[6] Yosida et al (1956), Bader (1962), Mellor (1964), Shinojima (1967)

and shear, positive or negative. The manner in which this variable is abstracted provides for breaking of bonds but not for the formation of new bonds, which could be seen as a limitation for cases where densification occurs and coordination number rises. This weakness is addressed in part by linking strength to density. The model shows promise because it captures to a degree the time dependent nature of deformation, but bond formation would need to be included if it is to be applied to large strains other than in tension. The model includes strain softening, but no length parameter is provided, which could make mesh-independent modelling of deformation localisation difficult.

An alternative model including a length parameter was put forward by Borstand and McClung (2011). In this case damage is driven by non-local deformation history, related to the principal stresses. This the model was applied to beam bending experiments on natural snow with good results, but can only realistically be used in cases where failure is in tension, as no healing or sintering process is provided for.

An option with a more obvious connection to the real microstructure is that pursued by Gagliardini and Meyssonnier (1997) for firn and later applied by Nicot (2004) and Nicot and Darve (2005) to snow. They describe snow using an orientation-dependent bond density function. A representative volume element contains a distribution of bond directions and a parameter providing for number and strength of said bonds. Bonds are assumed to show viscoelastic behaviour up to a certain limit of normal (to the surface of the grain) stress, at which point brittle failure occurs. This system of bond distributions and strengths is homogenised to derive a macroscopic stress-strain behaviour. In his later paper (Nicot and Darve 2005) the bond number is linked to volumetric straining (with compression therefore increasing strength). Once again, strengthening of bonds with time is not considered, and the model may also be criticised for excluding the possibility of bond failure under tangential stress. Examples are presented showing good results for creep under constant load, but the applicability at higher strain rates has not been demonstrated.

Some authors attempt to relate observed behaviour to microstructural parameters. Mellor (1975) described the dependence on density of several properties (including stiffness and strength in shear and compression) but noted that density alone is not sufficient to predict other properties. Golubev and Sokratov (2004) provided a list of no less than 6 parameters[7] which they felt fully characterised snow. Even if their characterisation were shown to be

[7] The histogram of the grain sizes; the histogram of the bond sizes; the histogram of the quantity of bonds per grain; number of grains per unit of volume; the dominant crystal form and the histogram of the crystal forms; stereograms of the snow-crystal optical-axes orientation

universal (it has not), there remains a question of how these parameters can quickly and reliably be measured, especially given that some were expressed as distributions (histograms) rather than constants. Further, whilst such correlation based approach can be used to estimate the outcome of specific mechanical tests, it lacks the generality of properly formed constitutive models. (One might be able to estimate stiffness from measuring density, but one could not, for example, conduct comparative simulations of different penetration test tip shapes using this approach).

There also exist models such as SNOWPACK (Bartelt and Lehning 2002, Lehning et al 2002a, 2002b), which seek to predict the morphological evolution of the snowpack over long timescales with varying temperature, additional precipitation, overburden, insolation etc. These models are beyond the scope of this work, but there may be interesting opportunities to use such models as a source of parameters for the aforementioned mechanical models.

7.3. Summary of models

Good results have been obtained from finite element models which apply the constitutive equations of ice to the microstructure of snow, but this method is too computationally intensive for either large specimens or cases where bond formation and time dependent bond growth play a significant role. Continuum models address this problem but none of the models put forward to date address all the features of snow deformation (vis: bond breaking, bond formation, time dependent bond growth, internal length scale) and thus all fall short when applied to certain deformation cases.

Both techniques can (and most probably will) be developed with time to provide viable universal models of snow. There arises a problem of parameterising both types of model – knowing the microstructure of the relevant snow. For snow in the laboratory this can be achieved by various routes, with x-ray tomography the current leader. For snow in the field, the development of long period morphological models is promising, but it may also be useful to look at the relationship between common field test results and the required parameters, perhaps by modelling the field tests.

A good model should be able to reproduce localisation patterns observed in experiments. This test cannot currently be applied as strain localisations have not been imaged. The work presented later in this thesis will address this need.

8. Artificial snow

Snow has been artificially produced for two main applications: as a substitute for natural snow in snow sports, and as a model material for snow science. Some of the work mentioned in section 5, including Yong and Fukue (1977) and Yong and Metaxas (1985) made use of artificial snow produced by crushing ice, but the method of production is not entirely clear and the resulting snow was not characterised or described in any great detail.

Nakamura (1978) proposed a method of producing snow from vapour, and his concept has been further explored by Schleef et al (2014). In both designs, air from a refrigerated laboratory was blown over a warm water bath to achieve supersaturation. The air then flows over strings or wires where ice crystals nucleate and then fall (Nakamura) or are bushed off (Schleef) into a collector. Schleef reported a range of densities and grain forms were possible, but there is not yet a significant body of work utilising these artificial snow types.

Artificial snow is produced very extensively for use in snow sports. Fauve et al (2002) provides an overview of the technologies in use. Snow for sports is almost invariably produced by spraying water into the air, often assisted by compressed air or fans. Small particles may be added to encourage nucleation of freezing (Liao and Ng 1990) but droplets usually freeze from the outside inwards. This results in broken hollow spheres quite unlike natural snow forms, but acceptable for snow sports.

9. Similar materials

Snow is not alone in being a cohesive granular material, and also has similarities to brittle foams. Experiments and models similar to those discussed above have been applied to other materials, but there are differences.

9.1. Foams

It is appropriate to make comparisons between snow and foams. Unlike sands and soils discussed later, foams can be produced to high porosities, however the rapid formation of new strong interparticle bonds found in snow is still not present. Gibson and Ashby (1997)

provide a very thorough examination of foams and other cellular solids. Their work draws on others to describe the state of the art, and the models they put forward are now widely accepted in the field.

Within the field of foams, it is natural to look most closely at open-celled brittle forms, as snow is an open–pored matrix of ice, which is brittle (at relevant strain rates). Compression results for brittle foams are quite similar to those for snow, as illustrated in Figure 13.

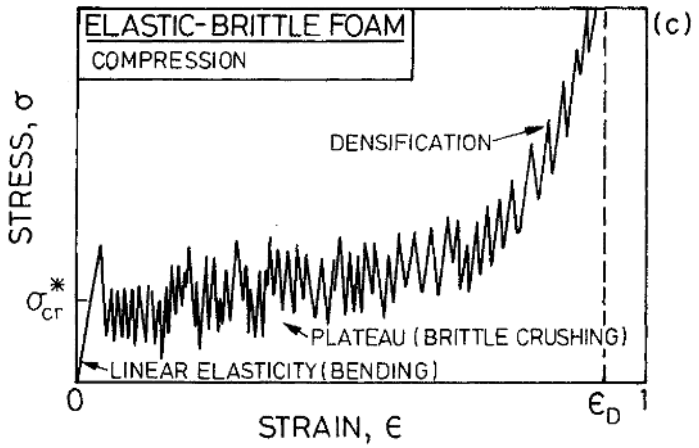

Figure 13: Compression test result for brittle foams, reproduced from Gibson and Ashby (1997). Note similarity with Figure 9.

Gibson and Ashby begin their analysis with either honeycombs or a hypothetical array of staggered cubic cells (illustrated in Figure 14), but the models are later generalised to other cell forms by eliminating constants related to cell geometry. They build up a model based on rigid beams undergoing bending, buckling and failure.

An interesting discussion arises that when load bearing members in such models attach to the middle of beams (as is the case in the cubic cellular model) the direction of buckling of said beams can have a big influence on Poisson's ratio. If the direction is random (and a large proportion of members are so connected), Poisson's ratio will be small. If the direction is spatially structured – perhaps as a result of some lateral prestraining – the Poisson's ratio can be large, or can be negative. Ratios as low as -0.8 have been demonstrated in real foams by this technique.

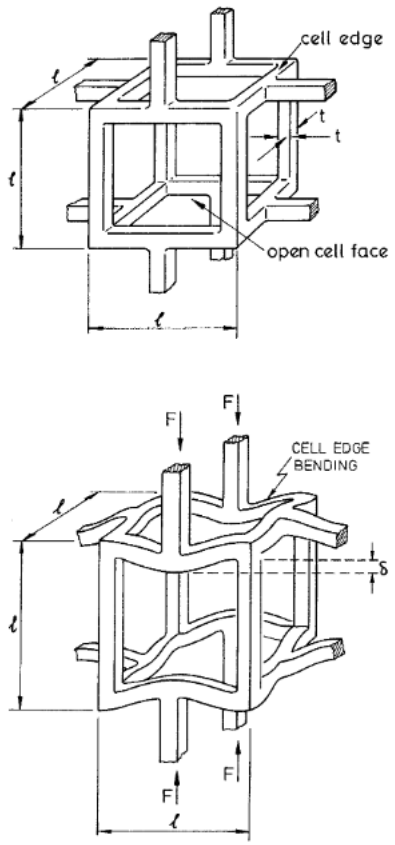

Figure 14: Offset cubic cell arrangement used by Gibson and Ashby (1997) to develop models (undeformed, top, and under vertical compressive loading, bottom)

From this proposed cellular structure, relationships between bulk properties of the foam and those of the constituent material can be derived, and a good correlation between this theory and experimental stiffness data in shear and compression from numerous experimental studies is presented (for list and citations see Gibson and Ashby 1997 fig 5.10 and 5.11, p192).

Up to this point the model is applicable only to small strains, but several collapse processes (recoverable and irrecoverable) are presented. The relevant one for snow is open cell brittle crushing. A modulus of rupture can be applied to each of the beams in the cellular model, and a crushing strength thus derived, though the correlation with experimental data is not as good as for stiffness.

Crushing will lead to densification, deformation will be arrested by the formation of new contacts between cell walls, and the (local) stiffness and strength of the foam will start to rise. If these crushing events occur serially at similar stresses throughout the material, the

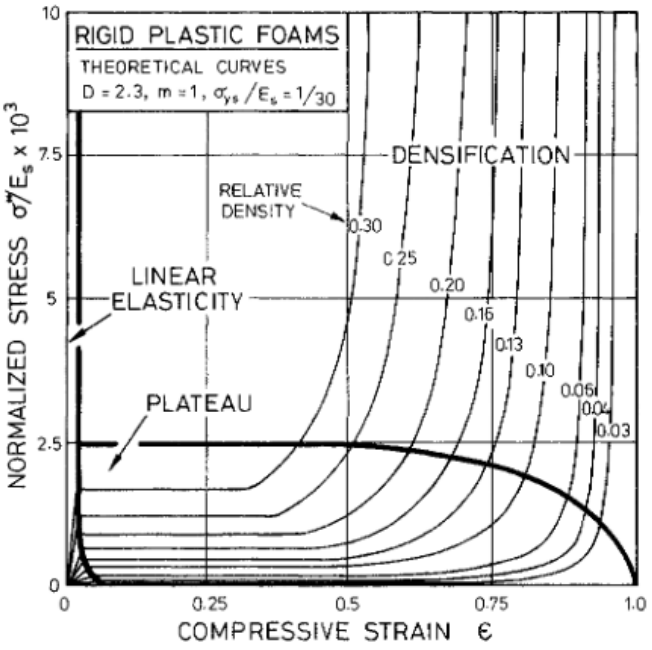

Figure 15: Stress-Strain behaviour for brittle open celled rigid foam, derived from the model discussed in the text. Stress normalised by that of the constituent material. Reproduced from Gibson and Ashby (1997). Entitled for plastic rather than brittle failure, but indicated in the text as applicable to both.

resulting bulk behaviour will be a stress plateaux followed by steep rise in stress as stiffness approaches that of the constituent material, as illustrated in Figure 15.

The only remaining difference between the theoretical curves and those observed (see Figure 13) is the presence of spikes or short term oscillations in the experimental data. This may be understood as an effect of specimen size in relation to the size of the collapse features (which may be larger than individual cells). If they are very different, the spikes will be smoothed out by averaging across the specimen, if the sizes are more similar the spikes will be visible. (Of course, if they are the same size only a single large spike will the recorded in place of the plateaux.)

Models of penetration testing in snow lean heavily on models developed for brittle foams, particularly those set out in Gibson and Ashby (1988), which are very similar to those presented in their 1997 work and to those discussed above in section 5.2. The similarity to section 5.2 is so great that I do not repeat the model here.

9.2. Geotechnical materials

Sands and soils are of great interest to geotechnical engineers, and have been extensively researched. The very rapid formation of strong inter-particle bonds found in snow is absent from sands and soils. This prevents them from reaching the high levels of porosity found in snow, and in turn excludes large volumetric compactions (though volumetric changes in soils can still be much greater than, for example, in metals).

Cone penetration tests (CPT) are frequently used to investigate soils in situ, and have similarities to the penetrometer instruments described in section 4.2. There is a large body of literature on the topic, and the technique has long since made the transition from academic study to widespread real-world application. As part of this transition CPT has been subject to formal standardisation, such as BS EN ISO 22476-1 or ASTM-D5778, which set out (among other things) the geometry and tolerances of the cone, the test speed, common designs of devices, positions for pore pressure measuring ports and general requirements and procedures for satisfactory testing. It also provides methods for calculating basic parameters of cone resistance, friction sleeve resistance and friction ratio and adjusting them for pore pressure effects.

A noteworthy difference between penetrometers used in snow and in geotechnical applications is the almost universal presence of friction sleeves on geotechnical penetrometers. These sleeves, riding behind the cone as illustrated in Figure 16, measure the friction between the instrument and material under test. This provides for adjustment of the cone resistance to account for friction between the cone and material, as well as being used for soil classification and to calculate other parameters. This innovation may have some benefit if applied to snow penetrometers as the friction coefficient does feature in some of the models presented in section 5.2. Measurement of pore pressure is also very common, but less applicable to snow which is rarely waterlogged or impermeable to the extent where this would be useful.

Mainstream use of CPT concentrates on extracting bulk properties – principally shear strength – rather than microstructural characterisation as is the case in snow. This difference in aims is reflected in the tendency to use bigger cones in geotechnical applications than in snow, with 10 and 15 cm^2 frontal areas being most common (Robertson and Cabal 2014), compared to 0.28 cm^2 for the SMP. Smaller devices are available, but the emphasis seems to be on portability and reduced thrust needs, rather than a desire to approach the

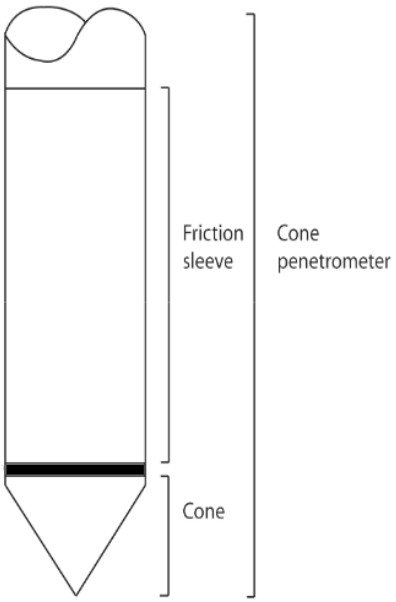

Figure 16: Typical CPT device. Both the friction sleeve and cone are subject to force measurement in the vertical direction.

microstructural scale. The vertical resolution is also lower – the minimum set out in the standards is 50 mm, compared to 4 μm for the SMP.

From the three initially recorded parameters (cone resistance, friction sleeve resistance and pore pressure) a broad set of parameters are claimed to be extracted. Robertson and Cabal (2014) suggest relationships for 14 parameters. Clearly one cannot extract 14 independent variables from three measured variables and indeed many are simply empirical maps of these parameters to the measured variables, based on commonly encountered soil types and calibration experiments. Whilst this approach has been useful in soil mechanics, it seems unlikely relationships derived way would apply to snow. There may be merit to performing calibration experiments on snow to develop relationships or classifications, but pore pressure and friction measurements in snow may not show such significant variation as in soils, leaving only cone resistance as a useful measurement.

A few mechanical properties can be reliably linked to measured parameters however, most significantly the (undrained) shear strength (S_u), which is calculated thus:

$$s_u = \frac{q_t - \sigma_v}{N}$$

Equation 3

Where q_t is the cone resistance, σ_v is the vertical stress (generally due to the weight of overlying material) and N is a 'cone factor', typically 10 to 18 (Robertson and Cabal 2014). This approach is both empirically successful and supported by some of the models discussed later.

Classification of soils by CPT could be seen to have parallels with the classification of stability by 'texture' of snow, but the methods are entirely different. Classification usually approached by use of soil behaviour type charts such as the one in Figure 17. The variables required are the cone resistance (cone force divided by frontal area) and friction ratio (the ratio of the vertical force on the cone to that on the friction sleeve, adjusted by the difference in areas for the two measurement devices). Charts of this sort are of empirical origin, rather than being derived from microstructural considerations (Robertson and Cabal 2014). The resulting type is a behavioural type – the soil is not guaranteed to have the physical characteristics of the detected type in terms of appearance, constitution, or microstructure: rather it will have mechanical characteristics of that type. This is in contrast to the stability classifiers described in section 5.2, where features of the force record are directly related to microstructural characteristics known to be risk factors.

The concept that deformation is limited to a small area local to the tip, presented in the snow models above, is absent in models of CPT in soils. This assumption is only possible in cases where the volume of the penetrometer can be accommodated by local volumetric strains, and thus where porosity is reasonably high. Where the propensity to volumetric straining is lower, the volume with which the penetrometer interacts must be larger – and in the extreme case of incompressible medium the space required for the penetrometer to advance must be provided by upward displacement of the free surface, known as heave.

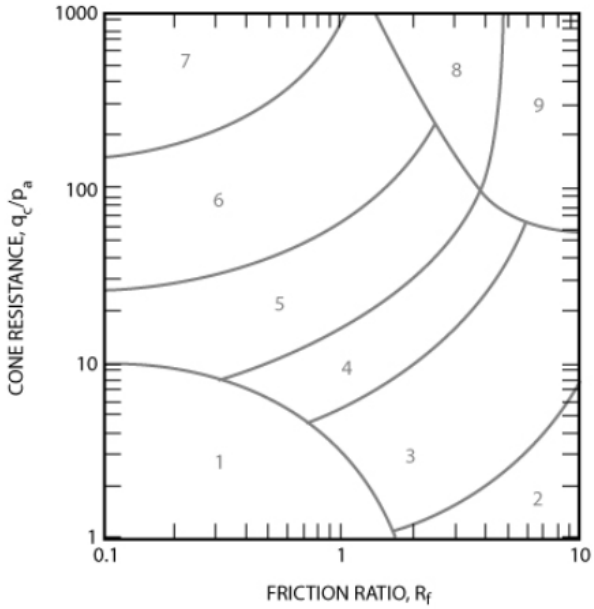

Zone	*Soil Behavior Type*
1	*Sensitive, fine grained*
2	*Organic soils - clay*
3	*Clay – silty clay to clay*
4	*Silt mixtures – clayey silt to silty clay*
5	*Sand mixtures – silty sand to sandy silt*
6	*Sands – clean sand to silty sand*
7	*Gravelly sand to dense sand*
8	*Very stiff sand to clayey sand**
9	*Very stiff fine grained**

** Heavily overconsolidated or cemented*

P_a = atmospheric pressure = 100 kPa = 1 tsf

Figure 17: Soil classification according to cone resistance and friction ratio, reproduced from Robertson and Cabal (2014).

One approach to modelling CPT is known as bearing capacity theory, so called because it used a similar mathematical approach to that used to describe the load bearing ability of foundations. In the simplest case, a failure surface is assumed and analysed as an equilibrium problem. Example failure surfaces are illustrated in Figure 18. A more rigorous approach combines a failure criterion of some sort with the equilibrium analysis. By this method a slip line network can be produced, avoiding the need to assume a deformation shape at the outset. Both approaches can be solved analytically, and yield cone factors for use in Equation 3. The bearing capacity approach has been criticised for assuming failure modes not generally observed in experiments (Yu and Mitchell 1998).

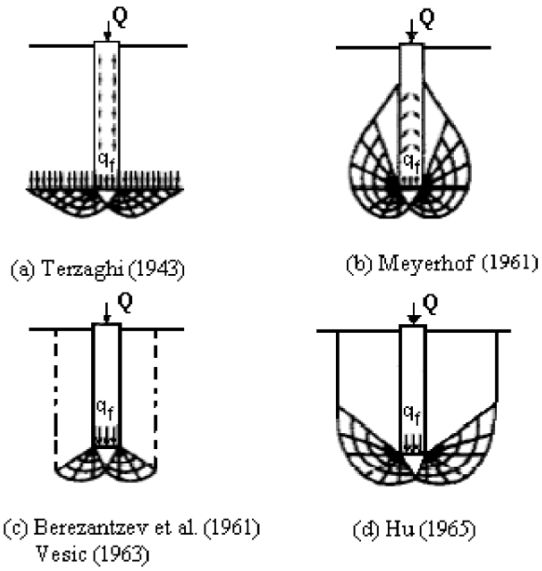

Figure 18: examples failure modes for bearing capacity analysis, reproduced from Yu and Mitchell (1998)

An alternative approach recognises that inserting a penetrometer into a substrate requires the formation of a void of equal volume to the device, to be occupied by it. So called cavity expansion models therefore model CPT in terms of the pressure required to expand a cavity, usually cylindrical but occasionally spherical, within the soil. Once again a cone factor can be derived analytically, though to do so requires some relationship between cone resistance and cavity pressure to be assumed, nonetheless Yu and Mitchell (1998) consider this approach superior to bearing capacity theory.

A final option is to pursue finite element methods. This route cannot lead to exact analytical solutions but avoids the need for the assumptions involved in the previous models. A constitutive model is required, and friction between the soil and cone must also be included.

A variety of constitutive models have also been put forward for soils, which were reviewed by Collins (2005). A wider variety of failure criteria have been explored for soils than for snow and models are generally more advanced. Models applied to soils have provided concepts and ideas which have been adapted for some of the models described in section 6.

Shearing in soils is able to cause volumetric changes (positive or negative), depending on the existing degree of compaction. Material which is sheared continually will approach steady density, known as a critical state in literature. This is a useful concept because once this state is reached the material properties can be assumed not to change with further shearing.

Unconfined compression tests in geomaterials generally lead rapidly to shear failure. When a confining pressure is applied the strength is increased but shear failure is still the norm (for example Alshibli and Sture 1999 or Wolf et al 2003). This type of well-defined failure in or near the plane of maximum shear is not observed for snow. When confinement is rigid, some geomaterials can be brought to failure in crushing, but this relates to the breaking up of particles rather than collapse of bonds between particles as would generally be assumed in snow.

Shear testing in geomaterials is often undertaken in order to capture parameters for constitutive models. Results from direct shear tests are commonly used to determine the values of c and θ in the Mohr coulomb failure criteria, which is one of the more popular failure criteria used for granular materials.

10. Summary

There is an extensive body of work on snow, including field observations, experimental results, and models. The wide range of observed properties is caused by differences in the microstructure of the snow. Some microstructural properties (such as density) are correlated to certain phenomena or physical properties (such as strength and stiffness), but the relationship between such macro-mechanical properties and the underlying microstructure is not fully understood. Large changes in deformation rate can cause phenomenological changes in deformation (i.e. from brittle to ductile to creep) but small changes in rate may not lead to different behaviour within any one regime.

The development of penetrometer instruments has highlighted a need to understand snow deformation on the centimetre scale, but such understanding would be more widely applicable, as it could help to provide the link between microstructure and macro-mechanical properties.

Strain localisation – which implies strain softening – is clearly present in laboratory shear tests and there are strong indications that it occurs in compression testing also. The concept is not well explored in the literature surrounding testing. Some models do incorporate a mechanism of softening or damage, and in some cases a basic strain hardening mechanism is present also. The models fail to fully capture the time dependent nature of bond formation and growth.

To understand the deformation of snow it is necessary to understand the strain softening phenomena. This thesis aims to experimentally characterise this strain softening and the deformation patterns that result.

Armed with this information it will be possible to develop new models, and to test them against observed behaviour. Only if the models can reproduce observed deformation patterns can they be considered successful. Observations of deformation patterns are therefore required for further advances in the field. Knowing the size of localisation features will be especially useful for future models based on fracture mechanics and the flow of energy.

Chapter III: Artificial snow

Aim

The aim of the work described in this chapter was to provide artificial snow for the experiments described later, and to provide a laboratory environment suitable for conducting the experiments.

1. Introduction

Natural snow exhibits a huge range of forms. For those wishing to work with snow in a laboratory this presents a problem: no two samples of natural snow can be guaranteed to be the same. This leads to experiments which cannot be reliably repeated. This is the motivation for the use of an artificial snow type in snow science experiments.

1.1. Natural snow, its formation and evolution

Before looking to produce artificial snow for experimental use, it is first necessary look to understand the natural snow.

Snowflakes start out as tiny particles of ice that are heterogeneously nucleated. This may occur at altitude in the atmosphere or directly on the ground. A small particle may be included in the growing snowflake, having provided the original nucleation point. The subsequent growth of the snowflake depends on humidity, temperature and pressure, all of which may change with time (Libbrecht 2005). These variables may even show gradients across the individual snowflakes. An example of this would be rime (a surface frost) forming in the wind: the air temperature is different to that of the substrate, and the wind produces pressure differentials around the growing grains.

The formation of the snow particles is only the start. Once lying on the ground, the snow pack undergoes constant change (Colbeck 1982, Blackford 2007). When a strong temperature gradient is present, vapour transport and grain growth dominate. Under isothermal conditions, sintering and rounding take over. Snow may even be picked up and broken by the wind, or crushed by an overburden of new snow.

Small variations in these processes lead to many different snow types. When designing artificial snow, this brings advantages and disadvantages. It would be very difficult to exactly reproduce all these processes (and therefore all possible snow types) in a laboratory. On the other hand, it means that the definition of snow is quite wide, making it easier to produce a material which can reasonably be described as ‘snow’.

1.2. Existing demand for artificial snow

Snow is artificially produced for two main reasons: snow sports and experimental use.

For snow sports, the main requirement is low cost. Large quantities are needed, and a high density is preferred to resist melting. The largest consumer is outdoor ski resorts, but there is also demand from indoor snow domes. No particular requirement is placed on grain form or size, save that the end product should resemble natural snow to the satisfaction of the end users.

Conversely, snow for experiments is often only needed in small quantities. The principal requirement is the consistent and repeatable nature of the snow. A realistic grain form is desirable, and ideally range of grain forms should be possible.

This chapter will concentrate on meeting the need for snow in experiments described in this thesis.

2. Specific requirements for artificial snow in this study

Whilst general requirements for artificial snow in experiments are discussed above, the requirements of the experiments discussed in later chapters were more specific. They would require:

- Snow production all year round.
- Snow that was repeatable: one freshly made batch should be indistinguishable from any other freshly made batch, even if years have elapsed between manufacture.
- Available on demand, or to a reasonably short lead time.
- Available in quantities around 1 to 10 kg per day.
- Have a microstructure which may realistically be found in real snow.

3. Possible methods of creating artificial snow

Artificial snow may be created by three methods: it may be deposited from vapour, frozen from liquid or mechanically processed from a solid form. Each option is discussed in turn.

3.1. Creating snow from vapour

Natural snow forms from vapour, so creating artificial snow from vapour has clear appeal. Snowflakes grown in this way are very sensitive to conditions of pressure, temperature and humidity. Libbrecht 2005 has demonstrated the ability to grow single crystals or small quantities of snow in laboratory conditions, and showed an ability to control the grain forms thus created. This method would be difficult to apply on a larger scale.

A simpler method, where only supersaturation and temperature are controlled, has been demonstrated by Nakamura (1978) and improved upon by Schleef et al (2014). Shleef reports reasonably large volumes being produced by this method. A significant amount of specialist equipment is required, and producing snow in this manner releases humid air into the cold laboratory.

3.2. Creating snow from liquid

Creating snow from a liquid is a familiar process to on-piste skiers. Water droplets are sprayed into cold air and allowed to freeze. In some cases compressed air is used alongside the water, to aid dispersion, nucleation and freezing of the droplets (Fauve et al 2002). Small particles may also be added to encourage nucleation of freezing (Liao and Ng 1990). The droplets frequently freeze from the outside in and may burst as they freeze, due to water having a higher density than ice. This method is impractical for use in a small laboratory, as it depends on a large supply of cold ambient air to remove the heat of transition. It also results in broken spherical grains which may be hollow and are not particularly similar to natural snow. Variants on this technique exist for use in snowdomes, where the water is misted and blown onto a collector of some type (Clulow and Winnett 2000), thus providing a more compact machine.

Blackford et al (2007) also described a process where water was sprayed into liquid nitrogen. While this proved useful for certain microstructural studies, it is not suitable for making the larger quantities required for the experiments.

3.3. Creating snow from solid

A final option, pursued in several studies (Fukue 1977, Yong and Fukue 1977, Yong and Metaxas 1985) is to crush ice from a solid form to provide artificial snow. It is a scalable process which can provide suitable quantities for most laboratory experiments. Only one snow type can generally be produced by this method, but it is consistent, as the method is not sensitive to ambient conditions. This was the option which was pursued in this project.

4. Process for making snow

4.1. Existing process for making snow

At the time this project began, a method of producing artificial snow by crushing ice already existed (Skouvaklis 2010). Ice chips from a commercial ice machine (Scotsman AF80) were placed in containers and cooled to -80 °C. These where then broken up and crushed in a food processor (Robot Coupe Blixer 6 V.V.) until it went quiet. The resulting snow was aged for 4 hours to allow the temperature to rise to that of the cold room.

4.2. Improved process of making snow

This process was reviewed and the influence of batch size and processing time was investigated. Batch size was found to have no significant effect unless the processor was overloaded. Longer running times were found to favour smaller grain sizes and lower densities up to a certain limit (depending on fill level), after which it made no difference, as illustrated in Figure 19.

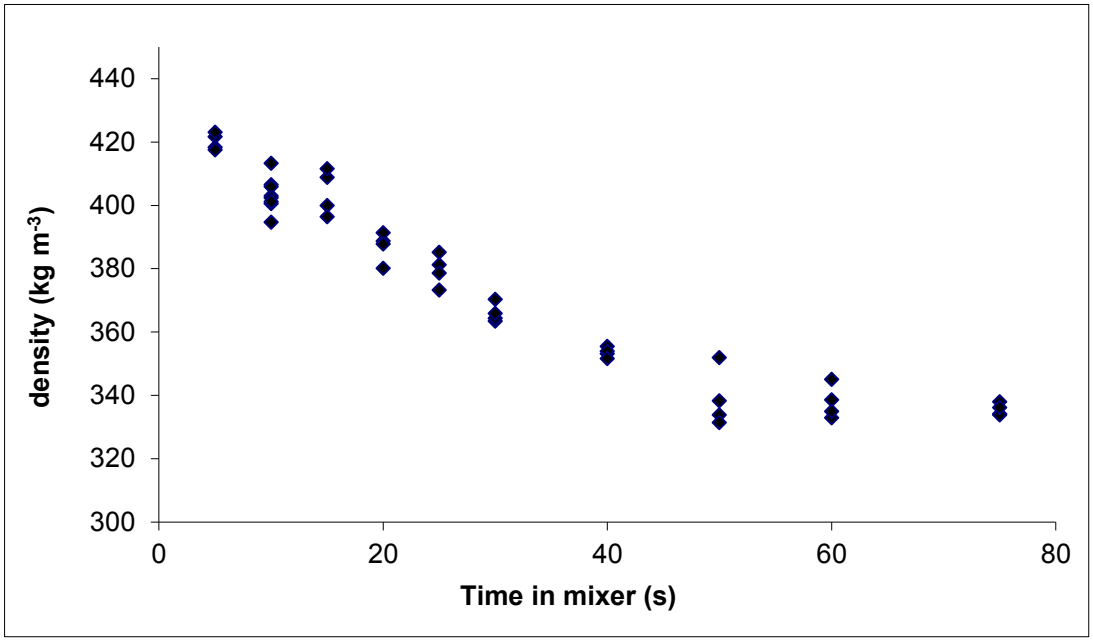

Figure 19: Influence of time in mixer on density of snow produced. Longer running times favour lower densities, up to 50 seconds, after which, there is no change. (2 kg fill)

The process for making snow was thus:

- Weigh out 2kg of ice chips into a nylon bag
- Place nylon bag in freezer at -30 °C for 24 hours
- Place nylon bag in freezer at -80 °C for 24 hours
- Break up fused mass of ice chips with a hammer and pour into crusher
- Start the crusher at minimum speed (300 rpm) and increase to full speed (3500 rpm) in 3 s
- Allow to run for a total time of 60 s
- Place in a container within the cold room and allow to warm up for 4 hours
- Sieve through 1.68 mm nominal aperture sieve. The snow should not be disturbed again, so if it is required to be in a certain container or apparatus, it is sieved directly into it at this stage.

Technical information about the components used, with additional photographs of the process, are located in appendix 1.

5. Characterisation of the artificial snow

In order to draw comparisons with natural snow, and to allow confirmation that the material was repeatable, it was necessary to thoroughly characterise the artificial snow. Characterisations were carried out for freshly made snow and at times of 1, 2 or 4 hours before being sieved (in accordance with the procedure set out in the previous section) and then again at 1, 2, 4, 7, 10 and 14 days. For each sample, the snow was allowed to develop isothermally in closed containers at -10 °C until needed for examination.

5.1. Methodology

The artificial snow was characterised by traditional field techniques, optical microscopy and by low temperature scanning electron microscopy

5.1.1. Characterisation by field techniques

Hardness was assessed by an experienced avalanche observer according to the *International Classification for Seasonal Snow on the Ground* (Fierz et al 2009). To do this, an object is pressed into the snow, the rating then being determined by the largest object which may be inserted with only moderate force. As is standard practice, this will be either: a knife; a pencil; a finger; four fingers held flat; or a clenched fist.

Density was measured with a "Hydrocutter" type rectangular density cutter with a 100 cm^3 volume. Mass was measured to the nearest 0.1 g. For measurements with this tool, an error of up to 4% is assumed, this being the level experienced in a thorough assessment of density cutters conducted by Conger and McClung (2009).

Snow samples were classified by an experienced avalanche observer according to the morphologies described in Fierz et al 2009. This was done with a small number of grains spread onto a slide, which were also photographed with a Canon 7d SLR camera fitted with a Canon 65 mm MP-E macro lens.

Grain size was assessed manually, using the method described by Fierz: the practitioner disregards any anomalously large or small grains and then records the characteristic size (or range of characteristic sizes) of those that remain. The characteristic size of any one grain is

defined as the largest measurement across it in any given direction. As all our samples show a range of grain sizes, this provides an upper and lower value for each sample.

5.1.2. Characterisation using low temperature scanning electron microscopy

Samples were imaged in a Hitachi 4700 II BioSEM low temperature scanning electron microscope (LTSEM). This instrument is nitrogen cooled and features a cold field emission electron source and Gatan Alto cryo-preparation system. Cylindrical samples of 7 mm diameter and 10 mm high were removed from the centre of the larger containers with a circular cutter and placed in two-part copper capsules. The capsules were sealed with thin copper sheets and placed in the vapour portion of a liquid nitrogen dewar for storage and transport, as indicated in Figure 20. This acted to quench the microstructure at specific times. Each capsule was removed from the dewar and placed in the cryo-preparation chamber of the LTSEM before being split open at its centre, fracturing the sample and revealing a new surface for imaging. A thin (c.1 nm) gold-palladium coating was applied by sputtering, to provide the electrical conductivity required for imaging. The temperature was maintained low enough to restrict sublimation into the instrument's vacuum and an acceleration voltage of 2 to 5 kV was employed. Imaging was stopped once delamination of the conductive coating, caused by sublimation, was observed.

Figure 20: Copper capsule with foil cover. The capsule was broken at the half-height horizontal join to expose the sample for imaging in the SEM. Capsule outer diameter 10 mm. Image credit James Floyer.

5.2. Results

Hand hardness was initially classified as “1 finger” and increased, reaching “pencil” after four days, with the rate of hardening decreasing with time (Figure 21).

The density of the artificial snow was around 350 kg m^{-3} when first produced, within 1 h increased to approx. 390 kg m^{-3}, and then remained constant within the measurement error (Figure 22).

In the freshly made snow, particle sizes showed a range from 0.01 to 0.5 mm. The larger grains remained as the material sintered while smaller grains were eliminated, with the lower bound for grain size reaching 0.15 mm after 7 days, as shown in Figure 23.

The freshly made snow has a frosty appearance in the optical image. This is revealed by the SEM image to be a profusion of small flakes or shards from the crushing process. At the scale shown in Figure 24 these appear angular and broken but at a finer scale rounding and sintering have already begun, as shown in Figure 25.

Within an hour this frosty appearance is reduced. After four hours the minimum grain size observed in the SEM images has risen from 0.01 mm to 0.05 mm, whilst the grains in the optical images take on a more glassy appearance. In SEM images, numerous examples of grains being consumed by their larger neighbours are found, as shown in Figure 24.

After sintering for 48 h the small shards are completely absent. After sintering for a week, the grains become progressively more fused to their neighbours - this is apparent both through the hardening of the snow and in the micrographs.

The snow classifications, according to Fierz (2009), were as follows: when its manufacture is taken into account “machine made crushed ice (abbreviation: MMci symbol:)”, though the standard does not include a reference appearance for this snow type. If classified by appearance, it resembles “wind broken precipitation particles (DFbk,)” when new, becoming “rounded grains (RG,)” or “polycrystals (MFpc,)” when older.

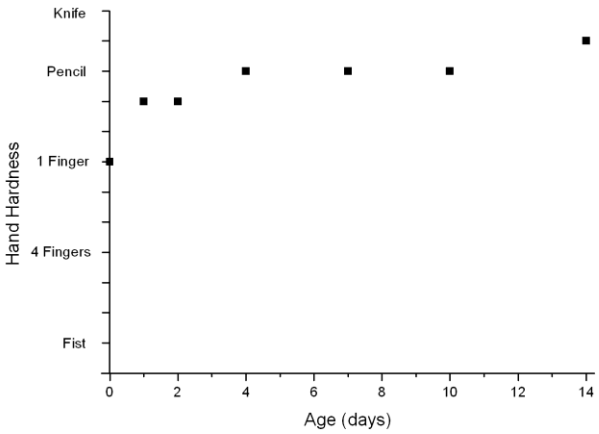

Figure 21 Variation in hand hardness of artificial snow with time

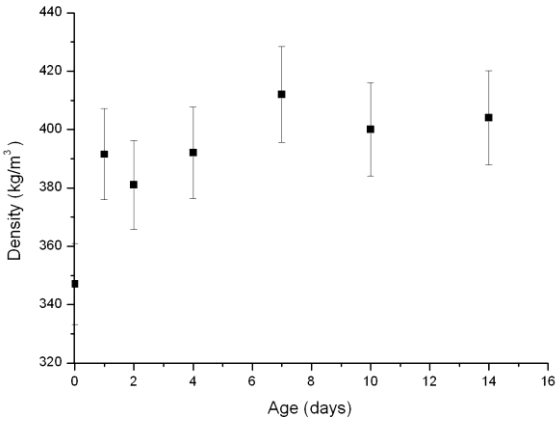

Figure 22: Variation in density of artificial snow with time

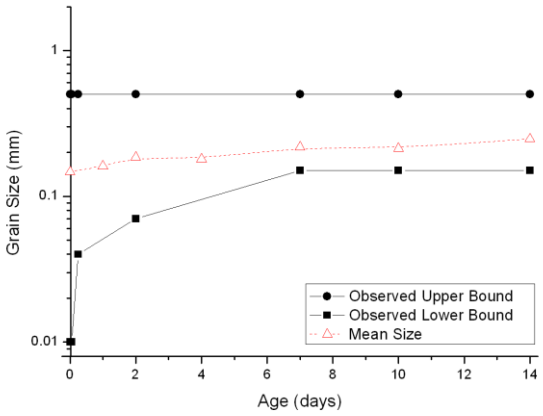

Figure 23: Variation in particle size in the artificial snow with time.

a)

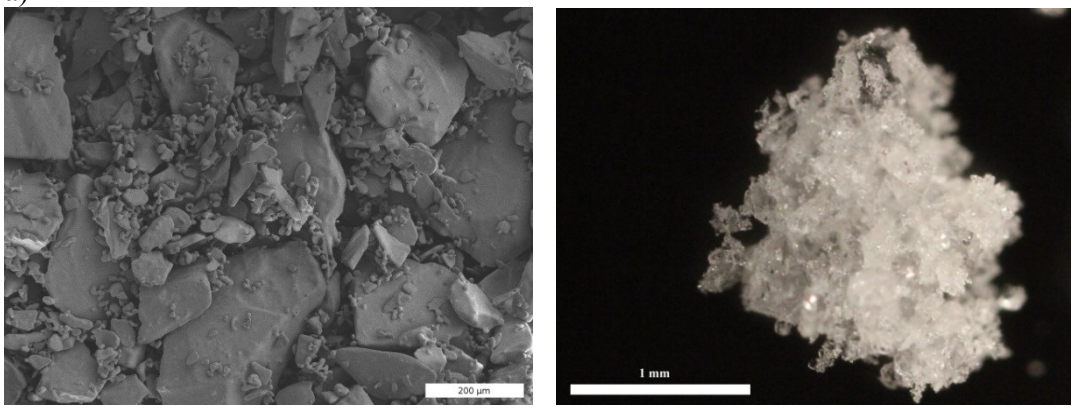

b)

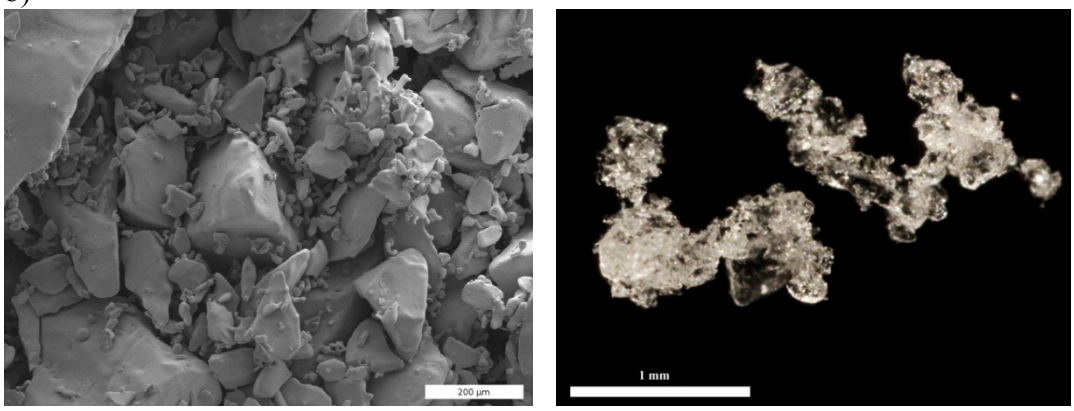

c)

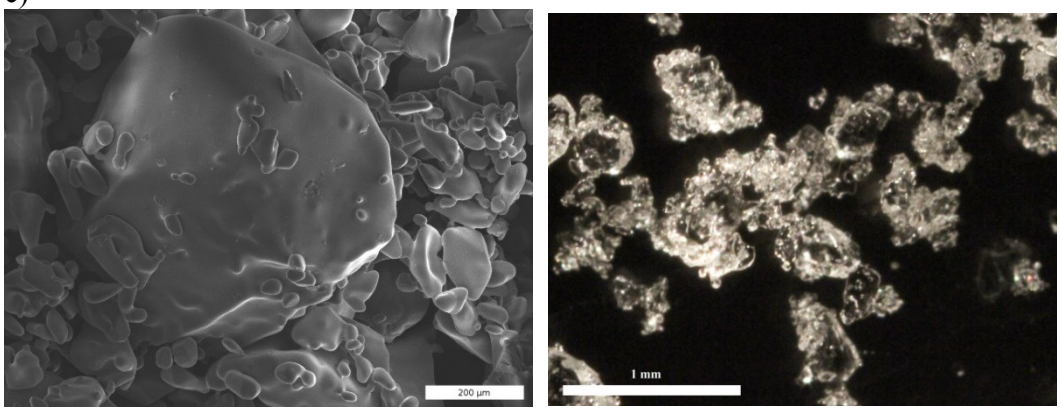

Continued overleaf…

Figure 24: Low temperature SEM (left) and optical (right) images of artificial snow. As-made (a); and after sintering at – 10 ˚C for 1 h (b), 4 h (c), 2 days (d), 7 days (e), and 14 days (f).

Continued from previous

d)

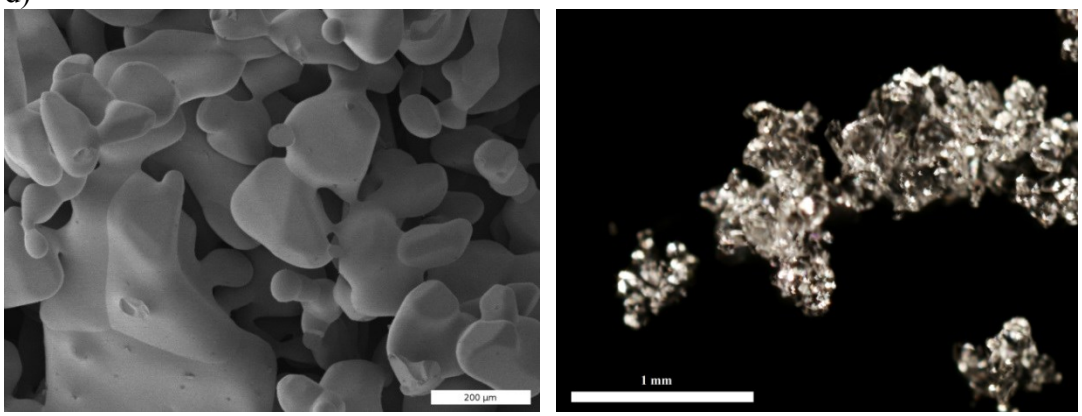

e)

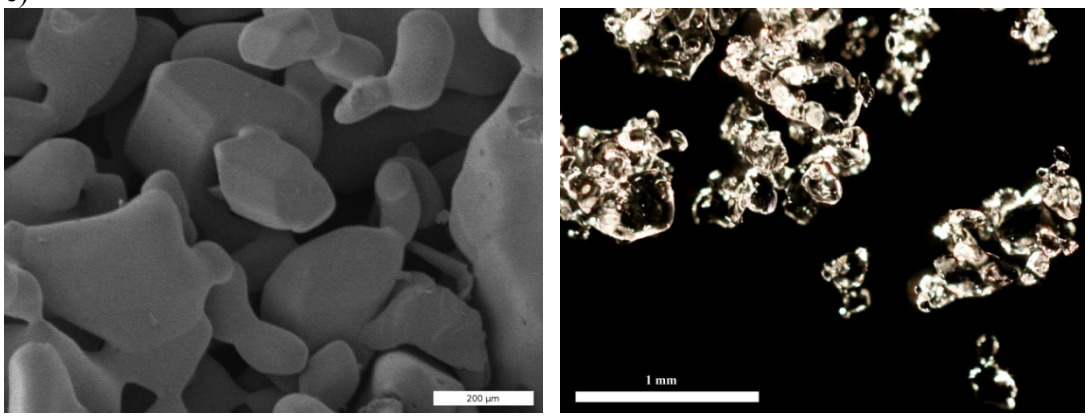

f)

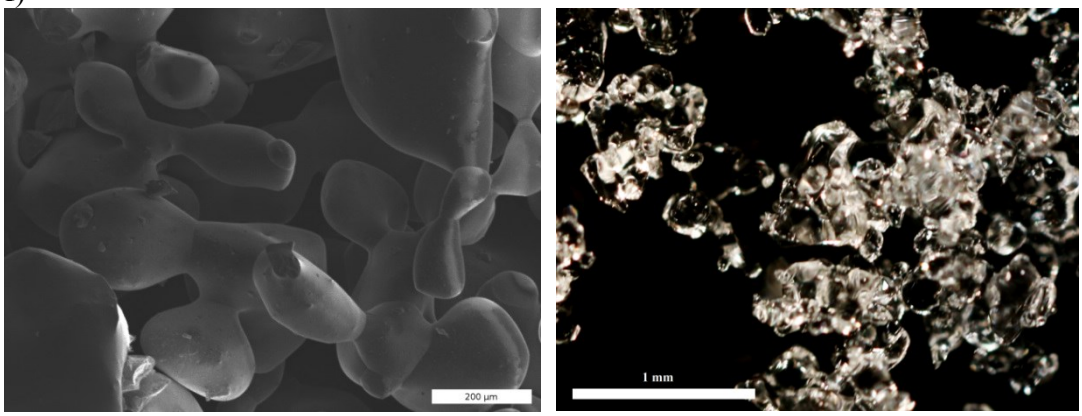

Figure 24: Low temperature SEM (left) and optical (right) images of artificial snow. As-made (a); and after sintering at – 10 ˚C for 1 h (b), 4 h (c), 2 days (d), 7 days (e), and 14 days (f).

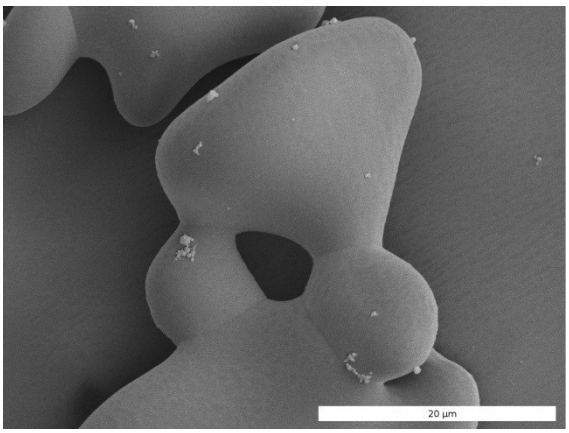

Figure 25: LTSEM image showing rounding and sintering of fine particles, in as-made snow.

6. Discussion

The density of the snow is higher than average for natural snow but still lies well below levels typically expected for random packing, and within the naturally occurring range (and within the range of field observations presented later). Snow does not normally reach typical random pack levels because bonds between particles prevent settling. The artificial snow has a higher density than many types of natural snow because its coarse round grains pack better than more complex shapes such as dendrites or stellar crystals.

The grain sizes found in the freshly crushed snow are not what would typically be found in natural snow, but even in the 4 hours required to bring the snow up to room temperature many of the smaller grains are lost. By the time the material is ready for use, the grain size is within the range expected for natural snow.

Sintering proceeds in the typical manner for an isothermal environment. Grains round and grow, with smaller grains being lost.

The artificial snow has physical properties lying within the range of those expected for natural snow (Shapiro et al 1997, Petrovic 2003). The snow has been thoroughly characterised by the described methods, provision of this information allows:

- Other scientists to confirm that they have created identical material in future.
- Analysis or modelling of experiments with accurate information about the snow.

7. Laboratory conditions

The Laboratory was installed in 2006 and was of a similar design to other cold laboratories worldwide. It consisted of two main rooms with temperature control nominally from -20 °C to 0 °C. Both rooms were protected from outside air by a small entrance chamber. Inside air was continually circulated over the evaporators of the refrigeration system while refrigeration compressors were cycled on and off to control the temperature. Every 4 hours the system entered an automated defrost cycle, with heating of the evaporator to remove any build-up of frost. The fans were automatically stopped during the defrost procedure to prevent warmer air being circulated, and the position of the evaporators in the ceiling of the laboratory minimised heat transfer by convection. The laboratory was vented by small tubes entering near the evaporator and remained at local atmospheric pressure.

7.1. Temperature of the laboratory

At the start of the project the temperature was found to vary according to figure 14. This was considered too large a variation for the planned research and the refrigeration control was modified to produce a more consistent temperature. After the modification the air temperature in the laboratory was found to be able to maintain a set temperature to within ± 1 °C, with a typical standard deviation of 0.49 °C and typical period of temperature oscillation of c. 5 minutes.

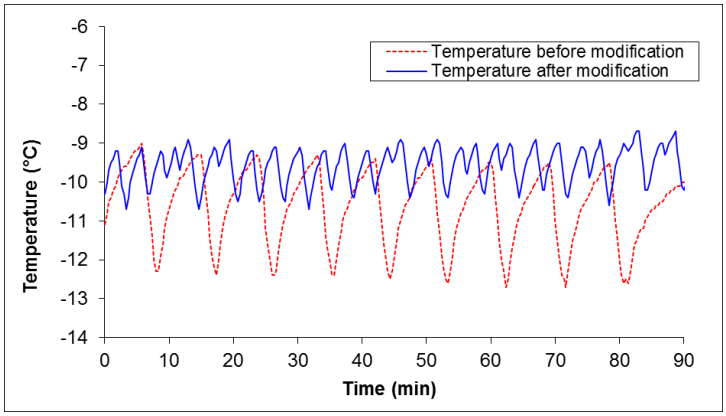

Figure 26:Laboratory air temperature variation before and after modification, Set point -10 °C.

For the purpose of the presented work, these conditions have been considered as isothermal for any enclosed sample or specimen not in contact with a wall or floor of the laboratory.

7.2. Humidity in the laboratory

Humidity in the laboratory was controlled by the temperature of the evaporator, with excess humidity from sublimation or respiration being deposited on the evaporator, and subsequently disposed of during the automated defrosting. This has the overall effect of maintaining a relative humidity close to 80%.

7.3. Temperature and humidity within a specimen

Throughout the period of the project, samples and specimens were kept in covered containers, and any further sampling or analysis of specimens was conducted using specimens from the centre of the container. The additional insulation afforded by the container and surrounding snow served to keep the centre of a typical sample at a constant temperature to within 0.1 °C.

The covering of containers also restricted sublimation and allowed the samples to achieve a natural equilibrium humidity at a higher level than that of the laboratory as a whole.

8. Conclusions

A process has been developed which will provide artificial snow suitable for the planned experiments. This snow has been characterised, allowing future comparison to other snow types. The properties of the snow lie within the range typically observed for natural snow. The snow can be produced to a 48 hour lead time and the process is scalable and easy to use.

The resulting snow has the following properties: when new, it has fragmented angular particles ranging from 0.01 to 0.5 mm and a density of 350 ± 20 kg m^{-3}. When aged, density

increases to 390 ± 20 kg m^{-3} with grains from 0.2 to 0.5 mm in size. Rounding and sintering produce the grain form known in snow science literature as polycrystals.

The laboratory provides a suitable environment for the described experiments: temperature may be controlled from -20 °C to 0 °C and once set, it may be considered to have a constant temperature and humidity.

Chapter IV: Snow in Scotland and the SnowMicroPen

Aim

The aim of the work described in this chapter was to compare the artificial snow to natural snow through the medium of a penetrometer instrument, and to determine if the artificial snow was a suitable model material with which to investigate penetrometer-snow interactions.

1. Introduction

As has been discussed in the previous chapter, an artificial snow was available and had similar characteristics to natural snow. This artificial snow had a very reproducible microstructure.

Thorough scientific study of penetrometer instruments (and snow science in general) has been hampered by the difficulty in finding, retrieving and preserving enough identical samples to allow for repeatable experiments. Conducting experiments on artificial snow provides for repeatable experiments, but only if the artificial snow is adequately representative of natural snow.

One of the main fields which would potentially benefit from my work is penetrometery, so it was necessary to confirm that the artificial snow described in the previous chapter would behave the same way as natural snow when tested with a field penetrometer.

The SnowMicroPen (SMP) is an example of a modern penetrometer, which has been introduced in Chapter II section 4.2. It uses a motorised rod to drive a 6 mm diameter 60° cone into the snow at 20 mm s^{-1}. The Force required to drive the cone is recorded at 4 μm intervals. This instrument was used to take measurements alongside traditional snow pits in the Scottish highlands and in aged artificial snow samples in a refrigerated laboratory. Comparisons are drawn between the two, with a view to using artificial snow for further study of snow indentation.

2. Snow and the Scottish climate

Scotland has a temperate, maritime climate. The low altitude and notoriously changeable weather mean that snow cover is restricted to the winter months, and temperatures can rise above freezing at any time of year. High winds lead to significant snow mobility, even when snow has hardened and densified significantly. The combination of these factors leads to a prevalence of rounded and decomposed grains, often interspersed with crusts or ice lenses and hardened by wind or freeze-thaw cycles. This is reflected in the observations discussed in the next section.

3. Snow observations in Scotland

Field tests with the SMP were performed between January and April 2010. In each case a series of SMP measurements were made and the locations marked. A pit was then dug to expose the tested snow and observations of grain size and type were recorded at 5 cm intervals (measured slope normal). Density was measured using a 100 cm^3 Taylor-LaChapelle density cutter and temperature was recorded with a type K thermocouple. A conventional layer-based observation was also conducted to complement the 5 cm samples, with hand hardness, grain type and grain size recorded according to Fierz et al (2009). Fierz's naming definitions are used here, with definitions available in the glossary.

Samples of natural snow discussed here originate from one of three snow pits. The first was taken on the 5th of January 2010 in dry powdery snow on a flat field. Recorded average density was 196 kg $m^{-3}$with temperatures just below zero as indicated in Figure 27a. Fragmented and decomposed precipitation particles dominated.

The second test was performed on the 10th of February 2010. Density ranged from 244 to 384 kg $m^{-3}$with temperatures around −4 °C. The pit was dug on a 30° southeast facing slope, in dry snow. Rounds and mixed forms made up the majority of the snow pack with several prominent layers of graupel. Observations are presented in Figure 27b

The final snow pit was dug on a southwest facing 15° slope on 14th April 2010. Temperatures were near zero and melting was evident. Recorded density ranged from 292 to 579 kg m^{-3}. The dominant snow types were rounded polycrystals and melt crusts. Observations are presented in Figure 27c.

All samples were taken in the area near the Cairngorm Ski Resort in the Grampian Mountains. The first one was at an altitude of 320 m and the other two at 1150 m.

The samples show less indication of hard windslab and melt-freeze metamorphism than normal for Scotland. This is due to the exceptionally cold nature of the winter 2009/2010.

From the three field tests, six examples of different snow types were extracted as shown in Figure 28. These six forms represent some of the most common snow types found in Scotland.

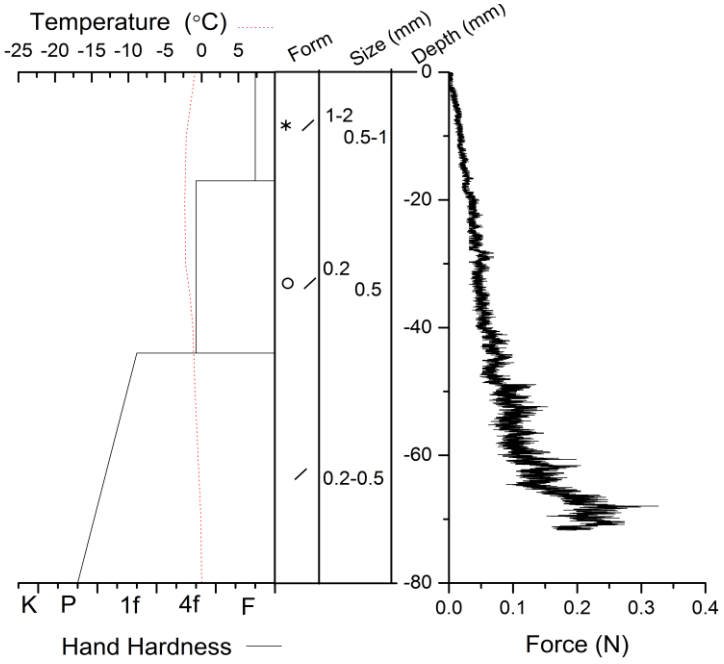

Figure 27a: Snow pit records for the 5th January 2010 field day, recorded in the traditional observer's style. Temperature and hand hardness (left), corresponding SMP records (right). Form symbols after Fierz et al, a table of definitions is available in the glossary.

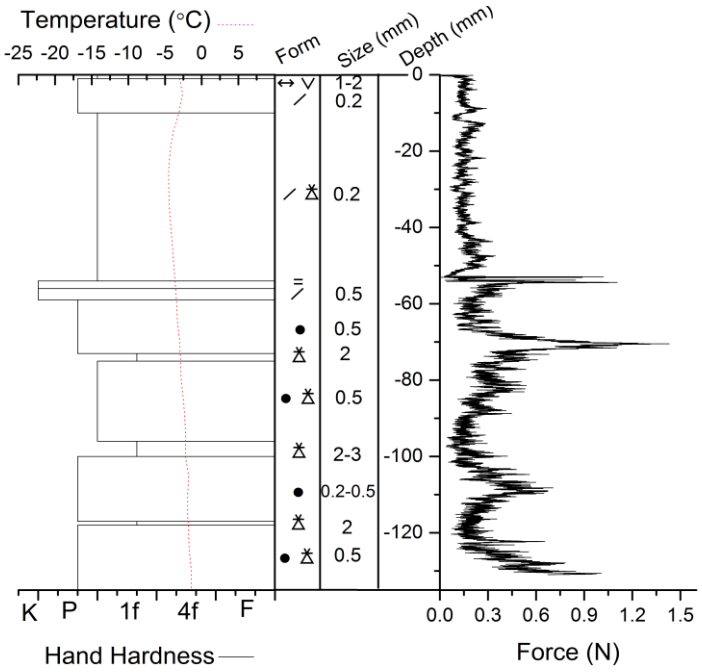

Figure 27b: Snow pit records for the 10th Febuary 2010 field day, recorded in the traditional observer's style. Temperature and hand hardness (left), corresponding SMP records (right). Form symbols after Fierz et al, a table of definitions is available in the glossary.

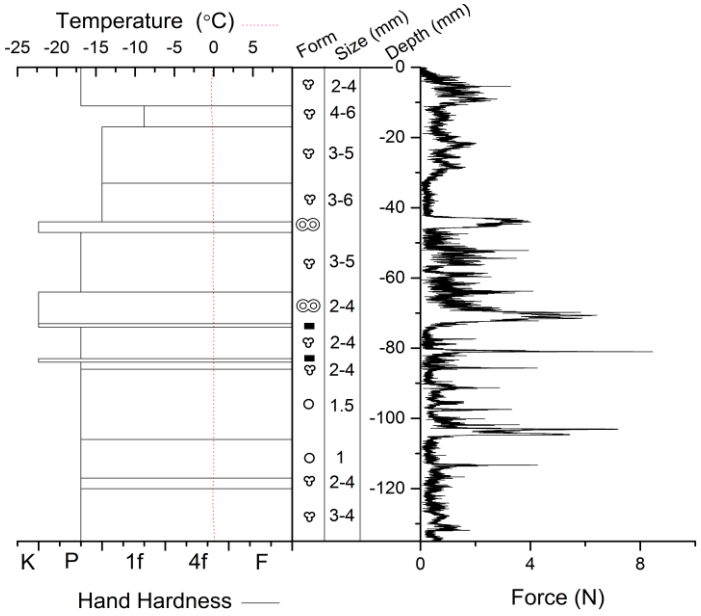

Figure 27c: Snow pit records for the 14th April 2010 field day, recorded in the traditional observer's style. Temperature and hand hardness (left), corresponding SMP records (right). Form symbols after Fierz et al, a table of definitions is available in the glossary.

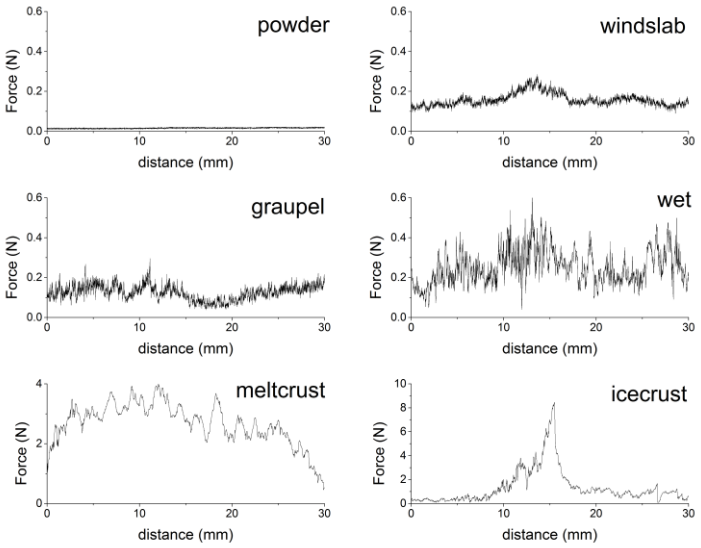

Figure 28: Samples of SMP data for six different snow types, extracted from data presented in Figure 27.

4. SnowMicroPen experiments on artificial snow

Artificial snow was made as discussed in the previous chapter. This artificial snow was sieved through a 1.68 mm aperture sieve into cylindrical containers 300 mm high and 110 mm in diameter. These were covered before being allowed to sinter for 0, 1, 2, 4, 7, 10 or 14 days in a cold room at −10 °C. Samples were uncovered and tested immediately with the SMP. The snow settled with time and did not bond significantly to the container walls.

Force-distance plots for the samples are seen in Figure 29. Ageing of artificial snow samples leads to an increase in penetration force from 0.04 to 0.26 N. The standard deviation of the signals also rose with age, with a coefficient of variation from 0.24 to 0.42.

In some of the oldest artificial snow, fracture of the entire sample within the canister was observed. This caused a sudden drop in penetration resistance. The 10 day and 14 day old samples in Figure 29 have been truncated at this point.

The distance travelled by the SMP before a steady state signal level was reached generally increased with age of the sample, ranging from 10 mm in the fresh snow to around 50 mm in harder, older samples.

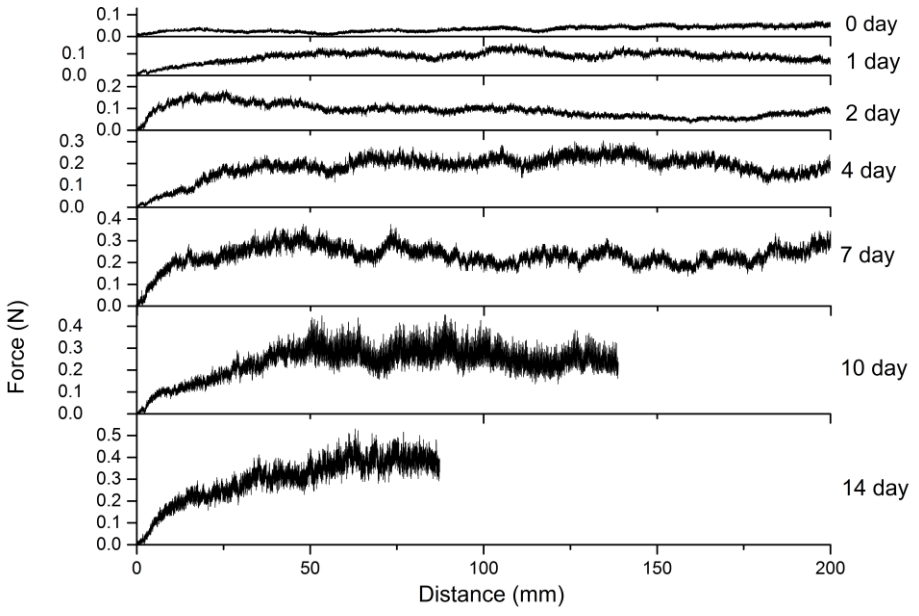

Figure 29: SnowMicroPen records for artificial snow at increasing ages. 10 and 14 day samples are truncated due to specimen fracture.

5. Discussion and comparisons

The windslab, graupel and powder snow produce the most homogeneous force-distance series, as seen in Figure 28. This may be due to their relatively easily separated, dry grains of a constant size. The meltcrust and polycrystalline wet snow show much more variation. This may be indicative of forces being spread over a larger area and larger volumes of grains acting as single units.

An interesting behaviour may be seen when the SMP strikes an ice lens or crust in the snow. The penetration force builds up rapidly before collapsing and rising again. This behaviour may occur three or four times over a distance of 3-4 mm. It is probable that this is caused when the conical tip flexes and then punctures the ice crust. Subsequent peaks correspond to enlargements of this hole until the probe may pass through. The force recorded over this period may be much higher than in the surrounding snow pack and may make detection of any thin layers above or below the ice crust difficult.

Artificial snow hardens with time if left to sinter in an isothermal setting. This sintering process decelerates with time, as would be expected as the snow approaches an equilibrium state.

Older artificial snow takes longer to reach a steady-state force under SMP testing, as seen in Figure 29. This may be indicative of the time required for an interaction volume to build up around the tip.

The range of mean forces for penetration of artificially produced snow covers the majority of the SMP traces taken in the field with the exception of the very soft powdery snow tested on the first day, and ice forms. The range of coefficients of variation from 0.23 to 0.42 also covers the majority of the natural snow except meltcrusts and ice lenses (for which a coefficient of variation cannot be easily defined). It could reasonably be assumed that by aging the snow for longer, higher forces could also be reached, up to a limit defined by the sintering processes.

The type of natural snow most similar to the artificial snow is wind slab. The SMP results for artificial snow reach the same level as wind slab after four days, with similar coefficient of variation also achieved. The artificial snow was denser, (380 kg m^{-3} vs 300 kg m^{-3} typical) but the similarities are reinforced by the microstructures, which are visually similar (see Figure 30)

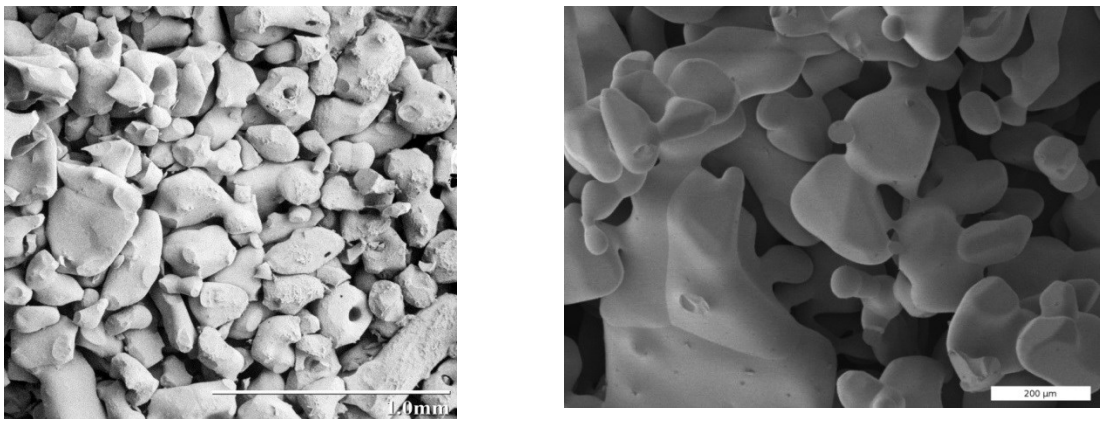

Figure 30: Low Temperature SEM images of wind blown natural snow (left) and 4 day old artificial snow (right). Natural snow image credit: Electron and Confocal Microscopy Laboratory, Agricultural Research Service, U. S. Department of Agriculture." Licence: public domain

6. Conclusions

As discussed in the previous chapter, the artificially produced snow consists of irregular angular fragments with a relatively wide grain size distribution. It is similar in appearance and microstructure to decomposed, windblown snow and windslab. These snow types also produce similar SMP results to artificially produced snow, with windslab (Figure 28) being most comparable to 4 day old artificial snow (Figure 29).

As the structure of the artificially produced snow is similar to some forms of natural snow, it is proposed that study of this artificial snow could lead to improvements in the understanding the origin of the mechanical behaviour of snow.

Chapter V: Designing the experiments

Aim

The aim of the work described in this chapter was to develop a machine capable of deforming snow and visualising the strain fields present in one-dimensional compression and indentation experiments in snow.

1. Introduction

In order to understand deformation in snow it is necessary to know how the deformation organises in space and time. In order to answer this question I conducted deformation experiments on snow and used digital image correlation (DIC) to derive strain fields. This chapter describes the development of the experimental equipment and techniques.

Two test geometries were required: a simple geometry where the sample should have an approximately constant stress tensor throughout and a second geometry providing a more complex stress field. It was envisaged that these two results would exhibit progressively more challenging phenomena for models to reproduce. Test methods capable of providing an approximately constant stress tensor can be broadly divided into two groups: shear and compression (tension being excluded because interesting phenomena were not anticipated for tension). For a material to exhibit train softening and strain localisation in shear is somewhat unremarkable, such behaviour is less common in compression testing. Strain softening in compression was anticipated due to the plateaux observed in stress-strain curves (see chapter II section 6). Furthermore, recent research (Heierli 2009) indicates that many avalanches may occur due to compressive collapse of weak layers, rather than shear failure as has traditionally been assumed. Compression was therefore viewed as more interesting to pursue than shear.

For a compressive experiment three options can be considered: hydrostatic, confined or unconfined. It is difficult to envision how a hydrostatic test could be performed without enclosing the specimen in a membrane or other apparatus, which would impede the DIC. Furthermore, the strain localisation would probably exhibit complex 3D topography, which would be difficult or impossible to interpret from surface observations alone. Unconfined compression (i.e. unidirectional compression of a specimen open to air, with zero radial stress at the surfaces) would be undesirable due to the formation of hoop stresses and the possibility of failure in shear, which as mentioned above was considered less interesting compression. The final option – confined compression – is most appealing.

One-dimensional compression was selected to provide a simple case for analysis and modelling, (that is to say applied strain in one direction with zero strain in the perpendicular directions).

Indentation testing was selected as the more complex geometry because it would allow an opportunity to investigate the behaviour of penetrometer instruments. Such instruments have been put forward as potential methods for assessing avalanche risk or retrieving microstructural information from the snowpack (see chapter II section 5.2). Numerous other test geometries would have satisfied this requirement for complex strain fields, but none other would have been as immediately applicable to current developments in the field of snow science.

2. Specification of the experimental equipment

2.1. Geometry options

Field penetrometers are mostly conical or hemispherical, providing an axisymmetric test condition. The deformation zone is hidden within the snow, and cannot therefore be imaged. An alternative geometry had to be found. Two geometries were considered, as illustrated in Figure 31. The first option was a half-conical tip running in a semi-cylindrical volume, resembling a field penetrometer split down its centre to provide a viewing plane. I will refer to this option as pseudo-axisymmetric (it is not truly axisymmetric as it is not a full cylinder). The second option a chisel-like tip running between parallel surfaces, referred to here as two-dimensional plane strain.

The pseudo-axisymmetric option was geometrically the most similar to conical or hemispherical field penetrometers. The two-dimensional plane strain was more similar to the less common blade penetrometers. The deformation pattern may be different in the two cases, and therefore if the results were to be directly compared to common modern penetrometers the pseudo-axisymmetric option should be preferred. For reasons discussed below, either option appears to be equally suitable for the one-dimensional compression experiments.

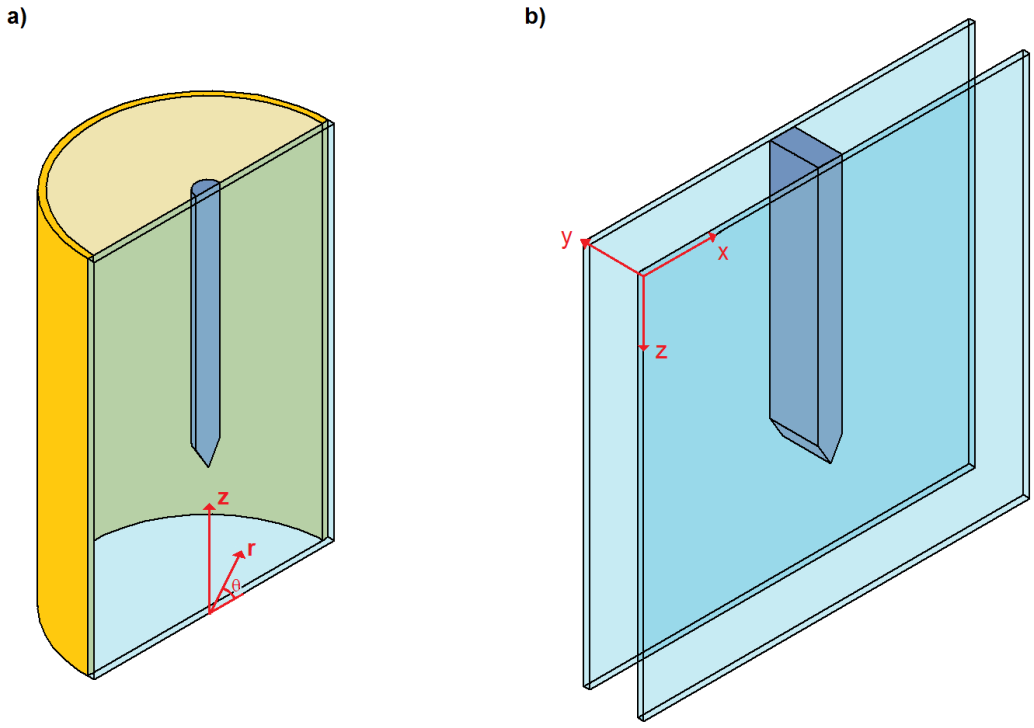

Figure 31: Possible experiment geometries: pseudo-axisymmetric (a), and two dimensional plane strain (b). Coordinate axes (in red) as referred to in the text.

2.1.1. Pseudo-axisymmetric option

The pseudo-axisymmetric option is intended to represent an axisymmetric situation. This is most closely achieved if the viewing plane is smooth and stiff, ideally providing a frictionless boundary with zero displacement normal to the plane of the boundary. For indentation tests, the upper boundary should be a zero stress boundary (i.e. open). The nature of the other (semi-circular and bottom) boundaries is irrelevant provided that they are sufficiently far from the indenter. Sufficiently far in this context means that both stress and strain (which are expected to reduce with distance from the indenter) should approach zero.

Ideally, for one-dimensional compression the curved rear boundary should, like the front plane, approximate zero normal displacement and should be frictionless. The lower boundary should be stiff, while the upper boundary is subject to the chosen test condition (e.g. imposed displacement rate or imposed load). The specimen would therefore experience zero lateral strain, and (for a completely homogeneous specimen) would have a constant stress tensor throughout. If these ideal boundary conditions were achieved, the experiment would be

equivalent to one where the specimen was infinitely wide in directions normal to the applied load.

Attaining sufficient stiffness of boundaries is trivial for experiments on snow, given the low stiffness of the specimen. Any common material from which the equipment may be made (such as metals or polymers) can easily be manufactured thick enough to be stiff relative to the specimen.

Snow, being made from ice, has a relatively low friction coefficient with most other materials, especially when close to its melting temperature. Friction at the boundaries was not therefore expected to disturb the deformation of the snow in the pseudo-axisymmetric option.

The pseudo-axisymmetric form would cause deformation to the rear of the indenter which could not be directly imaged, however, if the deformation is assumed to be axisymmetric, it is be possible to fully describe the strain field using only observation of the exposed plane.

Referring to the coordinate axes in Figure 31a, direct observation of displacement in vertical (z) and radial (r) directions was possible. Strain components (using Cauchy's notation) ε_{zz}, ε_{rr} and ε_{rz} can therefore be calculated:

$$\varepsilon_{rr} = -\frac{du_r}{dr} \qquad \varepsilon_{zz} = -\frac{du_z}{dz} \qquad \varepsilon_{rz} = \frac{\frac{du_r}{dz} + \frac{du_z}{dr}}{2}$$

Equations 4, 5 & 6

Where u represents displacement, in the direction indicated by the subscript, and strain is positive in compression.

If the experiment is axisymmetric, the circumferential displacement (u_θ) is zero throughout (axisymmetric rotation is prevented by the viewing plane). Circumferential strain ($\varepsilon_{\theta\theta}$) is then only a function of the change in circumference with respect to radius, thus:

$$\varepsilon_{\theta\theta} = -\frac{u_r}{r}$$

Equation 7

Conducting one-dimensional compression experiments in the same container was not expected to provide any significant additional challenges.

The axisymmetric option was discarded for two reasons: (i) The assumption that pseudo-axisymmetric boundary conditions would lead to axisymmetric deformation was considered questionable. The aim of the experiment is to examine strain localising phenomena, which may originate from random spatial fluctuations of strength within the snow. If these small strength variations were to cause symmetry breaking, observations from the viewing plane would inadequately describe the situation in the full test volume. (ii) In order to provide good texture for DIC, I planned to light the specimen from the rear. (The concept of DIC and texture is explored in chapter VI). Achieving even illumination of the viewing plane with the pseudo-axisymmetric option was expected to be challenging, given the variable thickness of specimen in the light path.

2.1.2. Two-dimensional plane strain option

The two dimensional option is illustrated in Figure 31b and will be described with reference to the coordinate axes shown there.

For plane strain, displacements on the viewing plane are related to strain components by:

$$\varepsilon_{xx} = -\frac{du_x}{dx} \qquad \varepsilon_{zz} = -\frac{du_z}{dz} \qquad \varepsilon_{xz} = \frac{\frac{du_x}{dz} + \frac{du_z}{dx}}{2}$$

Equations 8, 9 & 10

u_y is assumed to be zero, and ε_{yy} is therefore also zero.

The assumption that planar boundary conditions would lead to plane strain was considered questionable. It was considered likely that random spatial fluctuations in the strength of the snow could result in non-zero *y*-direction displacements and strains, which could make interpretation and analysis of the system challenging. The risk of this occurring can be minimised by choosing a small specimen length (*l*) in the *y* direction, as this would minimise strength variation in the *y* direction. More importantly, the boundary constraint forces y displacements to be zero at the boundary, and therefore close to zero throughout the sample for small *l*.

A small *l* value was also desirable from the perspective of illumination. As is discussed in section 3.4.2, significant illumination levels were required at the front face. Given that I intended to back-light the specimen, and that the snow would absorb some of the light, a thick specimen would have required an extremely bright light source. This could have heated

the specimen sufficiently to alter its behaviour, and to produce a temperature gradient across the specimen. This is a serious cause for concern, given that (for a test temperature of -10 °C) the snow is at 96% of its melting temperature. Even small temperature gradients will cause vapour transport, leading to undesirable changes in morphology and mechanical properties.

For indentation experiments, the two y-normal boundary planes (corresponding to viewing planes) should ideally be stiff and frictionless. This situation would then approximate an infinitely long blade type indenter. The upper boundary (*z*-normal) should be a zero stress boundary, allowing for possible heave of the upper surface of the specimen, as this most closely imitates actual field testing. The nature of the *x*-normal and other (lower) *z*-normal boundaries is irrelevant, provided they are far enough from the indenter.

For one-dimensional compression, ideally all boundaries should be stiff and frictionless (zero lateral strain and zero wall shear stress) with the exception of the upper (*z*-normal) boundary, to which the chosen displacement rate for the experiment would be applied at all points. If these ideal boundary conditions were achieved, the experiment would be equivalent one where the specimen was infinitely wide in directions normal to the applied load.

The advantages of choosing the container thickness *l* to be small have to be balanced against the drawback that small *l* exacerbates the influence of friction at the front and back walls . I discuss this aspect in detail for the case of one-dimensional compression:

Due to side wall friction, a shear stress is acting on the sample side faces. This has the effect of reducing axial stress in the lower part of the specimen when compared to the top. By considering the equilibrium of forces on a *z*-normal plane for a homogeneous specimen and an infinitely wide experiment (in the *x* direction), the average stress at a given *z* position ($\bar{\sigma}_{zz}$) is governed by the equation:

$$\overline{\sigma}_{zz} = \bar{\sigma}_{zz}^{0} - 2\tau_{yz}\frac{z}{l} + \rho g z$$

Equation 11

Where $\bar{\sigma}_{zz}^{0}$ is the stress applied at the top of the specimen, *l* is the length of the specimen in the *y* direction, τ_{yz} is shear stress at the walls (which is initially assumed to be constant), ρ is density (also assumed to be constant)and g is acceleration due to gravity.

An assumption that ρ is constant is valid until the point at which strain localisation occurs. An assumption that τ_{yz} is constant will introduce error, which is addressed below.

An alternate form of Equation 11, allowing for variation of τ_{yz} with z, is:

$$\frac{d\overline{\sigma}_{zz}}{dz} = -\frac{2\tau_{yz}}{l} + \rho g$$

Equation 12

Wall shear stress τ can be attributed to friction, and assuming Coulomb friction, can therefore be expressed as a function of normal stress (σ_{yy}) and friction coefficient (μ):

$$\tau_{yz} = \mu\sigma_{yy}$$

Equation 13

If the snow is behaving elastically, and a simplifying assumption is made that σ_{xx}, σ_{yy} and σ_{z} are principal stresses (a reasonable approximation if τ_{yz} is small), the condition of zero strain in the x and y directions can be used to derive:

$$\sigma_{yy} = \frac{\nu}{1-\nu}\sigma_{z}$$

Equation 14

Inserting this in Equation 13 gives:

$$\tau_{yz} = \frac{\mu\nu}{1-\nu}\sigma_{z}$$

Equation 15

Equation 12 then becomes:

$$\frac{d\overline{\sigma}_{z}}{dz} = -\frac{2\mu\nu}{l(1-\nu)}\overline{\sigma}_{z} + \rho g$$

Equation 16

This can be integrated from $z = 0$, where $\bar{\sigma}_{zz} = \bar{\sigma}_{zz}^{0}$:

$$\int_{\bar{\sigma}_{zz}^{0}}^{\bar{\sigma}_{zz}} \frac{d\bar{\sigma}_{zz}}{\left(\bar{\sigma}_{zz} - \frac{\rho g l(1-\nu)}{2\mu\nu}\right)} = -\frac{2\mu\nu}{l(1-\nu)} \int_{0}^{z} dz$$

Equation 17

Giving the following result for $\bar{\sigma}_{zz}$:

$$\bar{\sigma}_{zz} = \frac{\rho g l(1-\nu)}{2\mu\nu} + \left(\bar{\sigma}_{zz}^{0} - \frac{\rho g l(1-\nu)}{2\mu\nu}\right) \exp\left(\frac{-2\mu\nu z}{l(1-\nu)}\right)$$

Equation 18

This process makes two significant assumptions: coulomb friction and small (elastic) deformation. Coulomb friction is probably reasonable, as basic calibration experiments (discussed later) performed on the glass showed a linear relationship between normal and tangential forces. The assumption of elastic strain cannot be applied to most of the experiment. Not only will deformation quickly exceed the elastic limit but directional deformation is likely to make the stiffness anisotropic. Given that strain localisation was anticipated, it is reasonable to assume that plastic deformation would be confined to only small sections of the specimen at any one time. To treat the majority of the specimen as elastic is therefore reasonable, even if small volumes have previously undergone plastic deformation. Although the value of E may change through the experiment, the equations remain valid as long as local instantaneous vertical stiffness is the same as local instantaneous lateral stiffness. This leaves the question of anisotropy. The effect of deformation on subsequent stiffness is not known, but given that stiffness is closely related to density, the vertical and lateral values cannot be too different.

In an ideal experiment, $\bar{\sigma}_{zz}^{0} = \bar{\sigma}_{zz}$. For given values of ρ, g, z and τ, this can most closely be approximated by choosing a large value of l relative to the height (h) (the maximum value of of z). This is undesirable for reasons illumination, and to minimise out-of-plane displacements and strains.

As observed in chapter II section 4 snow has a very low Poisson's number. It therefore follows, taking a typical value of μ, that τ_{yz} is much less than $\bar{\sigma}_{zz}$. In light of this, it was expected that good results could still be obtained with a relatively small value of l, especially

when considering that the self weight opposes the wall shear. Further, if τ_{yz} is much less than $\bar{\sigma}_z$, then τ_{yz} does not significantly disturb the stress tensor within the specimen. A small value of *l* could be accepted if the value of μ and υ could be monitored during the experiment to confirm that $\bar{\sigma}_{zz}$ did not vary significantly.

The above discussion of course applies equally to the width (*w*) of the specimen in the x direction. This dimension is not subject to the same design constraints as the *y* dimension (*l*), and may therefore be chosen to be large without negative consequences.

2.2. Geometry selection

In light of the above discussions, a plane strain design was preferred to the axisymmetric option. The principal issues driving the selection of the plane strain option in preference to pseudo-axisymmetric were the ease of attaining even illumination from backlighting and the reduced risk of hard-to-interpret results being caused by symmetry breaking strain localisation.

Further, it was decided that length (*l)* should be less than height (*h*) but that the width (*w*) should be greater than the height (*h*). This would strike the best balance between reducing edge effects (caused by low *l* or *w* dimension) and the need to accommodate back lighting and to minimise potential strain variation in the *y* direction.

Indentation experiments were intended to resemble the SMP, which uses a 6 mm conical tip with an included angle of 60°. An indenter was therefore specified with a 6 mm width and 60 ° angle. Some penetrometers use hemispherical heads, and shapes without sharp edges are generally easier to model, so a semi-circular tip was also specified. To allow comparison with the sharp tip, this was also 6 mm wide (3 mm radius). To investigate the effects of size, 60 mm width rounded tip was also specified.

2.3. Specimen size

The general form of the apparatus being decided, size could be specified. The most important dimensions being the length of the specimen (*l*), of the sample, and the size of the section presented to the camera (*w* x *h*).

As discussed above, *l* had to be small to constrain out-of-plane deformation, but should be large to ensure an even stress distribution in the z direction. *l* must also be large enough to allow any microstructural deformation mechanisms to develop unhindered. A thickness of 20 mm was selected, being about 40 times the diameter of the larger snow particles, and 100 times that of the smaller ones.

Height (*h*) was decided by looking at the distance travelled by the SMP before steady state was established in the experiments in Chapter IV. This was up to 75 mm for aged snow. If a further 75mm was required between the bottom of the indenter and the base of the machine, and if 50mm of moving steady-state data was to be acquired, then the sample should be 200 mm tall.

As discussed in section 2.1, width (w) should be greater than height (h). Width was therefore set at 250mm.

These dimensions were set with limited foreknowledge of how the experiments would progress, and were believed to represent a good compromise between conflicting design pressures, especially in selection of the specimen length (*l*). In order to confirm the appropriateness of the design, the equipment was developed with a view to being able to measure the outward force on the walls and the coefficient of friction of the snow with the glass. This information could then be used to confirm that the influence of wall shear (as described in section 2.1.2) was small.

2.4. Displacement rate or load rate control

The experiment could be controlled in one of two ways: the indenter or anvil could be driven at a fixed speed (strain rate control); or the load on the indenter or anvil could be increased at a set rate (stress rate control). Field penetrometers are almost exclusively driven at a fixed speed, so displacement rate control is the obvious candidate in indentation experiments. For the one-dimensional compression tests, strain rate control was required because the snow was expected to undergo transient strain softening, so imposing a load might lead to large deformation in a short time, leading to poor time domain resolution in the DIC.

2.5.Speed

For indentation experiments, wide range of speeds were considered desirable. Field potentiometers are likely to be driven at relatively high speeds. The SnowMicroPen is motorised, providing a speed of 20 mm s^{-1}, but other designs (Bradley 1968, Mackenzie and Payten 2002) are hand driven and thus likely to experience higher speeds.

On the other hand, the limitations of high resolution image acquisition mean that lower speeds may be required for small enough deformations between consecutive images. It was decided that for indentation the apparatus should be designed to operate at speeds from 1 to 20 mm s^{-1}.

For one-dimensional compression, speed would be set by the desired strain rate. It was intended that the strain rate should lie in the brittle region (for discussion of the ductile to brittle transition observed in snow and the transition strain rate see chapter II section 6). The transition strain rate varies between $2x10^{-4}$ and $2x10^{-2}$ s^{-1}. For a specimen height of 200mm this corresponds to a crosshead speed of 0.04 to 4 mm s^{-1}. As with the penetration experiments, high speeds were expected to lead to poor time-domain resolution in the DIC data, so speeds only slightly exceeding the transition threshold should be selected (the brittle nature of the test being confirmed by examination of the recorded force). The specified speed range for indentation (1-20 mm s^{-1}) fits this requirement.

2.6.Measurement

2.6.1. Images

Image acquisition was intended to be the main form of measurement. It is often necessary to trade off resolution of images for frame rate. For my experiments, a high level of resolution was required to allow tracing of a texture provided by individual grains of snow, whilst still allowing a reasonably large area to be analysed (the concept of texture is explored in chapter VI). On the question of frame rate, it was anticipated that the strain rates could be reduced to accommodate frame rates available from high resolution cameras. It was therefore decided that still image cameras should be investigated in preference to video orientated devices.

2.6.2. Forces

Alongside the image acquisition, force would also be measured. It was intended that events or features in the force record could be associated with mechanisms detected through image analysis. For one-dimensional compression, the force would be decided by the size of the equipment along with the target stress. For indentation experiments, a much lower force would be required.

Indentation experiments were intended to investigate behaviour similar to that shown by the SnowMicroPen. This instrument has a 6 mm diameter conical tip and experiences a measured force of up to 0.5 N when applied to our laboratory made snow. By scaling according to the frontal area of the penetrometer, a 6 mm chisel tip indenter with a length of 20 mm should require approximately 2.2 N of force. By application of the same scaling technique, the force required for a 60mm indenter would be 22 N.

Due to the difference between a conical tip and a chisel, the applicability of this scaling was considered questionable. To ensure the experiments could proceed, a factor of safety was introduced for the measured forces. The measurement requirements were therefore set at 5 N for 6mm penetrometers, 50 N for 60mm penetrometers.

If the same scaling were applied to the anvil used in homogenous compression, the force required would be was 90 N, however two geometries may not be comparable as the homogenous compression experiment cannot push material aside. A simple deadweight experiment was conducted to estimate the strength of the snow, and the force for one-dimensional compression was thus set at 200 N.

2.6.3. Position

In the interest of accuracy, it was considered necessary to measure displacement of the indenter separately from the position instructed by the control system.

2.6.4. Wall shear

Whilst not forming part of the principal experimental results, it was necessary to make approximate measurements of the coefficient of friction between the snow and the viewing windows and to measure the outward force on the viewing planes. These two measurements taken together could then be used to confirm that the effect of wall shear on the experiments was small. Neither of these variables needed to be measured of a high degree of accuracy.

2.7. Control

It was considered desirable to have accurate speed or strain rate control and to have accurate, simultaneous recording of force, position and image data. In the interest of safety and equipment life, automatic detection of over-run and over-load conditions was considered desirable, as was automation of the test procedure.

2.8. Preparing the experiment

To ensure consistent and complete filling of the sample space with snow, it would be sieved into place. In the course of sieving it is possible to accidentally produce stratification of the snow, and an age differential will exist between the top and bottom of the specimen. The experiments aimed to test the properties of the underlying snow, not the properties of any induced stratigraphy. To minimise the effect of age differential and stratigraphy on the observed deformation pattern, it was considered desirable to sieve in the snow normal to the direction of applied strain. To facilitate this, one of the two viewing planes should be removable, and the equipment should pivot forward, placing the remaining viewing plane horizontal to allow filling from above.

3. Detail design and construction

In light of the specification developed above, a final design was developed, as shown in Figure 32. The remainder of this chapter explains the detail of the design and the reasons behind each design decision.

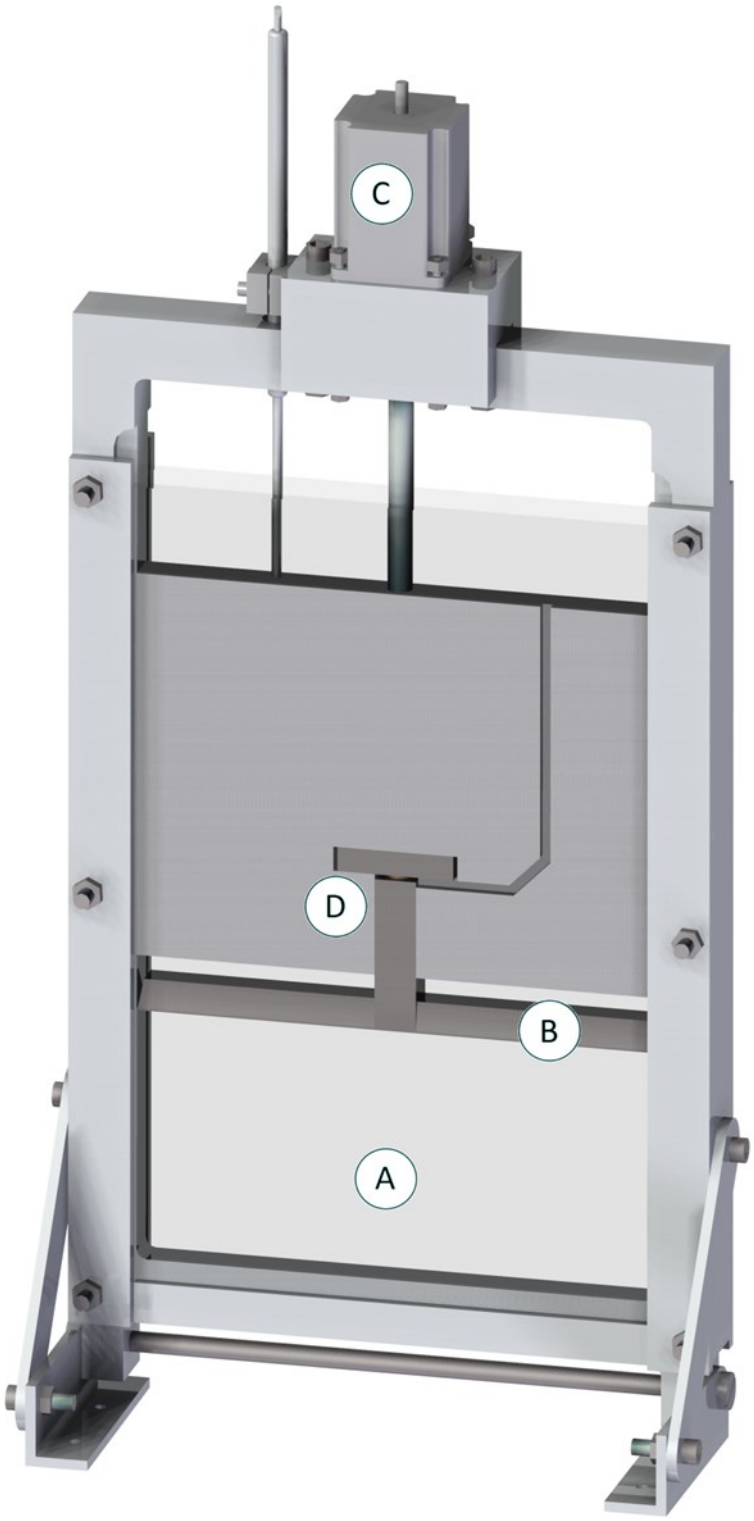

Figure 32: CAD drawing of the apparatus. Specimen area (A); anvil (B) which can be exchanged for indenters; drive motor with check potentiometer (C); and load cell assembly (D)

3.1. Uniaxial test machine vs motor drive

Two options for overall drive and measurement were considered: either a test cell could be constructed for use with an existing uniaxial test machine, or a complete system including motor drive and force measurement could be constructed.

Use of an existing uniaxial testing machine would accelerate development of a suitable experimental apparatus significantly. A machine was available: a J. J. Lloyd M30K uniaxial tester which was surplus to requirement and available for installation in the refrigerated laboratory. This machine had 1 kN load cells available, which would give acceptable accuracy for the one-dimensional compression experiments (target 200 N) but a smaller load cell would be needed for the indentation tests (target 5 N and 50 N). This system offered a maximum speed of 16.67 mm s^{-1}, below the target of 20, but similar enough to warrant consideration. Basic data logging was possible via a 0 – 10 volt output, or chart recorder.

Custom design and construction offered the advantage of higher speeds and integration of all control instructions through a single interface, as well as fully automated test procedures, simultaneous data logging (force and images) and greater future adaptability. A custom design would clearly entail greater commitment of time and resources.

It was decided that a uniaxial test machine based approach would offer the best option, as it would allow more time to be allocated to experiments, however the machine developed an electrical fault in early testing. It continued to operate but with a maximum speed of only 1.67 mm s^{-1}.

The manufacturer was not able to undertake a repair due to obsolescence, nor could they supply the technical information likely to be required for in-house repairs.

It was decided that the machine should be repaired, if possible, by the university technical staff. The repair was unsuccessful, causing further damage to the machine. Further repair work was considered uneconomical, and no alternative machine was available. It was therefore decided that planned use of a uniaxial test machine should be abandoned and a bespoke, motor driven apparatus should be designed and used instead.

3.2. Selection of drive type

Following the failure of the tensile testing machine, a new drive mechanism had to be found. Accurate speed and position were considered the main priority. Linear motors were considered but cost and availability indicated the use of a lead screw or ball screw system driven by a traditional rotating motor. Two motor types were considered: stepper or servo.

Stepper motors offer very reliable speed and position responses for given electrical inputs, provided that the load does not approach the stalling torque of the motor. Stepper motors do move in finite steps, resulting in torque peaks at lower speeds, but this effect becomes much less significant at higher speeds, where the inductance and inertia of the motor act to smooth the motor output.

Servo motors produce a smooth application of torque, but speed regulation requires continuous monitoring of position and application of a control regime. Control methods such as P.I.D. (Proportional Integral and Derivative) increase the control system overhead or may require designated servo control hardware, which may need to be tuned to the characteristics of the individual experiment to achieve reliable results.

In the interest of accurate and reliable speed and position response, a stepper motor based system was chosen. The actual motor and control electronics selected are discussed under section 3.6.4.

3.3. Measurement

Two principal measurements were required; force and position. Force was a desired experimental output whilst position was required only to check the motor drive was performing as expected.

3.3.1. Force

Two means of force measurement were considered: either the use of strain gauges on an appropriate calibrated part of the structure or incorporation of a small load cell. The use of a commercially manufactured load cell was preferred as it was expected to yield more accurate results and simplify construction.

Load cell selection was limited by the requirement that the cell must fit inside the thin experimental volume. This set an upper limit of 20 mm across the axis of the force. Several small load cells were available from a previous experimental campaign, these being Measurement Specialities ELFS and ELFF type. These load cells had ranges of 250 N and 25 N and had been thermally compensated for use below 0 °C.

The ultimate accuracy and sensitivity of the load cells would depend on the supporting electronics, being analogue devices there is theoretically no lower limit to resolution of a load cell. In reality, resolution for high frequency force components is limited by system noise. The load cell's own noise floor (Johnson-Nyquist noise) was calculated at c. 0.5% full scale output up to 100 Hz. (noise of this type can be reduced by filtering, and is therefore less at lower frequencies).

Accuracy was considered less important than sensitivity (the detail and shape of the force results was more important than the absolute value of force). These cells had a quoted non linearity of 0.5% full scale, and hysteresis of 0.5% full scale, which was considered to represent adequate accuracy and repeatability, given that snow is a highly disordered material where sample-to-sample variations of strength can easily been in the range of tens of percent for identically prepared samples.

Without being able to fully quantify system performance in advance, it was anticipated that the load cells could be operated down to 10% of their full range with reasonable results. The two cells therefore gave a usable range of 2.5 N to 250 N, covering the requirements set out in section 2.5.2 These cells had performed well in their previous use so were adopted for this project also.

3.3.2. Position

Position measurement would be used only for ensuring proper function of the experiment. A simple three wire potentiometer was considered adequate for this use.

3.3.3. Wall shear

To measure the wall shear between the snow and the viewing planes directly would be challenging, so I opted instead to measure the normal force and coefficient of friction. These measurements were not needed for every test, but only for a single 'proof of concept' experiment.

In order to measure the normal force during a test, it was considered sufficient to measure the deflection of the viewing planes as the experiment progressed. Two dial gauges were used for this purpose (front and rear). The stiffness of the glass was measured by means of a calibration experiment using the same clamping arrangement as in the actual experiments and was found to be c 290 N mm^{-1}.

3.4. Imaging and illumination

To enable tracking of particles, high resolution images were required. High frame rates, whilst desirable, were considered secondary to resolution. It was therefore decided to pursue still image cameras in preference to video cameras.

3.4.1. Resolution requirement

The area to be photographed and tracked was 200 mm wide. The grains to be tracked vary in size from 0.1 to 0.5 mm. Allowing 2 to 10 pixels per grain width and assuming a little extra image area to cover the boundaries, a horizontal pixel count of around 4200 was required. For a typical 3:2 aspect ratio image sensor this corresponds to a minimum requirement of 11.8 Megapixels. Actual images would of course be impaired by lens capabilities and image processing such as Bayer deconvolution and jpeg compression (if required), so a higher resolution would be preferred.

3.4.2. Illumination and shutter speed

For the avoidance of motion blur in the images, a high shutter speed was required. If the acceptable motion blur is set at 0.05 mm, the pixel pitch in the suggested resolution above, then for a 20 mm per second test speed the shutter speed would need to exceed 1/400 s. Realistically, a higher speed would be desirable, particularly if smaller areas were to be imaged at a higher resolution.

To maximise the resolution of the lens and offer reasonable depth of field, it was considered desirable to avoid use of a wide lens aperture. For a typical camera sensitivity, this requires extremely bright illumination. This was identified as a risk to the sample's thermal stability. To avoid this risk it was decided to use flash photography. Whilst the cameras discussed below cannot synchronise their shutters with flashes at speeds above about 1/250 s, a typical

flash lasts only about 1 ms, and thus can freeze motion adequately for these experiments. Due to the short duration of the flash, it was not considered a risk to the specimens.

3.4.3. Lenses

Alongside the requirements of the camera, a suitable lens must also be selected. To maximise the resolution of the finished images, the lens must be sharp. Field curvature, distortion and chromatic aberration were also considered undesirable. Lenses deigned or marketed for macro use were preferred, as they were expected to offer better performance given relatively small planned image area.

3.4.4. Imaging equipment selected

In light of the above discussion, it was decided that a consumer SLR type camera would be most suitable. Two brands dominate this market: Canon and Nikon. GeoPIV, (which will be discussed in chapter VI), had been validated with a range of Canon cameras and neither brand seemed to offer significant advantages over the other. It was therefore decided that Canon products should be further investigated.

The three main driving factors in selection of the specific model were resolution, frame rate and cost. The Canon 7D was selected. This camera offers an 18 megapixel sensor with a maximum frame rate of 8 per second, though images must be compressed (JPEG standard) to achieve this speed.

Canon and third party lenses were considered based on independent testing available through semi-scientific internet reviews as well as data published by the manufacturers. The main driving requirements were high resolution, low distortion, low optical aberration and cost. The lens selected was a Canon EF-S 60mm macro.

Having made the above selections, equivalent systems from other manufacturers were compared to the final Canon selection but found no to offer any significant advantage in price or performance.

3.5. Data acquisition and system control

A data acquisition system was required to record the electronic output of the load cell and potentiometer. A system was also required to drive the motor and trigger the camera. In the

interest of convenience, cost and system automation, it was decided to combine these functions into one control system. For clarity they are discussed sequentially.

3.5.1. Data acquisition options

A load cell requires a voltage excitation and provides a small (mV level) differential signal. It is necessary to record the excitation voltage in order to compensate for any variation in it, which will cause a linearly proportional change in output. Rather than considering these parts separately it was considered desirable to use an integrated strain gauge/load cell data acquisition device, which would combine all three requirements (excitation, excitation measurement and signal measurement) in one product.

A potentiometer also requires voltage excitation and excitation monitoring, but returns a voltage signal up to the full excitation voltage. Such a voltage cannot be attached directly to a dedicated load cell measurement device as the returned signal will be out of range. Two options for connecting the potentiometer were considered – either the signal could be attenuated with resistors to allow connection to a vacant channel in the load cell module or a specific 10 V module could be used. As the potentiometer was only to be used to confirm the correct motor action, the reduction in accuracy caused by the introduction of resistors was considered acceptable, and the cost and complexity of additional acquisition hardware avoided. The potentiometer was connected as shown in Figure 33. This method increased Johnson-Nyquist noise in the system, but the resulting signal to noise ratio was considered acceptable.

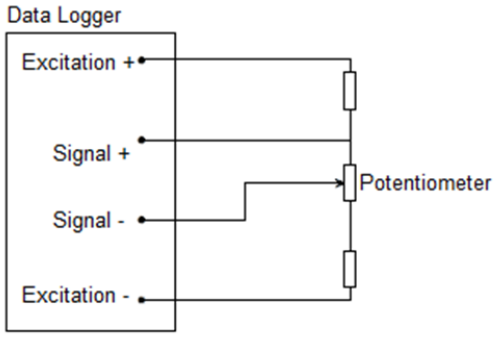

Figure 33:Electrical connection between potentiometer and data logger used to attenuate the potentiometer signal to ±25 mV/V so that its output may be read by the load cell module

3.5.2. Equipment selected for data acquisition

Due to the differing specific requirements of data logging and output control (as discussed below), a modular system was required. This could either consist of either: basic logger with external signal conditioning and electrical interfacing components; or an integrated modular logger with specific modules for each application. The second option would be preferred for ease of assembly and control integration.

As discussed in section 3.6.2 the university had a subscription to National Instruments LabView software, making their products the default choice unless other options were demonstrably superior in some way. Following consultations with National Instruments and an onsite demonstration, a system consisting of a NI-9174 chassis with NI-9237 Bridge module was selected. The bridge module had an advertised accuracy of 0.0375 mV/V and 24 bit DAC, corresponding to a 0.2% accuracy over the full scale output of the load cells.

3.6. Motion control options

3.6.1. Motor drive electronics

A stepper motor, as selected in section 3.2, requires a current to be supplied to certain coils make one step, and then to different coils to make the next. The inductive nature of the coils means that current cannot flow instantaneously but will rise from zero in a finite time. The higher the driving voltage, the faster the design current, and therefore the design torque, is achieved. A suitable motor for this application would require 2 A nominal current and have a nominal 4 mH inductance. For a target speed of 50 mm/sec and a lead screw pitch of 3 mm a step speed of 3333 steps per second would be required. Thus to reach a 2 A current in the required $3x10^{-3}$ s, a voltage in excess of 27 V was needed.

Two arrangements of drive electronics were considered. Either an integrated controller allowing control from a computer, or a step and direction controller which could be separately controlled by a digital output on a data logger.

An integrated driver offers a simple and convenient package which would typically be supplied with software. Whilst this would be convenient to assemble, integration of the drive software with the experimental control programme could be difficult.

A step and direction controller requires a signal to set direction and a separate pulse train to trigger steps. If these could be supplied from the data logger it would make program

integration significantly easier, at the cost of increased wiring complexity. This option was also expected to have a lower cost.

It was decided that a step and direction controller linked to the logger would offer the best solution overall. A module would be required for the data logger which would allow rapid switching of three external outputs, two for connection to the motor controller and one for the camera.

3.6.2. Triggering the camera

It was necessary to acquire photographs at specific intervals. The camera provided a 3.3 V contact designed for passive external triggers. The shutter would operate if these contacts were shorted together. A module selected for motor drive (as discussed below) offered 5 V terminals which could be switched as required. A suitable interface was implemented using a transistor and resistor as shown in Figure 34.

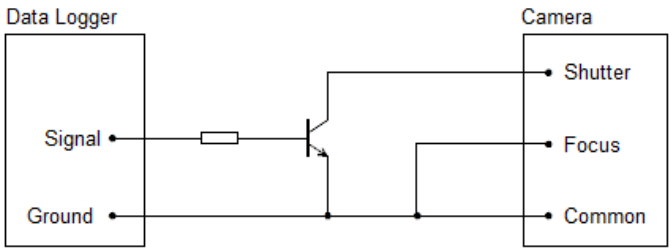

Figure 34: Electrical connection between camera and data logger used to trigger the shutter by converting from 5 V signal to 3.3 V signal

3.6.3. Programme and control

The university has a site licence for national Instruments LabView. As both the drive and data acquisition could be controlled from the data logger, the use of platform independent programming offered no advantage over programming languages provided specifically for the data logger. It was therefore decided to develop the control system in LabView. The programme followed a loop as indicated in Figure 35. The effect of this loop was that the potentiometer and load cell were continually monitored for overload or overextension, whilst the motor ramped up to the desired speed and then ran until the intended distance was complete. The loop iterated at a fixed interval of 5 ms.

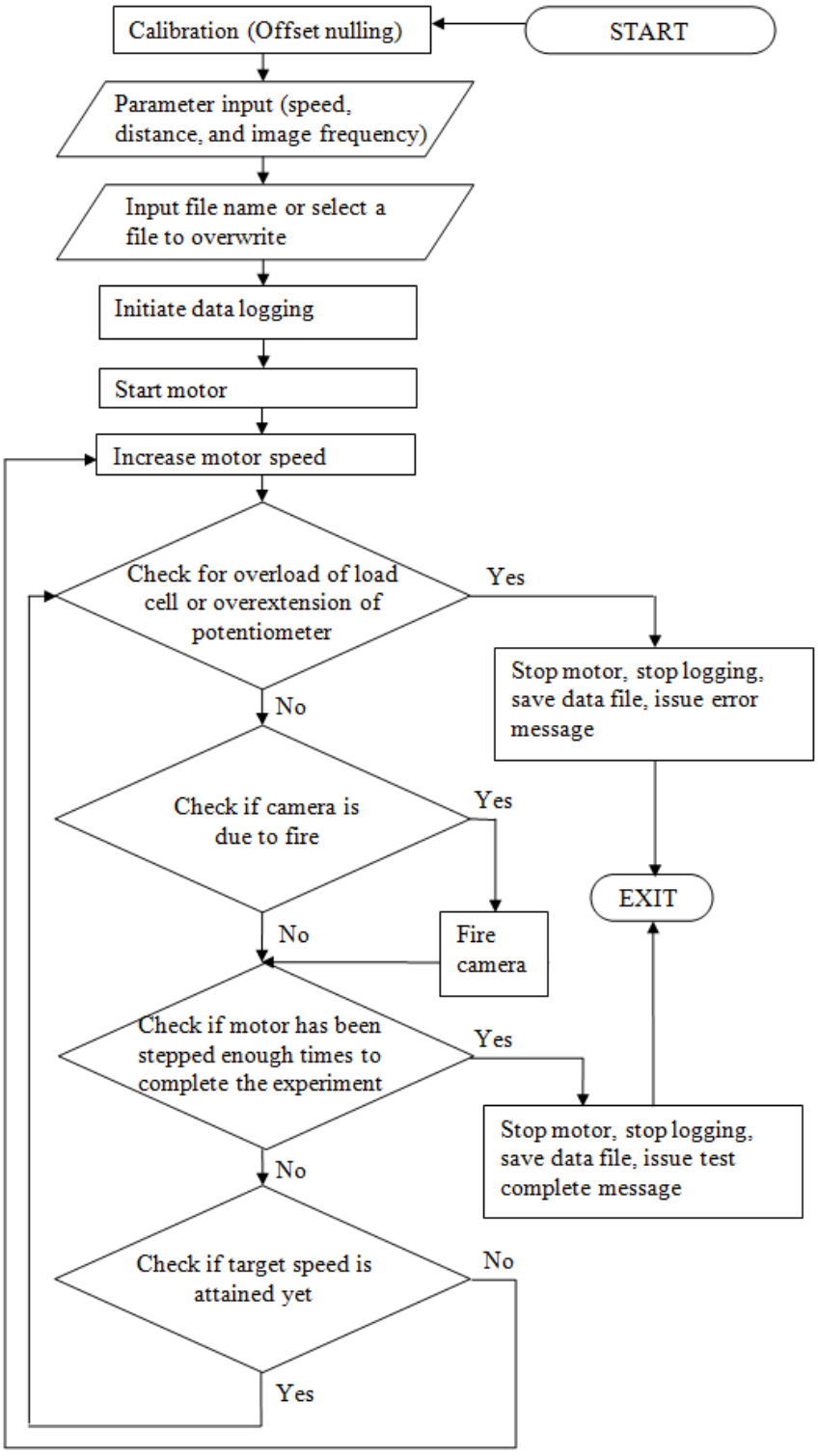

Figure 35: Block diagram of program control sequence used for conducting the experiment. Loop execution (upward arrows) ran at a 5 ms interval.

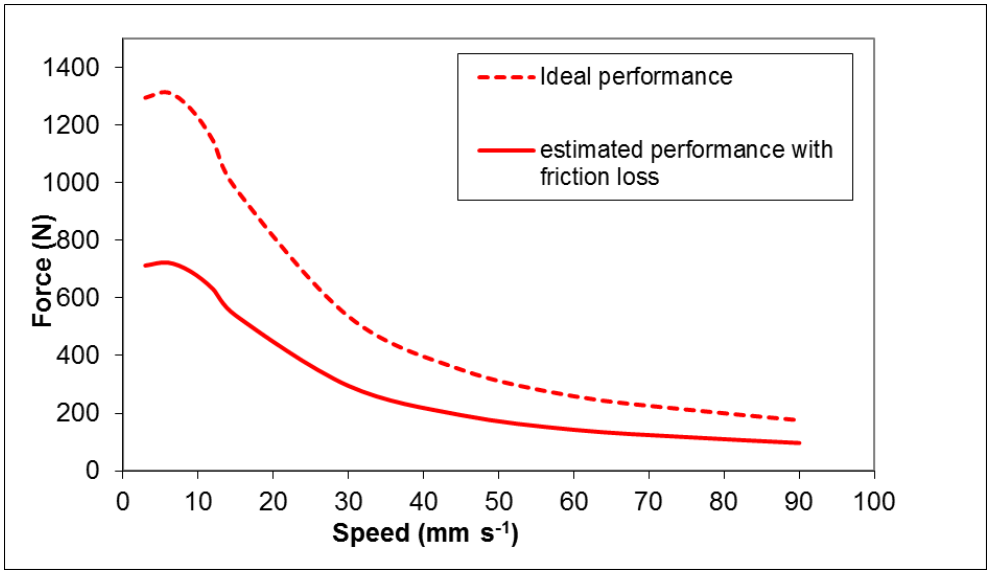

Figure 36: Expected motor performance for lead screw of 3mm pitch with polymer bearings and drive nut. Curves indicate the maximum achievable force (stalling force) Based on manufacturer provided torque-speed data.

3.6.4. Equipment selected for motion control

Taking into account the previous sections, a final product selection could be made. For motor selection, no particular manufacturer or supplier was expected to outperform any other, so a motor was selected from an existing university supplier. The motor was selected in unison with the stepper motor controller, as the properties of both affect the selection of the other. The selected motor was a Mouser HT23-400 with Applied Motion PD02035 controller. Both were supplied by Mouser, who provided expected performance curves. When used with a 3 mm pitch lead screw this combination was expected to give a performance as shown in Figure 36. Friction in the bearings and on the lead screw were estimated using manufacturer quoted values for friction coefficient in dry polymer bearings and leadscrews.

For control of the motor driver, an NI-9401 digital input/output module was added to the logger. This module offers eight 5 V input/outputs with internal clocks to ensure accurate rapid switching. The maximum current sourced by this device is only 2 mA, slightly below that recommended for the optio-isolated inputs of the stepper controller but found to be sufficient in testing.

3.7. Custom made parts

Once components had been selected it was necessary to design and make the main frame and other custom made parts for the experiment.

3.7.1. Frame

An overall frame was required to mount the relevant parts and to confine the snow under test. In the interest of high stiffness and dimensional accuracy, especially parallelism of the main slide, it was decided that the frame should be cut from a single part. A bolted or jointed frame was considered, but would have introduced unnecessary opportunity for misalignment or play. A welded frame was also considered, but offered no advantage over a monolithic structure when the requirement for machining was taken into account. Aluminium alloy was selected as the preferred material due to corrosion resistance and the availability of appropriate machining capacity and skills.

The frame forms part of the boundary for the experiment. As discussed in section 2.1.2 it should be stiff and have low friction. Being made from aluminium alloy and 30 mm thick in the direction of loading, it was clearly much stiffer than the snow specimen, and offered a reasonably low coefficient of friction with snow.

3.7.2. Viewing panes

The viewing panes had to be transparent. Two materials were considered: glass or clear polymers (known as Plexiglas, Lexan, Perspex etc). The viewing pane forms part of the specimen boundary, which needed to be stiff and have a low coefficient of friction with snow. The stiffness should not, however, be too great, or the intended measurement of normal force by observing deflection of the front and rear panes would be frustrated.

Friction was expected to be similar for both materials, but glass was preferred for flatness, optical quality, scratch resistance and surface finish. The final material chosen was float glass which was then toughened for safety reasons. A thickness of 6 mm was chosen to give a reasonable balance between the need for stiff boundary conditions whilst still providing enough deflection for measurement. The clamping arrangement of the frame was designed to accept different thicknesses should this initial estimate prove incorrect.

3.7.3. Slide

It was necessary to ensure that the load cell measured only the loads due to the experiment, and not friction or momentum changes in the drive parts. To achieve this it needed to be as close to the snow sample as possible. Two positions were considered: either in the frame at the base or on the slide, supporting the indenter (or anvil). Incorporating the load cell into the slide was simpler than into the frame. The load cell was incorporated into the slide as shown in Figure 37. To avoid any risk of off-axis loading of the cell, a small spreader was incorporated into the slide. This spreader was free to rotate and move horizontally whilst transferring force vertically to the slide.

The slide provides both the running surface for the drive parts and a running surface for the small displacements which would operate the load cell (Figure 37). Low friction between the indenter and slide was imperative to accurate measurement, whilst low friction between the slide and frame or glass was desirable to reduce the load on the motor. To avoid contamination of the samples, lubricant would not be used, so a material with a low 'dry' friction against aluminium and glass should be selected. PTFE was selected as an appropriate low friction material with adequate machinability. This introduced an issue of

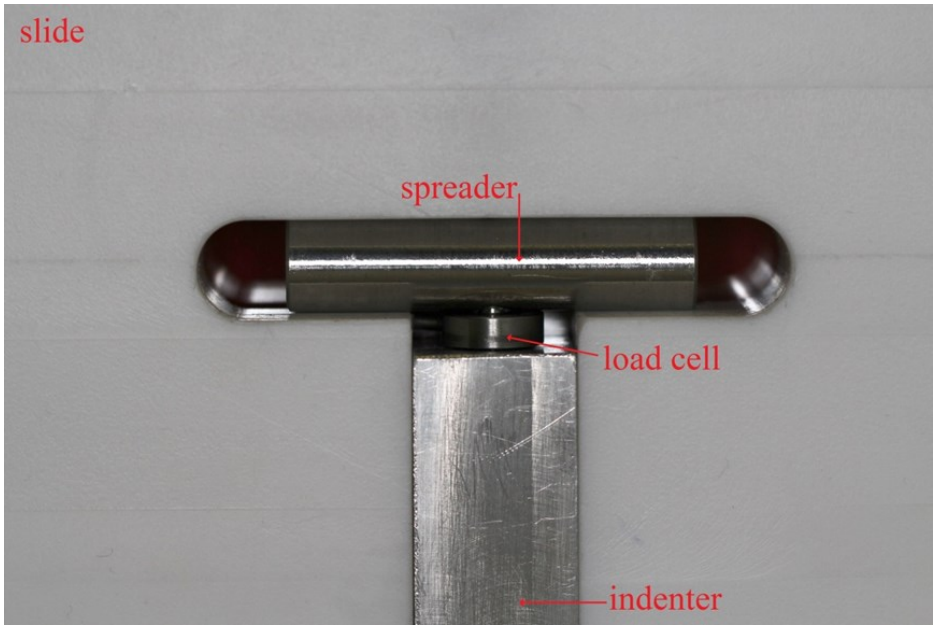

Figure 37: Photograph of load cell mounting arrangement (region D in Figure 32). The spreader is free to move horizontally and to rotate about its axis, thus reducing off axis loading or bending of the load cell.

differential thermal expansion between the PTFE slide and aluminium frame, which was combated with set screws at the corners of the slide which had the effect of swelling the slide to take up any play generated as the device cooled.

3.7.4. Indenters and anvil

An anvil was required for one-dimensional compression tests and indenters for indentation tests. These needed only to be hard and stiff relative to snow. Aluminium alloy was selected for corrosion resistance and availability of relevant machining capacity and skills.

3.7.5. Drive screw assembly

The drive screw assembly consists of the drive screw and nut, plus a suitable bearing to position the shaft and react the main drive force to the frame. For ease of manufacturing a steel drive screw and an unlubricated polymer nut were bought in from Igus. The nut was pressed into the slide and the screw attached to a boss, thus providing a suitable flange for the bearing and allowing easy attachment of the motor. The bearings required to react the drive force to the frame and position the assembly in the frame were of a dry polymer type, supplied by Igus.

3.7.6. Ancillary parts

Feet, props and a pivot were required to allow the frame to fold forward to be filled with snow. With the exception of the pivot these parts were made from aluminium cut from standard sections for ease of manufacture. The pivot was made from ground steel rod, as this was easily available with a good surface finish and accurate dimension.

4. Acceptance experiment for wall shear

In order to confirm that the influence of wall friction on the experiments was small, an initial acceptance experiment was conducted, providing numerical values which could be input into Equation 18.

As will be discussed in the following chapters, strain was observed to be heavily localised. This localisation meant that stress applied to the glass would not be evenly distributed. There were however points in experiment when the strain was approximately constant though out

the specimen. These were (a) up to the first appearance of strain localisation, and (b) at the end of each wave of compaction. No measurable deflection of the glass plates occurred before the first occurrence of strain localisation. This analysis of wall friction is therefore based on snapshots of the experimental condition at the end of the first compaction.

The deflection of the glass plates at this point was 50 microns each side. For a measured stiffness of 290 N mm^{-1} this corresponds to a load of 15 N. The area of the specimen impinging on the glass at this stage is 0.042 m^2 so the stress applied to the glass is therefore 340 Pa. The force recorded by the load cell at this point was 60 N, so the vertical stress $\overline{\sigma}_{zz}$ is 6 kPa. Poisson's ratio is therefore estimated at 0.054.

Coefficient of friction could be measured using the force measurement components from the one-dimensional compression experiment. The equipment was placed horizontally and the drive system used to push a block of semi-compacted snow along the glass plate, recording the force required to do so. Masses were added to the block of snow in order to adjust the normal force. The driving force and normal force were found to show strong correlation (as would be expected for coulomb friction) and to have a coefficient of friction of 0.34.

The numerical values presented above can be used, with Equation 14, to estimate the variation of vertical stress with height through the specimen. This is illustrated in Figure 38.

The variation in $\overline{\sigma}_{zz}$ between the top and bottom of the specimen is thus estimated at 28%. As will be described later, the strain localisation features observed are of the order of a few mm in size. The strain variation across such features is therefore only c. 1%. Given the natural small-scale heterogeneity of the material (and attendant heterogeneity of local stress) it is implausible that the strain gradient across the specimen would alter the nature of such features, however it may affect their location within the specimen, favouring deformation near the top.

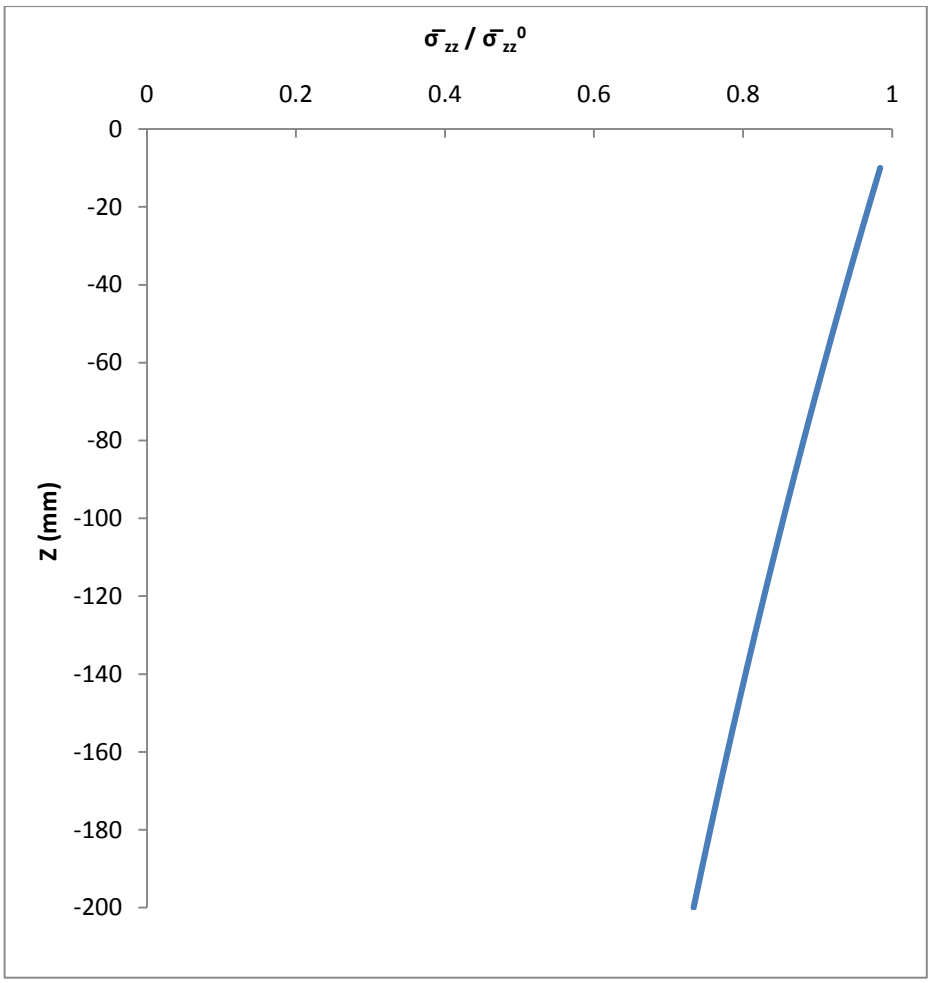

Figure 38: Variation $\bar{\sigma}_{zz}$ resulting from wall shear.

5. Summary

An experimental apparatus, shown in Figure 32, was designed and developed. It was designed to offer confined (zero lateral strain) compression and indentation experiments with speeds from 1 to 20 mm s^{-1} and to expose the deformed snow to a camera. It had a maximum measured force of 250 N with sub-newton resolution and c. 2 N accuracy in one-dimensional compression mode or 25 N maximum force with c. 0.2 N accuracy in indentation mode. It had a sample size of 200 by 250 mm. Final engineering drawings are available in appendix 2.

An acceptance experiment was conducted which showed the experiment functioned as intended and that the variation in stress due to friction with the walls was small.

A method of interpreting the images to provide strain fields was also required, and is described in the next chapter.

Chapter VI: Analytical methods

Aim

The aim of the work discussed in this chapter was to develop a method to process the data from the experiments in order to provide displacement and strain visualisations, and to remove artefacts from the data.

1. Introduction

A series of experiments were conducted with the apparatus described in chapter V. Each experiment provided a time-series record of the force experienced by the indenter or anvil and also a series of images showing the sample as it deformed.

Experiments were chosen to explore speed effects in one-dimensional compression and indentation with the sharp tipped indenter. The range of speeds was chosen to be representative of the drive speeds of penetrometer instruments, speeds were close to the brittle-ductile transition outlined in chapter II, but remained in the brittle region according to most classifications. Experiments with the round tipped indenters were only performed at one speed, as little speed effect had been observed in earlier tests.

2. Validation of results

Before analysis began, the data sets were checked to confirm that the experiment had succeeded and the data was valid. To be accepted, the data was required to pass the tests described below. Data that passed some tests but not others (for example, if the force data were missing or unreliable due to a frozen load cell) could still be useful and was classified as partially valid.

2.1. Position validation

The instructed position and recorded position of the indenter or anvil should be the same throughout the test. To confirm this, the instructed position and recorded portion were plotted against time and manually compared, as seen in Figure 39. Small differences in gradient (as visible in this example) are not considered significant. They are attributed to gain drift in the potentiometer due to temperature changes. This process confirms that the motor did not slip or stall during the test. No datasets were excluded for failing this test.

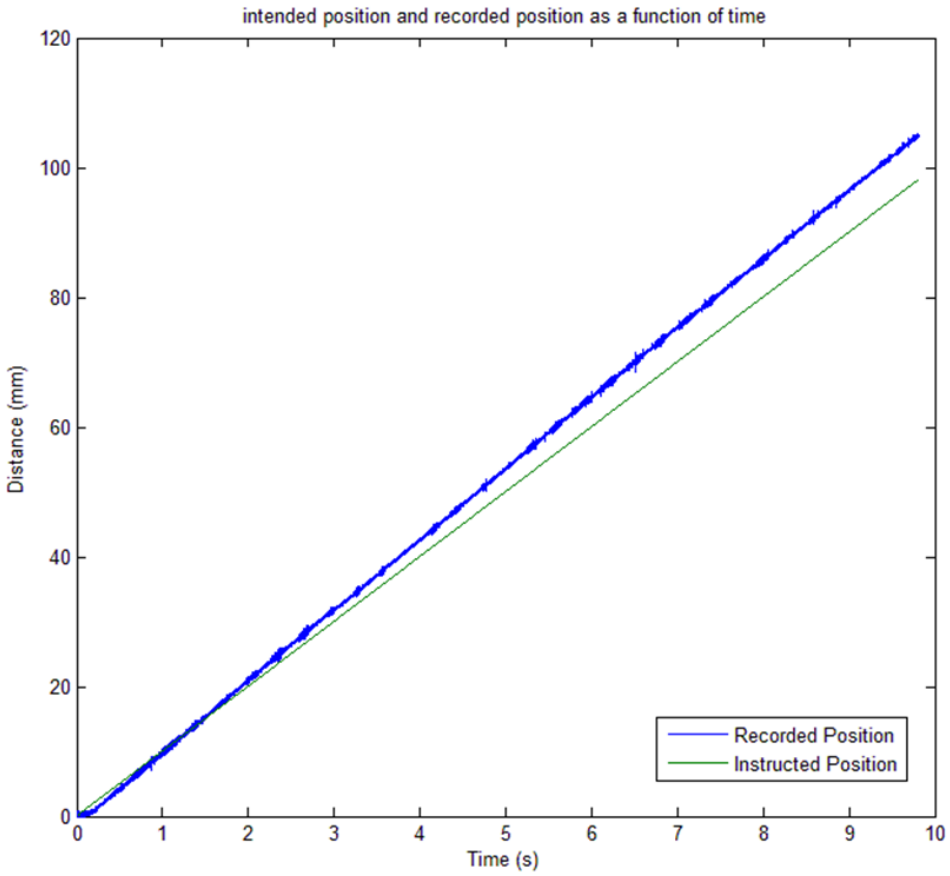

Figure 39: Example position data used to validate the test. The test is accepted as valid if the recorded position is straight and within 10% of the instructed position.

2.2. Force validation

The force record was plotted against position and manually checked for unrealistic results, such as spurious full-scale readings or indications that the sensor may have stuck. 6 datasets were excluded for failing this test.

2.3. Image record validation

The image sets were inspected to ensure that all images were present, in focus and correctly exposed. 14 datasets were rejected for having missing or unusable images, including all those illuminated from the front of the specimen.

3. Summary of valid results

22 tests were accepted as valid and 11 as partially valid. The accepted tests were distributed across 4 geometries and 5 speeds as indicated in Table 1. Tests accepted as partially valid are shown in brackets.

	One-dimensional compression	6mm sharp indenter	6mm round indenter	60mm round indenter
1.125 mm/s	7(1)	1		
5 mm/s	3(5)	2(1)	2(1)	4(2)
10 mm/s		1(1)		
15 mm/s	1			
20 mm/s		1		

Table 2: Summary of valid results by speed and geometry, additional partially valid results in brackets

4. Filtering the force record

The motor used was of a stepper design. This brought advantages in control of the experiment but introduced noise into the force record. Each time the motor stepped, a force peak was recorded by the load cell. As the frequency of the motor steps was known, this oscillation could be filtered out. An example of this is shown in Figure 40.

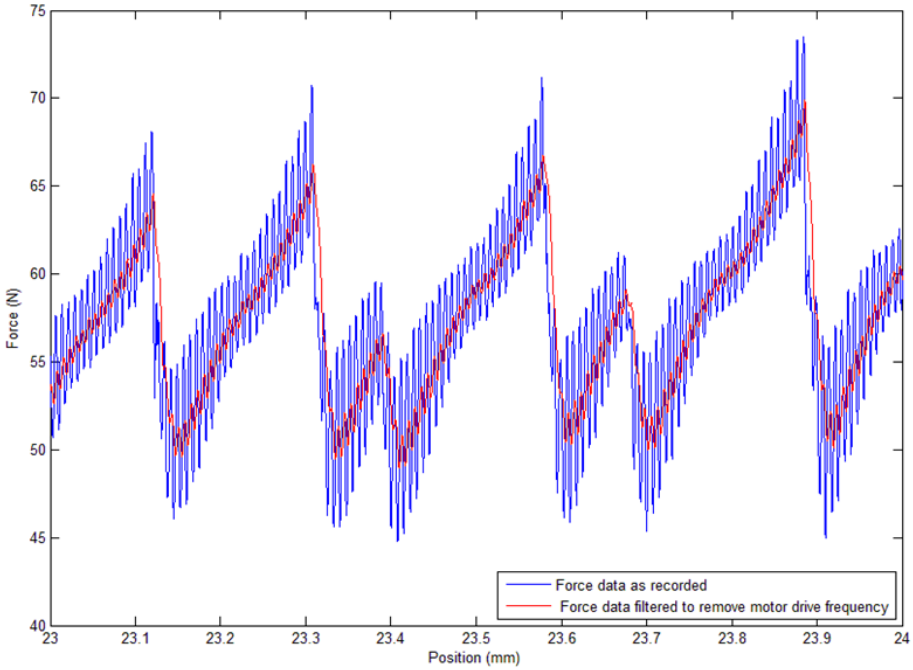

Figure 40: Force record detail before and after filtering to remove motor frequency.

5. Processing the image record

Each experiment yields a sequence of images. These images were analysed in two ways. Firstly, directly viewing the images yields qualitative information about the density (and therefore strain) of the specimen. Secondly, the images were analysed using digital image correlation (DIC).

5.1. Direct viewing of images

The samples appear to exhibit a difference in transmissivity according to density. The sample was flash-lit with diffuse light from the rear, so these differences appear as lighter or darker areas in the photographs. An example image is shown in Figure 41, with a compressed region at the top. (The darker regions towards the edge of the snow are not interpreted as denser areas; this instead represents areas where light has been lost by absorption to the frame or anvil).

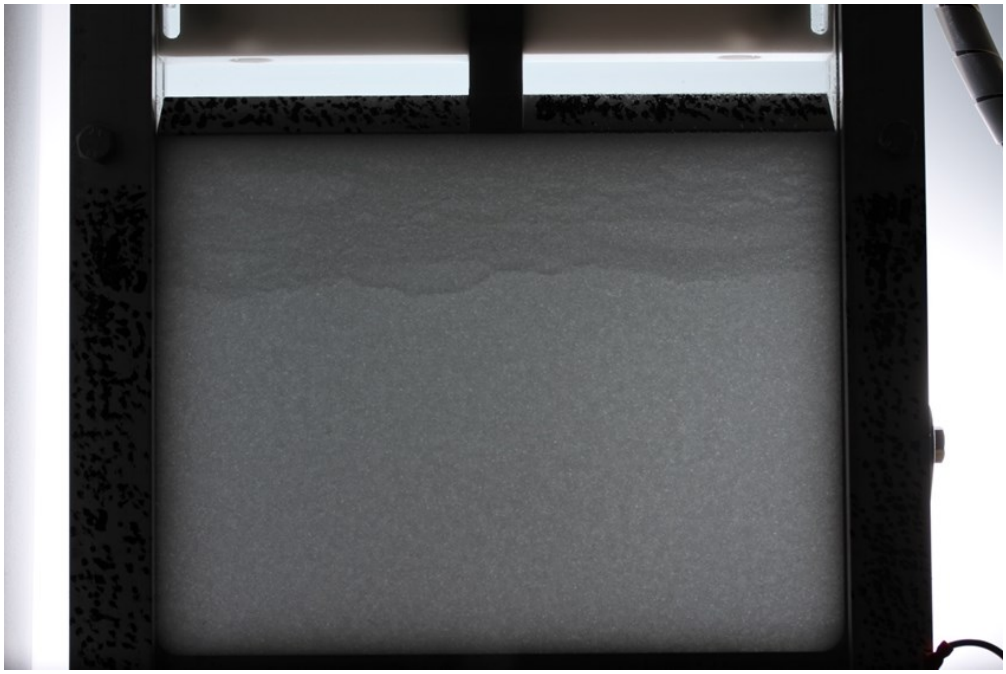

Figure 41: An example image from a one-dimensional compression experiment.

These darker areas represent areas of compressive strain. Tensile strain would in theory be shown as lighter areas, but significant tensile strains are not present.

The extent to which this technique reveals the state of the snow at the surface or presents an average through the thickness of the specimen is somewhat unclear. Macroscopic light loss is presumed to be related to through-thickness average density, but it must be noted that snow is an effective diffuser of visible light, and therefore fine detail will not be projected through the specimen from the rear plane. Fine detail in the images is therefore attributed to surface or near-surface features, whilst macroscopic features are attributed to a through-thickness integration of density.

5.2. Digital image correlation

Digital image correlation (DIC) is a branch of digital image processing applied to tracing moving objects in a series of digital images in order to derive displacement. These displacement vectors can then be used to calculate strain. Because DIC tracks the movement

of visible (i.e. exposed) particles, it should be interpreted as providing observations of the surface of the snow only.

5.2.1. DIC – principal of operation

DIC works by taking a small section of an image (a 'patch') and comparing it to the subsequent image. The patch from the first image is moved around the second image pixel by pixel, and the image data for the patch is checked for correlation with the overlapping part of the next image. The point at which it is best correlated is taken to be the location of the patch in the next image. The principal of operation is illustrated in Figure 42.

To avoid excessive computational loads, the area searched in this way is usually only a small part of the full image. The area to be searched is known as the search zone.

Whilst this method gives a location to the nearest pixel, some DIC software (including GeoPIV, discussed later) claims to offer higher accuracy. This may be achieved by looking for trends in strength of correlation, and interpolating to locate a theoretical point of highest correlation. An alternative method of achieving sub-pixel accuracy is to fit a curve to (or perform a furrier transform on) both the patch data and candidate image data, and try to correlate these curves.

As the analysis progresses, it may become harder to locate the patches if their appearance changes. To avoid this, the patch data from the first image may be updated with data from a later image.

5.2.2. Applying DIC to snow

DIC has been applied to snow in past studies: Reiweger et al (2010) describe an apparatus using DIC to track shear deformation in spray-painted snow; Foyer and Jamieson (2010) used chilli flakes as a tracer particle to investigate penetrometers in snow; Herwijnen and Heierli (2009) utilised a regular grid of markers to analyse snow slab movement at the point of initiation of an avalanche.

In all past studies a tracer substance or array of tracer objects have been added to the snow. This was done to improve the texture of the images. DIC depends on being able to recognise shapes from one image in the next - the ability to do this is a function of the contrast and shape of features in the image. The combination of contrast and shape is known as texture.

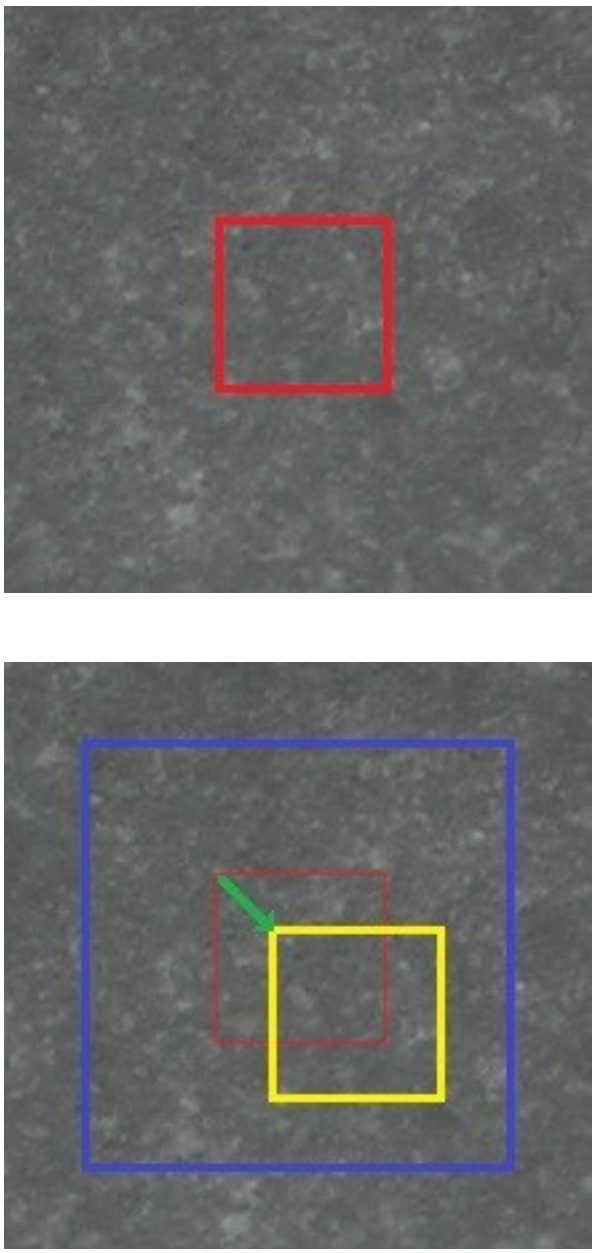

Figure 42: Principal of operation for DIC A patch (64x64 pixels in this case) of data is selected from the first image (top, in red). In the second image a searchzone (160x160 in this case) is defined (blue). The searchzone is completely filled with overlapping candidate patches at 1 pixel intervals (9216 in this case) which are checked for correlation with the patch in the first image. The best correlated patch (yellow) is kept, and the distance between it and the original patch is the displacement vector for that patch in that image interval (green arrow).

A homogeneous snow sample has almost no texture at large scales, appearing plain white. At a smaller scale the texture is better due to the visibility of individual grains, but the contrast remains poor.

The potential disadvantage of the technique of using tracers is that the tracers do not accurately represent the behaviour of the underlying snow. This could occur because the tracer has disturbed the behaviour of the specimen, or because the tracer has not moved with the specimen. The application of a tracer also becomes a matter of balance: too little and the DIC resolution will be low, as large patches have to be used to guarantee the inclusion of a tracer particle. With too much tracer and the risk of upsetting the experiment would increase.

For the experiments described here, a high resolution was required, but the avoidance of tracer particles was considered desirable. After a series of practical tests, it was determined that a light placed behind the specimen coupled with a slight underexposure would provide sufficient contrast for the DIC programme to track the natural texture of the snow. Examples of the texture are shown in Figure 43.

5.2.3. Software selection

The software package used for this work was GeoPIV8. GeoPIV is a matlab-based DIC package (White et al 2003). It is available directly from the authors for academic research and is not available for sale to the general public.

GeoPIV was selected because it was already in use within the department and had produced good results.

5.2.4. Software configuration

GeoPIV has a number of options, which must be adjusted to give optimum performance.

Patch Size is the area of the image which will be taken and searched for in the next image. Larger patches are in general easier to find in subsequent images, but are also more likely to be significantly deformed, which could prevent detection. After some experimentation a patch size of 64 pixels was found to work well, corresponding to an area of 4.5 x 4.5 mm.

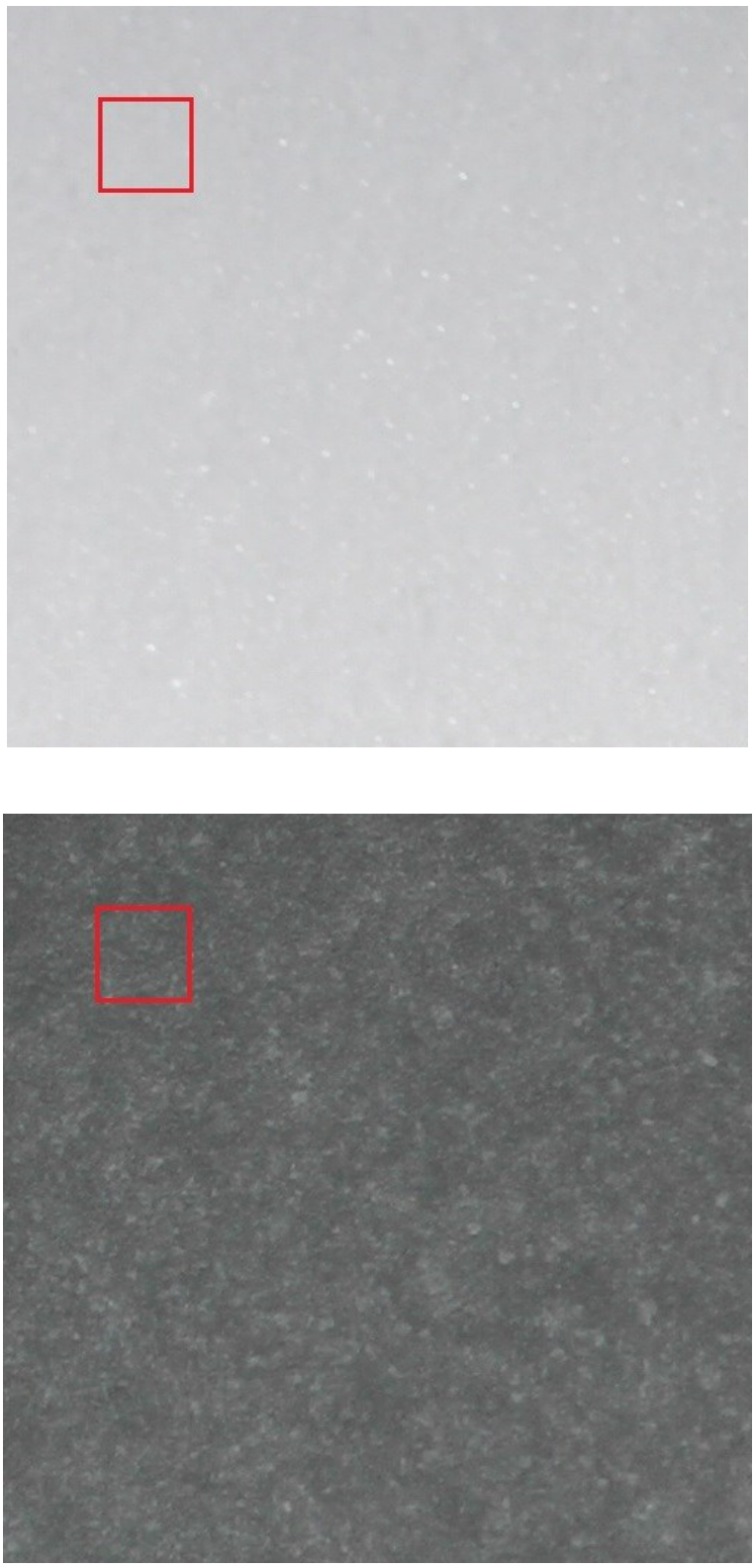

Figure 43: Examples of image texture. Snow in normal illumination (top) results in poor texture. With back lighting and slight underexposure (bottom) the texture is much more pronounced. The red box indicates the size of a patch. (Imaged area c. 35 mm wide).

Search zone size is the area of the image which will be searched when looking for a given patch. If the search zone is too small, the patch will not be found and a false displacement vector will be recorded. Computational expense is related to the square of the search zone size, so a large search zone should be avoided. Search zone size was adjusted by starting with a small value (leading to failed analysis) and increasing it until the analysis was consistently successful. This threshold was found to be slightly above the maximum distance a given patch was expected to travel between images (defined as the speed of the indenter or anvil). The search zone was therefore set at 110 % of the distance travelled by the indenter or anvil (converted to pixels).

The leapfrog variable relates to the frequency with which patch data is refreshed. If the patches from the first image are used to search all the later images, it is likely to fail due to changes in the appearance of the patch over the course of the experiment. This could be caused by deformation or rotation of material in the patch, changes in illumination angle or changes in viewing angle as the patch moves past the camera. Refreshing the patch with data from a later image, however, reduces the accuracy of the analysis. Due to high local strain rates, it was found necessary to refresh the patches in every image.

5.2.5. Calibration and noise reduction

Two sources of noise were present in the output data, firstly: stray displacement vectors from failed search attempts, and secondly: rigid body translations.

Stray displacement vectors occur when the program fails to find a patch within the search zone. A false vector will be recorded, usually extending to near the edge of the search zone. Such vectors may be hard to automatically identify but are easy to pick out by hand. An example is shown in Figure 44. These vectors were manually removed from plots using vector viewing software included with GeoPIV.

Rigid body translations affect all locations in the sample equally. They are caused by vibration or movement of the camera relative to the sample. Rotation of the camera will present as translation in the results with relatively little distortion due the long viewing distance of the camera. Because these translations affect the fixed frame as well as the sample, they can be calculated and removed from the results. A paint-speckle was applied to the frame which was then tracked with GeoPIV. As the speckle was not expected to move,

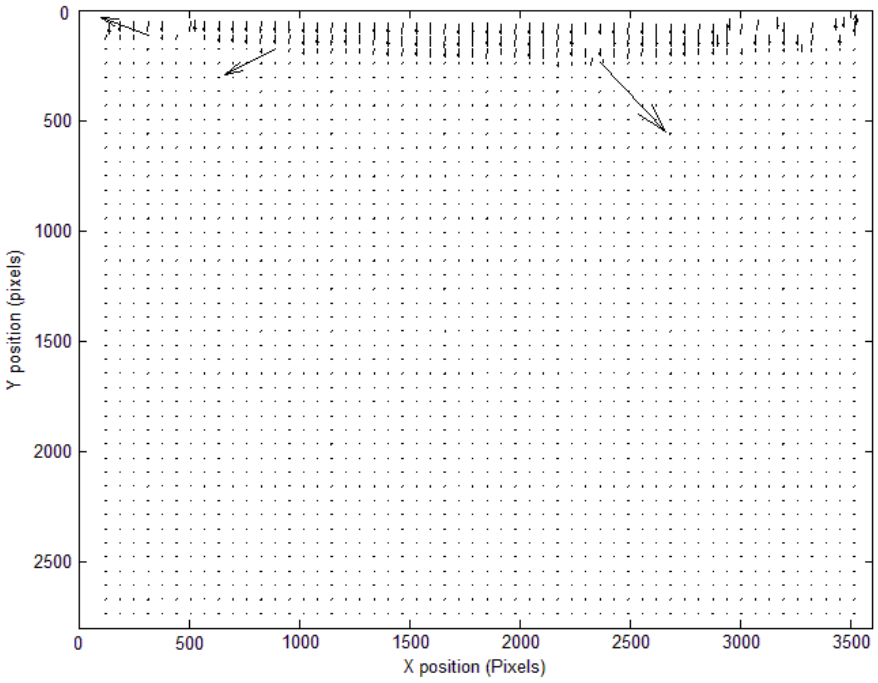

Figure 44:Example displacement vector field showing erroneous large displacement vectors. Displacements are magnified to 3x relative to the position scales

the search zone was reduced and leapfrog was turned off (see section 5.2.4 for explanation of these settings). The translations recorded by this method were then subtracted from the dataset. An example is shown in Figure 45.

5.2.6. Deriving a Strain field

Data from GeoPIV was converted to VTK format using a python script written by Stefan Liebenstein. The data was then loaded into visualisation programme *paraview*, which was used to calculate the gradients of the incremental and cumulative displacement fields, thus producing incremental and cumulative strain fields, such as those seen in Figure 47.

5.2.7. Assessment of Accuracy of GeoPIV

An assessment of the accuracy of DIC used in similar circumstances to those described above is available in Hoult et al 2013. He found close agreement with other measurement techniques even at strains much smaller than observed in my experiments. Nonetheless, it was felt necessary to confirm the tracking ability and accuracy specifically for my application.

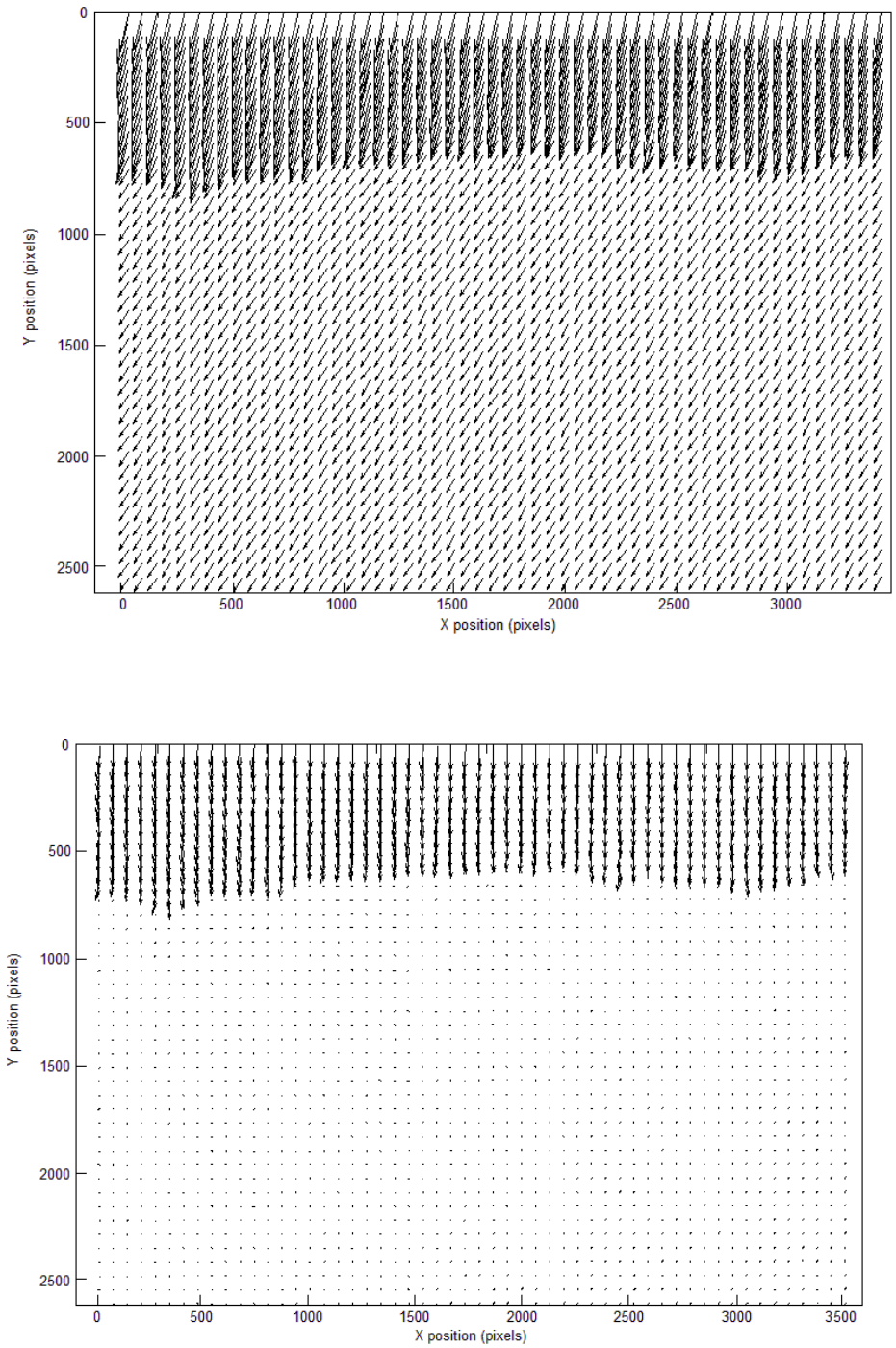

Figure 45: Correction of displacement fields for rigid body translations. Example displacement vector field (top) including rigid body translation and (bottom) after removal of translations. Displacements are magnified to 30x relative to the position scales.

A set of 10 images of an undeformed specimen were taken, with a small displacement between each. These images were analysed using the same GeoPIV settings as were used for the main analysis. 2576 patches were generated, and were then tracked across 10 frames, giving 23185 displacement vectors. To remove the rigid body translations, an average displacement vector was calculated and subtracted from each frame. The remaining displacement recorded was presumed to represent the typical error in the GeoPIV tracking. The errors in x and y directions were distributed as shown in Figure 46. The mean error was 0.37 pixels in x and 0.43 pixels in y. This corresponds to 26 μm and 30 μm respectively.

These errors do not appear random, but are instead related to uncorrected rotations of the camera relative to the specimen. It would probably be possible to correct for them using more advanced calibration techniques. Improvement in accuracy was not considered worth the cost. It would require more processing resources and more of the image frame would need to be devoted to calibration markers. Errors due to rotation should affect neighbouring patches almost equally, and thus should affect strain data less than displacement data.

This method of assessing accuracy may have given an underestimate of error, as the undeformed specimen will be easier to track than a deforming one. Nevertheless, this result was considered excellent.

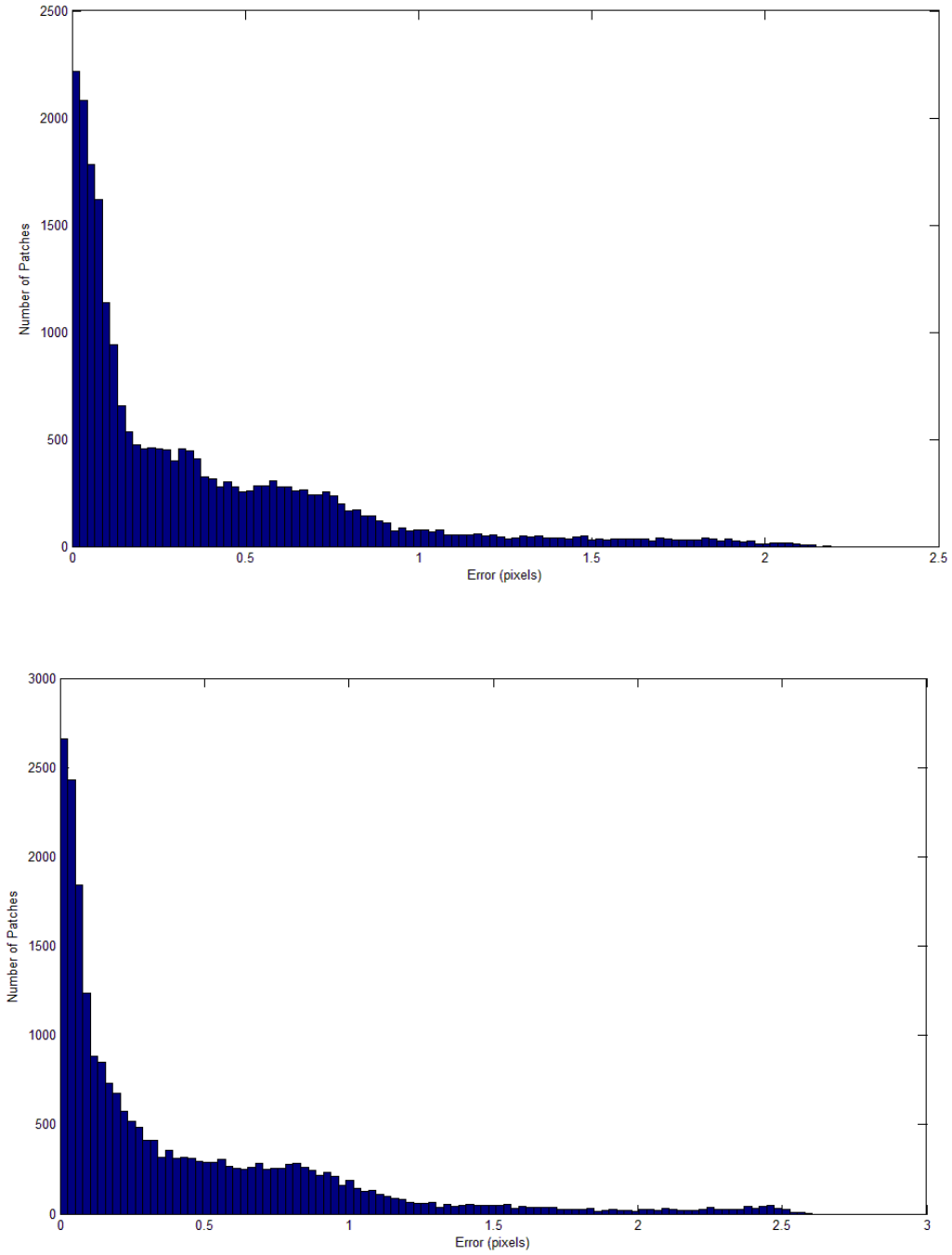

Figure 46: Error distribution for 23185 patch-searches in an example PIV analysis. Errors correspond to falsely recorded displacements in horizontal (top) and vertical (bottom) directions.

Chapter VII: One-Dimensional Compression Results

Aim

The aim of this chapter is to present the results of the one-dimensional compression experiments and discuss the observed deformation patterns.

1. Introduction

A series of one-dimensional compression experiments were conducted and analysed using the methods set out in chapters V and VI to track deformation and strain. In all cases, compaction was localised, with narrow bands straining sequentially rather than homogeneously all throughout the specimen.

In all cases compaction began at the top of the specimen and propagated downwards, as a horizontal band or front. An example of this behaviour is illustrated in Figure 47. In order to consider the evolution of this front with time, one can take an average of incremental strain across the specimen (relying on the front being horizontal) and plot this against time, thus observing the changing vertical position of the front with time. This representation is presented in Figure 48.

Once the front had passed through the whole specimen and compacted it, the process started again, with a new compaction front initiated as seen in Figure 48. This second front often began at the top of the specimen (7 out of 11 experiments), or at the bottom (3 of 11). In some cases a third front was observed (4 of 11). It is considered likely that a third front, and possibly subsequent fronts, would have been observed in all cases had the experiments continued to higher strains. In a small number of cases the compaction front appeared to stall, with a new one then initiated, such as in Figure 48b. Later fronts were more likely to show this phenomenon than the initial one (2 of 11 for initial front, 6 of 16 for later fronts).

As will be explained below, the force required to progress the deformation of the specimen has components relating to the stress required to deform the compaction band and an additional force required to displace the upper part of the specimen against wall friction. This in turn implies that the stress in the upper part of the specimen is at times significantly higher than the lower part, and yet the lower part may experience greater strains. This effect cannot be explained by self-weight, but is instead attributed to the interplay of age hardening and front propagation.

In some cases, small areas remained uncompacted as the compaction front passed over them. These areas tended to be compacted, at least partially, in the next compaction front.

The mechanisms and implications of these observed behaviours are discussed in the remainder of this chapter.

The darker area at the top of the image indicates the area which had been compacted

From the incremental displacement field it is apparent that the compacted region was moving and the rest of the sample was stationary

The strain was concentrated at the boundary of the compacted region; this phenomenon is referred to here as the compaction front.

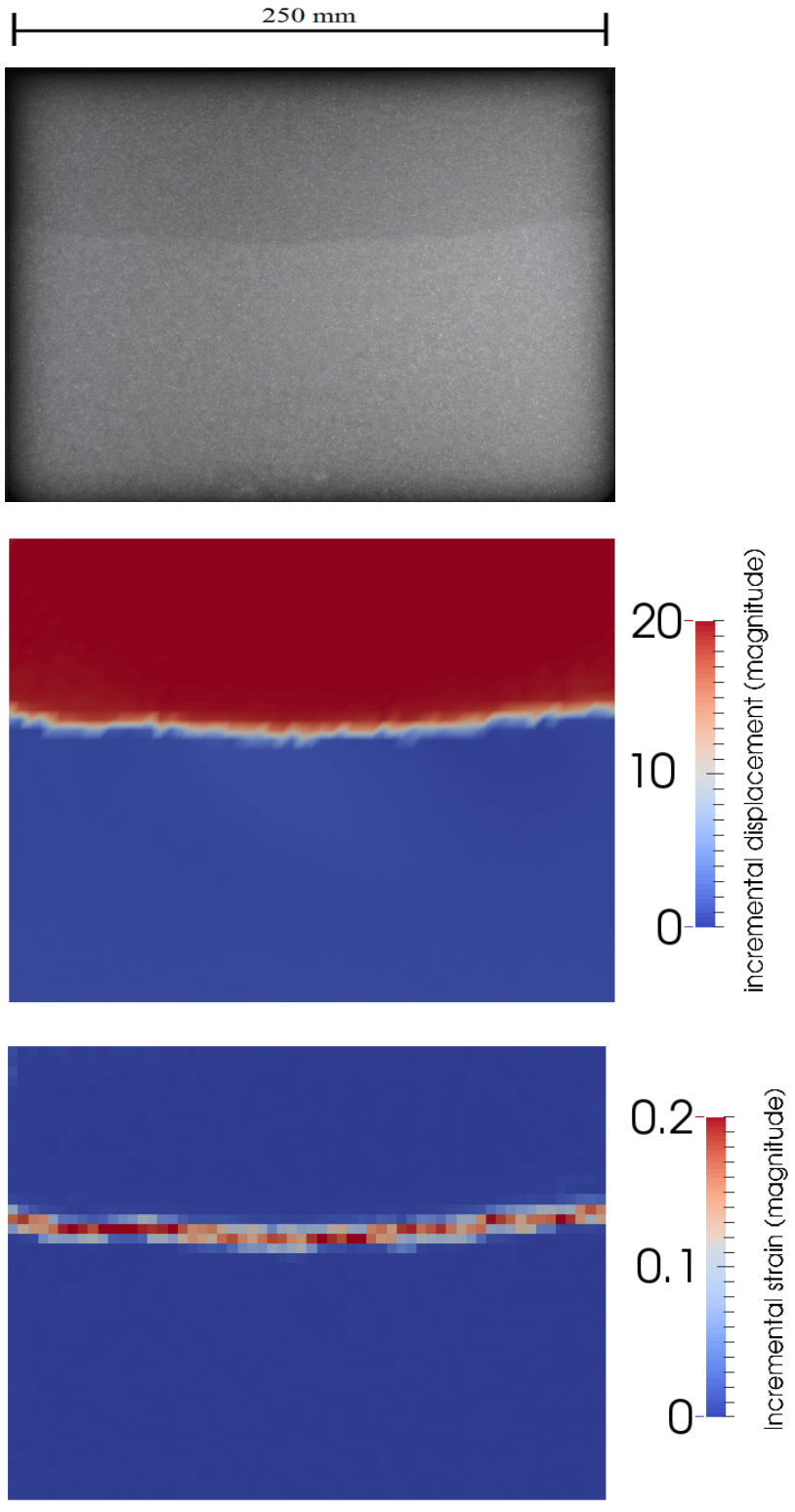

Figure 47: compaction is localised as front stretching across the sample. Shown here as a photograph (top), corresponding incremental displacement field (middle) and the incremental strain field (bottom).

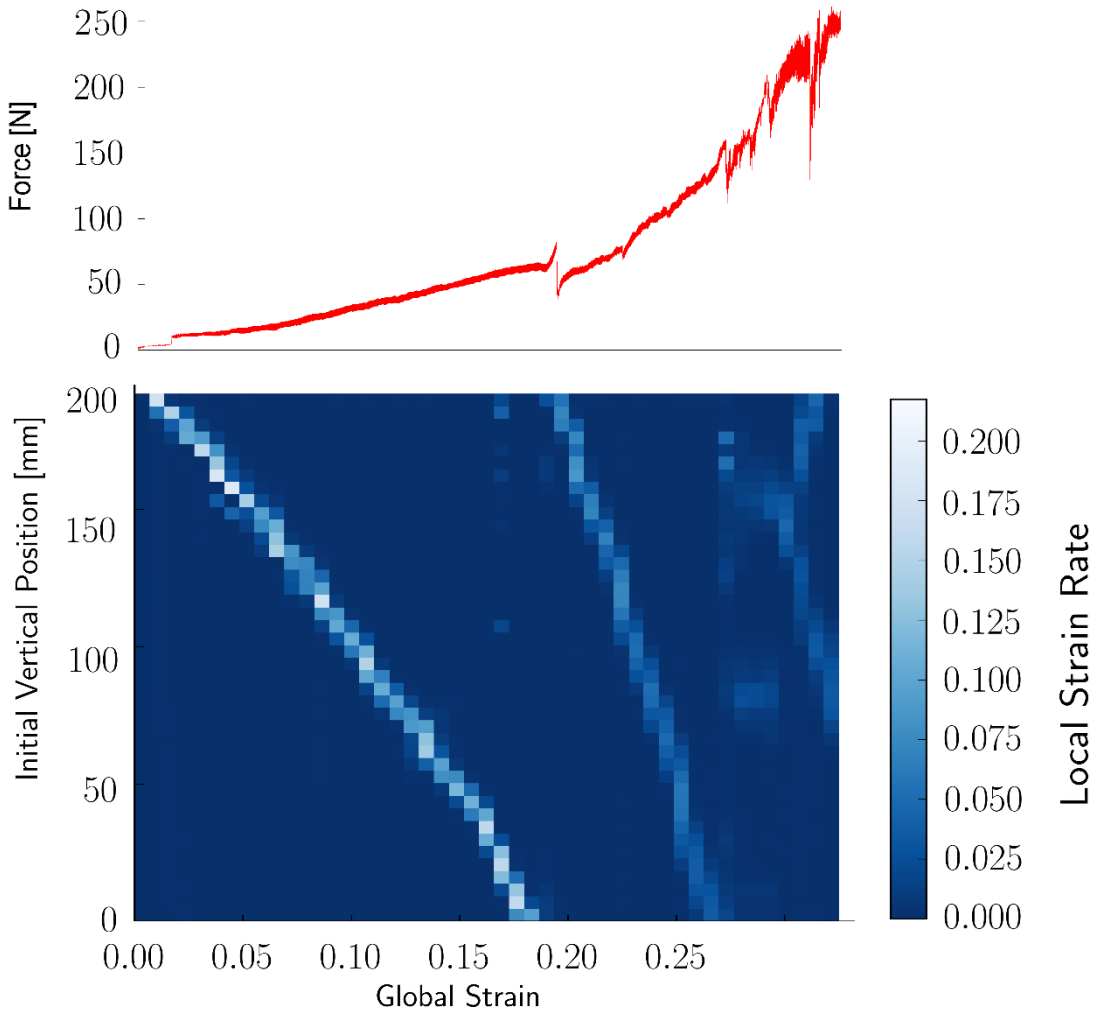

Figure 48a: Vertical position of compaction activity as a function of global strain (time) with corresponding force records. Global strain rate $2.56 \times 10^{-2}\ s^{-1}$, velocity 5 mm s-1. In this example there are three consecutive compaction fronts, each beginning at the top and requiring a near constant force to propagate downwards.

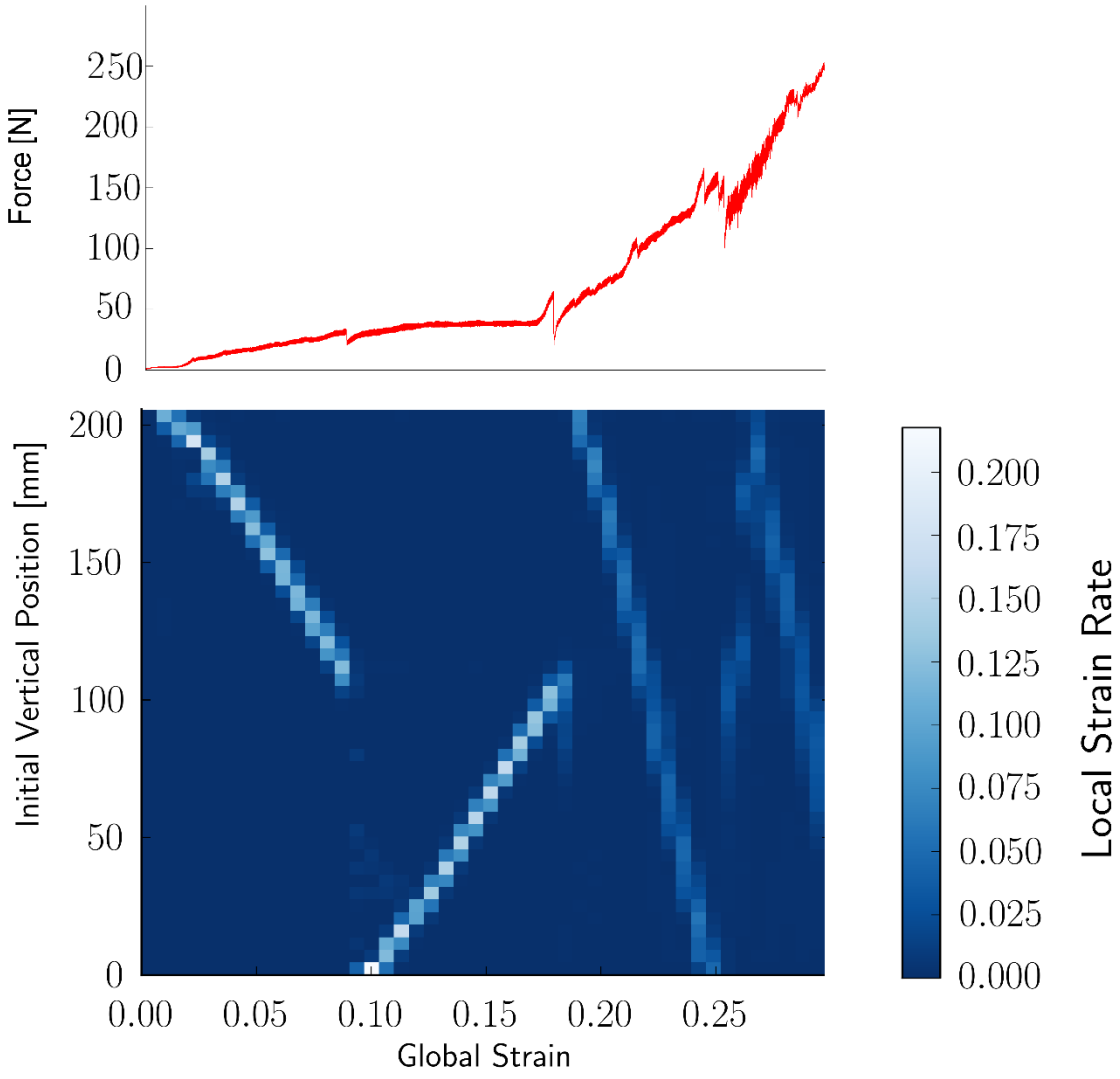

Figure 48b: Vertical position of compaction activity as a function of global strain (time) with corresponding force records above. Global strain rate $2.56 \times 10^{-2}\ s^{-1}$ velocity 5 mm s^{-1}. In this example the first compaction wave stalls, and begins again at the bottom of the specimen.

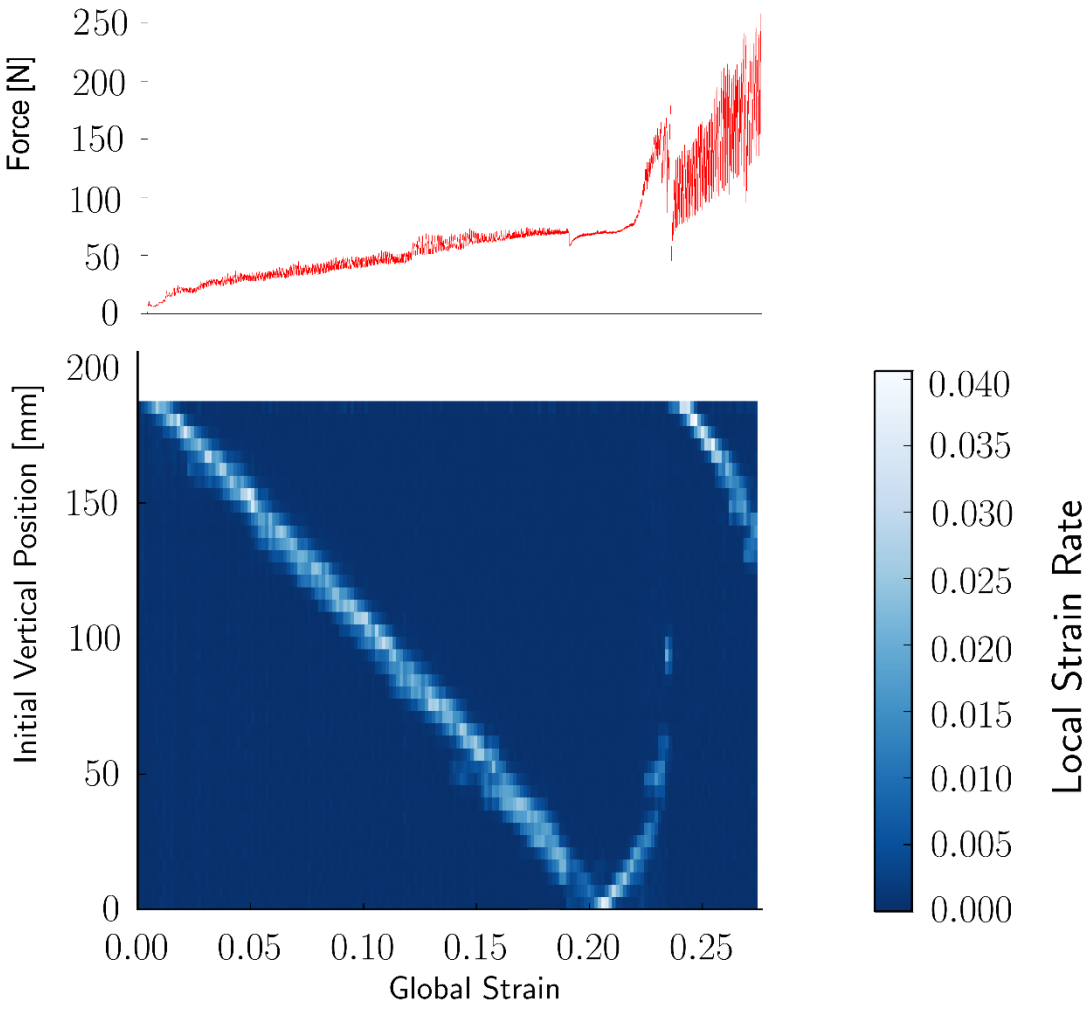

Figure 48c: Vertical position of compaction activity as a function of global strain (time) with corresponding force records above. Global strain rate 5.77×10^{-3} s^{-1}, velocity 5 mm s^{-1}. In this example the second compaction front begins at the bottom, but stalls and begins again at the top.

2. Localisation of compaction: snow is a strain softening material

In most materials, the force needed to deform a small arbitrary volume increases as strain increases. This leads to an even distribution of strain across the material. In some materials, a deformed area may weaken: this is known as strain softening. Examples materials which strain soften in compression include some metal and ceramic foams and some cohesive granular materials. Strain softening has the effect of concentrating any further strains into the deformed, weakened region. The observed localisation of compaction in the one-dimensional compression experiments implies that snow is strain softening.

Strain softening behaviour in snow is not unexpected. Snow may be considered as hard particles connected by brittle necks. Breaking the brittle necks will soften the material, as illustrated in

Figure 49. Strain softening in the presence of compressive volumetric straining cannot continue indefinitely. At some point the force required to compact an arbitrary volume must rise and the deformation will move on to a new area (otherwise, an infinite density would be attained). In snow this most likely occurs due to an increase in packing density. Increasing density leads to increasing number of contacts per particle (increasing coordination number) and thus causes the instantaneous yield stress to increase above the applied stress and irreversible straining is arrested.

It is useful to consider these behaviours from the perspective of instantaneous yield stress and strain, as irreversible strain will occur whenever local applied stress exceeds local instantaneous yield stress.

The behaviours illustrated in Figure 50 will result. The shape of each curve is not known exactly, but general concepts can be described, and shapes assumed:

- For the elastic section linear behaviour is assumed, as no significant bond breaking or change in coordination number occurs.
- For the strain softening curve, a sharp drop in stress resulting from bond breaking is expected, but this curve does not fall to zero, as I elect to include inter-particle friction with the stronger mechanical bonds.
- For the strain hardening curve, an exponential or asymptotic increase is anticipated, as coordination numbers rise towards a close pack, or else jamming occurs.

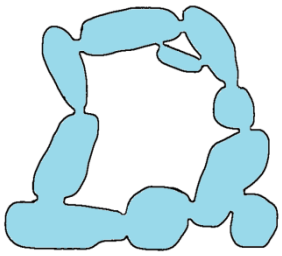

1. The initial state is a porous assembly of ice particles joined by solid ice necks.

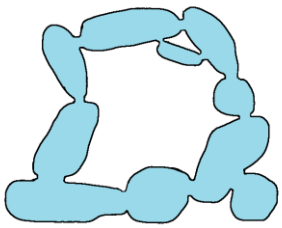

2. The snow compresses elastically.

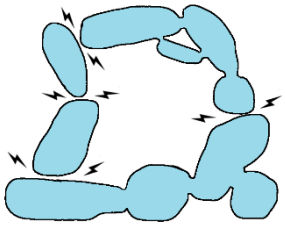

3. Yield and softening occurs due to failure of the ice necks

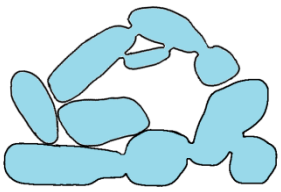

4. Particles or (groups thereof) move and rotate, allowing straining. Stress may be diverted to neighbouring volumes, which are momentarily stiffer (they are at point 2 or 5 in this process). Deformation stops due to increasing coordination number.

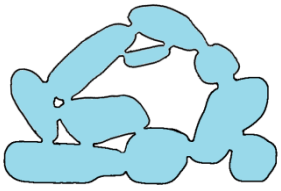

5. New ice necks quickly form, restoring strength and stiffness in a time dependent way. The process may repeat if high enough stresses are applied.

Figure 49: 2D representation of how bond breaking leads to strain softening,

followed by time dependent hardening.

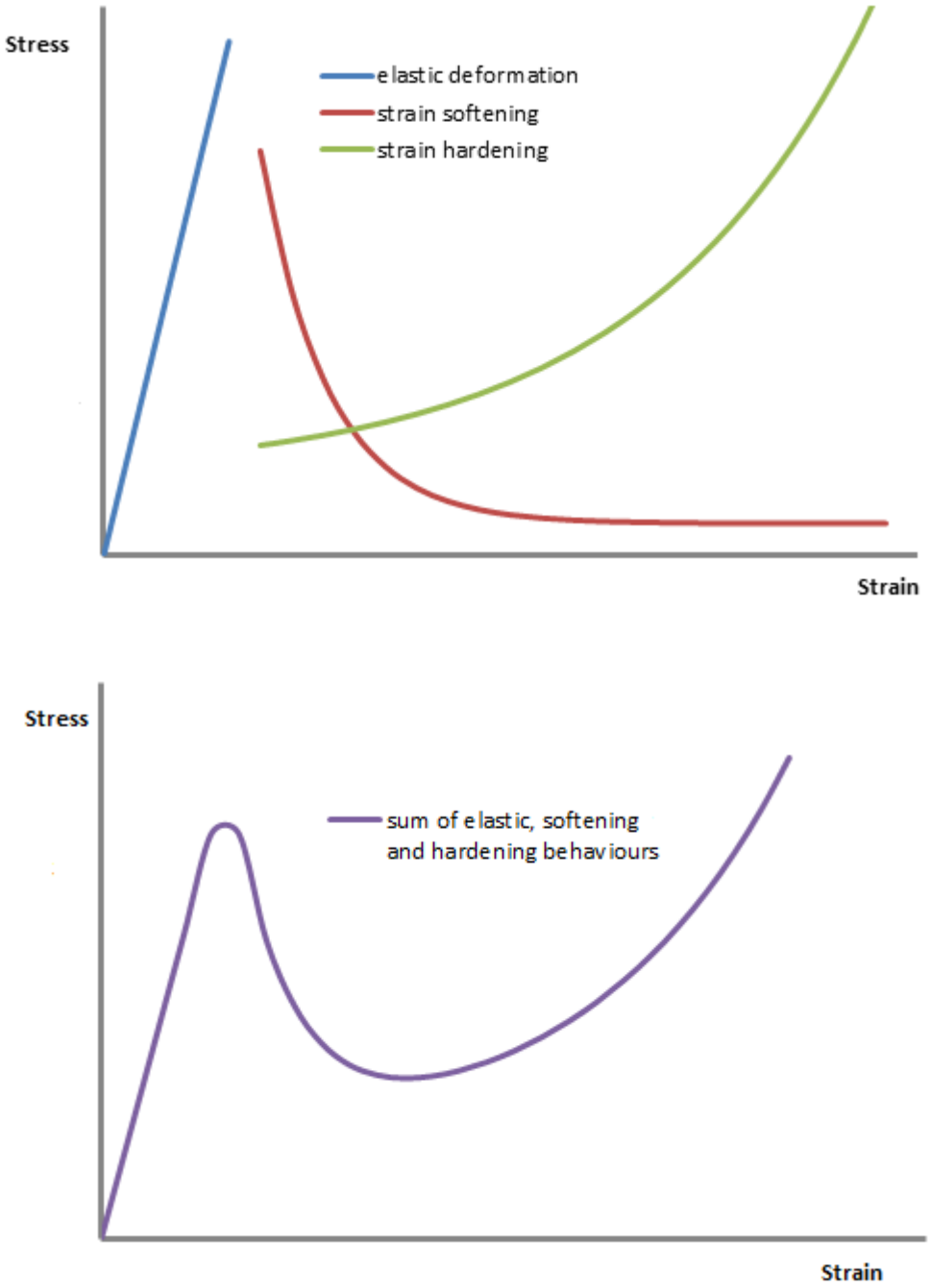

Figure 50: Contribution to instantaneous yield stress from elastic, strain softening and strain hardening phenomena (top) combine to give an overall hardening-softening-hardening response (bottom). The exact form of the curves is not known.

When the elastic, strain softening and strain hardening behaviours are taken together, the overall behaviour of a small volume of snow is as indicated by the purple line in Figure 50

It should be noted that strains in these experiment are almost entirely compressive and the graphs are drawn with this in mind. Shear strain would lead to a softening behaviour not unlike that illustrated, but strain hardening by increasing coordination number would not be present in the absence of a significant volumetric strain component.

Other shapes for these curves could be proposed, but it is difficult to foresee an overall description not leading to an "N" shaped curve for the combined behaviour illustrated in the lower graph of Figure 50. Such N-shaped curve is a requirement for the occurrence of the strain localisation, which has been observed.

The porosity of the artificial snow is around 0.60 before compaction falling to 0.50 after the first front of compaction has passed (corresponding to a critical strain of 0.2).

3. Nature of the deformation front

The strain localisation in one-dimensional compression takes the form of bands of compacted material normal to the applied load. Rather than occurring at random locations, this band generally progress down the specimen in the form of a moving deformation front. The reasons for this are discussed in section 3.2, but first I seek to characterise the formation of the deformation front.

3.1. Formation

A compaction front begins with the yielding of an arbitrary small volume. As snow is strain softening, the stiffness of that volume decreases and the volume rapidly deforms. This has the effect of transferring stress to neighbouring volumes, which then also yield. Quite rapidly, this mechanism will lead to a horizontal band forming across the specimen. This band formation process is illustrated in Figure 51. Because small volumes yield sequentially,

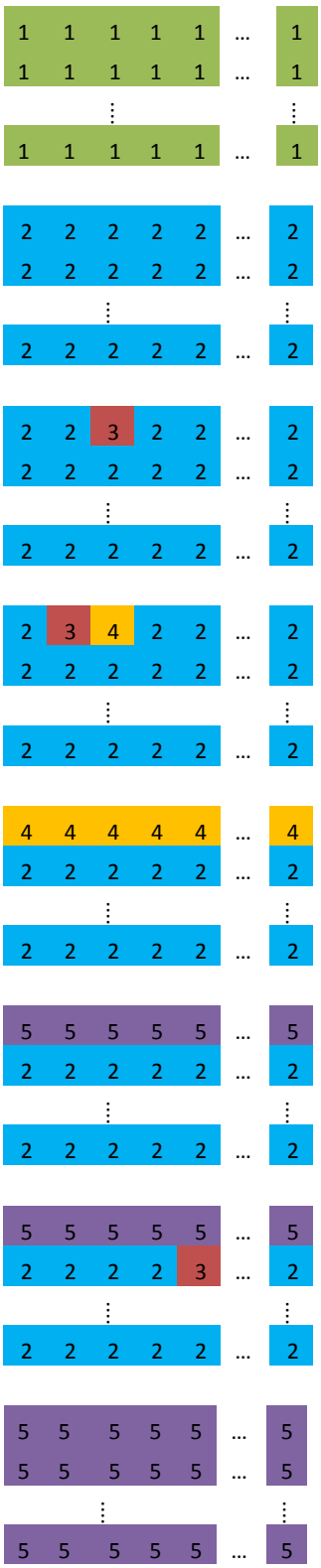

a) The specimen is initially free of stress and strain.

b) Elastic strain is distributed throughout the specimen

c) Yielding occurs at a random location in the top row.

d) The yielded volume softens, causing stress to be distributed to other parts of the same horizontal plane. Another volume in the same plane yields.

e) The process repeats until the whole top layer has yielded.

f) Once a critical strain is reached, the top layer begins to harden.

g) The process begins again (from point c) in the second layer. The first layer continues to harden.

h) Once all layers have hardened, the whole-specimen stiffness rises. A new band may form, as state h is analogous to state b, except that a gradient in yield stress will exist due to differences in hardening time across the specimen.

Figure 51: formation of horizontal bands. Self weight and wall friction are ignored. States (1-5) as follows: 1: relaxed state, 2: elastic strain, 3: yield point, 4:softened state, 5: age hardening state

the peak in force implied by Figure 50 will not be observed in the whole-specimen force record. This broadening of the force peak will be further exaggerated by the spatially fluctuating mechanical properties of the specimen.

3.2. Propagation pattern

The pattern of propagating fronts and the force recorded by the load cell may be explained by an interplay of the developing material properties of the snow and friction with the walls.

3.2.1. The first front

The first compaction front consistently occurs at the top of the specimen. It may seem that the front ought to form at a random location – wherever the specimen is weakest. This does not occur for two reasons:

Firstly, there will be some degree of friction or adhesion between the walls and the specimen, even from the very beginning of the experiment. Elastic straining of the specimen will produce lateral expansion, leading to further friction with the walls. This effect encourages yielding to begin at or near the top of the specimen. Self weight would oppose this effect, but as all fronts began at the top, the effect of friction and adhesion must be greater than that of self weight. The equations governing the variation in stress distribution with height through the specimen were explored in chapter V, section 2.1.2. Taking typical values (density 380 kg m^{-3}, friction coefficient 0.34, Poisson's ratio 0.054, measured load 20 N) for this stage in the experiment (and including self weight) the stress at the top of the specimen is c. 4 kPa, whilst at the bottom it is only c. 3.4 kPa.

Secondly, the specimen will encompass spatial fluctuations in strength and stiffness. In the bulk of the specimen, stress is diverted away from weak regions towards stronger ones, (as stronger regions are also likely to be stiffer). The anvil is much stiffer than the specimen, it does not deform to accommodate such redistributions of stress. Stress concentrations in the very top layer of the specimen are therefore greater than elsewhere, and the compaction front therefore initiates immediately below the anvil.

3.2.2. Subsequent fronts

At the end of the first compaction front, the specimen has experiences a lateral stress according to Poisson's ratio. This causes friction between the specimen and the walls and,

taking account of self weight, causes the stress at the upper part of the specimen to be significantly higher than at the base.

Referring again to Equation 18 in Chapter V Section 2.1.2, the stress at the top and bottom of the specimen are estimated at 14 kPa and 10 kPa respectively.

It is therefore expected that subsequent compaction fronts would start at the top of the specimen, however, a significant proportion (3 of 11) of fronts start at the bottom of the specimen. This is because the material at the base of the specimen has been more recently deformed than that near the top. It has therefore had less time to age harden (sinter). The difference in yield stress between the top and bottom must exceed the difference in stress caused by wall friction.

The shape of the hardening curve for snow at such short timescales is not well understood, but is accepted to have a shape generally as illustrated in Figure 52, with rapid initial strengthening, the rate of which reduces over time. When this curve is compared to the projected stress variation with height as derived from Equation 18, it is clear that the compaction fronts should begin at the top (where stress and strength are high) or bottom (where both are lower) but not in the centre, where the difference between the two is greatest. Further, the greater separation of the curves at the centre of the specimen may explain the tendency of compaction fronts to stall, before initiating again at the top or bottom (observed in 6 of 16 cases).

The presence of two converging fronts in such circumstances is unlikley, as such situation is unstable. If either of two such fronts is softer than the other, deformation will favour that front. The material consisting the other front, deprived of ongoing deformation, will rapidly harden and the front will extinguish.

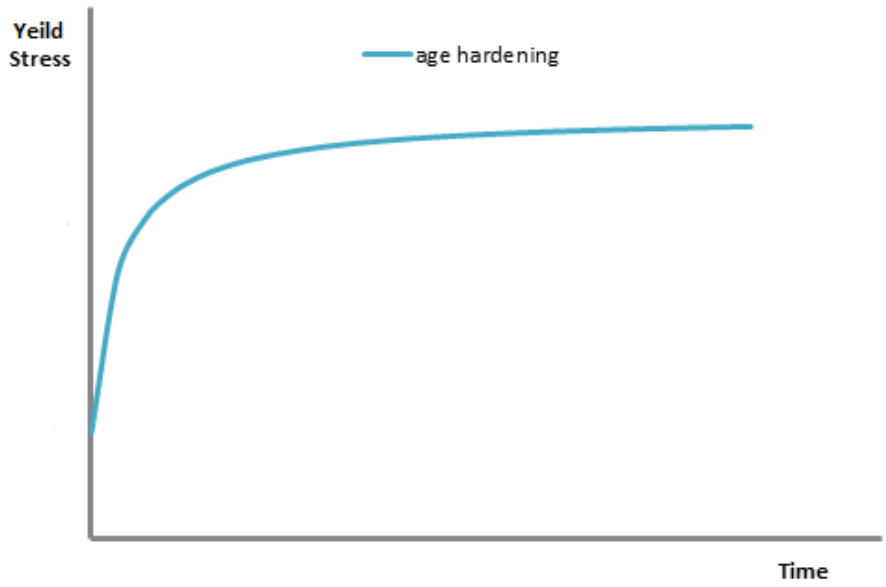

Figure 52: General indication of the change in yield stress of snow with respect to time since the last deformation.

3.2.3. Proposed propagation pattern in the absence of friction

In the absence of friction or gravity, the deformation could be expected to start at the top of the specimen where the hard, stiff indenter comes abruptly into contact with the softer snow. A compaction band would form, and would propagate downwards at a constant force, the material being at this stage homogenous on the macro scale. Upon reaching the bottom of the specimen the band would 'reflect' back up. The force recorded would increase during this second transit as the band encounters progressively more aged material, having the same general form as illustrated in Figure 52. The band would then proceed to 'bounce' up and down the specimen, with increasing macro stress, for an unknown maximum number of repeats. Figure 53 expresses this hypothesised behaviour in the same format as the previous Figure 48.

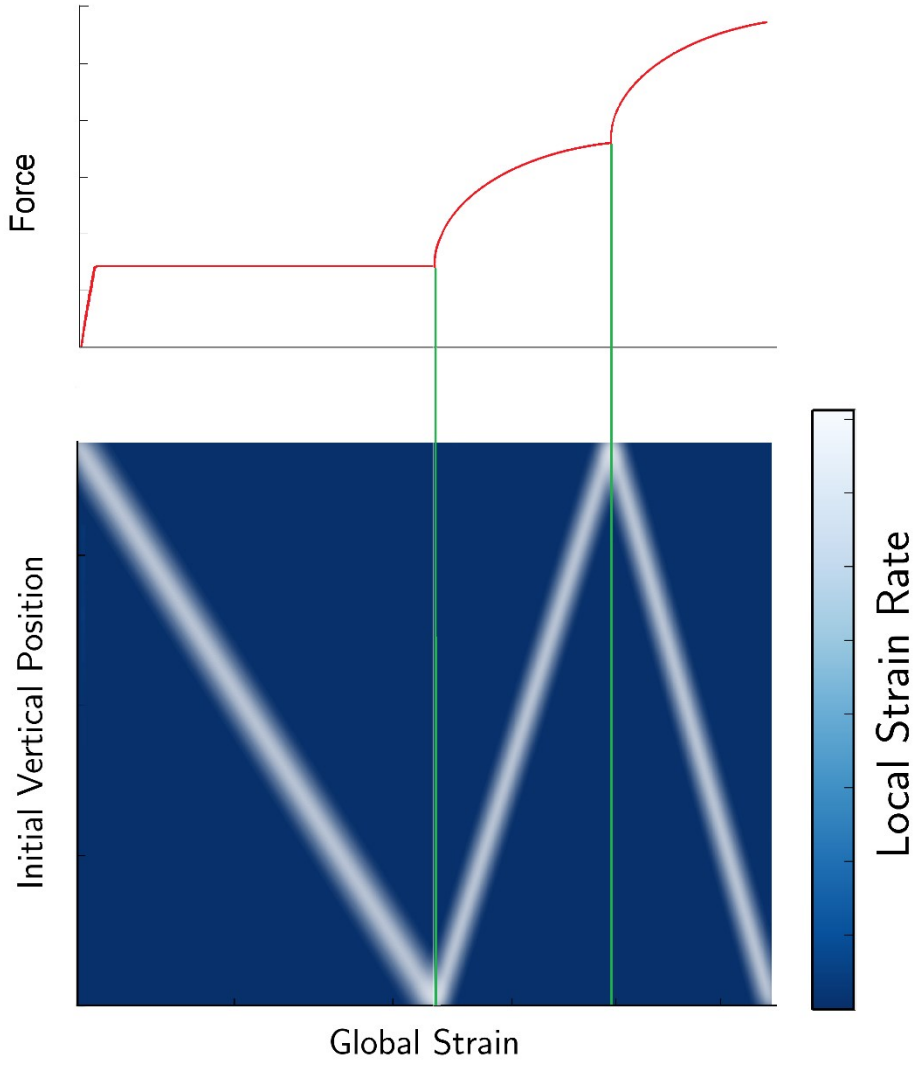

Figure 53: hypothesised behaviour of the compaction band in the absence of gravity or friction, in the same style as Figure 48.

The proposed behaviour is similar to the observed behaviour, but not identical. The curvature of the force record in non-initial compaction fronts is not discernible in the experimental data. This may be because the degree of curvature is not known and is potentially quite slight, it may also be because of the apparent 'noisiness' of the data. This 'noise' is probably not noise as such, but is a genuine result of the deformation process: the result of the building up of stress and subsequent relief as local collapse events occur, in the manner described for brittle elastic foams in chapter II section 9.1. It therefore seems reasonable to presume that larger experimental apparatus, accommodating a larger specimen, would have a

reduced noise effect and more closely approach the hypothesised behaviour set out in Figure 53.

A further difference is that the presented theory shows constant force during the propagation of the first compaction front, whilst experimental data shows rising force. This difference is due to friction between the walls and the specimen. As the front propagates downward a zone of compacted material develops in front of the anvil and grows linearly in size, thus causing a linear growth in the contribution to measured force originating from friction. To understand this better it is informative to look at Figure 48b. In this experiment the first compaction front stalled and initiated again from the bottom of the specimen. With the front propagating upward from the bottom the zone of compacted material in front of the anvil remains of constant size, and thus the force recorded is constant.

A final difference of note is that the experimental data shows a drop in force when compaction band propagations begin and end. This is simply attributed to the presence of a compacted zone in front of the anvil. If a compaction band jumps to a higher location in the specimen the contribution due to friction between said zone and the walls is abruptly removed from the measured force.

3.3. Deformation front propagation speed

Assuming that no volumetric strain occurs out with the moving front, the speed of propagation of the damage front may be derived from the speed of the anvil and the difference in density across the front. By conservation of mass entering and leaving the band, it must be true that:

$$\rho_1 V_f = \rho_2 (V_f - V_a)$$

Equation 19

And thus

$$V_f = \frac{V_a \rho_2}{\rho_2 - \rho_1}$$

Equation 20

Where ρ_1 = initial density, ρ_2 = compacted density, V_a = the velocity of the anvil, V_f is the velocity of the front.

The assumption of zero strain out with the moving front will not be entirely true. At the very least, creep will occur throughout the specimen. It may be observed that the assumption is reasonable, as the paths described but the fronts in Figure 48 are virtually straight. In the early part of the experiment, with a front moving downwards, deformation occurring below the front would cause the band to move faster than predicted. In contrast, at the end of the first compaction front, deformation occurring above the band would cause it to move more slowly that predicted. Thus, if significant deformation were occurring out with the front the paths in Figure 48 would be curved.

It should be noted that front propagation speed is independent of the size of the specimen, and therefore of the global strain rate, but depends only on the velocity of the anvil and density change. It is commonly accepted that strain rate may be used to classify deformation of snow into brittle and ductile regions, but it may be more appropriate to use boundary displacement velocity to describe the kind of behaviour observed here. The boundary displacement velocity and the global strain rate are of course related by specimen size. It is therefore reasonable to describe the observed behaviour as specimen size dependent.

3.4. Quantifying local strain rates

Deformation behaviour in snow is sometimes categorised by global strain rate (chapter II section 5). Low strain rates are generally described as ductile and high rates are brittle with a transition range in between. Knowing local strain rates may allow a similar categorisation within the transitional region.

The photographs, taken at 0.25 s intervals, provide snapshots of the deformation only. It is possible to state that a given local strain has occurred between consecutive images, but this sets only a lower bound on the strain rate. It is not possible to know for how much of the window between images any given strain zone was active, with lower proportions of time corresponding to higher strain rates. Local image-to-image strains of up to 0.20 were observed, corresponding to a local strain rate not less than 0.80 s^{-1}.

It is theoretically possible to infer strain rate by measuring the width and speed of the propagating compaction front (thus inferring the time active for any given volume, and from

that the strain rate). The width of the front could not reliably be inferred from these experiments.

4. Small volumes that resisted compaction

As the compaction front propagates through the specimen, small undeformed areas are sometimes incorporated into the compacted region. This was more common and the regions were larger at lower speeds. An example of this is shown in

Figure 54.

These undamaged zones may be explained by random variations in local strength, or may be an inherent feature of the compaction process. One possible mechanism is as follows: the compacted band below the preserved region propagates as an anticrack, and then quickly hardens (Szabo and Schneebeli 2007) to form an arch, which protects the undeformed region. An anticrack is a term given to a rapidly progressing collapse feature, where energy required to break inter-particle bonds is provided by relief of local strains. It is equivalent to fracture propagation in classical fracture mechanics, but occurring in compression of a porous material instead of tension. The concept has been explored on a larger scale as a means of avalanche release by Heierli et al (2008).

5. Effect of strain rate

Strain rates tested ranged from 5.77×10^{-3} s^{-1} (corresponding to a speed of 1.125 mm s^{-1}) to 7.69×10^{-2} s^{-1} (15 mm s^{-1}). This range remained in the brittle region with all experiments showing the same fundamental behaviour.

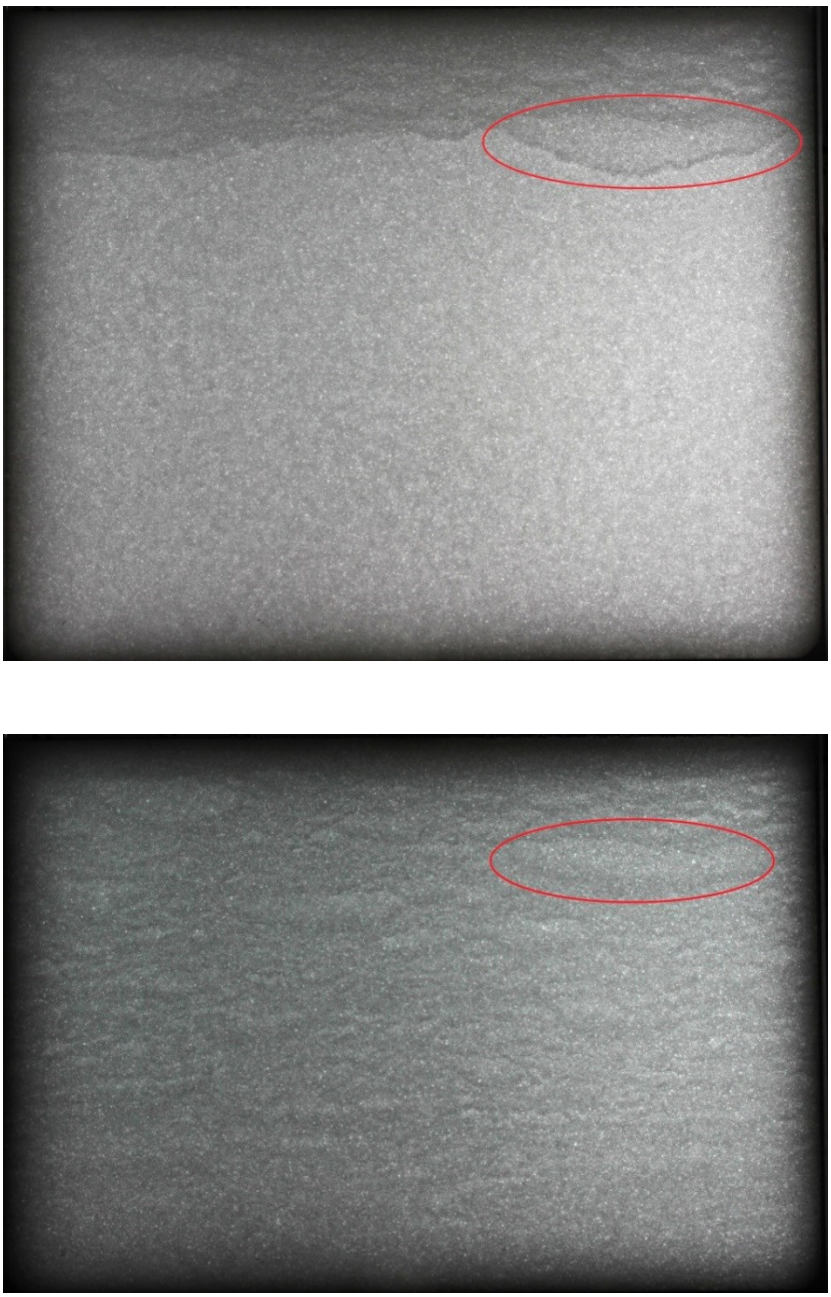

Figure 54: Example photograph of a small volume which resists compaction shown at point of at formation (top) and the same volume at point of collapse (bottom), after the lower part of the sample has been strained.

5.1. Strain rate or velocity?

Whilst strain rate is an appropriate method of categorising deformation in to brittle or ductile (which can also now be understood as strain-softening and non strain-softening respectively), crosshead velocity is perhaps more relevant once strain has localised. As illustrated by Equation 19, the propagation speed of the front is related only to the crosshead velocity not to strain rate. The critical strain achieved within the compaction front seems to be independent of strain rate (see below) and one can imagine that any other characterisation one might apply to the front would be similarly decoupled from strain rate. Nonetheless, there are still features which are better described by strain than displacement, which leads to the somewhat uncomfortable position of using strain, strain rate and velocity to describe experiments.

This is best evidenced by a thought experiment: imagine two specimens identical except that one is twice the height of the other. They are compacted by anvils moving at identical velocities. Assuming that both show brittle deformation (a *strain rate* consideration) the deformation patterns will be identical (related only to crosshead *velocity*) until the compaction band reaches the bottom of the shorter specimen. The shorter specimen shows a rise in stress and a second compaction band forms. The same will occur in the taller specimen when its compaction front reaches the boundary, having taken twice the time and displacement but occurring at the same *strain*.

This situation is inevitable, and is most pragmatically addressed by using velocity, strain and strain rate according to which option most usefully characterises the phenomena under discussion.

5.2. Rate effects

Imaging of the deformation showed some small regions which survived undamaged as the compaction front passed. These volumes appeared to be both larger and more common at lower speeds.

A slight tendency for the first compaction front to achieve a greater strain at lower velocities than at higher ones was not considered significant (for a linear fit, R^2=0.46). It may be an artefact of the relatively small sample size.

The force required to propagate a compaction front appears slightly higher at lower velocities (and this difference is visible in Figure 48) but, across the full set of results, this trend is not significant (for a linear fit, R^2=0.16).

The range of speeds tested does not exclude significant speed effects at other speed ranges. At lower speeds, snow is known to display ductile behaviours (see chapter II section 5.1) whilst at higher speeds, issues such as momentum exchange and pore pressure will come into play. The strain rates explored here are widely considered to fall close to the brittle to ductile transition for snow. Local strain rates, however, are much higher and fall within the brittle region.

6. Conclusions

Snow shows strain softening characteristics when deformed at rates above the brittle-ductile transition, it therefore displays deformation localisation. Snow may undergo more than one softening and subsequent hardening sequence as it is compacted.

In one-dimensional rigidly confined compression, damage takes the form of a front perpendicular to the load, which propagates parallel to the direction of the load. Such fronts may propagate in either direction through the specimen several times, and the sequence of propagation can be explained by considering age hardening of material behind the fronts. Deformation out with this band is insignificant.

Strain softening in snow causes local strain rates much higher than the global strain rate. These effects will also be scale dependent, as a larger specimen will require a lower strain rate in order to equate to the same damage front propagation speed.

Strain rate may influence the stress required to propagate the compaction front and level of strain achieved by the compaction front, but this study is inconclusive in this regard.

Chapter VIII: Indentation Results

Aim

The aim of this chapter is to present the results of the indentation experiments and discuss the deformation patterns present.

1. Introduction

A series of indentation experiments were conducted and analysed according to the methods set out in chapters V and VI. Different shapes of indenter were found to cause significantly different behaviour, with sharp tipped indenters pushing material to the side and round tips tending to push it down. Tip shapes tested are indicated in Figure 55. Large plugs of material were observed to form around the round tip, extending asymmetrically to the side of the indenter. Speed was found to have only minor effect in the case of sharp tipped indenter and only one speed was tested for the round tipped indenters.

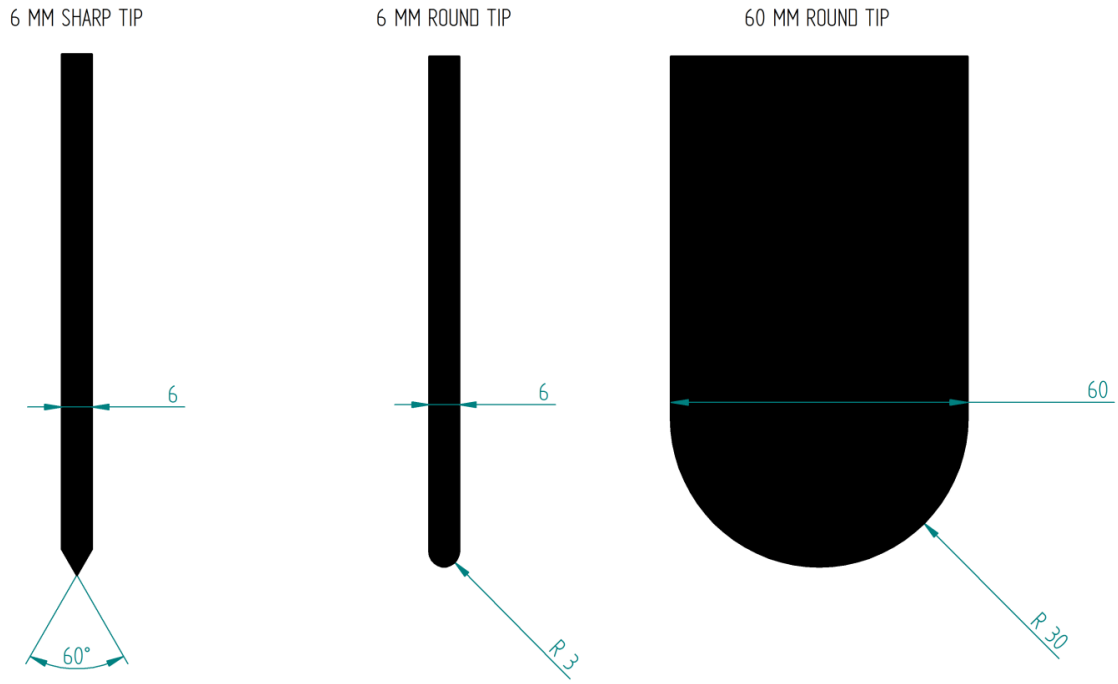

Figure 55: Tip shapes used in the indentation experiments. All indenters were 20 mm thick.

2. Behaviour of the 6mm sharp tipped indenter

The sharp tipped indenter was observed to push material aside as it progressed, forming a band of compacted material to both sides of the indenter. Material did not flow smoothly but instead was displaced as discrete chunks, as illustrated in Figure 56. The observed width of the volume of interaction was c. 35 mm or 6 times the width of the indenter. The maximum

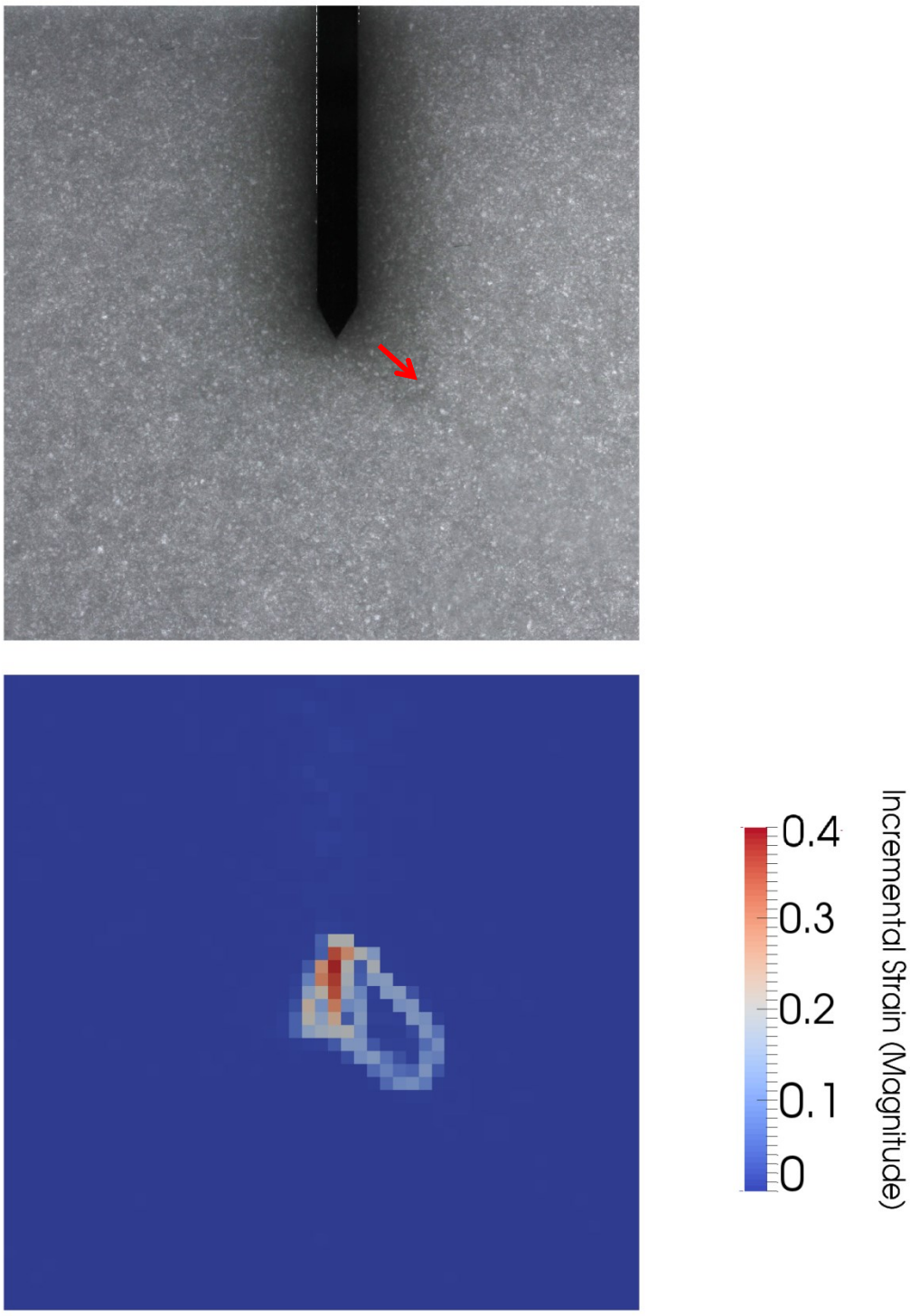

Figure 56 Chunk of material pushed down and right by the chisel tipped indenter. Photograph (top) and local incremental strain (bottom). The moving chunk has negligible internal strain. Speed is 5 mm/sec image interval 0.25 sec, indenter 6mm width.

height of the volume of interaction from the tip of the indenter to the lowest strained volume was c. 18 mm, or 3 times the width of the indenter. This lowest point occurred to one side of the indenter, corresponding to the bottom of one of the chunks of material being pushed aside.

Deformation does appear to be confined to a process zone immediately around the indenter. There was no detectable heave (upward flow of material leading to displacement of the free surface) except for at the very start of the experiment where the process zone could be interpreted to overlap with the free surface. Movement of the free surface was arrested after c. 7.5 mm of indentation at which point the shoulder of the indenter is c. 2.3 mm below the level of the undisturbed surface. Nor was there measurable strain of material away from the

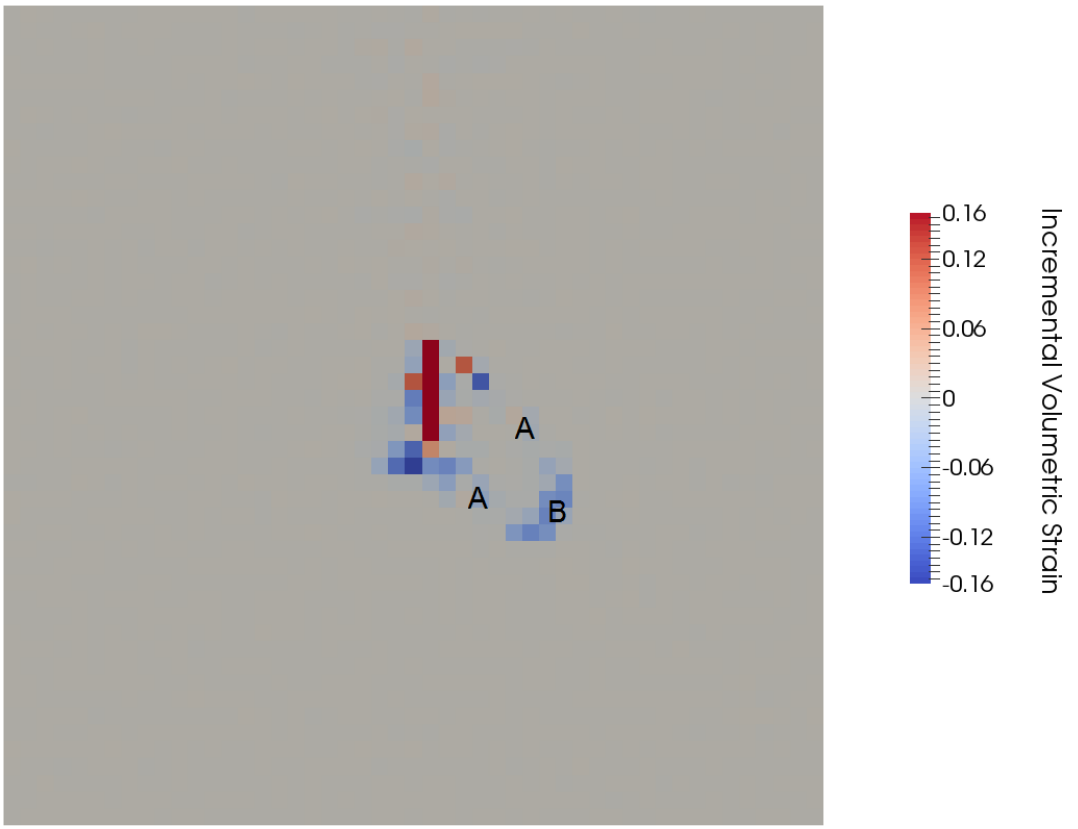

Figure 57: Volumetric strain components to at the same point as Figure 56. Deformation around the moving chunk can be categorised as two high-shear low-volumetric planes (A) and a high-volumetric low-shear (B) zone. Large dilatational strains in the centre (red) are clipped (calculated values exceed colour map), this area corresponds to now ruptured elements being separated as they pass to each side of the indenter, strains in this region are therefore a function of mesh size and indenter shape rather than corresponding to real strain in the material. Scale 2 mm per pixel.

indenter elsewhere in the specimen, (although it should be assumed that elastic strains are present in this area but are merely too small to observe).

To better understand the nature of the deformation around the mobile chunks of material illustrated in Figure 56 it is informative to look at the volumetric component of the deformation, as in Figure 57. Here we find that the volumetric straining associated with the phenomenon is predominately located in a low-shear zone at the end of the rectangular moving chunk, with relatively little contribution from the high shear zones at the sides of the moving chunk. As the deformation progress the boundary of the compressive zone extends further from the indenter, as illustrated in Figure 58: consecutive frames showing incremental volumetric strain, as in Figure 57. Note a similar phenomenon occurring to the left of the first two frames. Cropped with cross added as a visual reference (same location in each frame). 0.25 s interval 5 mm s^{-1} indenter velocity. Scale 2 mm per pixel.. This is behaviour interesting because it shows a considerable similarity to the compaction fronts exhibited in one-dimensional compression.

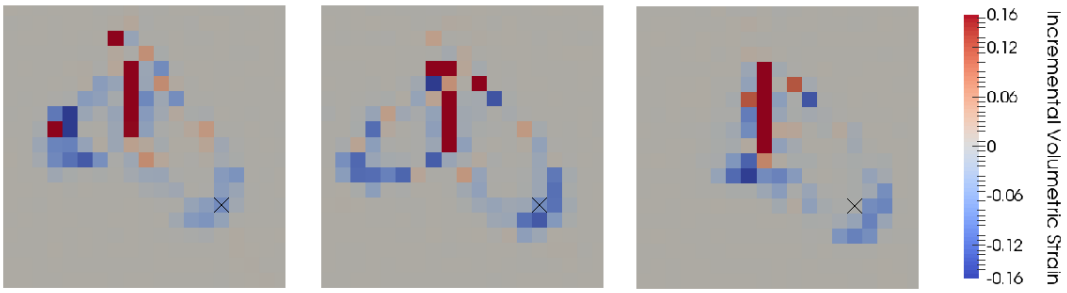

Figure 58: consecutive frames showing incremental volumetric strain, as in Figure 57. Note a similar phenomenon occurring to the left of the first two frames. Cropped with cross added as a visual reference (same location in each frame). 0.25 s interval 5 mm s^{-1} indenter velocity. Scale 2 mm per pixel.

It stands to reason that the energy invested in maintaining the two shear planes at the side of the moving chunks is not very great, or else damage would occur closer to the indenter. These shear planes are perhaps best viewed as consisting of material softened by compaction and subsequently kept soft by continuous shearing as the compaction band propagates away from the indenter.

This observed phenomenon is surprisingly similar to the observations of Fukue (1977), who conducted penetration experiments with a flat-faced penetrometer, except that he observed a compaction zone directly below of the indenter rather than to the sides. This difference in position is attributable to indenter shape. His experiments were not continued long enough to

reach a steady state, nor is it clear how this would happen if the compaction zone is in the path of the indenter.

2.1. Width of volume of interaction

In the absence of heave, and assuming no deflection of the boundaries, the volume occupied by the indenter must be provided for by volumetric strain in the material. Given the observations in the previous section it is reasonable to compare these volumetric strains to the compressive strains investigated in chapter VII. If we assume that this volumetric straining is contained entirely within a volume of interaction we can calculate the width of said volume thus:

$$W_v = \frac{W_i}{\varepsilon_v}$$

Equation 21

With W_v as the width of the interaction volume, W_i as the width of the indenter, ε_v as volumetric strain, positive in compression. The geometry of this situation is shown in Figure 59. Expressed in this way, ε_v must be constant throughout the deformed margin and no voids may form, though these assumptions can be relaxed if ε_v is viewed as an average ($\bar{\varepsilon_v}$). The Assumption of no heave is borne out by the observations, whilst the assumption of no deformation at the boundaries is reasonable given their high stiffness relative to the snow and the observations of deflection in chapter V section 4.

It was observed in the one-dimensional compression experiments that the artificial snow used in these experiments was strain softening, and exhibited a critical strain (under one dimensional compression) of 0.2 before hardening in the first instance. For $\varepsilon_v = 0.2$ the width of the volume of interaction predicted by Equation 21 is four times that of the indenter.

The observed width of interaction is larger than predicted by this simple theory (c. 6 times the width of the indenter) but the difference is not very great. The observed width corresponds to $\bar{\varepsilon_v} = 0.17$.

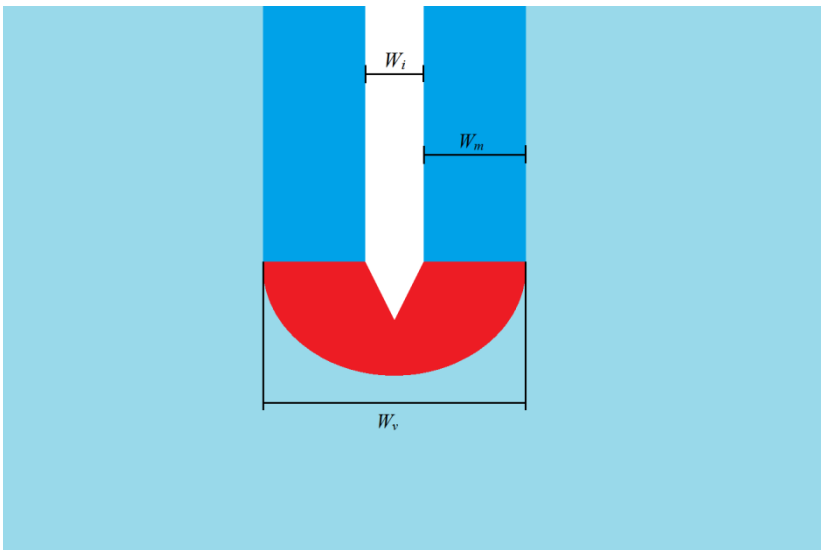

Figure 59: Nominal geometry of interaction volume. Indenter in white (width Wi), undeformed material in light blue, deformed margin in dark blue (width Wm), and arbitrarily shaped volume of interaction in red (width Wv).

The difference between the critical strain in the one dimensional experiments and the value of $\overline{\varepsilon_v}$ calculated above can be attributed to differences in strain regime (that is to say volumetric strain in areas under significant shear strain may be different to that under one-dimensional compression). There is also significant deformation occurring very close to the tip of the indenter which is inadequately resolved. The difference is relatively small however, (some 15%) which implies that there may be benefit to developing penetration theories according to this interpretation.

2.2.Force required to drive the indenter

The force delivered to the load cell was very low: Variation of about 0.2 N was observed, compared to an estimate at the design stage of 2.2 N. This level of force should have been just within the measurable range of the 25 N load cell but useful results could not be extracted. This is attributed to three main factors:

1. Friction and possible binding due to icing between the inventor and slide attenuated/damped the mechanical signal (displacement) delivered to the load cell.
2. Slight misalignment of the drive screw or whirl thereof caused a small oscillation in force to be recorded, which obscured the results
3. The measured load was too close to the noise floor of the load cell.

Point 1 and 2 combine to make useful examination of mean force impossible (as might be useful to the type of interpretation applied in geotechnical engineering, see Chapter II, section 9.2). Points 1 and 3 make examination of high frequency components impossible (as would be described in penetrometer analysis models presented in Chapter II section 5.2 or models for foams in section 9.1) as the attenuated force cannot be separated from the Nyquist noise.

2.3. Effects of indenter speed

Speeds of 1.125, 5, 10 and 20 mm s^{-1} were tested. The macroscopic deformation flow pattern remained the same, but the lower speeds tended to produce more visible tearing around the indenter, as indicated in Figure 60. The size of the chunks pushed aside was smaller at higher speeds.

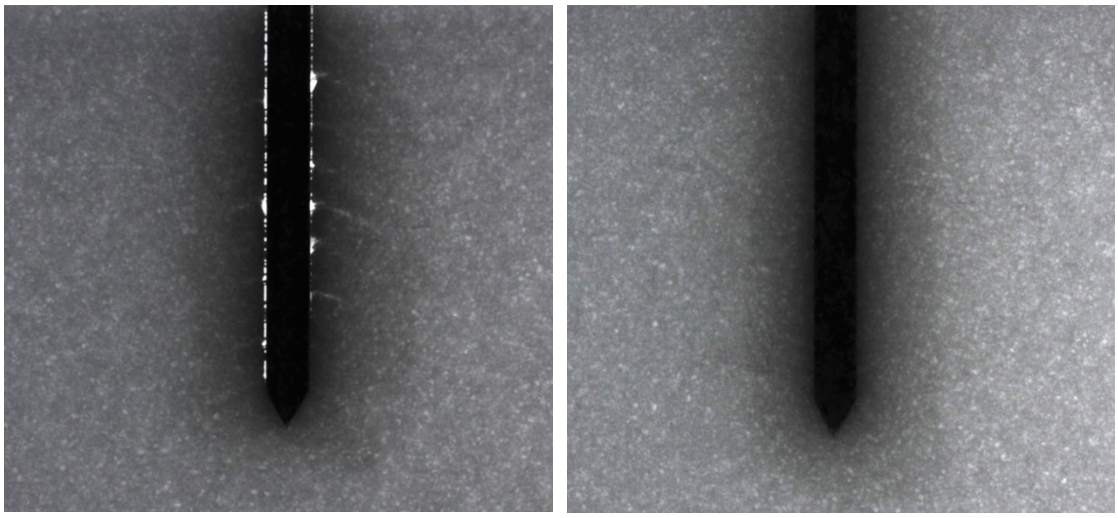

Figure 60: Tearing of snow at the sides observed at lower speeds (left) was absent at higher speeds (right). Left image speed 1.125 mm/s right 20 mm/s.

2.4. Comparison to the three dimensional case

The experiment was conducted in a thin slice of snow. Neglecting wall effects, the sharp tipped indenter is equivalent to an arbitrarily long sharp blade of 6 mm thickness. It may be useful to consider comparison to a 6mm conical tip.

For this case, the Equation 21 may be derived instead as:

$$W_v = \frac{W_i}{\sqrt{\bar{\varepsilon_v}}}$$

Equation 22

Thus, for $\bar{\varepsilon_v}$=0.2, W_v becomes $2W_i$, or for $\bar{\varepsilon_v}$=0.17, W_v becomes $2.4W_i$, indicating a much smaller diameter for the volume of interaction.

The change in geometry would also change the way that forces are distributed in the volume of interaction. (For example, if a force were to decrease linearly with distance from the indenter in two dimensions, it may decrease with the square of distance in three dimensions). This may lead to a change of mechanism of deformation which cannot easily be predicted. It is thought possible that deformation zones highlighted in Figure 56 Chunk of material pushed down and right by the chisel tipped indenter. Photograph (top) and local incremental strain (bottom). The moving chunk has negligible internal strain. Speed is 5 mm/sec image interval 0.25 sec, indenter 6mm width.and Figure 57 would form differently (or not at all) in three dimensions. If the deformation were axisymmetric such zones would have to assume an annular (as opposed to rectangular) form when viewed from above, though a non-axisymmetric deformation, with mobile zones and static ones radially interspersed is also possible. Hypothesised shapes are set out in Figure 61. Boundaries between such zones would be shear planes, formed in a similar manner to those shear planes above and below the compaction zone discussed in Section 2.

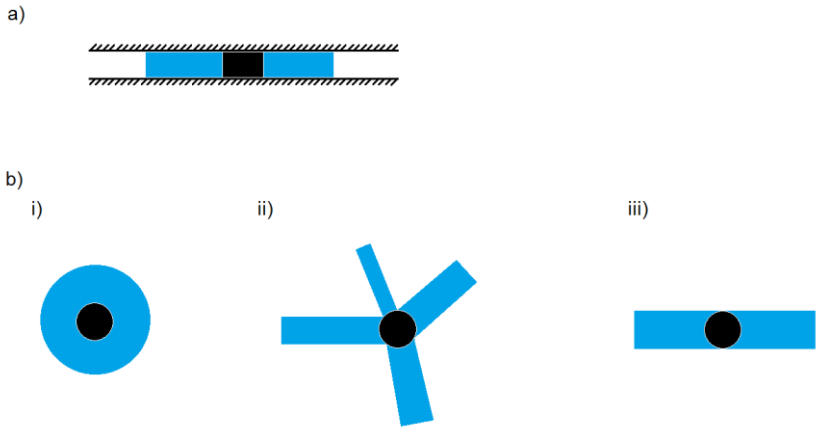

Figure 61: Hypothesised deformation zones (Blue) viewed from above. In my experiments (a) they are assumed to be rectangular, in 3d (b) they could be annular (i), rectangular radially distributed (ii) or two opposing zones (iii)

In the case of annular, axisymmetric deformation, radial displacement implies circumferential tensile strain, which could have an unpredictable influence on deformation, possibly leading to radially aligned fractures. In the absence of void formation, Equation 22 would apply to this case, but the value of $\overline{\varepsilon_v}$ under this different strain environment might be rather different to that observed in my experiments.

In the case of the non-axisymmetric deformation modes hypothesised in Figure 61: Hypothesised deformation zones (Blue) viewed from above. In my experiments (a) they are assumed to be rectangular, in 3d (b) they could be annular (i), rectangular radially distributed (ii) or two opposing zones (iii)Equation 22 would not apply. The distance the deformation zones would extend from the indenter would instead be similar to that found in my experiments. In case of two opposing zones forming, it is virtually identical to my experiments, except that such zones must always form in the plane of the apparatus in the experiments, whilst in 3d space they would probably form at different orientations as the indenter progresses.

3. Behaviour of the 6mm round tipped indenter

The round tipped indenter was observed to form large asymmetric bodies of compacted material, referred to here as compacted masses. These compacted masses rotated as they expanded and were associated with the formation of fractures in the snow as the compacted material was driven down by the indenter and parted from the material above. This is illustrated in Figure 62.

3.1. Formation of compacted masses

The compacted masses formed by the round tipped indenter are much bigger than the small chunks pushed aside by the sharp tipped indenter. As nothing else was changed, the difference must be down to the shape of the tip. In the case of the sharp tip, the active surfaces are at 30° to the direction of motion, while the round tip presents a large central area approximately perpendicular to the direction of motion. The angle of this area is not sufficient for material to be pushed aside, so it is instead carried down with the indenter. The growing volume of material driven in front of the indenter is asymmetrical, presumably due

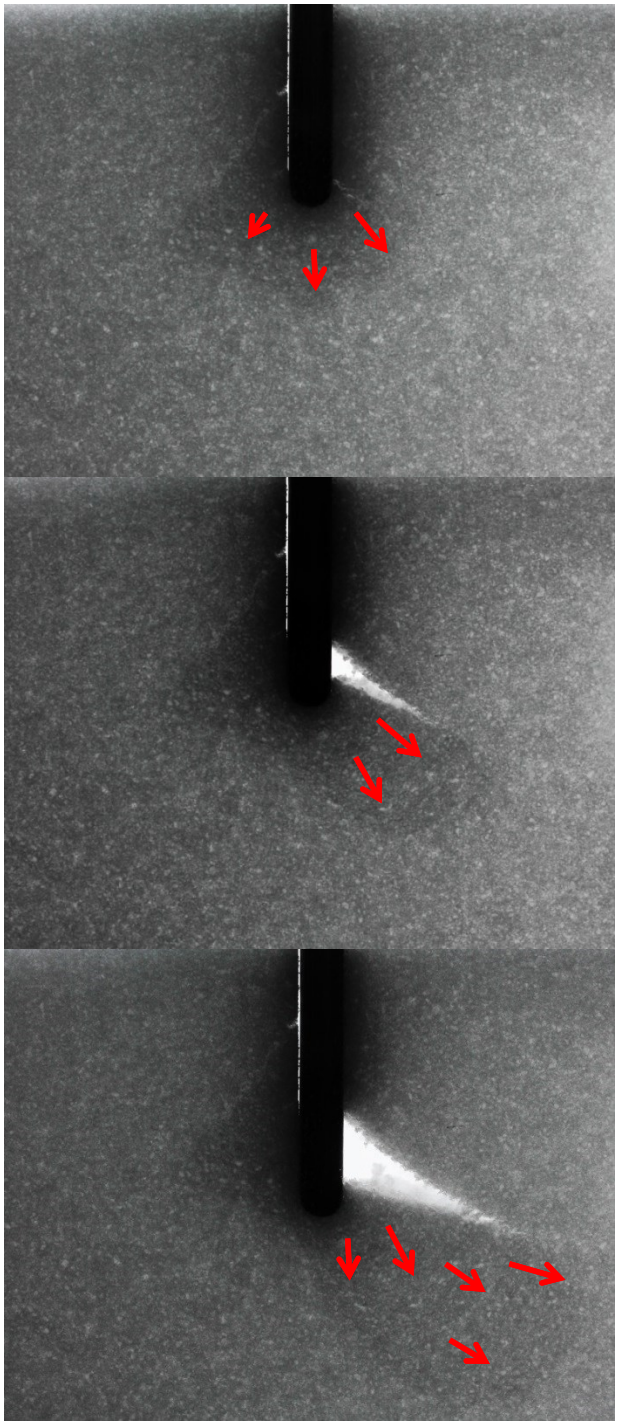

Figure 62: Process of formation of the compacted mass. The mass initiates as a small volume at the tip of the indenter (top) and expands to the side and rotates anticlockwise (middle and bottom) before breaking off from the indenter, at which point it stops moving

to random fluctuations in physical properties at the micro scale. The offset between the position of the indenter and the bulk of the compacted mass causes it to rotate and expand laterally, increasing the volume of material which has to be compacted for the mass to move. Eventually the force exceeds the strength of the connection between the mass and the indenter, the mass separates and stops moving while the indenter continues. This process is illustrated in Figure 62. The larger compacted masses extended 60 mm from the indenter, or 10 times its width. As with the sharp tip, no heave was observed.

3.2. Force required to drive the indenter

As with the 6 mm sharp indenter, the recorded force was too low to draw reliable conclusions about the 6 mm round tipped indenter, or to link features in the force results to those observed in the images.

3.3. Comparison to the three dimensional case

The observed behaviour may be less likely to occur in a 3D experiment (which is to say, if a hemispherical tip were used). In this case the central, high-angle area makes up a smaller proportion of the frontal area of the indenter and it is not clear what shape the compacted mass would adopt. It is considered likely that the phenomenon would still occur but that the compacted mass would extend in three directions instead of two. This would result in the force rising more quickly and probably cause the mass to detach sooner.

4. Behaviour of the 60 mm round tipped indenter

The volume of snow in the tests was too small to allow the 60 mm round tipped indenter to establish a ‘steady state’ condition. Instead, the process went through three distinct phases, as illustrated in Figure 63.

- Initially the indenter built up a compacted zone below its tip. This zone expanded downwards to produce a column of compacted material.

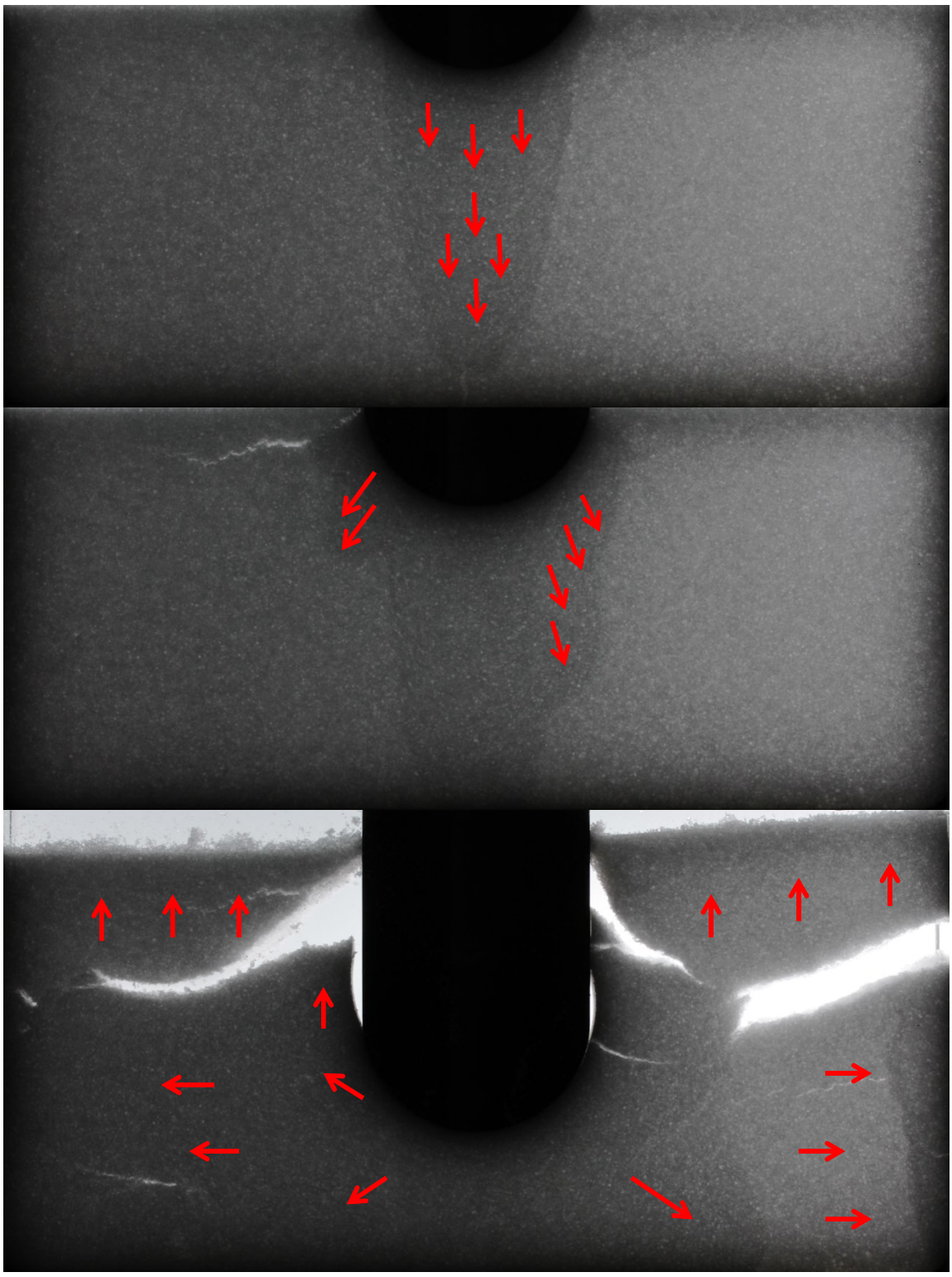

Figure 63: Evolution of the specimen with the 60 mm indenter. Initially a column of compacted material formed under the indenter (top), when this reached the base of the specimen chamber, material was instead pushed aside from the front of the indenter (middle). Eventually the whole specimen broke up and started to move (bottom).

- When the column reached the bottom of the specimen, material began to be pushed out to the sides of the tip of the indenter. The material behaved in a similar way to the compacted masses identified in section 3.1, extending outwards and downwards with some rotation and causing tearing as they separate from the material above.
- Once the compacted masses began to reach the bottom or sides of the specimen, it began to break up and flow upwards at the side of the indenter.

4.1. Force required to drive the indenter

The larger size of the 60 mm round tipped indenter lead to larger forces than the 6 mm indenters, and the results were thus greater that the instrument noise. An example force result is shown in Figure 64. The force during the first phase, when the vertical column is established, remains low and relatively stable, not exceeding 1 N. Once the column of compacted material reached the base of the specimen chamber, the force rapidly rose. The formation of fractures as the material breaks up acts to relieve the force, but not entirely. The overall rise in force continued to the end of the experiment.

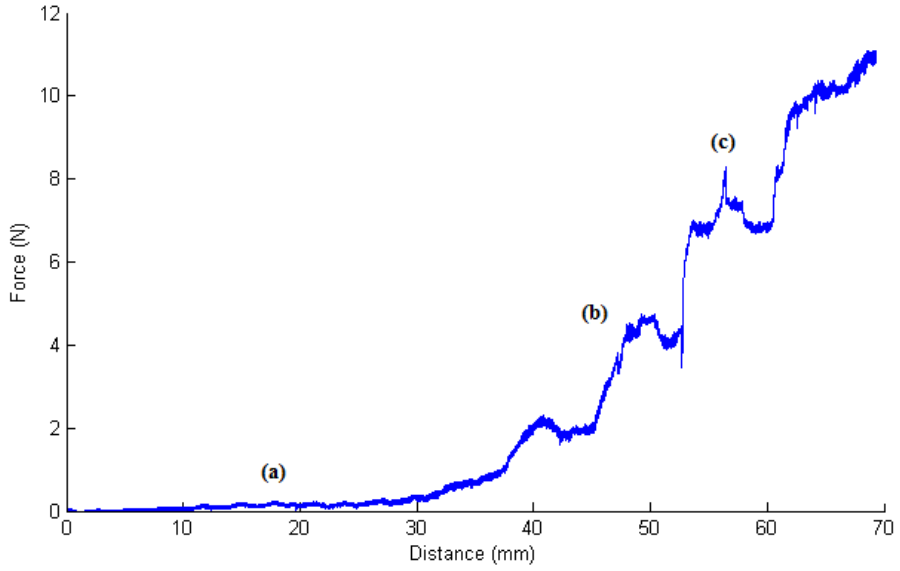

Figure 64: Force results for the 60mm indenter. The initial column of compacted snow was formed at relatively low force (a), Pushing material aside at the front of the indenter required a higher force (b) but fractures act to relieve some of the force (c).

5. Discussion

Straining of snow was observed up to a radius of c. 3 times width of the 6 mm sharp indenter from its tip. This is much further than is anticipated in snow penetrometer models (Johnson and Schneebeli 1999, Marshall and Johnson 2009, Löwe and Herwijnen 2011). While the 2D nature of the experiments may increase the size of the volume of interaction, the volume found in a 3D experiment is still likely to be significant. Furthermore, the stress field will extend beyond the strain field measured here (as elastic strains are too small to observe). It is likely that a more heterogeneous specimen (such as layered seasonal snow) would experience a larger volume of interaction as stresses seek out the weakest part. Speed was found to have only minor effect, reducing the size of the chunks of material being pushed aside and reducing the associated tearing.

The 6 mm round tip exhibits unstable behaviour. Its failure to push aside compacted and hardening material lead to the rapid growth of very large compacted masses which move with the indenter. This phenomenon is less likely for 3D application, but is still cause for concern in penetrometer design. A conical tip should be preferred to a hemisphere.

The moving compacted masses bear a passing resemblance to the deformation shapes seen in geotechnical applications, but as these are transient, asymmetric features the related models will not apply. Nor is it possible to look at the type of equations put forward above for the sharp tipped indenter, as significant void formation is present and the width of the volume of interaction varies significantly.

For the 60 mm round tipped indenter, it is important to note that after the column of compacted material reaches the base of the specimen, the behaviour is dominated by edge effects. If the indenter were run in a much larger specimen, the results would be different. It is not impossible that a situation similar to the 6mm round tipped indenter could develop, though the tall column of compacted material observed under the 60 mm indenter was not observed for the 6 mm round tip.

All three tested geometries provide insights into the behaviour of the snow, and could provide interesting test pieces for future models of the snow behaviour.

6. Conclusions

The sharp tipped indenter pushed material aside, disturbing a region 6 times its own width. The material did not flow continuously, but rather moved as discrete chunks of denser material proceeded by compaction fronts similar to those seen in the one dimensional experiments.

The 6 mm round tipped indenter caused the formation of large compacted masses which were driven downwards and outwards by the indenter, causing deformation to an area more than 3 times the width of that deformed by the sharp tip. This phenomena is transient and irregular, it is very undesirable from the perspective of penetrometry instruments.

The 60 mm indenter suffered from wall interaction, but the initial stages of the test appeared to develop differently to the smaller round tipped indenter, highlighting the importance of scale.

Chapter IX: General Conclusions

Aim

The aim of this chapter is to draw general conclusions from the proceeding work and identify their implications for the field of snow science

1. Artificial snow

Artificial snow was reliably and repeatably produced by processing solid ice chips at low temperature. Artificial snow thus produced was found to have density, grain size, and microstructure falling within the range of found in natural, seasonal snow. It was most similar to a wind-beaten and melt-altered spring snow forms or to windslab. The artificial snow was also found to respond to penetrometer experiments (with an SMP) in a similar way to natural snow.

The artificial snow has been characterised, both when fresh and after isothermal ageing, by applying the following techniques:

- Low-temperature SEM
- Optical microscopy
- Standard field classification

To extract the following characterizations:

- Hardness
- Grain form
- Density
- Grain size distribution
- Micrographs (optical and SEM)

A detailed method of production has been presented, which would allow identical snow to be produced for future experiments at Edinburgh or elsewhere. The artificial snow is considered a good candidate for use in experimental investigations of snow properties, because it is reproducible and reasonably representative of natural snow.

2. DIC and experimental method

Digital image correlation techniques were used to track displacement and strain in snow without the application of tracer particles or substances. For this to succeed the camera must be capable of resolving individual ice particles within the snow. Texture in the resulting photographs is greatly improved by transmitted light illumination. Tracking of image

features still occasionally fails but the results are sufficiently good for strain fields to be derived and analysed.

Experiments were conducted in rigidly confined compression and indentation using three shapes of indenter (6 mm 60° sharp tip, 6 and 60 mm rounded tips). The “thin” nature of the experiments effectively restrained deformation to 2 dimensions, but wall interactions were significant. These interactions altered the defamation patterns in the one-dimensional experiments but there is no reason to believe they significantly affected the indentation tests.

3. One-dimensional compression experiments

One-dimensional compression of snow was found to cause strain localisation. This implies that snow is a strain softening material. Localisation was found to take the form of moving fronts, which lay normal to load and propagated through the specimen. Material was compacted as the front passed over it. In some cases the front did not pass through the whole specimen contiguously, but rather stopped at some location and began again elsewhere.

The sequence of compaction was found to occur more than once, and may occur many times. Each successive compaction front achieved lower level of strain than its predecessor. No significant rate effects were observed.

Boundary effects (wall friction) altered the front propagation pattern. A proposed behaviour without these effects is presented. The boundary effects are not thought to have influenced the formation or micro-scale movement of the compaction fronts, but only the large scale pattern.

The observed behaviour is explained by an interplay of strain softening (corresponding to bond breaking) and strain hardening (due to volumetric straining) followed by age hardening once straining is arrested.

4. Indentation experiments

Indentation experiments were conducted with one sharp tipped indenter and two sizes of round tipped indenter. Round tipped indenters were found to deform a much larger area than sharp tipped ones.

Deformation around the sharp tipped indenter seems to be characterised by compression fronts, similar to those observed in one-dimensional compression, moving outward approximately parallel to the surface of the indenter. This invites comparisons between the two geometries, though the critical strain achieved be the fronts is different (by c 15%), and some deformation occurs outside these areas.

The failure of force measurement on the smaller two indenters prevented interpretation according to the current leading edge models, but observations cast doubt on some of the assumptions intrinsic to these models. The implications for future models are discussed later.

The two different sizes of round tipped indenter caused different deformation patterns. This highlights the fact that scale is important when considering snow deformation.

5. Further experimental work

There may be some benefit to constructing a more sensitive version of the experiment in order to investigate the relationship between penetration force and deformation events for small indenters. Without force measurements from my experiments it is impossible to relate the penetration force to the observed deformation patterns but it seems likely that the existing assumption that the force would be a superposition of many small peaks related to individual element ruptures (Chapter II Section 5.2) is oversimplistic. The implications of this work for future penetration models are discussed later.

There may also be benefit to exploring other snow types, strain rates, and temperatures in order to define a parameter envelope where the observed behaviours could be expected to occur. It is thought likely at this point that the observed compaction fronts in one-dimensional compression would be present throughout the brittle region, but this has not been confirmed by experiment.

It would be useful to repeat the indentation experiments in an axisymmetric environment in order to make the results more applicable to field penetrometers. If the resulting deformation is symmetry-breaking it may be difficult to fully image it, but phenomenological observations could help develop an understanding of penetration testing in snow. In understanding the differences between 2D and 3D cases, it may also be useful to conduct plane strain cavity expansion experiments (representing a horizontal slice through traditional vertical penetration experiment) to investigate the axisymmetric (or otherwise) nature of the deformation. This could resolve the discussion of potential deformation shaped hypothesised in Figure 61 in chapter VIII, though it should be noted that penetration through a slice and cavity expansion within it are not exactly the same thing. A fully 3D experiment could be conducted using X-ray computer tomography but, given the typical speed with which penetration tests are undertaken, together with the need to acquire multiple X-ray images without any deformation in between, this may not be possible with current technology. Another approach would be to advance a penetrometer and then withdraw it and section or CT the resulting specimen, but without the benefit of consecutive (in time) images strain would have to be inferred from density rather than differential movement. I suspect the random nature of the microstructure may make such inference difficult.

6. Implications for constitutive modelling

It is clear from the work presented here that snow is a strain softening material: that is to say it not only softens in the usual circumstances (tension, shear) but in all probability will show softening in all irreversible deformation cases. Strain softening introduces an implicit scale (which could be viewed as the characteristic size of spontaneously forming deformation features). This limits the scalability of some models or experiments: these deformation features do not scale with specimen size. In the case of continuum models solved in a finite element framework, this characteristic size will naturally derive from the mesh density. This is generally viewed as undesirable, solutions should be mesh independent (particularly if mesh density will vary across the simulation, or mesh-size convergence studies are to be conducted). To address this models must include their own internal characteristic length.

For cases where this characteristic length is larger than the mesh size, it can be viewed as a need to take into account the state of neighbouring elements when calculating the stress-strain response. Where the mesh is larger, the required action is less clear.

The behaviour of the one-dimensional compression experiments can be explained by careful consideration of the microstructural processes underway in snow (vis: strain softening, strain hardening and age hardening). Good models must include all three effects if they are to reproduce the observed behaviour. This requires models to take account of strain history and (real) time as well as the momentary stress and strain states. It should be noted that the degree of strain softening and strain hardening must relate to the strain tensor: compressive volumetric straining leads to both hardening and softening, whilst tensile volumetric straining or shearing leads only to strain softening (though of course any type strain not taking particles out of contact will be followed by age hardening)

If deformation is understood as an interplay of these three phenomena, it may be possible to develop models which span the ductile to brittle transition. Brittle deformation (now understood to be strain softening or deformation localising) is simply a case where strain softening exceeds the combined effect of strain hardening and age hardening. Ductile behaviour is the reverse.

The experimental results presented here provide test pieces of progressively greater complexity. A well formulated one-dimensional model ought to be able to reproduce the results of the one-dimensional compression experiments. A two-dimensional model should reproduce the one-dimensional compression tests and the sharp tipped indentation tests, whilst modelling the round tipped tests will require models which can exhibit failure in tension and significant void opening.

7. Implications for penetrometer instruments (and models thereof)

The rounded tips used in the experiments disturbed a far greater amount of material than the sharp one. In the field of penetrometry, where a small interaction volume is required in order to resolve thin layers, sharp tips should therefore be preferred to rounded ones.

The observed deformation is considerably more complex than is assumed in current models of penetrometer-snow interaction (these models were described in Chapter II section 5.2). It seems that the assumptions underlying current penetration theory in snow may be violated: peaks in recorded force cannot be assumed to relate only to the brittle rupture of elements

local to the indenter, but might relate to distant tearing or compaction events. Certainly the observed zone of interaction is much larger than allowed for in these models.

Direct application of models from the field of geotechnical engineering is probably not viable, as the deformation flow patterns for snow appear different to those typically used to formulate geotechnical models. Geotechnical models tend to relate penetration force to shear strength, neither of which were measured in this study, preventing any direct assessment of their accuracy. Nonetheless, it may be possible to make use of modified versions of geotechnical models in future, perhaps by substituting observed deformation patterns for the assumed patterns present bearing capacity type geotechnical models (see chapter II section 9).

Application of models from foams has already been attempted, but must now be criticised for assuming that deformation is limited to elements touching the indenter or to a vertical column of material below it. The apparent success of this approach should not be disregarded, however. It is possible that the deformation process in the mobile deformation zones observed in chapter VIII are sufficiently similar to that hypothesised in the models that they do still apply, all be it that the location of the deformation is different. It is clear that the size of the interaction zone ought to feature in some of the equations set out in Table 1[8] in Chapter II, but given that the thresholds for these parameters (used in classifiers) are determined empirically, adjustment of the equations might not yield very great improvements in the avalanche stability classifiers.

[8] All except element rupture strength rely on the frontal area of the penetrometer, which is effectively treated as the plan area of the zone of interaction.

References

Abele, G. and Gow A. J. 1976. *Compressibility characteristics of compacted snow.* Cold regions research and engineering laboratory. Report number 76-21.

Agrawal K. C. and Mittal R. K. 1995 *Influence of microstructure on mechanical properties of snow.* Defence science journal. vol. 45, No 2, p 93-105

Alshibli K. A. and Sture S. 1999. *Sand shear band thickness measurements by digital image techniques*. Journal of computing in civil engineering. Vol. 13, No. 2, p 103-109

ASTM D5778-12. 2012. *Standard Test Method for Performing Electronic Friction Cone and Piezocone Penetration Testing of Soils*, ASTM International, USA

Bader H. (1962). *The physics and Mechanics of snow as a material*. USA Cold Reigons and Engineering Laboritory, Monogrpah II-B, P79.

Bartelt P. and Lehning M. 2002. *A physical snowpack model for the Swiss avalanche warning Part 1: numerical model*. Cold regions science and technology. 35, p 123-145

Borstad C.P. and McClung D.M. 2011. *Thin blade penetration resistance and snow strength*. Journal of Glaciology vol.57, no. 202.

Borstad C.P. and McClung D.M. 2011. *Numerical modelling of tensile fracture initiation and propagation in snow slabs using nonlocal damage mechanics.* Cold reigoons science and technology. Vol 69. P 145-155.

Bellaire S. and Schweizer J. 2011. *Measuring spatial variations of weak layer and slab properties with regard to snow slope stability*. Cold regions science and technology. 65. p 234–241

Bellaire S, Pielmeier C, Schneebeli M. and Schweizer J. 2009. *Instruments and Methods Stability algorithm for snow micro-penetrometer measurements*. Journal of glaciology, Vol. 55, No. 193.

Blackford J. R. 2007. *Sintering and Microstructure of Ice: a review.* Journal of physics D: applied physics. 40.

Blackford J. R, Jeffree C. E, Noake D. F. and Marmo B. A. 2007. *Microstructural evolution in sintered ice particles containing NaCl observed by low-temperature scanning electron microscope.* Proceedings of the institution of mechanical engineers, part L: Journal of materials mesign and applications.

Bradley C. C. 1968. *The resistograph and the compressive strength of snow*. Journal of glaciology. Vol. 7, No. 51.

BS EN ISO 22476-1 2012 *Geotechnical investigation and testing. Field testing. Electrical cone and piezocone penetration test.* British standards institution. ISBN 978 0 580 77121 7.

Clulow M. G. and Winnett D. F. 2000. *Snow making machine*. Patent number WO 00/34722

Colbeck S. C. 1982. *An Overview of Seasonal Snow Metamorphism*. Reviews of geophysics and ice physics. Vol 20, No. 1, p 45-61

Conger S. M. and McClung D. M. 2009. *Comparison of density cutters for snow profile observations*. Journal of glaciology, Vol. 55, No. 189,

Cresseri S. and Jommi C. 2005 *Snow as an elastic viscoplastic bonded continuum: a modelling approach.* Rivista Italina di Geotcnica. 4/2005.

Cresseri S. Genna F. and Jommi C. 2010. *Numerical integration of an elastic-viscoplastic constitutive model for dry metamorphosed snow.* International journal for numerical and anylitical methods in geomechanics. Vol 34. P 1271-1296

de Montmollin 1982. Listed below under Montmollin

Desrues J, Darve F, Flavigny E, Navarre J. P. and Taillefer A. 1982. *An incremental formulation of equations for deposited constitutive snow.* Journal of glaciology, Vol. 25, No. 92.

Fauve M, Rhyner H. and Schneebeli M. 2002. *Preparation and Maintenance of pistes*. *Handbook for practitioners*. Swiss federal institute for snow and avalanche research, Davos, Switzerland.

Fierz, C., Armstrong, R.L., Durand, Y., Etchevers, P., Greene, E., McClung, D.M., Nishimura, K., Satyawali, P.K. and Sokratov, S.A. 2009. *The International Classification for Seasonal Snow on the Ground*. IHP-VII Technical documents in hydrology N°83, IACS Contribution N°1, UNESCO-IHP, Paris.

Floyer J. A. 2008. *Layer detection and snowpack stratigraphy characterisation from digital penetrometer signals.* PhD thesis. University of Calgary, Alberta.

Floyer J.A. and Jamieson B. 2006. *Empirical analysis of snow deformation below penetrometer tips*. Proceedings of the 2006 international snow science workshop in Telluride, Colarado, USA.

Floyer J.A. and Jamieson B. 2010. *Rate-effect experiments on round-tipped penetrometer insertion into uniform snow.* Journal of Glaciology, Vol. 56, No. 198

Fukue M. 1977. *Mechanical performance of snow under loading*. PhD Thesis. McGill university, Montreal.

Fukuzawa T. and Narita H. 1993. *An experimental study on the mechanical behaviour of a depth hoar layer under shear stress.* Proceedings of the 1992 international snow science workshop, Breckenridge, Colorado, USA

Gagliardini O. and Meyssonnier J. 1997. *Flow simulation of a firn-covered cold glacier.* Annals of glaciology 24.

Gibson L. J. and Ashby M. F. 1997 *Cellular Solids.* Cambridge university press.

Golubev V. N. and Sokratov S. A. 2004. *Regular packing of grains as a model of snow structure.* Annals of glaciology 38.

Hagenmuller P. Theile T.C. and Schneebeli M. *Numerical simulation of microstructural damage and tensile strength in snow.* Geophysical research letters Vol 41. P 86-89.

Hoult N. A., Take W. A, Lee C. and Dutton M. 2013. *Experimental accuracy of two dimensional strain measurements using Digital Image Correlation*. Engineering structures. 46. p 718–726

Heierli J, Gumbsch P. and Zaiser M. 2008. *Anticrack nucleation as a mechanism for snow slab avalanches.* Science. Vol. 321, p 240-243.

Jamieson J. B. and Johnson C. D. 1993. *Rutschblock precision, technique variationsand limitations*. Journal of glaciology, Vol. 39, No. 133,

Johnson J. B. 2003. A statistical micromechanical theory of cone penetration in granular materials. Cold regions research and engineering laboratory. report number TR-03-3.

Johnson J. B. and Schneebeli M. 1999 *Characterizing the microstructural and micromechanical properties of snow.* Cold regions science and technology 30.

Kadu D. and Herrmann H. J. 2011. *Density profiles of loose and collapsed cohesive granular structures generated by ballistic deposition.* Physical review E.

Klein G. J. 1946. *Method of measuring the significant characteristics of a snow-cover*, National research council of Canada associate committee on soil and snow mechanics, Ottawa. Technical memorandum 5.

Lehning M, Bartelt P, Brown B, Fierz C. and Satyawali P. 2002a. *A physical snowpack model for the Swiss avalanche warning Part II. Snow microstructure*. Cold regions science and technology 35. p 147-167.

Lehning M, Bartelt P, Brown B. and Fierz C. 2002b. *A physical snowpack model for the Swiss avalanche warning part iii: meteorological forcing, thin layer formation and evaluation.* Cold regions science and technology 35. p169– 184.

Liao J. C. and Ng K. C. 1990. Effect of ice nucleators on snow making and spray freezing. Industrial engineering and chemistry research. 29, p 361-366

Libbrecht K. G. 2005. *The physics of snow crystals*. Reports on progress in physics. 68. p 855-895

Löwe H. van Herwijnen A. 2012. *A shot-noise model for snow micro-penetration.* Cold regions science and technology, 70, p 62-70.

Lowe H, Egli L, Bartlett S, Guala M. and Manes C. 2007. *On the evolution of the snow surface during snowfall*. Geophysical research letters, vol. 34

Mackenzie R. and Payten W. 2002. *A Portable, Variable-Speed, Penetrometer for Snow Pit Evaluation*. Proceedings of the 2002 international snow science workshop, Penticton B.C. Canada.

Marshall H-P. and Johnson J. B. 2009. *Accurate inversion of high-resolution snow penetrometer signals for microstructural and micromechanical properties*. Journal of geophysical research, vol. 114.

Mellor M. 1964. *Properties of snow.* USA cold regions research and engineering laboratory monograph III-A1.

Mellor M. 1975. *A review of basic snow mechanics*. The international symposium on snow mechanics, Grindelwald, Switzerland, 1974. IAHS-AISH publication 114.

Meschke G. Liu C. and Mang. H.A 1996 *Large strain finite-element analysis of snow.* Journal of engineering Mechanics. Vol 122. P 591-602.

de Montmollin V. 1982. *Shear tests on snow explained by fast metamorphism.* Journal of glaciology, Vol. 28, No. 98

Nakamura H. 1978. *A new apparatus to produce fresh snow*. (In Japanese with English summary). National research centre for disaster prevention. 19, 229-237.

Nicot F. 2004. *Constitutive modelling of snow as a cohesive-granular material*. Granular matter 6, 47-60.

Nicot F and Darve F. 2005. *A multi-scale approach to granular materials*. Mechanics of materials, 37, p 980–1006.

Pielmier C. and Marshall H-P. 2009. *Rutschblock-scale snowpack stability derived from multiple quality-controlled SnowMicroPen measurements*. Cold regions science and technology. 59, p 178-184.

Pielmier C. and Schweizer J. 2007. *Snowpack stability information derived from the SnowMicroPen signal*. Cold regions science and technology, 47, p 102–107.

Reiweger I, Schweizer J, Ernst R. and Dual J. 2010. *Load-controlled test apparatus for snow*. Cold regions science and technology, 62, p119–125.

Reiweger I. and Schweizer J. 2010. *Failure of a layer of buried surface hoar*. Geophysical research letters, VOL. 37.

Robertson P. K. 1990. Soil classification using the cone penetration test. Canadian geotechnical journal. Vol.27. iss.1. p 151 -158

Robertson P. K Cabal K.L. 2014 *Guide to Cone Penetration Testing for Geotechnical Engineering 6th Edition* Gregg Drilling & Testing, Inc. USA

Roch A. 1948. *Disscussion sur valeur du nombre de poisson pour la neige, (text in French). Institut fur schnee und lawinenforschlung, interner bericht no 98.*

Petrovic J. J. 2003. *Mechanical properties of ice and snow*. Journal of materials science, 38, p 1– 6

Salm B. 1975. *A constitutive equation for creeping snow*. The international symposium on snow mechanics, Grindelwald, Switzerland, 1974. IAHS-AISH publication 114.

Salm B. 1982. *Mechanical Properties of Snow*. Reviews of geophysics and space physics, vol. 20, no. 1, p 1-19

Sanger F.J 1964. *Properties of snow.* Cold regions science & engineering laboratory, US army, report III-A1.

Schaap L. H. J. and Fohn P. M B. 1987. *Cone penetration testing in snow*. Canadian geotechnical journal. Vol 24. Iss 3 p 335-341

Schleef S, Jaggi M, Löwe H. and Schneebeli M. 2014. *An improved machine to produce nature-identical snow in the laboratory*. Journal of glaciology, Vol. 60, No. 219.

Schneebeli M, Pielmeier C. and Johnson J. B. 1999. *Measuring snow microstructure and hardness using a high resolution penetrometer.* Cold regions science and technology 30. p 101-114

Schneebeli M. and Sokratov S. *Tomography of temperature gradient metamorphisum of snow and associated changes in heat conductivity*. Hydrological Processes. Vol 18, 3655-3665.

Schweizer J. 1998. *Laboratory experiments on shear failure of snow*. Annals of glaciology vol. 26. p 97 -102.

Schweizer J. and Jamieson J. B. 2010. *Snowpack tests for assessing snow-slope instability*. Annals of glaciology. 51(54)

Schweizer J, Jamieson J. B. and Schneebeli M. 2003. *Snow avalanche formation*. Reviews of geophysics, 41.

Schweizer J, Kronholm K, Jamieson J. B. and Birkland K. W. 2008. *Review of spatial variability of snowpack properties and its importance for avalanche formation*. Cold regions science and technology. 51. p 253-272.

Shapiro L. H, Johnson J. B, Sturm M. and Blaisdell G. L. 1997. *Snow Mechanics review of the state of knowledge and applications*. Cold regions research and engineering laboratory. Report Number 97-3.

Shinojima K. (1967) *Study on visco-elastic deformation of deposited snow*. Proceedings of the international conference on the on physics of snow and ice. Sapporo Japan 1966 Vol 1 Hokkaido University.

Skouvaklis G. 2010. *Rubber friction on ice and snow surfaces*. PhD thesis, University of Edinburgh, Scotland.

Szabo D. and Schneebeli M. 2007. *Subsecond sintering of ice.* Applied physics letters. 90.

Takeuchi Y, Nohguchi Y, Kawashima K. and Izumi K. 1998. *Measurement of snow-hardness distribution*. Annals of glaciology. 26.

van Herwijnen A. and Heierli J.2009 Measurement of crack face friction in collapsed weak snow layers. Geophysical research letters. vol. 36.

White D.J. Take W.A. & Bolton M.D. 2003. Soil deformation measurement using particle image velocimetry (PIV) and photogrammetry. Geotechnique 53 7 p 619-631

Wolf H, König D. and Triantafllidis T. 2003. *Experimental investigation of shear band patterns in granular material.* Journal of structural geology. 25. p 1229–1240

Wong J. Y. 1992. *Expansion of the terrain input base for nepean tracked vehicle performance-model, NTVPM, to accept Swiss rammsonde data from deep snow.* Journal of terramechanics. Vol. 29. Iss. 3. p 341 -357

Yang R. N, Zou R. P. and Yu A. B. 2000. *Computer simulation of the packing of fine particles*. Physical review E, vol. 62, no 3.

Yong R. N. and Metaxas I. 1985. *Influence of age-hardening and strain-rate on confined compression and shear behaviour in snow*. Journal of terramechanics. Vol. 22. No. 1. p 37-49.

Yong R. N. and Fukue M. 1977. *Performance of snow in confined compression*. Journal of terramechanics. Vol. 14. No. 2. p 59-82.

Yosida Z. Oura H. Kuroiwa D. Huzioka T. Kojima K. Aoki S. and Kinoshita S. (1956) *Physical studies on deposited snow. II, mechanical properties.* Contributions from the institute of low temperature science. No 9. P 1-81.

Yu H. S. and Michell J. K. 1998. *Analysis of cone resistance: review of methods*. Journal of geotechnical and geoenvironmental engineering. vol 135, no 2.

Appendix 1: Snow making procedure

Remember! Working in the cold room is subject to health and safety restrictions. Refer to the current version of the risk assessment. Wear gloves and warm over clothes when preparing snow.

1. Ice chips are produced by a Scotsman AF 80 ice chip maker. Up to three bags may be filled at any one time without using the very wet chips from the base of the machine. Chips enter the machine from a refrigeration unit at the back of the machine and then continually melt whilst sitting in the insulated vat.

2. The ice chips are wet, at temperature near 0 °C, and 0.5 to 3 cm across.

3. The ice chips are placed in polymerised nylon bags, 2kg per bag, ± 0.1kg. It is helpful to slightly flatten the bags to assist step 6.

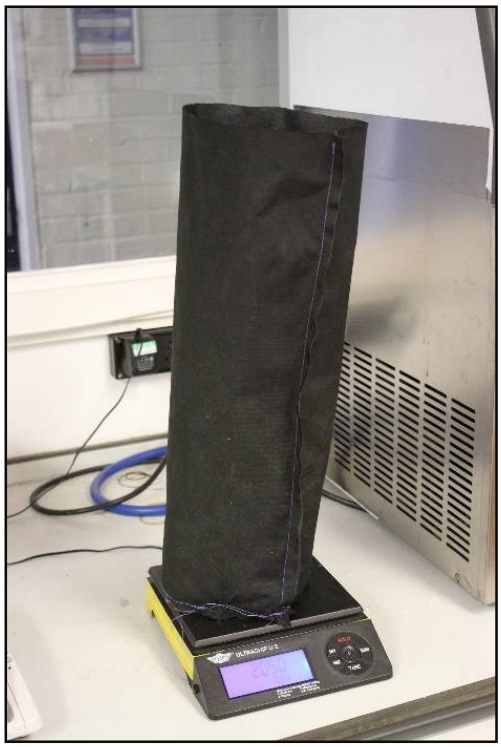

4. The bags are placed in a freezer at -30 °C for a minimum of 24 hours (no maximum time)

5. The bags are moved to a freezer at -80 °C for a minimum of 24 hours (no maximum time)

6. The bags are removed from the freezer and the contents broken up with a lump hammer (2kg) until chunks are no bigger than 80 mm

7. The ice chips are poured into the blender any solid ice chunks are disposed of. Large quantities of solid ice imply that the chips were too wet, and the batch is abandoned. The blender is a Robot Coupe Blixer 6 v. v.

8. The mixer is started at minimum speed and accelerated to full speed over 3 seconds.

9. The paddle/scraper is agitated to ensure no unprocessed chips are caught behind it, and ice is flowing smoothly.

10. The mixer runs for 60 seconds total.

11. The snow is placed in black polymer buckets in the cold room and covered. They must not be placed on the floor as it is heated to protect the foundations from freezing.

Continued overleaf…

12. Snow is scooped out of the buckets and sieved through the 1.68 mm sieve. A 100 g mass is used to agitate the snow and prevent the sieve clogging up.

13. Wear thick gloved to prevent heat transfer to the sieve. Take care to avoid placing your hand under the edge of the sieve as this can catch and then drop chunks of snow into the experiment.

Appendix 2: Engineering drawings

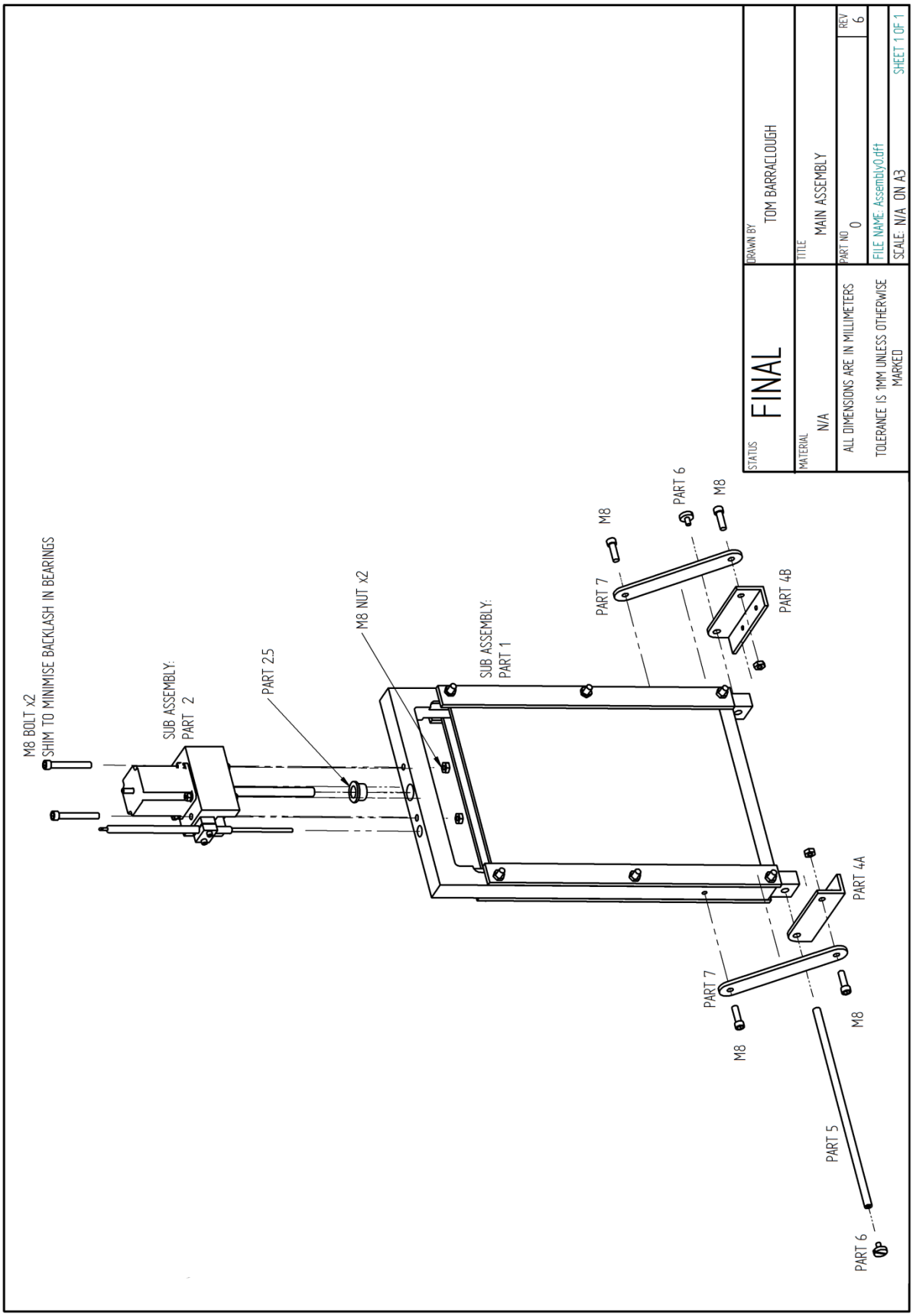
M8 BOLT x2
SHIM TO MINIMISE BACKLASH IN BEARINGS
SUB ASSEMBLY:
PART 2
PART 25
M8 NUT x2
SUB ASSEMBLY:
PART 1
PART 7
M8
PART 6
M8
PART 4B
PART 4A
PART 7
M8
M8
PART 5
PART 6
STATUS
FINAL
DRAWN BY
TOM BARRACLOUGH
MATERIAL
N/A
TITLE
MAIN ASSEMBLY
PART NO
0
REV
6
ALL DIMENSIONS ARE IN MILLIMETERS
TOLERANCE IS 1MM UNLESS OTHERWISE MARKED
FILE NAME Assembly0.dft
SCALE N/A ON A3
SHEET 1 OF 1

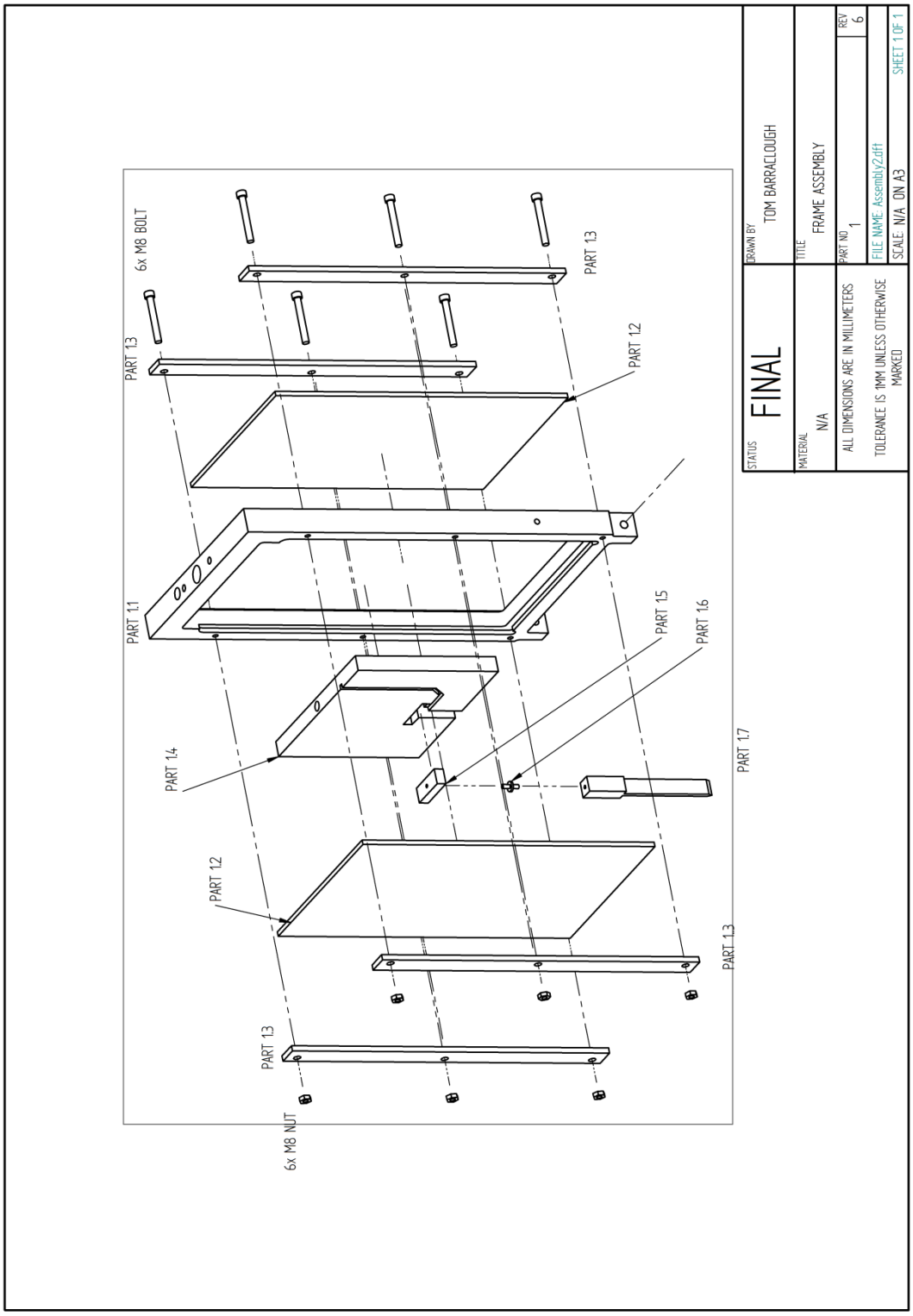
6x M8 BOLT
PART 13
PART 13
PART 12
PART 1.1
PART 1.5
PART 1.6
PART 14
PART 1.7
PART 12
PART 1.3
PART 13
6x M8 NUT
STATUS
FINAL
MATERIAL
N/A
ALL DIMENSIONS ARE IN MILLIMETERS
TOLERANCE IS 1MM UNLESS OTHERWISE MARKED
DRAWN BY
TOM BARRACLOUGH
TITLE
FRAME ASSEMBLY
PART NO
1
REV
6
FILE NAME Assembly2.dft
SCALE N/A ON A3
SHEET 1 OF 1

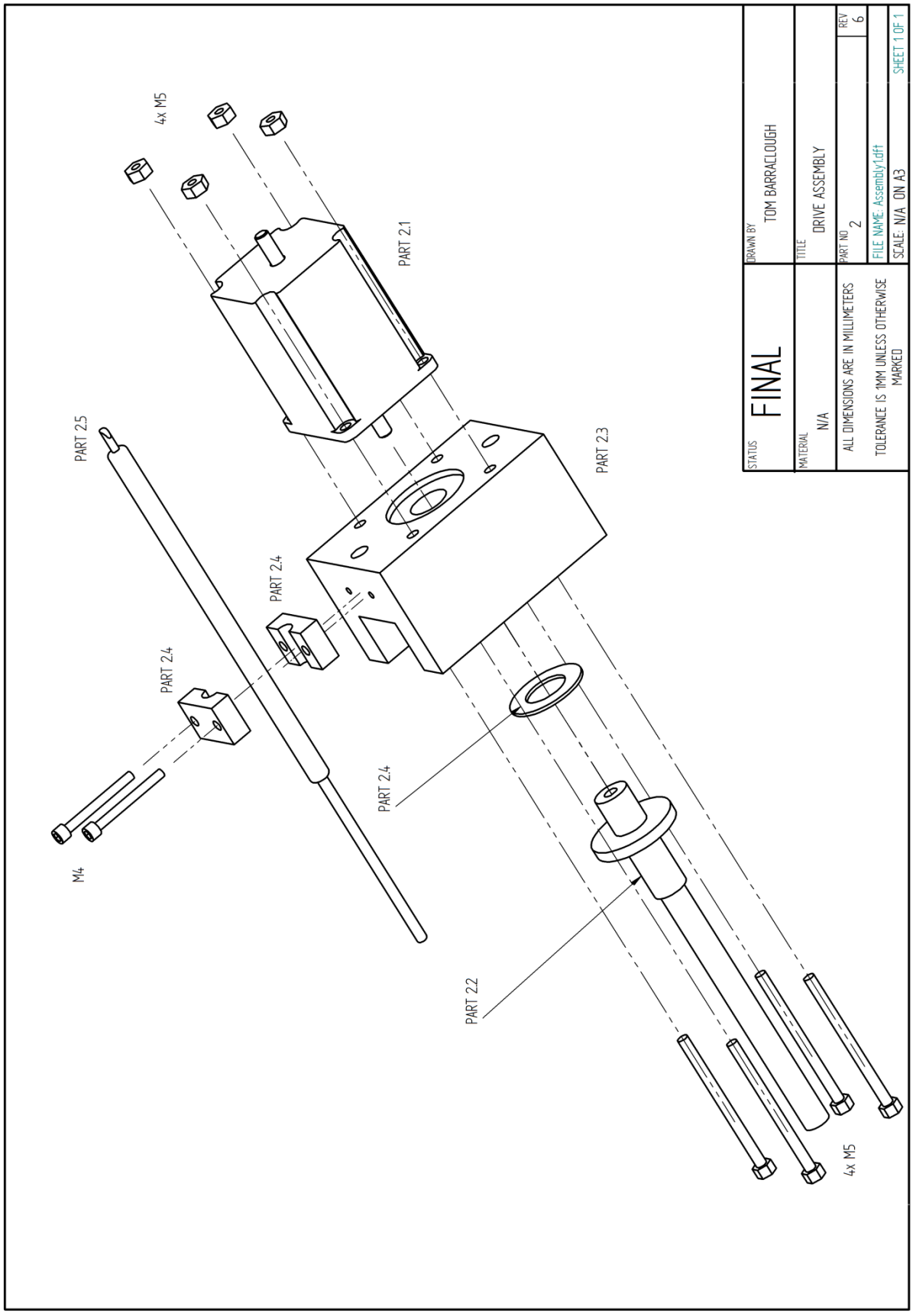
4x M5
PART 2.1
PART 2.5
PART 2.3
PART 2.4
PART 2.4
PART 2.4
M4
PART 2.2
4x M5
STATUS
FINAL
DRAWN BY
TOM BARRACLOUGH
MATERIAL
N/A
TITLE
DRIVE ASSEMBLY
PART NO
2
REV
6
ALL DIMENSIONS ARE IN MILLIMETERS
TOLERANCE IS 1MM UNLESS OTHERWISE MARKED
FILE NAME: Assembly1.dft
SCALE: N/A ON A3
SHEET 1 OF 1

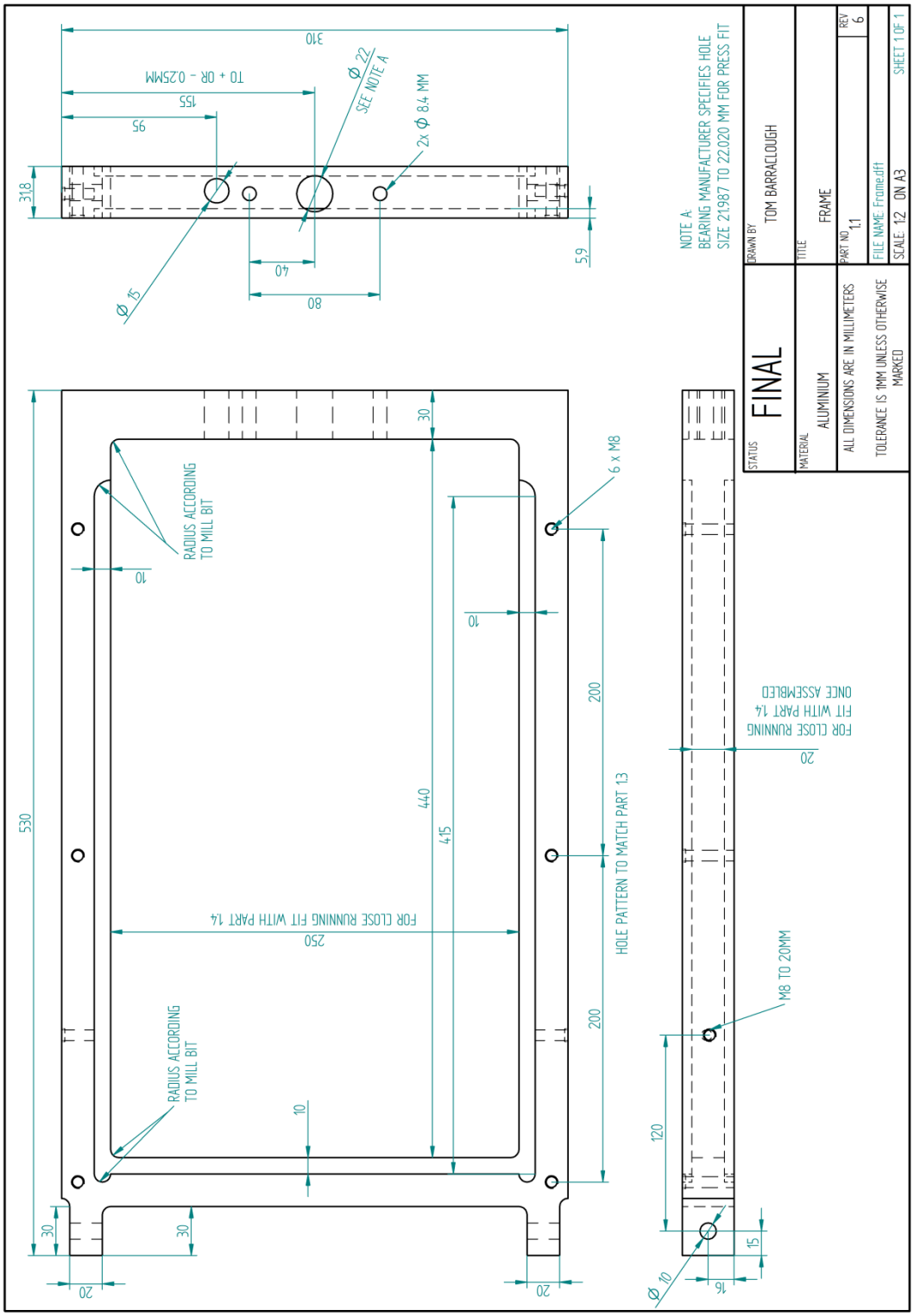
310
T0 + 0R - 0.25MM
155
95
Ø 22
SEE NOTE A
2x Ø 8.4 MM
318
5.9
Ø 15
40
80
NOTE A:
BEARING MANUFACTURER SPECIFIES HOLE
SIZE 21.987 TO 22.020 MM FOR PRESS FIT
DRAWN BY
TOM BARRACLOUGH
TITLE
FRAME
REV
6
PART NO.
1:1
STATUS
FINAL
MATERIAL
ALUMINIUM
ALL DIMENSIONS ARE IN MILLIMETERS
TOLERANCE IS 1MM UNLESS OTHERWISE MARKED
FILE NAME: Frame.dft
SCALE: 1:2 ON A3
SHEET 1 OF 1
530
30
RADIUS ACCORDING TO MILL BIT
10
6 x M8
200
440
415
HOLE PATTERN TO MATCH PART 13
FOR CLOSE RUNNING FIT WITH PART 14
250
RADIUS ACCORDING TO MILL BIT
10
30
30
20
20
FOR CLOSE RUNNING FIT WITH PART 14 ONCE ASSEMBLED
20
M8 TO 20MM
120
15
Ø 10
16

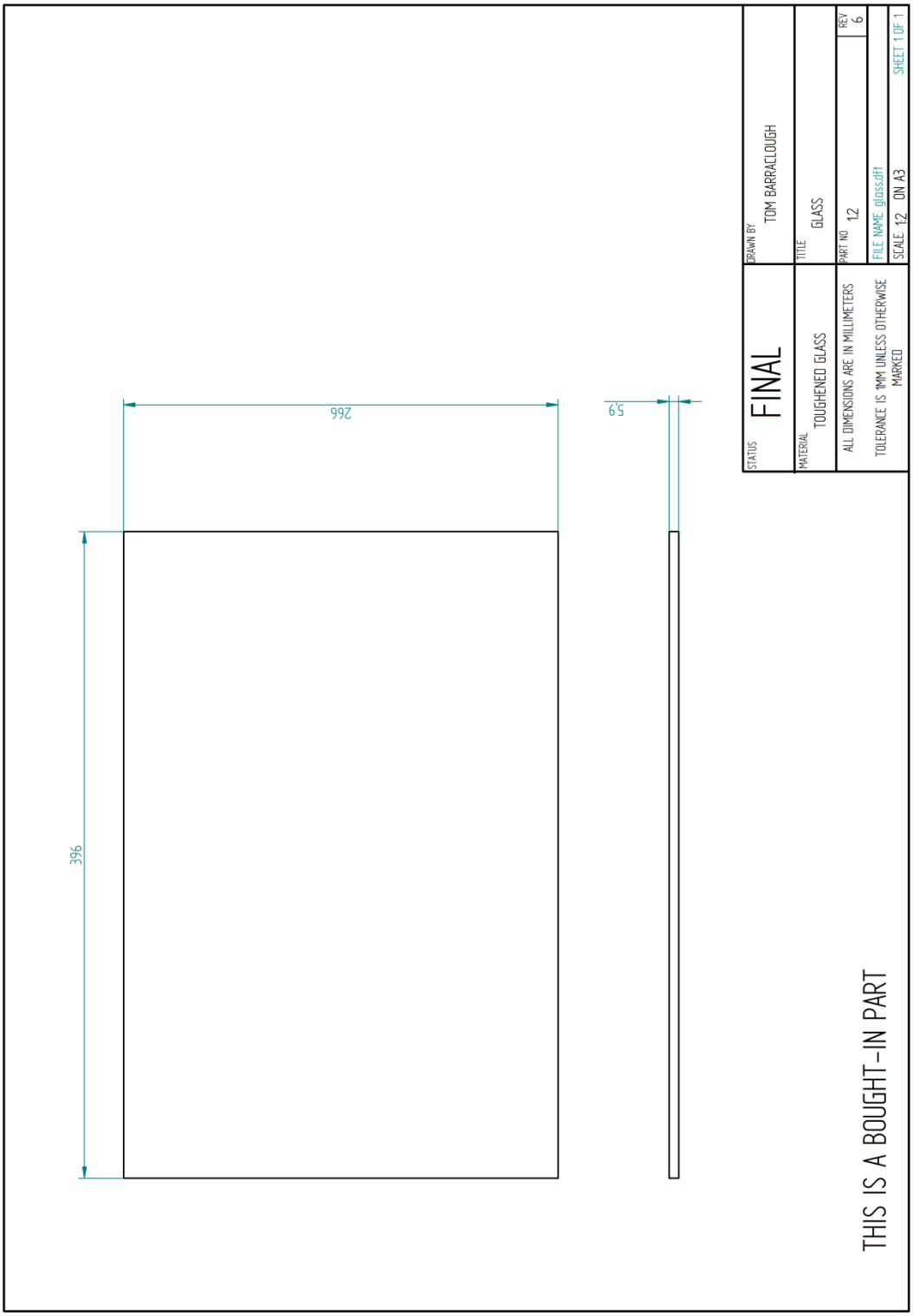
266
396
5.9
STATUS
FINAL
DRAWN BY
TOM BARRACLOUGH
MATERIAL
TOUGHENED GLASS
TITLE
GLASS
ALL DIMENSIONS ARE IN MILLIMETERS
PART NO
12
REV
6
TOLERANCE IS 1MM UNLESS OTHERWISE MARKED
FILE NAME: glass.dft
SCALE: 1:2 ON A3
SHEET 1 OF 1
THIS IS A BOUGHT-IN PART

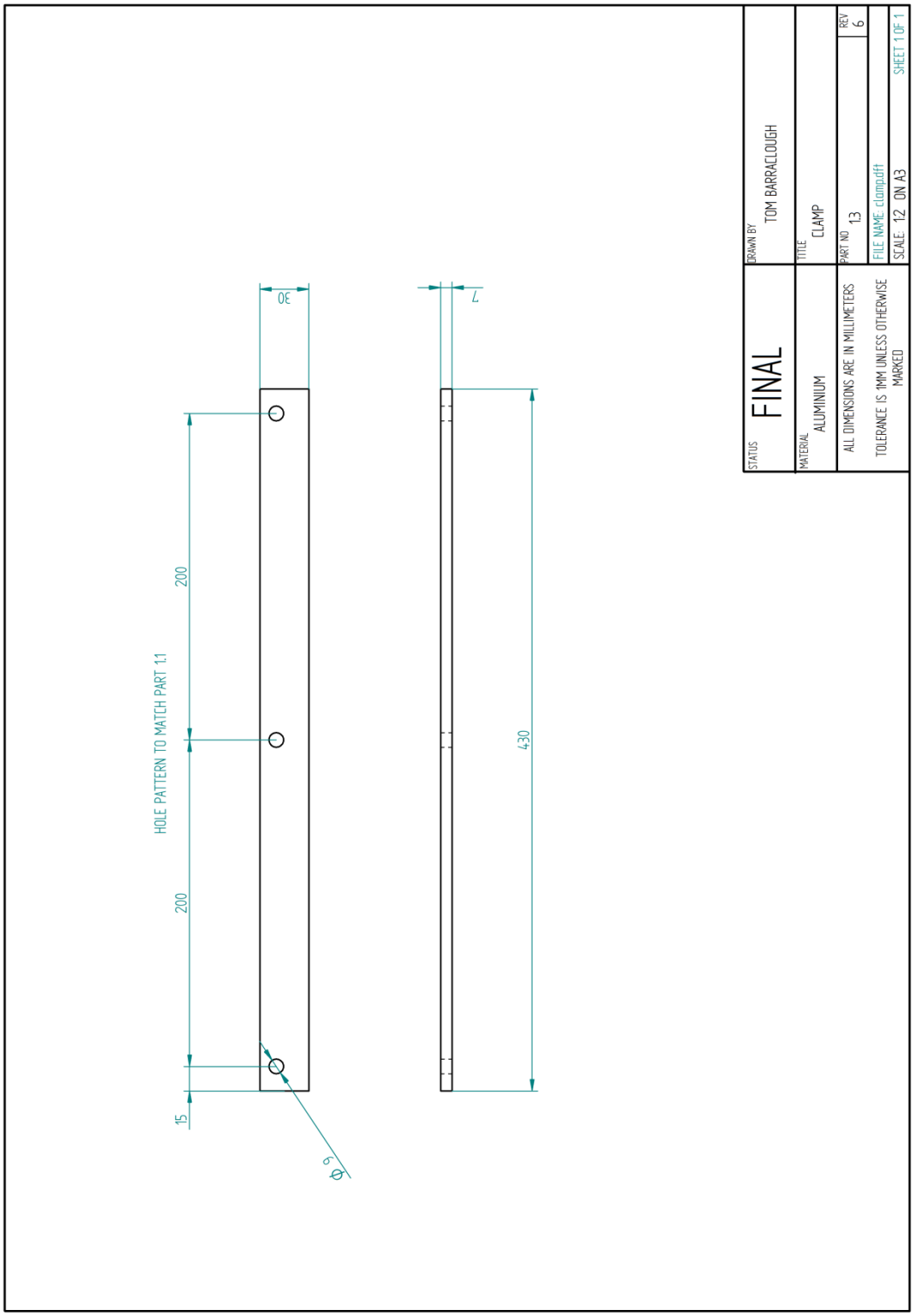
30
7
HOLE PATTERN TO MATCH PART 1:1
200
200
15
430
9
DRAWN BY
TOM BARRACLOUGH
TITLE
CLAMP
PART NO
1.3
REV
6
FILE NAME clamp.dft
SCALE 1:2 ON A3
SHEET 1 OF 1
STATUS
FINAL
MATERIAL
ALUMINIUM
ALL DIMENSIONS ARE IN MILLIMETERS
TOLERANCE IS 1MM UNLESS OTHERWISE MARKED

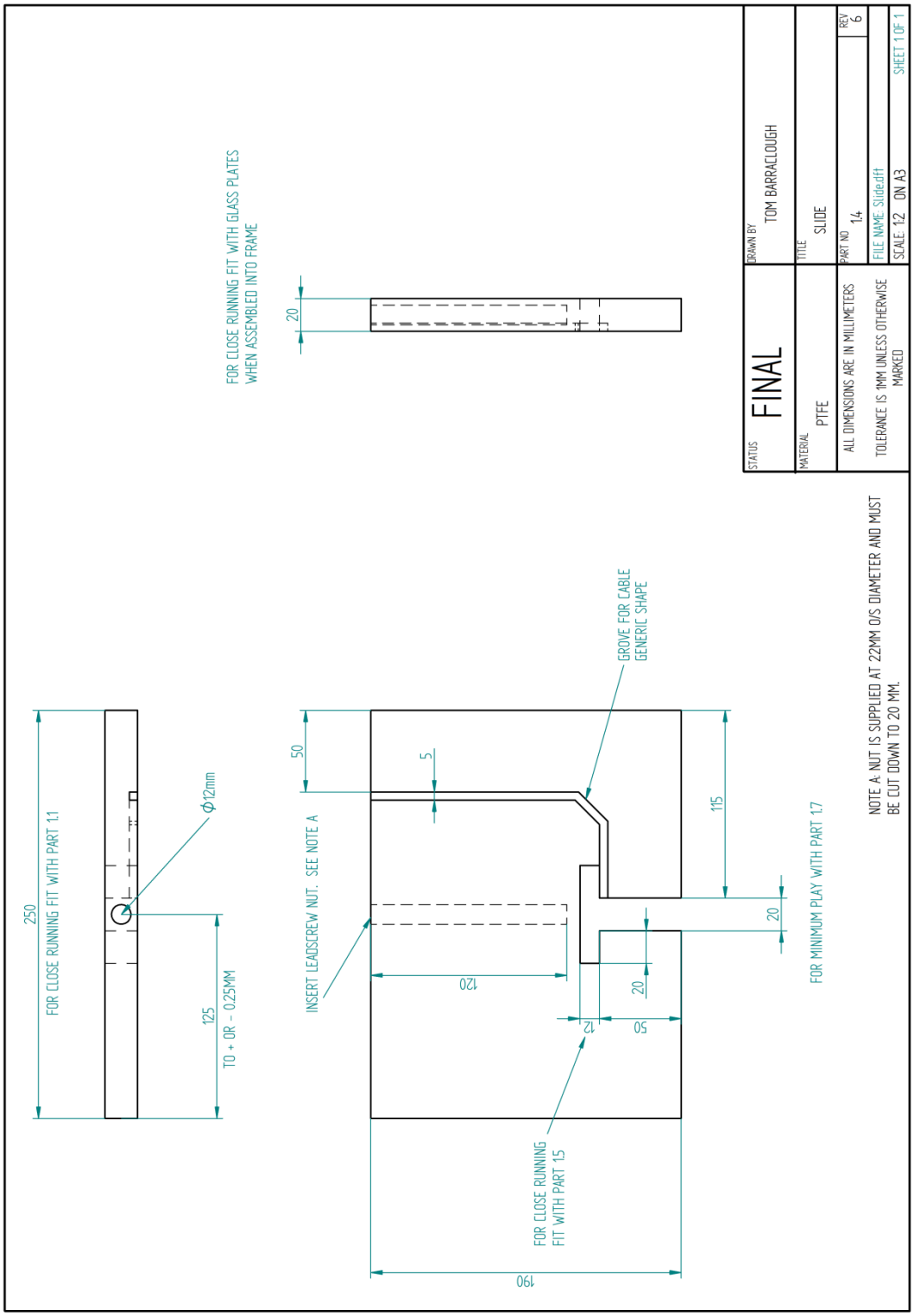
FOR CLOSE RUNNING FIT WITH GLASS PLATES
WHEN ASSEMBLED INTO FRAME
20
STATUS
FINAL
DRAWN BY
TOM BARRACLOUGH
MATERIAL
PTFE
TITLE
SLIDE
ALL DIMENSIONS ARE IN MILLIMETERS
PART NO
1.4
REV
6
TOLERANCE IS 1MM UNLESS OTHERWISE MARKED
FILE NAME: Slide.dft
SCALE: 1:2 ON A3
SHEET 1 OF 1
NOTE A: NUT IS SUPPLIED AT 22MM O/S DIAMETER AND MUST BE CUT DOWN TO 20 MM.
250
FOR CLOSE RUNNING FIT WITH PART 1.1
Φ12mm
125
TO + 0R - 0.25MM
50
5
INSERT LEADSCREW NUT. SEE NOTE A
GROVE FOR CABLE
GENERIC SHAPE
115
20
120
20
12
50
FOR MINIMUM PLAY WITH PART 1.7
FOR CLOSE RUNNING
FIT WITH PART 1.5
190

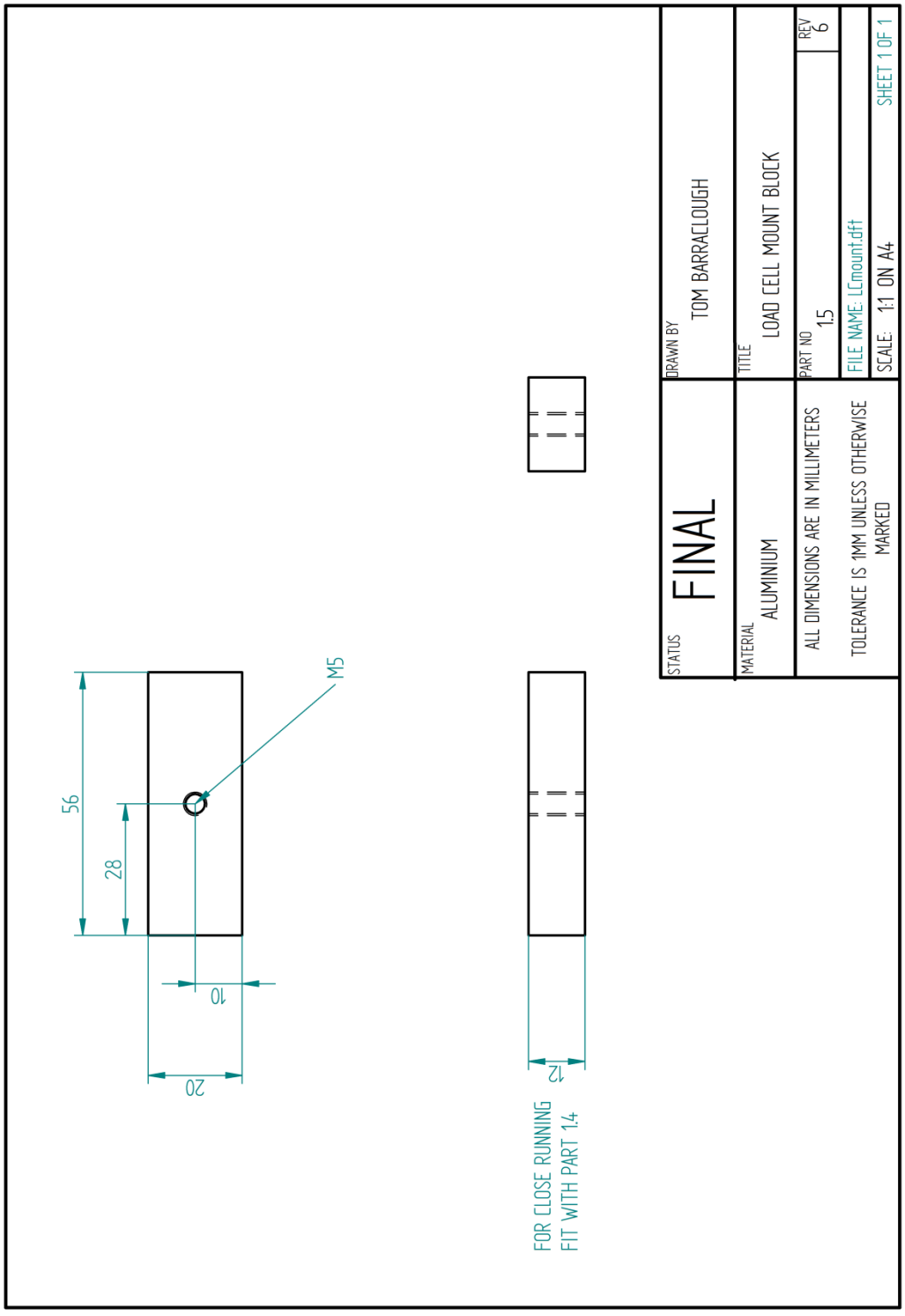
M5
56
28
10
20
12
FOR CLOSE RUNNING
FIT WITH PART 14
STATUS
FINAL
DRAWN BY
TOM BARRACLOUGH
MATERIAL
ALUMINIUM
TITLE
LOAD CELL MOUNT BLOCK
PART NO
1.5
REV
6
ALL DIMENSIONS ARE IN MILLIMETERS
TOLERANCE IS 1MM UNLESS OTHERWISE
MARKED
FILE NAME: LCmount.dft
SCALE: 1:1 ON A4
SHEET 1 OF 1

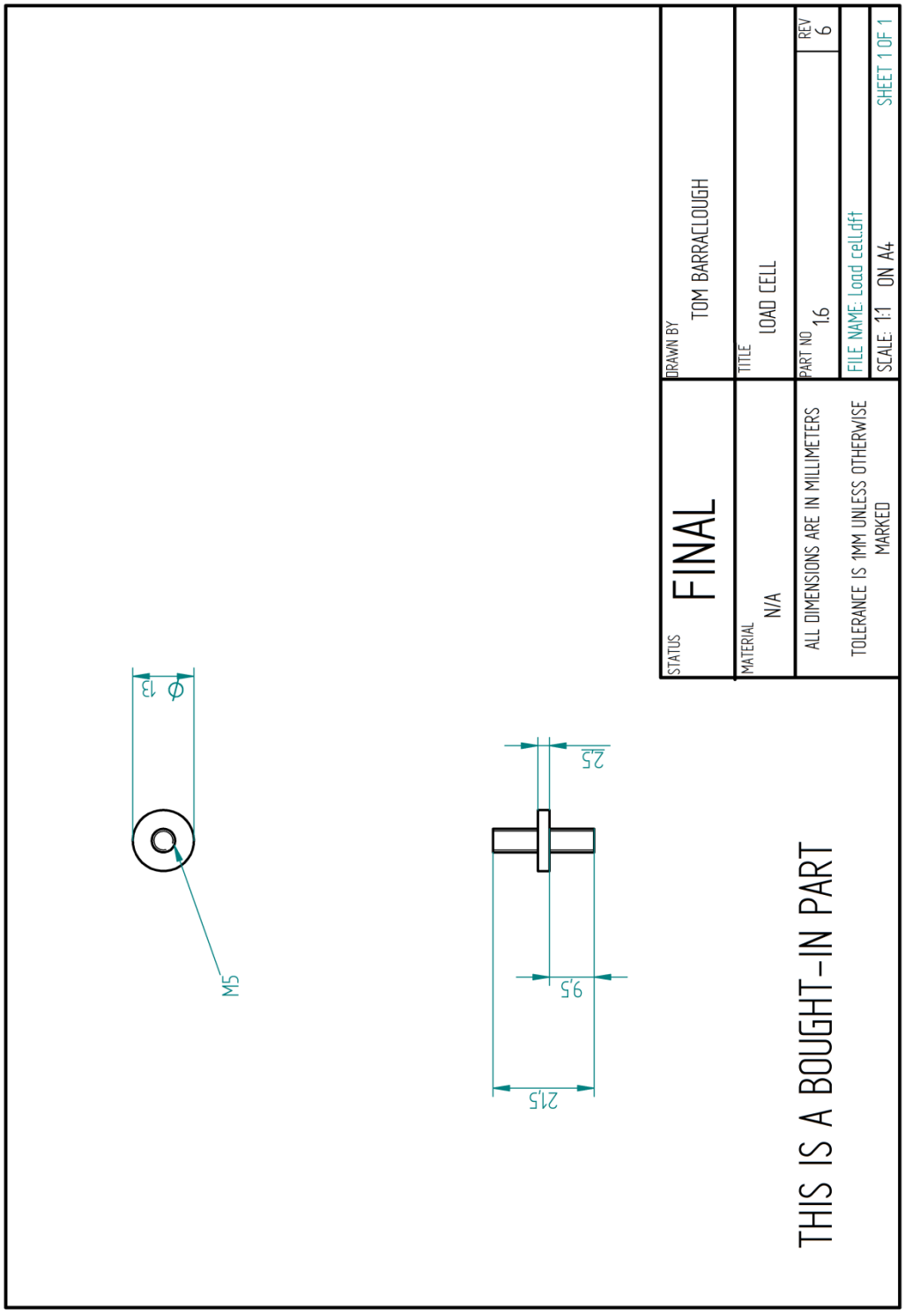
THIS IS A BOUGHT-IN PART
M5
ϕ 13
2.5
9.5
21.5
STATUS
FINAL
MATERIAL
N/A
DRAWN BY
TOM BARRACLOUGH
TITLE
LOAD CELL
PART NO
1.6
REV
6
ALL DIMENSIONS ARE IN MILLIMETERS
TOLERANCE IS 1MM UNLESS OTHERWISE MARKED
FILE NAME: Load cell.dft
SCALE: 1:1 ON A4
SHEET 1 OF 1

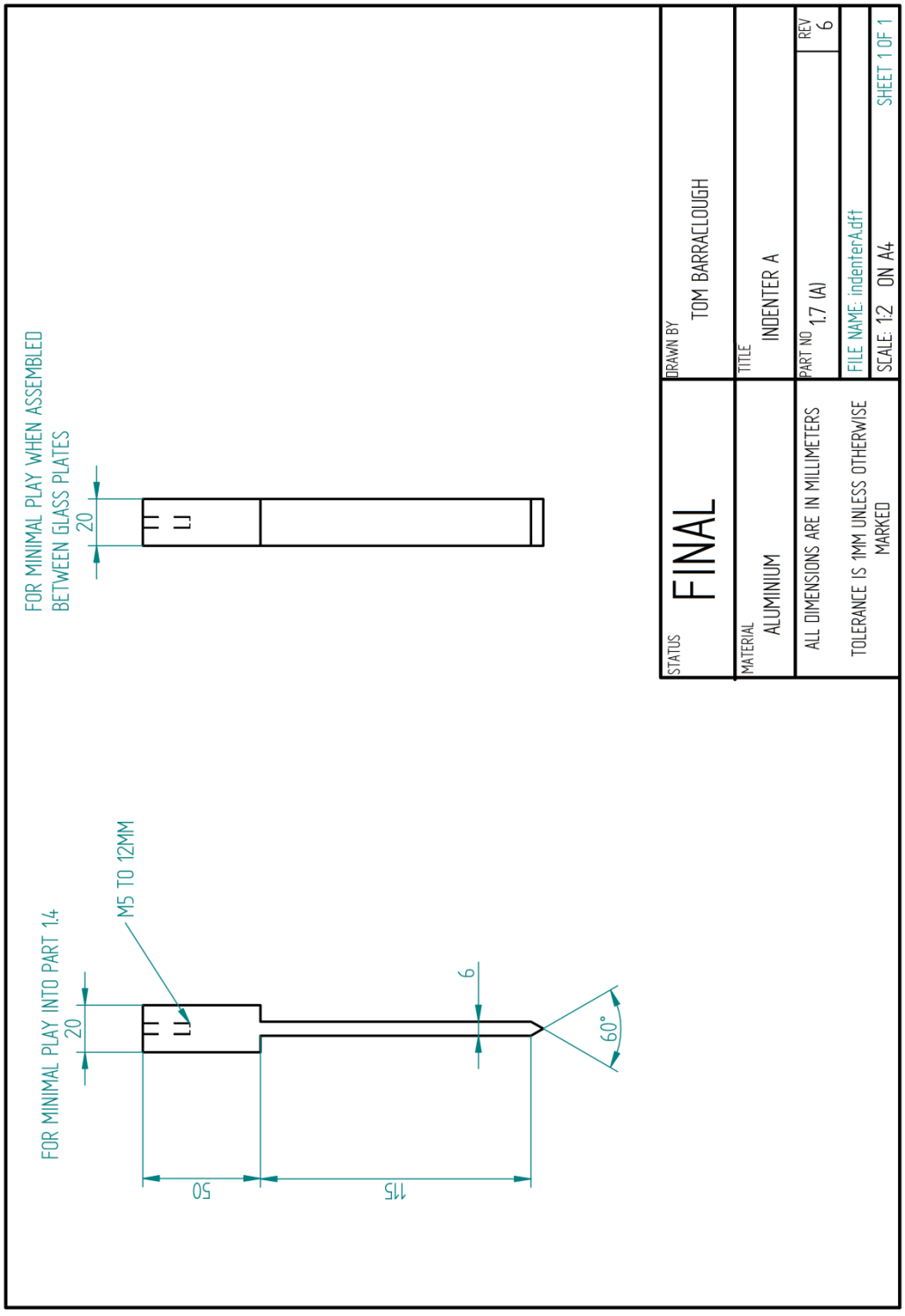
FOR MINIMAL PLAY WHEN ASSEMBLED
BETWEEN GLASS PLATES
20
FOR MINIMAL PLAY INTO PART 14
20
M5 TO 12MM
6
60°
50
115
STATUS
FINAL
MATERIAL
ALUMINIUM
DRAWN BY
TOM BARRACLOUGH
TITLE
INDENTER A
PART NO
1.7 (A)
REV
6
ALL DIMENSIONS ARE IN MILLIMETERS
TOLERANCE IS 1MM UNLESS OTHERWISE MARKED
FILE NAME: indenterA.dft
SCALE: 1:2 ON A4
SHEET 1 OF 1

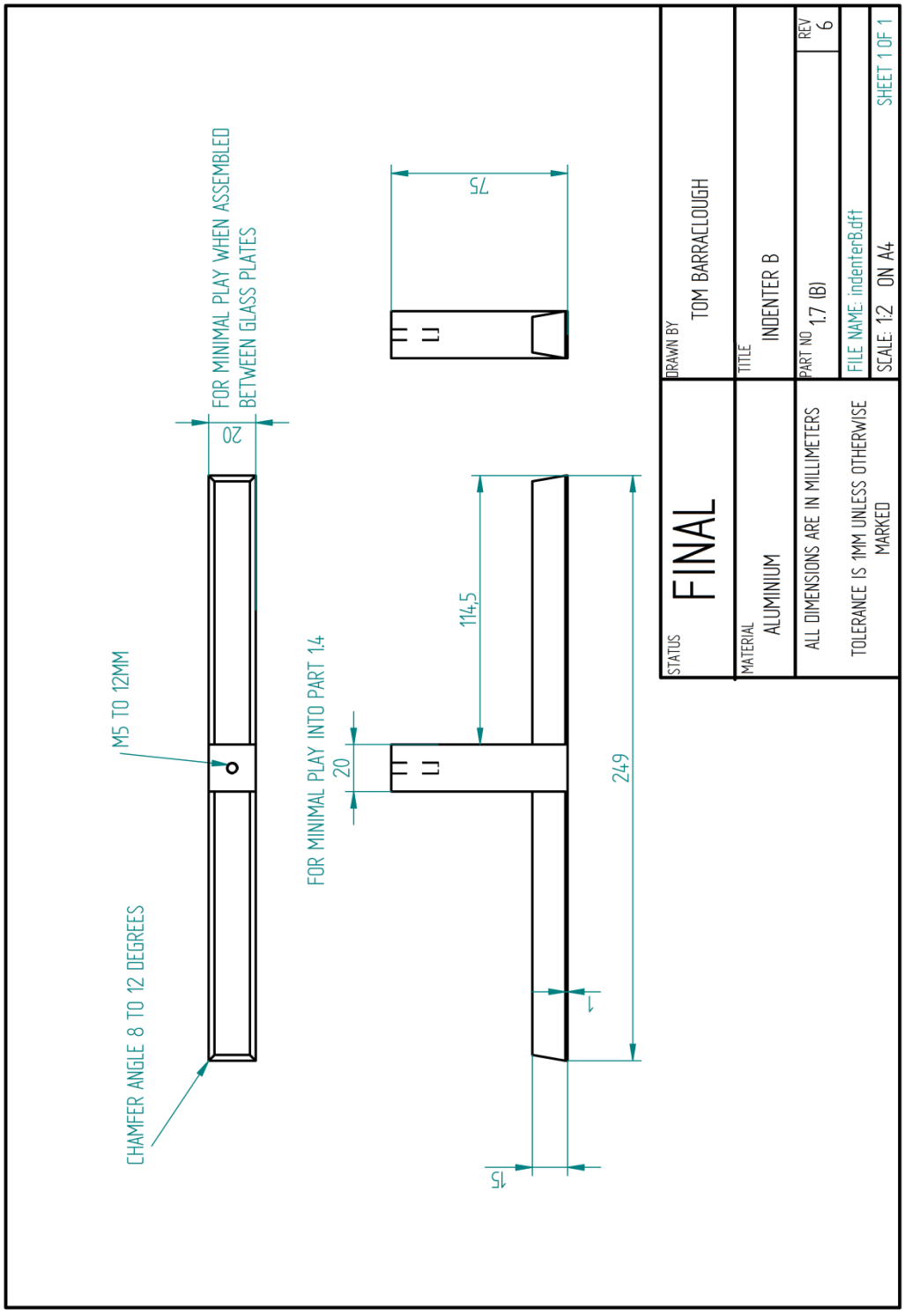
FOR MINIMAL PLAY WHEN ASSEMBLED
BETWEEN GLASS PLATES
20
75
M5 TO 12MM
CHAMFER ANGLE 8 TO 12 DEGREES
FOR MINIMAL PLAY INTO PART 1.4
20
114.5
249
1
15
STATUS
FINAL
MATERIAL
ALUMINIUM
DRAWN BY
TOM BARRACLOUGH
TITLE
INDENTER B
PART NO
1.7 (B)
REV
6
ALL DIMENSIONS ARE IN MILLIMETERS
TOLERANCE IS 1MM UNLESS OTHERWISE MARKED
FILE NAME: indenterB.dft
SCALE: 1:2 ON A4
SHEET 1 OF 1

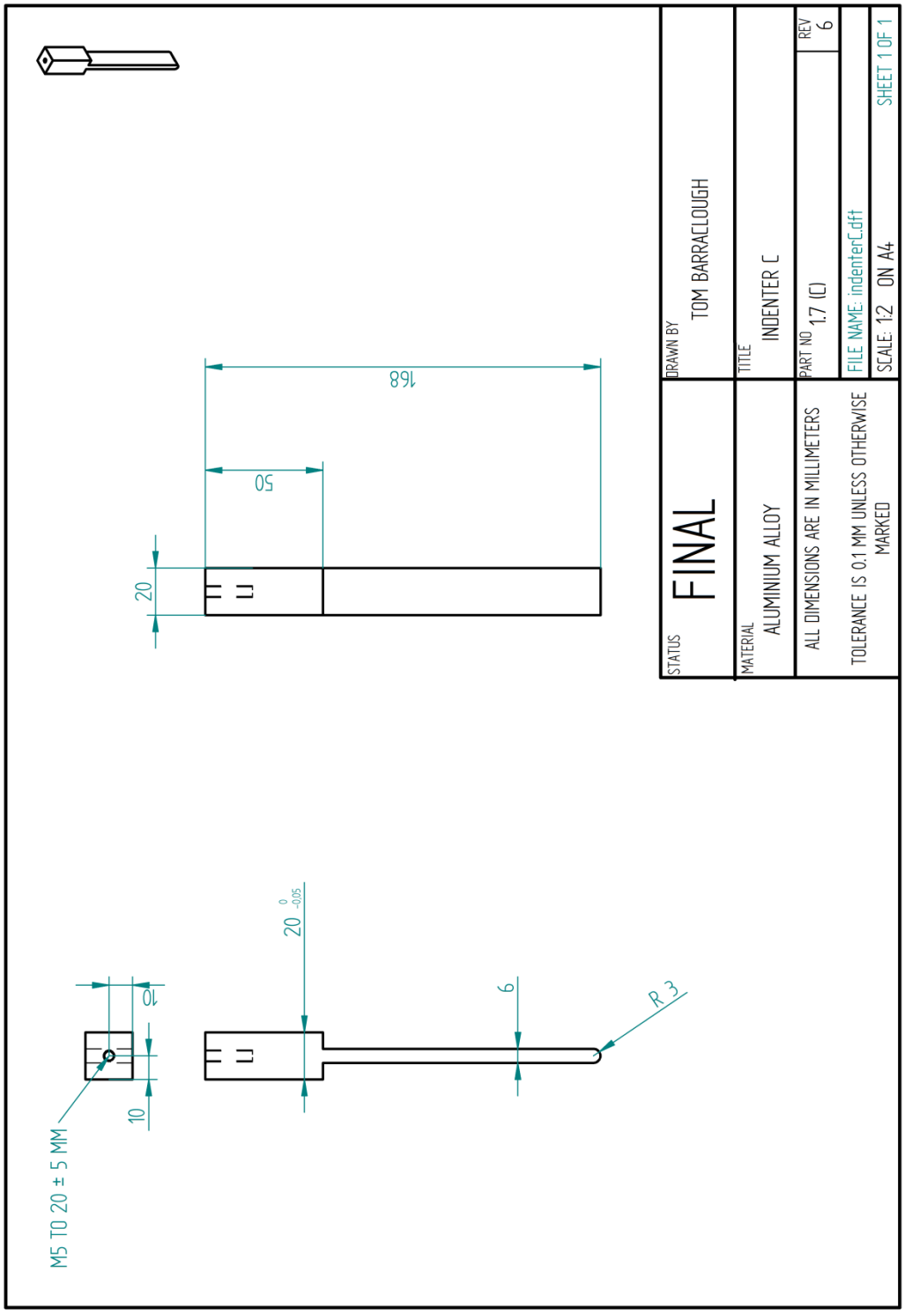
168
50
20
20 0 -0.05
6
R 3
10
10
M5 TO 20 ± 5 MM
STATUS FINAL
DRAWN BY TOM BARRACLOUGH
TITLE INDENTER C
MATERIAL ALUMINIUM ALLOY
PART NO 1.7 (C)
REV 6
ALL DIMENSIONS ARE IN MILLIMETERS
TOLERANCE IS 0.1 MM UNLESS OTHERWISE MARKED
FILE NAME: indenterC.dft
SCALE: 1:2 ON A4
SHEET 1 OF 1

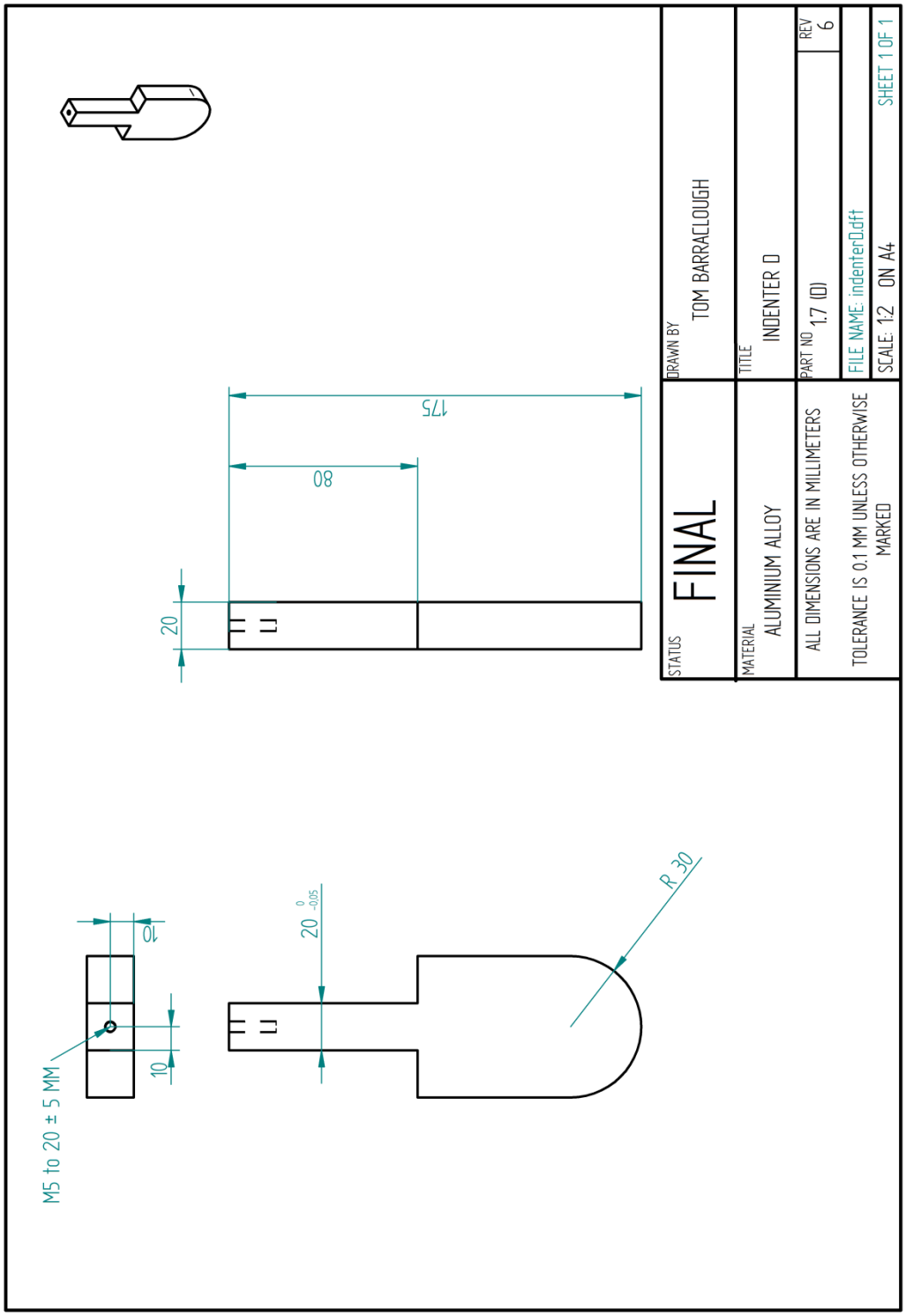
175
80
20
R 30
20 0 -0.05
10
10
M5 to 20 ± 5 MM
DRAWN BY
TOM BARRACLOUGH
TITLE
INDENTER D
PART NO
1.7 (D)
REV
6
FILE NAME: indenterD.dft
SCALE: 1:2 ON A4
SHEET 1 OF 1
STATUS
FINAL
MATERIAL
ALUMINIUM ALLOY
ALL DIMENSIONS ARE IN MILLIMETERS
TOLERANCE IS 0.1 MM UNLESS OTHERWISE MARKED

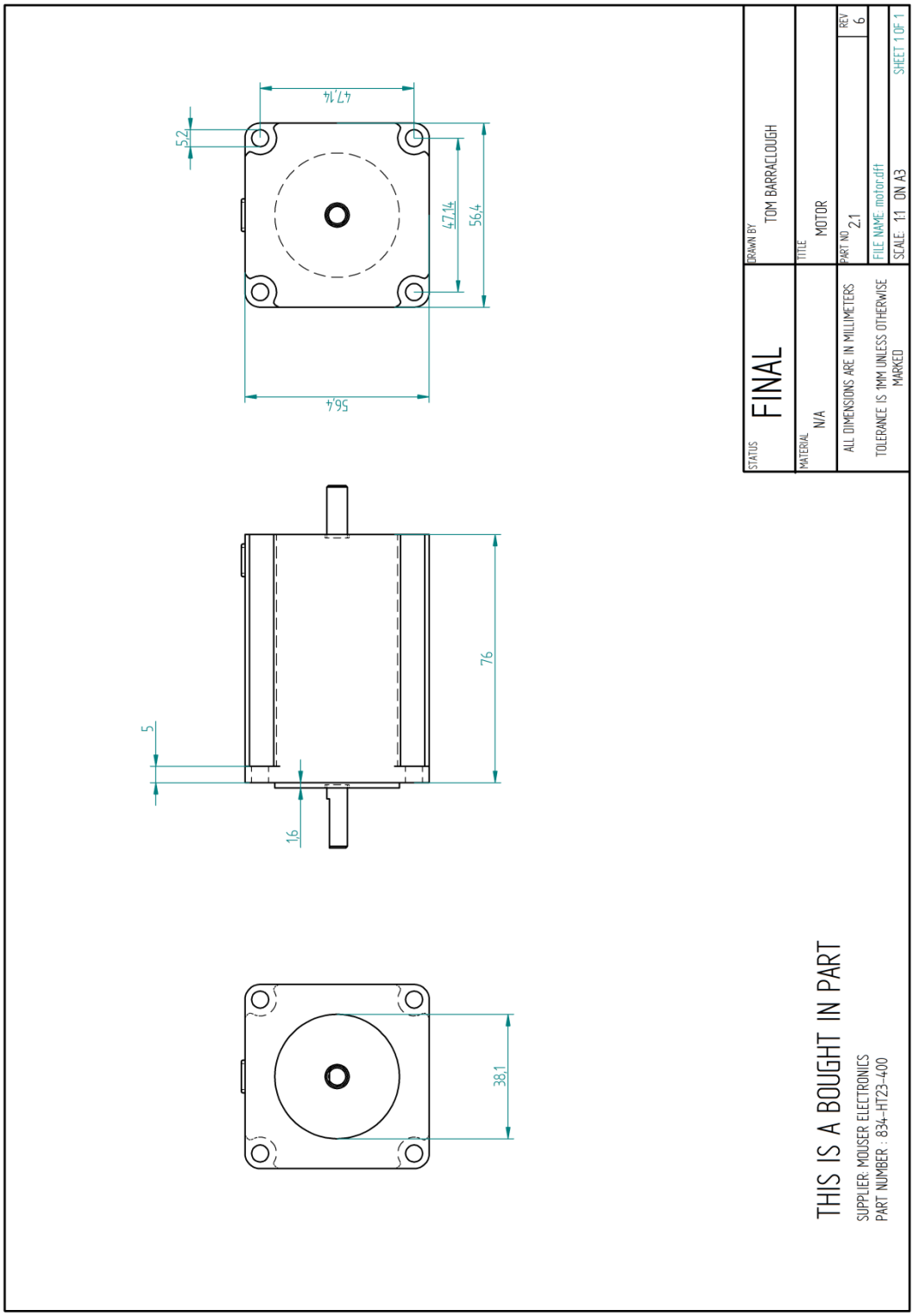
47,14
5,2
47,14
56,4
56,4
76
5
16
38,1
STATUS
FINAL
DRAWN BY
TOM BARRACLOUGH
MATERIAL
N/A
TITLE
MOTOR
ALL DIMENSIONS ARE IN MILLIMETERS
PART NO
2.1
REV
6
TOLERANCE IS 1MM UNLESS OTHERWISE MARKED
FILE NAME motor.dft
SCALE 1:1 ON A3
SHEET 1 OF 1
THIS IS A BOUGHT IN PART
SUPPLIER: MOUSER ELECTRONICS
PART NUMBER : 834-HT23-400

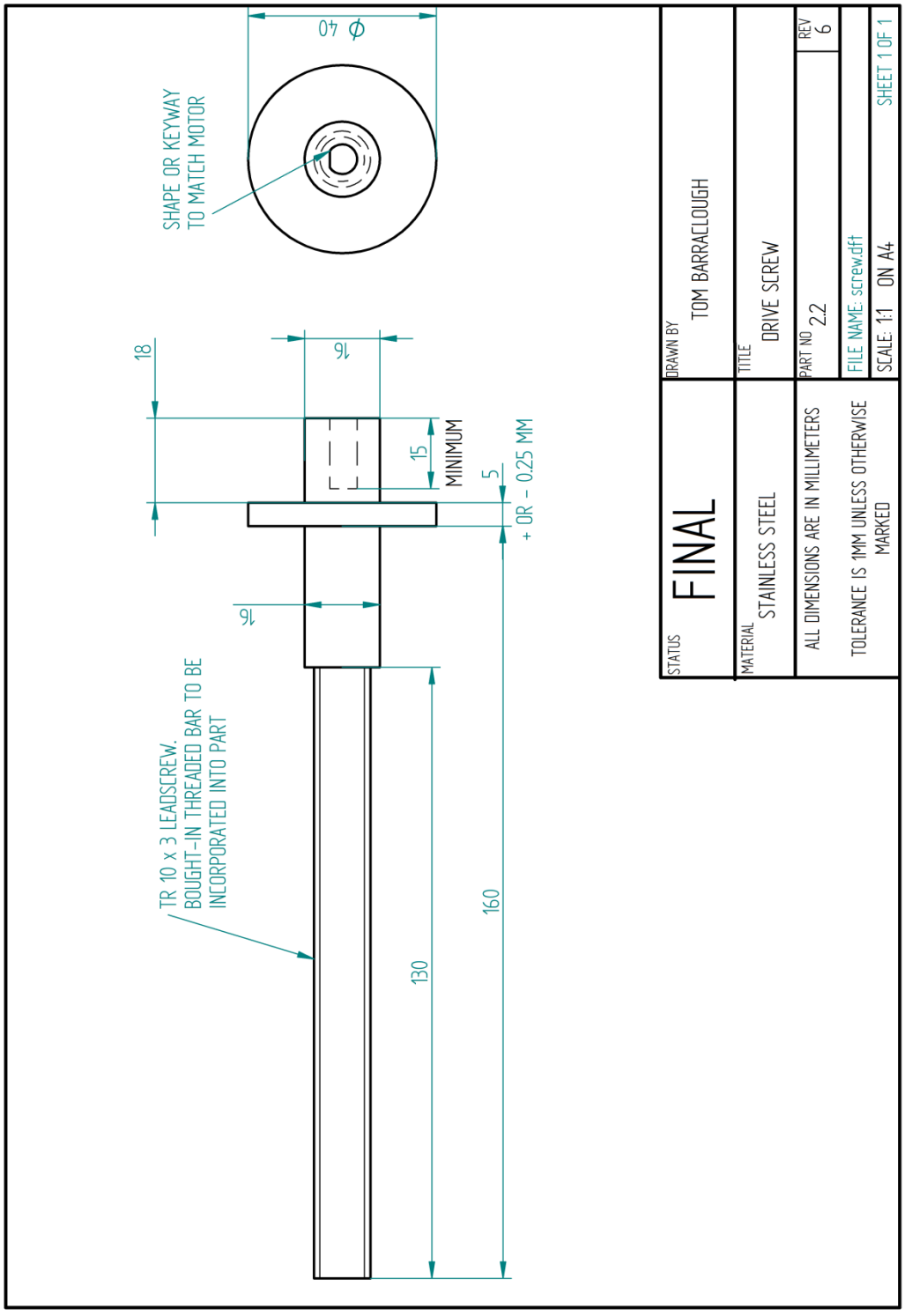
Ø 40
SHAPE OR KEYWAY
TO MATCH MOTOR
18
16
15
MINIMUM
5
+ OR - 0.25 MM
16
TR 10 x 3 LEADSCREW.
BOUGHT-IN THREADED BAR TO BE
INCORPORATED INTO PART
130
160
STATUS
FINAL
DRAWN BY
TOM BARRACLOUGH
MATERIAL
STAINLESS STEEL
TITLE
DRIVE SCREW
PART NO
2.2
REV
6
ALL DIMENSIONS ARE IN MILLIMETERS
TOLERANCE IS 1MM UNLESS OTHERWISE
MARKED
FILE NAME: screw.dft
SCALE: 1:1 ON A4
SHEET 1 OF 1

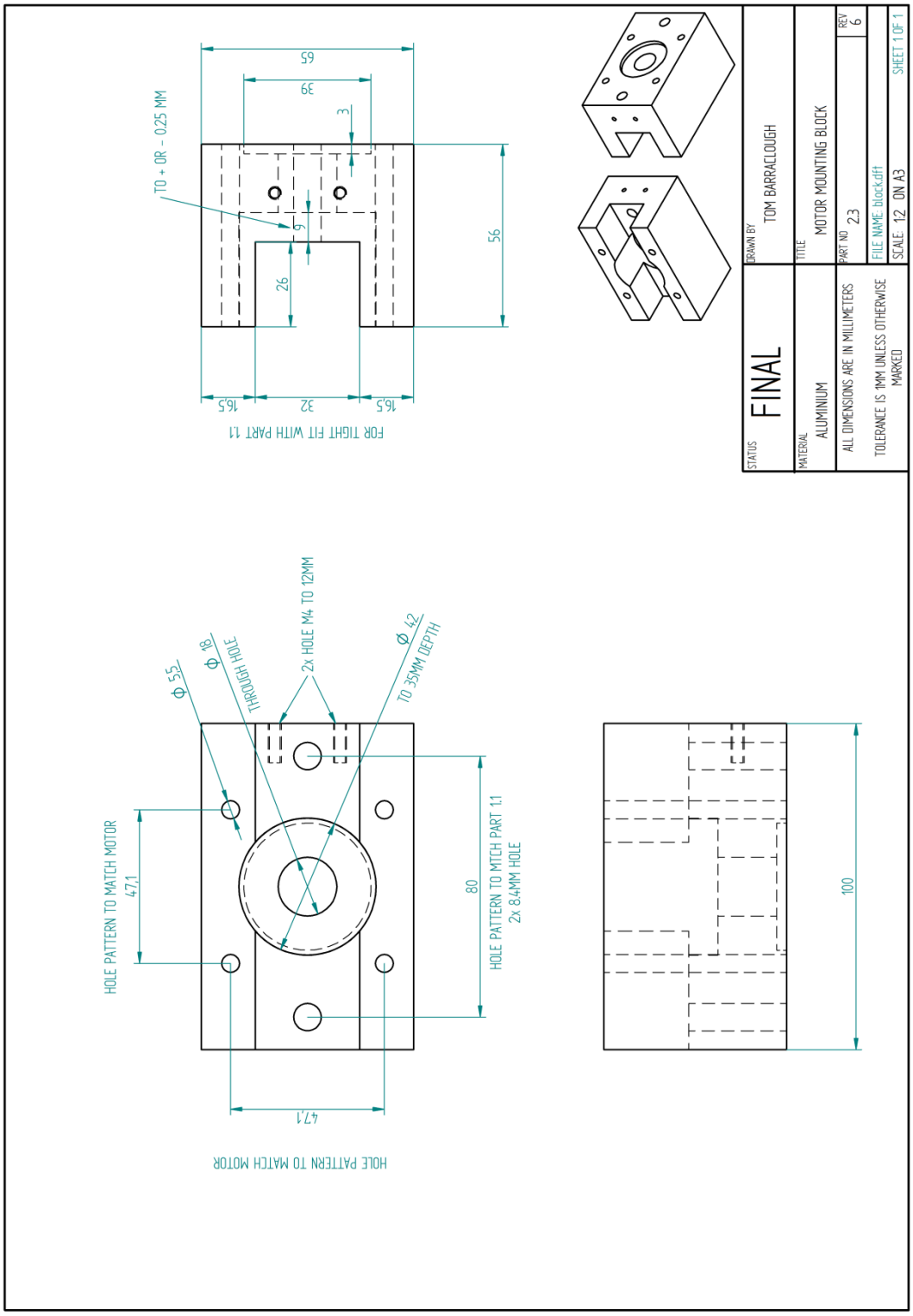
65
39
3
TO + OR - 0.25 MM
9
26
56
16.5
32
16.5
FOR TIGHT FIT WITH PART 1.1
STATUS
FINAL
DRAWN BY
TOM BARRACLOUGH
MATERIAL
ALUMINIUM
TITLE
MOTOR MOUNTING BLOCK
PART NO
2.3
REV
6
ALL DIMENSIONS ARE IN MILLIMETERS
TOLERANCE IS 1MM UNLESS OTHERWISE MARKED
FILE NAME block.dft
SCALE: 1:2 ON A3
SHEET 1 OF 1
Φ 55
Φ 18
THROUGH HOLE
2x HOLE M4 TO 12MM
Φ 42
TO 35MM DEPTH
HOLE PATTERN TO MATCH MOTOR
47.1
80
HOLE PATTERN TO MTCH PART 1.1
2x 8.4MM HOLE
47.1
HOLE PATTERN TO MATCH MOTOR
100

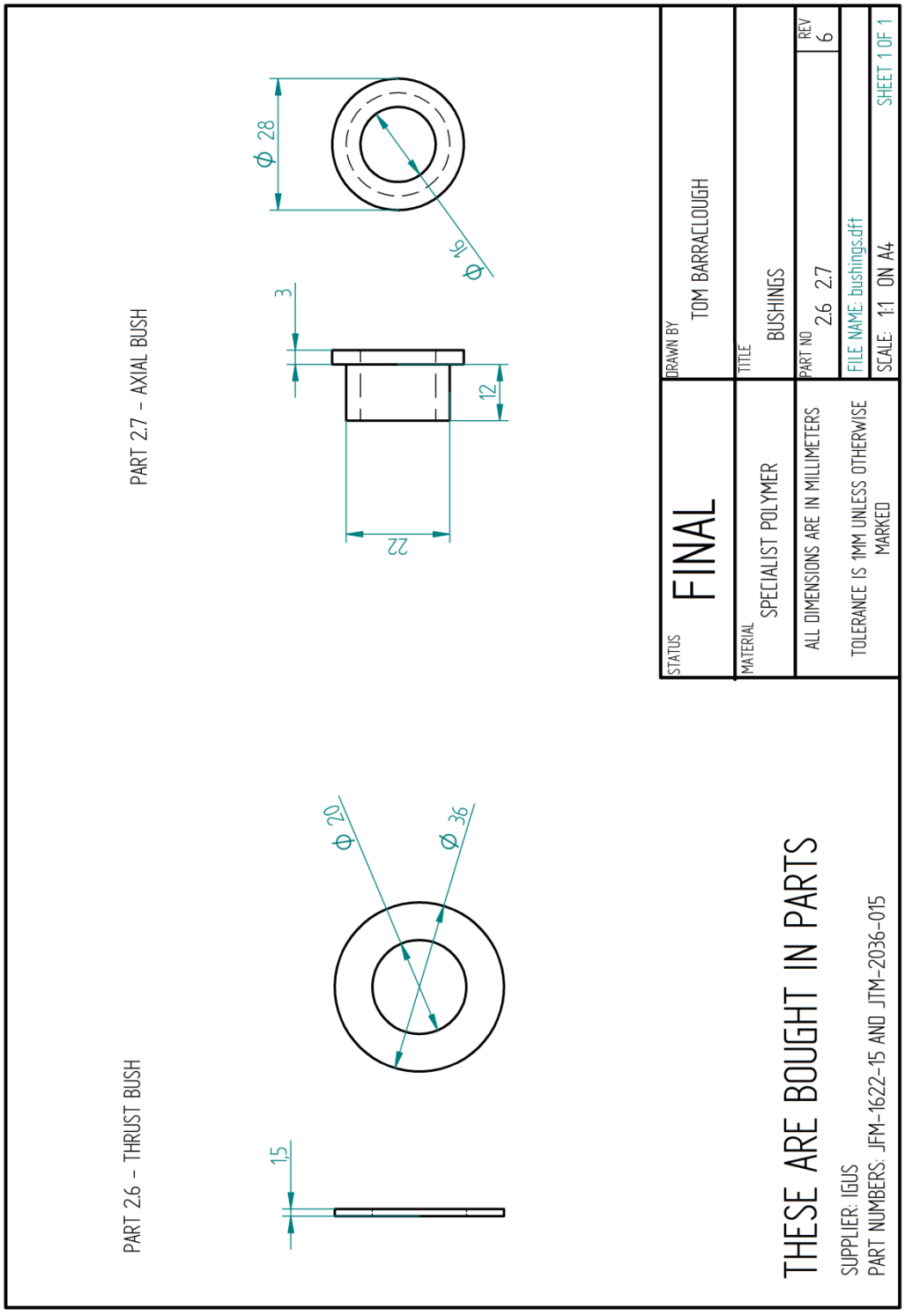
PART 2.7 - AXIAL BUSH
Φ 28
Φ 16
3
12
22
PART 2.6 - THRUST BUSH
Φ 20
Φ 36
1,5
THESE ARE BOUGHT IN PARTS
SUPPLIER: IGUS
PART NUMBERS: JFM-1622-15 AND JTM-2036-015
STATUS FINAL
DRAWN BY TOM BARRACLOUGH
MATERIAL SPECIALIST POLYMER
TITLE BUSHINGS
PART NO 2.6 2.7
REV 6
ALL DIMENSIONS ARE IN MILLIMETERS
TOLERANCE IS 1MM UNLESS OTHERWISE MARKED
FILE NAME: bushings.dft
SCALE: 1:1 ON A4
SHEET 1 OF 1

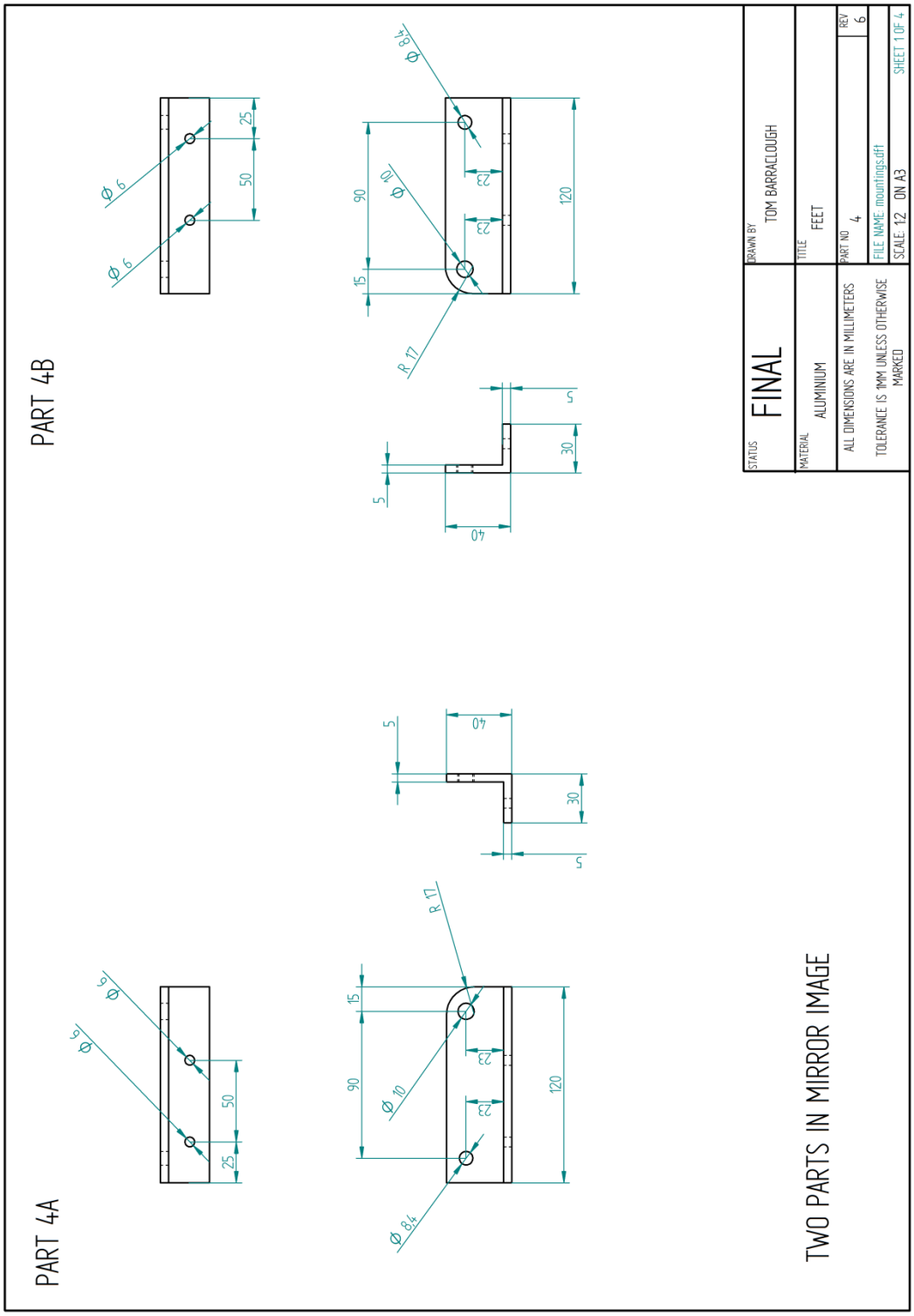
PART 4B
PART 4A
TWO PARTS IN MIRROR IMAGE
STATUS FINAL
DRAWN BY TOM BARRACLOUGH
TITLE FEET
MATERIAL ALUMINIUM
PART NO 4
REV 6
ALL DIMENSIONS ARE IN MILLIMETERS
TOLERANCE IS 1MM UNLESS OTHERWISE MARKED
FILE NAME: mountings.dft
SCALE 1:2 ON A3
SHEET 1 OF 4

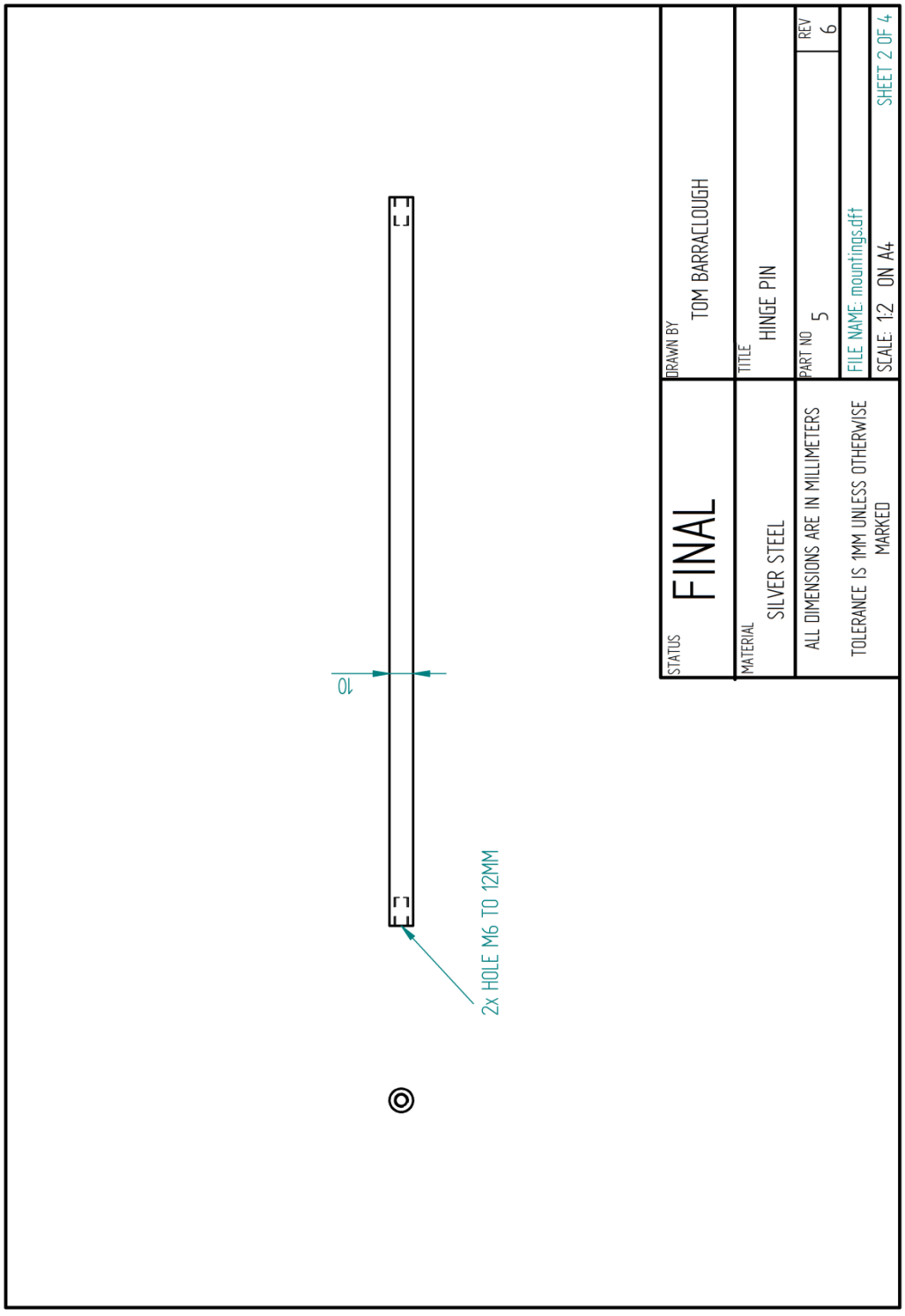
10
2x HOLE M6 TO 12MM
STATUS
FINAL
DRAWN BY
TOM BARRACLOUGH
MATERIAL
SILVER STEEL
TITLE
HINGE PIN
PART NO
5
REV
6
ALL DIMENSIONS ARE IN MILLIMETERS
TOLERANCE IS 1MM UNLESS OTHERWISE MARKED
FILE NAME: mountings.dft
SCALE: 1:2 ON A4
SHEET 2 OF 4

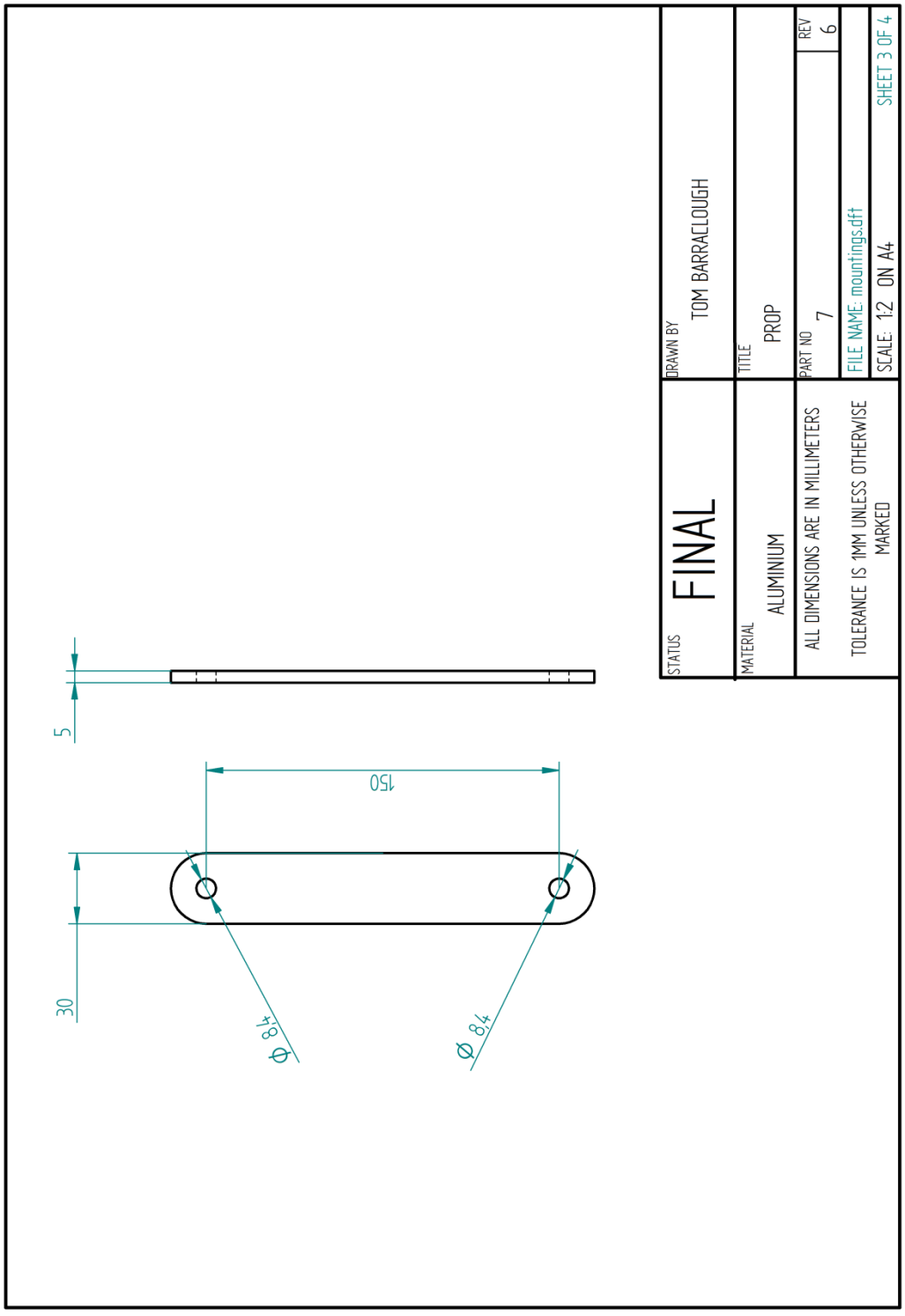
5
150
30
Ø 84
Ø 84
STATUS
FINAL
DRAWN BY
TOM BARRACLOUGH
MATERIAL
ALUMINIUM
TITLE
PROP
PART NO
7
REV
6
ALL DIMENSIONS ARE IN MILLIMETERS
TOLERANCE IS 1MM UNLESS OTHERWISE MARKED
FILE NAME: mountings.dft
SCALE: 1:2 ON A4
SHEET 3 OF 4

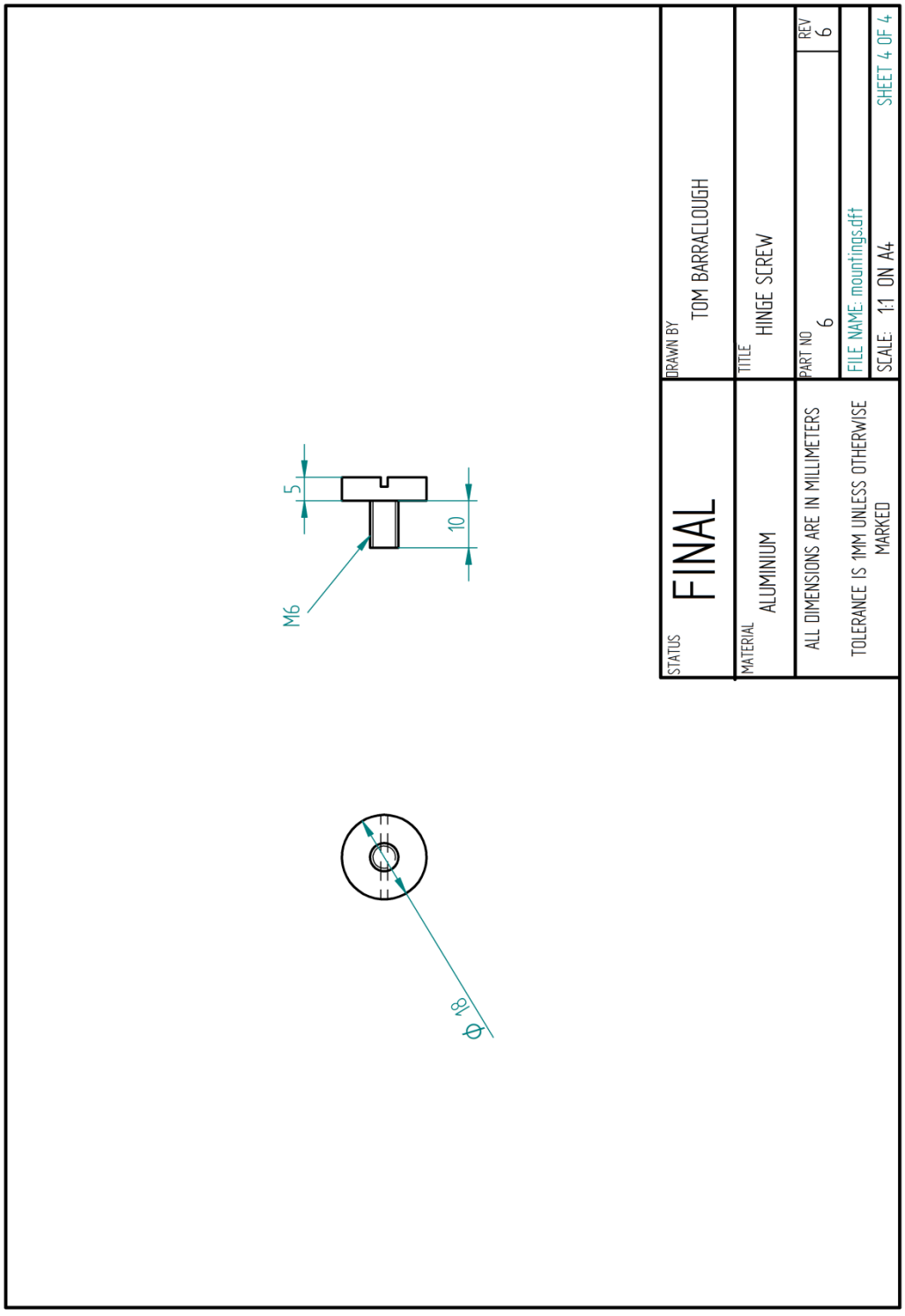
5
10
M6
Φ18
STATUS FINAL
DRAWN BY TOM BARRACLOUGH
MATERIAL ALUMINIUM
TITLE HINGE SCREW
PART NO 6
REV 6
ALL DIMENSIONS ARE IN MILLIMETERS
TOLERANCE IS 1MM UNLESS OTHERWISE MARKED
FILE NAME: mountings.dft
SCALE: 1:1 ON A4
SHEET 4 OF 4

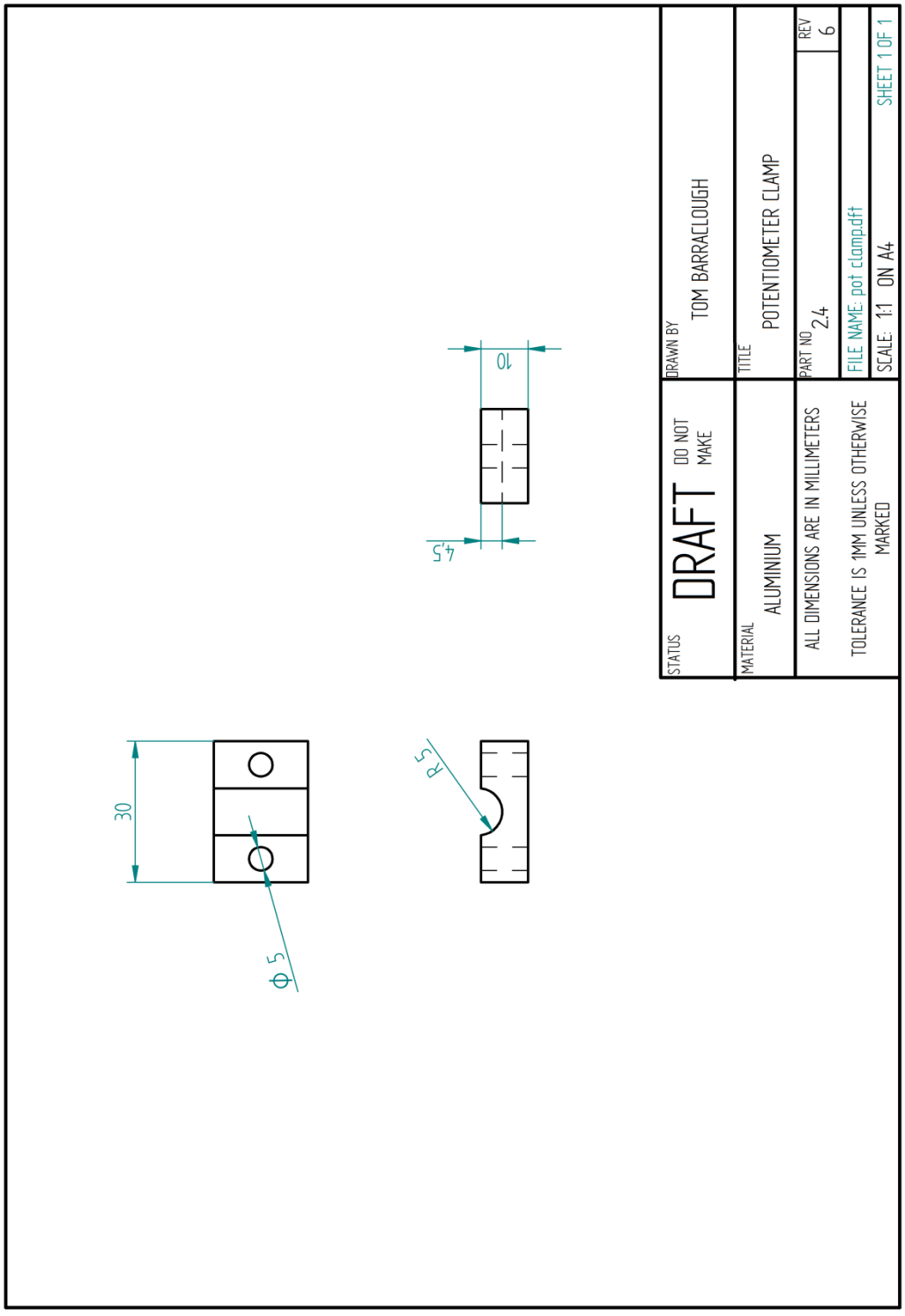
10
4,5
30
Φ5
R5
STATUS
DRAFT
DO NOT MAKE
DRAWN BY
TOM BARRACLOUGH
MATERIAL
ALUMINIUM
TITLE
POTENTIOMETER CLAMP
PART NO
2.4
REV
6
ALL DIMENSIONS ARE IN MILLIMETERS
TOLERANCE IS 1MM UNLESS OTHERWISE MARKED
FILE NAME: pot clamp.dft
SCALE: 1:1 ON A4
SHEET 1 OF 1

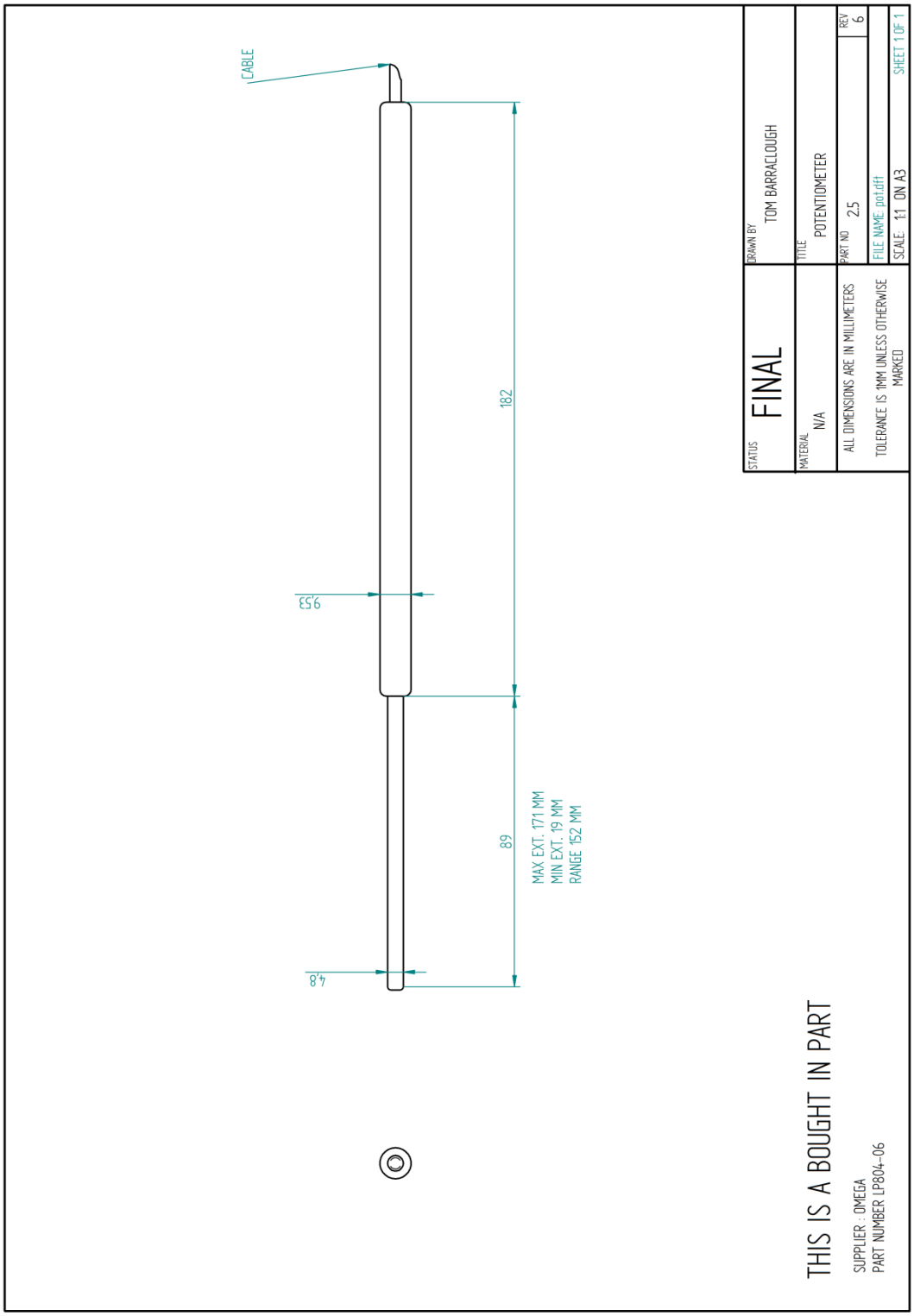
CABLE
182
9.53
89
MAX EXT. 171 MM
MIN EXT. 19 MM
RANGE 152 MM
4.8
THIS IS A BOUGHT IN PART
SUPPLIER : OMEGA
PART NUMBER LP804-06
STATUS FINAL
MATERIAL N/A
DRAWN BY TOM BARRACLOUGH
TITLE POTENTIOMETER
PART NO 2.5
REV 6
ALL DIMENSIONS ARE IN MILLIMETERS
TOLERANCE IS 1MM UNLESS OTHERWISE MARKED
FILE NAME pot.dft
SCALE 1:1 ON A3
SHEET 1 OF 1